UNIVERSIDAD POLITÉCNICA DE MADRID
Escuela Técnica Superior de Ingenieros Industriales

High Power Density, Low-Profile Three-Phase LLC Converters for Next-Generation Aircraft DC Power Systems

DOCTORAL THESIS

Submitted for the degree of Doctor by:

Daniel Ríos Linares

Máster Universitario en Ingeniería Electrónica
Escuela Técnica Superior de Ingenieros Industriales
Universidad Politécnica de Madrid

Madrid, 2025

UNIVERSIDAD POLITÉCNICA DE MADRID
Escuela Técnica Superior de Ingenieros Industriales

Doctoral Degree in Electrical and Electronic Engineering

High Power Density, Low-Profile Three-Phase LLC Converters for Next-Generation Aircraft DC Power Systems

DOCTORAL THESIS

Submitted for the degree of Doctor by:

Daniel Ríos Linares

Máster Universitario en Ingeniería Electrónica Industrial
Escuela Técnica Superior de Ingenieros Industriales
Universidad Politécnica de Madrid

Under the supervision of:

Dr. Miroslav Vasić (Supervisor)

Madrid, 2025

Title: High Power Density, Low-Profile Three-Phase LLC Converters for Next-Generation Aircraft DC Power Systems
Author: Daniel Ríos Linares
Doctoral Programme: Electrical and Electronic Engineering

Thesis Supervision:

Dr. Miroslav Vasić, CEIMM UPM (Supervisor)

External Reviewers:

Thesis Defense Committee:

Thesis Defense Date:

This thesis has been partially supported by the Spanish Ministry of Science and Innovation: Project PID2020-117582RB-I00, also known as Wi-Batt Project, that has been financed by MICIU/AEI/10.13039/501100011033; and by the Spanish Ministry of Universities through the FPI grant intended for forming researchers: Reference PRE2021-099407.

Acknowledgments

Every person has their first memory. Mine involves biting and getting shocked by a coaxial cable used for TV. Do not judge me, it was before I was able to stand on my two feet. But discovering the wonders of electricity this way is not the reason for my choice to start a career in electronics, it is most certain that my parents are to blame for this decision. My father José Ríos Martín, an electronics teacher himself, and my mother María Dolores Linares Manzano, a teacher of technology, both being inventive in their day to day probably had the most impact in me.

I met Miroslav Vasić, my mentor on this work, when I was searching for a topic for my master's thesis. I approached it with the determination of working at the highest voltage I could find. Looking back, I see much of my work as a series of mistakes, blunders, and serious oversights. Yet, each failure never occurred for the same reason.

He must had seen some potential however, because one year passed, and I became a PhD student of his. I started at the same time as Nikola Mirković, my laboratory companion throughout the journey. During the following years, we would share with each other an endless share of ideas, some brilliant, some questionable, and a fair number that revealed their absurdity after a small piece of paper.

There, I would meet also some more people, special place belongs to Carlos Jiménez Guerra and Miguel Ángel Moya Garrido, whom I consider my friends.

Another person I cannot omit from thanking is Alberto Delgado Expósito, after all of my interrogation about magnetics I am probably just a copy-paste version of his brain regarding that matter.

My most sincere encouragement and support to all of the PhD students in the laboratory after me: Gabriel Luis Maldonado Roldán, Xianghao Mo, Álvaro Rodríguez Fuentes, Lufan Zhou, Luis Ruiz Chamorro and Alexander Francisco de Miguel Lamminen. Best wishes also to Lucía Clavero Ordóñez and Miguel Astudillo Martínez, who are working abroad.

My appreciation also goes to my colleagues at *Università degli Studi di Padova*, special thanks to Professor Paolo Mattavelli for giving me the opportunity to work with his team during my three-month stay. I am also grateful to Tommaso Caldognetto and Matteo Vazzoler for their invaluable help throughout the work.

Thanks to my closest friends from Granada: Jésica Trinidad Sevilla Vázquez, capable of writing my biography better than I can; Adrián Leyva Martín, my oldest friend; Guillermo Alcalde Barros, the kind; and Antonio Ruiz Avilés, the wise.

Abstract

The increasing electrification of aircraft imposes demanding constraints on on-board power conversion. Converters must achieve high power density and efficiency while meeting stringent electromagnetic compatibility limits and operating within low-profile formats. The LLC resonant converter family is well suited to these requirements due to its intrinsic zero-voltage switching across the load range, enabling high-frequency operation and compact magnetics. The main challenge is the very large step-down typically required in aircraft DC distribution: from 235 V to 285 V nominal down to a tightly regulated 28 V. Achieving this conversion with a low-profile transformer, minimal filtering, and robust soft-switching demands a system-level approach that integrates topology, magnetic design, and layout.

This thesis proposes a three-phase LLC resonant converter with a wye-delta transformer connection as a scalable architecture for next-generation aircraft DC/DC systems. The three-phase arrangement naturally interleaves energy transfer, reducing input and output current ripple and thus relaxing filter size and mass when power density is the driving metric. The wye-delta transformer introduces an inherent $\sqrt{3}$ step-down factor, lowering the required turns ratio, easing window utilisation, and reducing copper and proximity losses. The shared magnetic paths allow integration of the transformer and resonant inductors into compact three-port planar components within a strict 12.7 mm height limit.

A complete design methodology is developed for the resonant tank and magnetics, so that the switching-frequency excursion remains within 10 % to 15 % while covering the full input and load range. The method combines fundamental-harmonic analysis to shape the gain characteristic with an exact time-domain model to set inverter-to-rectifier phase shift in off-resonant operation. The approach is anchored to a 1 kW, 1 MHz target with 235 V to 285 V input and a regulated 28 V output, enforcing <1 % output-voltage ripple with a practical multilayer ceramic capacitor bank.

Analytical modelling, finite-element simulation, and experimental prototyping confirm the effectiveness of the proposed architecture. The compensated magnetic design achieves balanced flux distribution, mitigates circulating energy, and ensures uniform thermal behaviour. The prototype validates the predictions, maintaining soft-switching, delivering regulated 28 V, and reaching a peak efficiency of 96.5 % at 1 kW.

Overall, the thesis contributes a topology-aware magnetic synthesis method, a resonant-tank design procedure that respects narrow frequency windows, and

practical PCB layout guidelines. Together, these enable high-gain, high-frequency operation in compact three-phase LLC converters and are broadly applicable to other multi-phase isolated resonant architectures requiring balanced flux, compact magnetics, and repeatable high-frequency performance.

Resumen

La creciente electrificación de la aviación impone exigentes restricciones a la conversión de potencia a bordo. Los convertidores deben alcanzar alta densidad de potencia y elevada eficiencia, cumplir estrictos límites de compatibilidad electromagnética (CEM) y operar en formatos de bajo perfil. La familia de convertidores resonantes LLC se adapta bien a estas condiciones gracias a su conmutación a tensión cero (ZVS) en todo el rango de carga, lo que permite trabajar a alta frecuencia y, por tanto, utilizar magnetismos compactos. El principal desafío es el gran escalón de tensión requerido en la distribución en corriente continua de la aeronave, típicamente desde 235 V to 285 V nominales hasta 28 V regulados. Satisfacer esta conversión con un transformador de bajo perfil, bajo esfuerzo de filtrado y conmutación suave robusta exige un enfoque de sistema que integre topología, diseño magnético y enrutado.

Esta tesis propone un convertidor resonante LLC trifásico con transformador en conexión estrella-triángulo como arquitectura escalable para la conversión DC/DC de próxima generación en aeronáutica. La disposición trifásica interconecta de forma natural la transferencia de energía, reduciendo el rizado de corriente de entrada y salida y, en consecuencia, el tamaño y la masa de los filtros cuando la densidad de potencia es el criterio principal. El transformador estrella-triángulo introduce un factor de reducción $\sqrt{3}$, disminuyendo la relación de espiras necesaria, liberando ventana y reduciendo pérdidas por cobre y proximidad. Al compartir trayectorias magnéticas, el transformador y los inductores resonantes pueden implementarse como componentes planares trifásicos compactos que cumplen con una restricción de altura de 12.7 mm.

Se desarrolla una metodología completa de diseño para el tanque resonante y los elementos magnéticos, de modo que la excursión de frecuencia de conmutación se mantenga dentro de 10 % to 15 % cubriendo todo el rango de entrada y carga. La metodología combina una aproximación por armónica fundamental para perfilar la ganancia con un modelo exacto en el dominio temporal para fijar el desfase inversor-rectificador fuera de resonancia. El proceso se valida con un objetivo de 1 kW a 1 MHz, entrada 235 V to 285 V y salida regulada de 28 V, garantizando un rizado de <1 % con un banco práctico de condensadores cerámicos multicapa (MLCC).

Los modelos analíticos, las simulaciones por elementos finitos y los resultados experimentales confirman la validez de la propuesta. La compensación geométrica de los núcleos trifásicos logra un reparto equilibrado de flujo, reduce energía circulante y asegura un comportamiento térmico uniforme. El prototipo experimental

mantiene conmutación suave, entrega 28 V regulados y alcanza una eficiencia pico del 96.5 % a 1 kW.

En conjunto, la tesis aporta un método de síntesis magnética consciente de la topología, un procedimiento de diseño del tanque resonante que respeta ventanas de frecuencia estrechas y pautas prácticas de layout en PCB. Estas contribuciones habilitan la operación de alta ganancia y alta frecuencia en convertidores LLC trifásicos de bajo perfil, y resultan aplicables a otras arquitecturas resonantes aisladas polifásicas que requieran distribución equilibrada de flujo, magnetismos compactos y prestaciones reproducibles a alta frecuencia.

Contents

List of Tables

List of Figures

Acronyms

CO_2 a naturally occurring greenhouse gas and by-product of fossil fuel combustion.

GaN a wide bandgap semiconductor (3.4 eV) used in power electronics for its high efficiency, fast switching, and high-temperature operation.

SiC a wide bandgap semiconductor (3.3 eV) in research and early mass production that provides fast, high-temperature and high-voltage devices.

Si a conventional semiconductor that has dominated electronics and power device manufacturing for decades, offering mature processing, low cost, and well-established fabrication technologies.

AC type of current in which the flow of electric charge reverses periodically, commonly used in power distribution.

AC/DC conversion of alternating current into direct current, typically performed by a rectifier.

AEA aircraft fully powered by electrical energy, eliminating conventional combustion engines and aiming at zero in-flight emissions.

CM type of noise or signal where identical voltages or currents appear simultaneously on multiple conductors with respect to a common reference, typically ground.

CSI parasitic inductance present in all switching elements (transistors) where the same current path is shared between the driving and gate loops.

DAB isolated bidirectional DC/DC topology with two active bridges and a high-frequency transformer.

DAL safety classification level defined by aviation certification standards (e.g. DO-178/DO-254) that determines the rigour of development processes.

DC type of current where the flow of electric charge is unidirectional, commonly used in electronics and batteries.

DC/DC conversion of direct current voltage from one level to another using switching regulators or linear techniques.

DCM operating mode of switching converters in which the inductor current falls to zero during part of the switching cycle, typically at light load conditions.

DCX isolated DC/DC stage with fixed conversion ratio, typically implemented as a soft-switched resonant converter or switched-capacitor network, providing galvanic isolation and leaving tight voltage regulation to upstream or downstream stages.

DM type of noise or signal represented by the voltage difference between two conductors, often the intended transmission mode in power and signal circuits.

DoF independent control variables or parameters in a system that can be adjusted without affecting others; in power electronics, DoFs often refer to modulation or topology options that provide additional flexibility in operation and control.

DPT methodology for measuring the switching parameters and evaluate the dynamic behaviours of power devices by making it switch twice in a way that both soft and hard switching are tested.

DuT device that is being tested to determine its performance.

EASA European authority responsible for civil aviation safety regulation and certification.

EHLA actuators that combine hydraulic power transmission with electronic control for high force applications.

EHSA self-contained actuators where hydraulic power is generated locally by an electric motor driving a pump.

EMA actuators that use an electric motor to directly generate mechanical movement.

EMC ability of equipment to function satisfactorily in an electromagnetic environment without introducing intolerable interference.

EMI disturbance generated by external sources that affects electrical circuits through electromagnetic induction or radiation.

EPR in an lumped model component, it represents the parasitic resistance lumped together as an equivalent value in parallel.

ESD sudden flow of electricity between charged objects, a source of damage to sensitive electronics.

ESL in a lumped-model component, it represents the equivalent parasitic inductance of the component.

ESR in a lumped-model component, it represents the equivalent parasitic resistance of the component.

EUROCAE European standardisation body for aviation systems and airborne equipment.

EV vehicle powered entirely or partially by electric motors using energy stored in batteries.

FAA United States national aviation authority responsible for regulating civil aviation.

FDTD a numerical method for solving partial differential equations in the time domain, by discretising space and time into a grid of finite differences.

FEA simulation of a physical magnitude discretized (small elements) and solved via mathematical numerical techniques.

FEM a numerical technique for solving partial differential equations by discretising a domain into finite elements.

FHA simplified analysis method for resonant converters that considers only the fundamental harmonic of the excitation.

FM technique of encoding information by varying the instantaneous frequency of a carrier wave.

FoM performance metric used to compare components, typically combining parameters to evaluate design suitability.

FPGA a reconfigurable integrated circuit consisting of an array of programmable logic blocks, enabling customised hardware implementations.

GDP macroeconomic indicator representing the monetary value of all finished goods and services produced within a country over a given period.

GHG gases in the atmosphere that trap heat, such as carbon dioxide, methane, and nitrous oxide, contributing to global warming.

GPU a highly parallel processor widely used for scientific computing, machine learning, and acceleration of numerical simulations.

HEA aircraft that combines conventional propulsion with electric propulsion to reduce emissions and fuel consumption.

HEMT a field-effect transistor that leverages a heterojunction between two semiconductor materials to create a two-dimensional electron gas with very high carrier mobility, allowing high switching speeds, and low on-resistance.

HOC large parasitic output capacitance of a device that impacts switching losses and soft-switching conditions.

HVDC DC power distribution at kilovolt levels, which, in the context of aircraft, it is aim to reduce cable weight and improve efficiency compared to AC systems.

ICRI a magnetic structure in which phase windings are inversely coupled so that mutual fluxes oppose each other, shaping the inductance matrix of a multiphase magnetic link to improve current sharing.

IDG integrated circuit combining control logic and gate drivers for power semiconductors.

IGBT a three-terminal power semiconductor device used as an electronic power switch, developed as a high-efficiency and high blocking voltage switch.

IGSE empirical extension of Steinmetz's equation that estimates core losses under arbitrary flux waveforms.

IPCC United Nations body for assessing the science related to climate change, established in 1988 by the World Meteorological Organization (WMO) and the United Nations Environment Programme (UNEP).

LLC a resonant converter topology composed of two inductors and one capacitor that enables soft-switching and high efficiency.

MEA aircraft architecture that progressively replaces hydraulic and pneumatic systems with electrically powered systems.

MLCC a number of individual capacitors are stacked in parallel and contacted together to the terminals, made out of finely grounded granules of paraelectric/ferroelectric raw materials modified by additives.

MOSFET a three-terminal unipolar semiconductor device (switch) where the channel is fabricated with a controlled oxidation. The voltage at the gate determines the electrical conductivity of the channel.

NASA United States of America federal agency responsible for civilian space exploration, aeronautics, and aerospace research.

ODE mathematical equation involving functions of one independent variable and their derivatives, used to model dynamic systems and physical phenomena.

OTC a control strategy for resonant converters that computes optimal switching trajectories to achieve seamless transitions between operating points.

PCB mechanical support for the electrical connections of electronic components via conductive tracks (copper), including pads for the components to be soldered mechanical and electrically.

PEMFC an electrochemical device that converts hydrogen and oxygen into electricity using a polymer electrolyte membrane.

PoL a power conversion stage located close to the load it supplies, typically used in distributed power architectures to provide regulated low voltages.

PSFB isolated DC/DC topology using a full-bridge and phase-shift control to achieve zero-voltage switching and high efficiency.

PSM modulation technique in which the phase shift between switching signals controls the power transfer.

PWM modulation technique where the duty cycle of a square wave is varied to encode information or regulate power.

RMS statistical measure of the magnitude of a varying signal, representing the equivalent DC value for power calculations.

RTCA nonprofit corporation that develops consensus-based recommendations for communications, navigation, and aviation systems.

SRC a resonant DC/DC converter topology in which the resonant tank consists of a series connection of the resonant inductor and capacitor, enabling sinusoidal current waveforms.

VFX modulation technique to modify the effective AC gain seen by the tank, compressing the required operating frequency span and thus, requiring lower switching frequency.

VSCF electrical generation system where variable input speed is converted to constant frequency output, common in aircraft power systems.

WBG a semiconductor with a large value of bandgap; for example, SiC and GaN are wide-bandgap semiconductors.

ZCS soft-switching technique where the switch transitions when current is zero, reducing switching losses and electromagnetic interference.

ZVS soft-switching technique where the device turns on or off only after its voltage has reached its end state, reducing switching losses and electromagnetic interference.

Nomenclature

a_n Amplitude of the cosine term of the n-th harmonic in the Fourier series.

b_n Amplitude of the sine term of the n-th harmonic in the Fourier series.

C_L Output filtering capacitance.

C_r Resonant capacitance.

C_{iss} Input capacitance $C_{iss} = C_{gs} + C_{gd}$ of a transistor seen from the gate-source terminals.

C_{oss} Output capacitance $C_{oss} = C_{ds} + C_{gd}$ of a transistor seen from the drain-source terminals.

C_{oss} Reverse charge transfer capacitance $C_{rss} = C_{gd}$ of a transistor seen from the gate-drain terminals.

I_I DC input current.

I_O DC output current.

L_μ Magnetising inductance.

L_f Output filtering inductance.

L_r Resonant inductance.

L_{ZVS} Series inductance designed to achieve ZVS during switching transitions.

n Index of the n-th harmonic in the Fourier series decomposition.

n_n Primary-to-secondary transformer winding turns ratio $n_n = n_p/n_s$.

n_p Number of turns of the primary winding of the transformer.

n_s Number of turns of the primary winding of the transformer.

P_I DC input power $P_I = V_I \cdot I_I$.

P_O DC output power $P_O = V_O \cdot I_O$.

R_L Load resistance $R_L = P_O/I_O$

R_{ac} Equivalent AC resistance in FHA modelling (related to R_L).

V_I DC input voltage.

V_O DC output voltage.

Z_μ Characteristical impedance when L_r, L_μ and C_r resonate together.

Z_r Characteristical impedance when L_r and C_r resonate together.

CHAPTER 1

Introduction

> Todos debemos desear el progreso científico de la humanidad, pero sin dejar atrás su progreso moral.
>
> — Emilio Herrera Linares

Air transport plays a vital role in connecting cities and people, particularly in cases where geography, travel time or cost leave alternatives unfeasible. This global connectivity enables strong annual economic growth, ultimately contributing 3.6 % of global Gross Domestic Product (GDP) and supporting over 65 million jobs worldwide [1].

However, it is also responsible for approximately 2.5 % of global anthropogenic CO_2 emissions, this is expected to increase to around 3 % by 2050 [2]. Greenhouse gas (GHG) emissions from the transport sector have tripled since 1970, growing at a faster rate than any other end-use energy sector. In 2024, it reached 9.2 Gt of CO_2 equivalent (see fig. 1.1)[1], reflecting a 28 % increase over 15 years [3, 4]. By 2030, approximately 27,000 additional aircraft are expected to enter service. If the expansion trends in the sector progress at the current pace, aircraft will be a significant source of pollution for years to come [5].

[1] CO_2 equivalent units are used throughout this chapter to represent direct emissions. In some literature, only CO_2 emissions are reported; for most transport modes, however, non-CO_2 gases account for less than 5 % of total vehicle emissions and 4 % of overall impact [2].

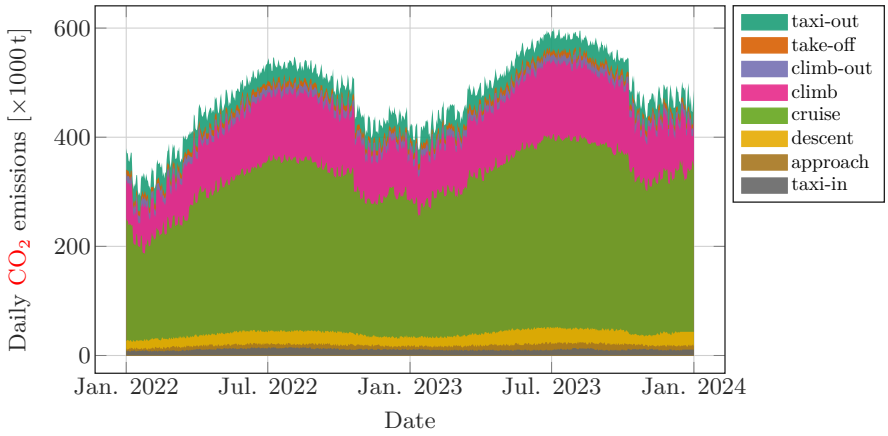

Figure 1.1: Daily CO_2 emissions across the EUROCONTROL area (Europe and surrounding regions) in 2022 and 2023 [6]

It is estimated that for every metric tonne (t) of fuel saved, an equivalent amount of 3.15 t of CO_2 can be avoided [6]. With this in mind, the aircraft industry has worked diligently to limit its impact on the environment, aircraft today are 80 % more fuel efficient per seat than they were when jets were becoming a more common sight in cities around the world [7]. But this is by no means the end of these efforts, with the transport sector responsible for 24 % of global emissions, improvements in efficiency have proven insufficient to stop emissions growth in aviation, continuing to rise at an average annual rate of 3.4 % [8].

Beyond environmental concerns, there is a strong demand for techniques to reduce the direct operating costs of aircraft. The airline industry is particularly competitive, as it is a constantly growing sector, driven by the demand of flights. Low-cost carriers have been driving down profit margins, increasing pressure on cost efficiency. To address this challenge, aircraft manufacturers are placing greater emphasis on technological advancements and innovation, especially in areas that impact maintenance costs and fuel consumption.

1.1 History of the Innovation of Aircraft Technology

Aircraft technology is a monument of modern civilization. Motivated by the ambition to conquer the skies, innovation has been the main driving force behind its evolution, propelling it from its rudimentary beginnings to the safest mode of transportation.

The sophisticated systems we are so accustomed to seeing every day—and that no longer seem to impress us—were not developed overnight. Advancements in aircraft technology, as with any complex engineering system, have not followed a steady, linear trajectory from the earliest known triumphs to the present day. Instead, progress has historically occurred in irregular bursts of enlightenment and rapid evolution, alternating with phases of marginal growth as existing technologies matured; reflecting social priorities, economic pressures, and technological breakthroughs.

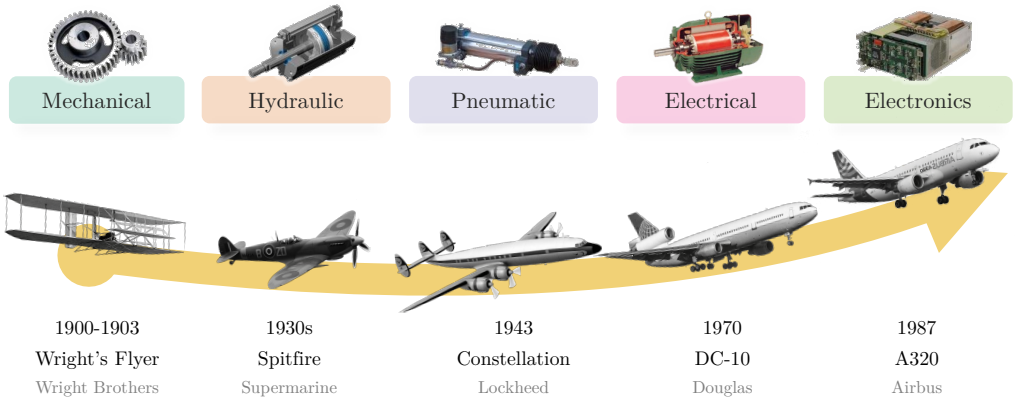

Figure 1.2: Representation of technological advancements in aircraft system capabilities over time[2], highlighting key aircraft from different eras.

In the development of aircraft systems, several key technological milestones can be identified that have played a decisive role in advancing flight performance. These are illustrated in fig. 1.2 and further explained in the following paragraphs.

Building on the work of Sir George Cayley (1773–1857) on aeroplanes, Orville Wright (1871–1948) and Wilbur Wright (1867–1912) (the Wright Brothers) achieved the first successful powered flight in the early 20th century. Their success was driven by critical innovations: an aluminum-cast engine with the necessary power-to-weight ratio, three-axis control system (wings twisting), and the invention of an efficient aerial propeller capable of generating sufficient thrust to sustain flight [9].

In the context of the World War I (1914-1918), the demands for speed, manoeuvrability, resistance and carriage capacity characterised this early period of aviation by **mechanical** innovations: higher power engine delivery, improved aerodynamics and constant speed propellers [9]. Aircraft were initially constructed using wood and fabric, but the development of stronger and lighter materials offered higher strength and stiffness, the all-metal fuselage was adopted, improving aerodynamics [10].

In the 1930s, aircraft grew larger, faster, and more complex, forcing the adoption of **hydraulic** systems [11]. Their use of incompressible fluids to transmit power allow precise and high-force outputs with smaller components, making them ideal for flight surface control (ailerons, elevators, slats, spoilers, flaps and rudder), brakes, and landing gear.

Pneumatic systems, which use compressed air, are lighter and simpler at the expense of providing less force and precision compared to hydraulics. They were adopted in applications where weight savings and simplicity are more critical than power output, and they are commonly used for tasks such as starting engines and operating environmental control systems due to their simplicity and reliability. This technology gained significance by the late 1950s, with the use of fuselage streamlines as operating agents, eliminating additional mechanical moving parts [12].

[2]Note: the scale serves only as an illustrative guide to highlight relative progress.

Propulsive efficiency was a major contributor of the 1950s, largely due to the innovations in **jet propulsion** engines. Innovations in these engines synergised improvements in thrust-to-weight ratios and fuel efficiency, enhancing overall aircraft performance [10]. Together with advancements in aerodynamics, thermodynamics, and materials science, allowed aircraft to fly faster, longer and higher than before.

1.2 Electrification in Air Transportation

In parallel with the rest of technologies, electrification has been a concept present in air transportation since the 1940s, driven by the need to optimize performance and reduce both operating and maintenance costs in the aviation industry. Over the decades, the transition to **electric** systems has gained momentum, primarily to address inefficiencies and environmental concerns.

Nowadays, **power electronics** play a crucial role for aircraft electrification, this role becomes more critical as MW-class flight critical turboelectric propulsion systems are involved. Power electronics are used for power conversion (motor drives) and distribution (circuit breakers and protections).

High specific power is achievable through advancements in those components that make power electronics heavy: materials (magnetic cores, dielectrics, insulation varnishes), switching devices (transistors), passive components, packaging, and thermal management systems (heatsinks, fans, hot/cold plates...). The role of a power electronics engineer is to strategically integrate these components, optimizing their performance through circuit topologies and design approaches.

1.2.1 Evolution of Installed Power in Aircraft

Since the earliest attempts at electric-powered air transport, the concept of the More Electric Aircraft (MEA) has steadily gained ground. First explored during World War II with the Focke-Wulf FW 190A in 1941, aircraft have since seen a continuous rise in generator ratings and on-board electrical power demand [13]. As illustrated in fig. 1.3, this evolution reflects the broader shift in aviation toward replacing other technologies (hydraulic, pneumatic, and mechanical) with electric ones.

Initially limited to small generators, aircraft power systems advanced to engine-driven Direct Current (DC) units and later to AC generators capable of higher voltages and power densities [14]. Nowadays, aircraft such as the Airbus A380 or Boeing 787, has brought unprecedented levels of electrical generation, enabling electric actuation and environmental control. This trajectory mirrors wider transport electrification trends, where efficiency, reduced fuel use (efficiency), and lower operating costs continue to drive the move toward electric architectures.

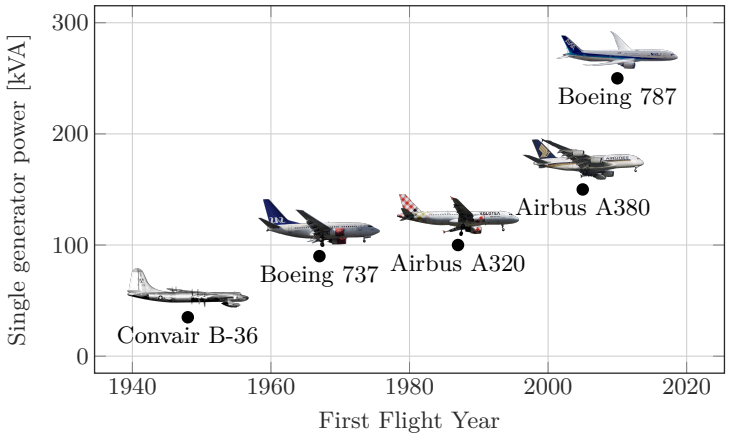

Figure 1.3: Evolution of single generator ratings in commercial aircraft as a function of first flight year, illustrating the most representative increase in on-board electrical power demand throughout aviation history [14]. *Images source: Wikimedia Commons*

Electric systems offer several advantages, including reduced weight, lower emissions, and improved fuel efficiency [15], while enhancing aircraft controllability and reliability [13, 16]. Furthermore, electrification reduces the mass of aircraft, leading to lower fuel consumption and emissions, while providing quicker failure resolution and increased reliability, key factors in aviation safety standards [17].

Traditionally, aircraft have relied heavily on **mechanical**, **hydraulic**, and **pneumatic** systems for actuators, propulsion, and power generation. These systems, while effective, have several drawbacks, such as inefficiency, or high maintenance costs. Substituting these with electric alternatives offers multiple benefits [14]:

- **Efficiency:** The conventional aircraft system is complex, and the multiple conversion steps reduce the entire system's efficiency. Electric systems reduce energy losses commonly associated with mechanical and fluid transmission, delivering power more directly by optimising their voltage and current conversion for energy distribution, minimizing losses and saving weight.

- **Maintenance:** With fewer moving parts, electric components experience less wear and tear, resulting in reduced maintenance requirements and longer service intervals.

- **Environmental Benefits:** Eliminating hydraulic and pneumatic systems removes the risk of fluid leaks, which can harm the environment and necessitate costly cleanups.

- **Weight Reduction:** Electrical elements are often lighter than their mechanical or hydraulic alternatives, specifically the piping structure of the hydraulic actuation system, enhancing fuel efficiency and lowering operational costs.

- **Reliability:** Electric systems demonstrate higher reliability and resilience under extreme conditions, improving safety and reducing downtime.

- **Scalability and Flexibility:** Electronics enable modular and adaptable designs, facilitating advancements like distributed propulsion and fly-by-wire technologies.

- **Energy Recovery:** Integration of regenerative braking and energy recovery technologies further boosts operational efficiency.

- **Unified Infrastructure:** Replacing both hydraulic and pneumatic systems with electric systems allows the same power distribution lines to serve multiple subsystems. This simplification reduces installation complexity and enhances overall system integration.

The shift from **mechanical** to **electrical** flight control systems, exemplified by the advent of *Fly-by-Wire* [18], greatly enhanced the precision and reliability of aircraft control [10]. This transformation was underpinned by significant advances in **electrical** and **electronics** engineering, which have become integral to modern avionics systems, this transition is illustrated in fig. 1.4, where parts of the conventional flight control system was substituted by electrical parts, simplifying the systems and reducing the amount of moving parts [18].

The evolution of avionics, has contributed to the sophistication of today's aircraft. Innovations in avionics, from early radio communications and navigation systems developed after World War I to the digital displays in modern cockpits, have been key drivers of aircraft performance and efficiency [19].

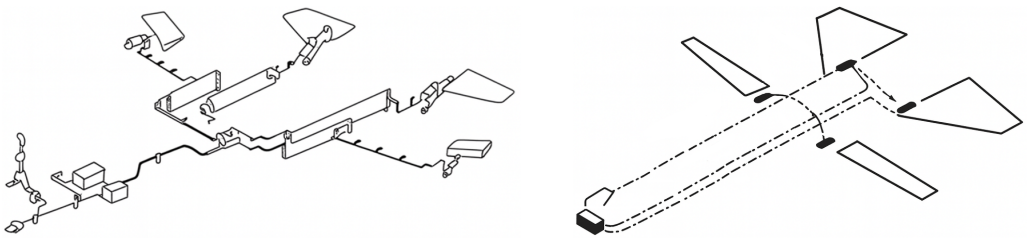

(a) Mechanical,pneumatical and hydraulical flight control system

(b) *Fly-By-Wire* flight control system with servosystems

Figure 1.4: Substitution of mechanical, hydraulic and pneumatic components for electric actuators to develop a unified electric power distribution line (*Fly-By-Wire* concept) [18]

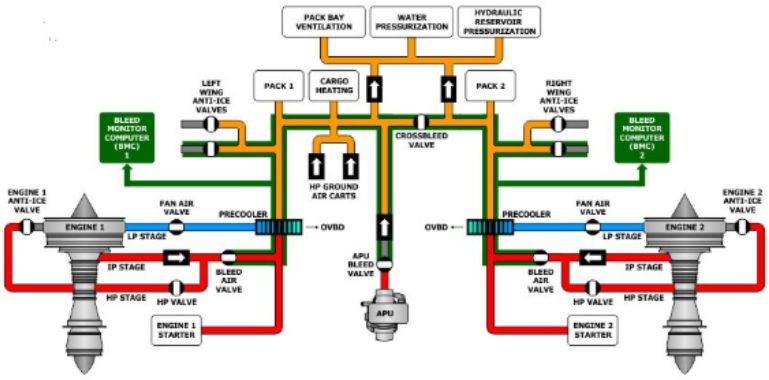

(a) Pneumatic system layout

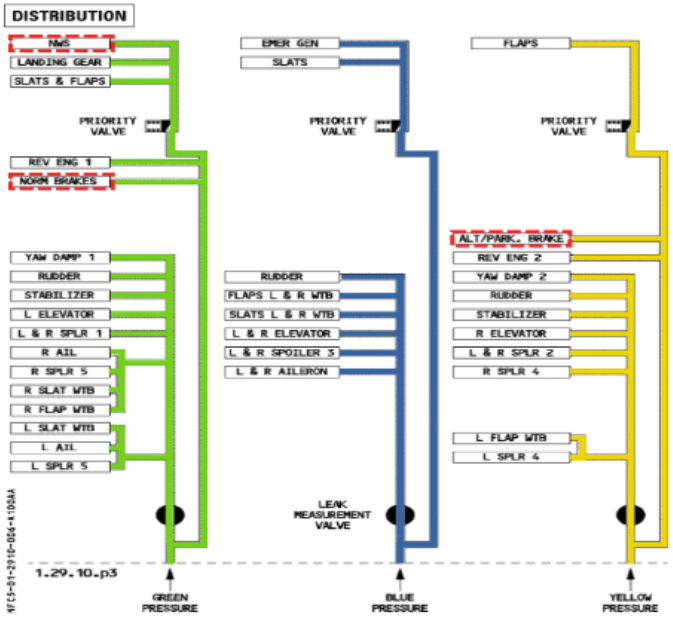

(b) Hydraulic system layout

Figure 1.5: Example of an hydraulic and pneumatic system layout of Airbus A320 [19]

1.2.2 More Electric Aircraft (MEA)

The More Electric Aircraft (MEA) evolves from the *Fly-By-Wire* concept, aiming to replace traditional mechanical, hydraulic and pneumatic systems with electrical systems, enhancing efficiency, reducing emissions, and lowering maintenance costs. This evolution is driven by the increasing need to improve aircraft performance while mitigating aviation's environmental impact [15, 20].

These systems offer the potential to reduce fuel consumption and emissions significantly, making them a promising alternative for future aviation [21, 22]. In any case, their feasibility is constrained by the efficiency of electric generators, motors, and power converters, as well as the added weight of the electrical distribution system.

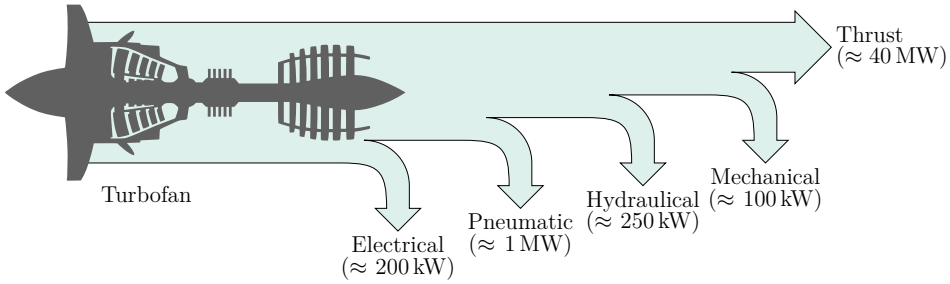

(a) Conventional system

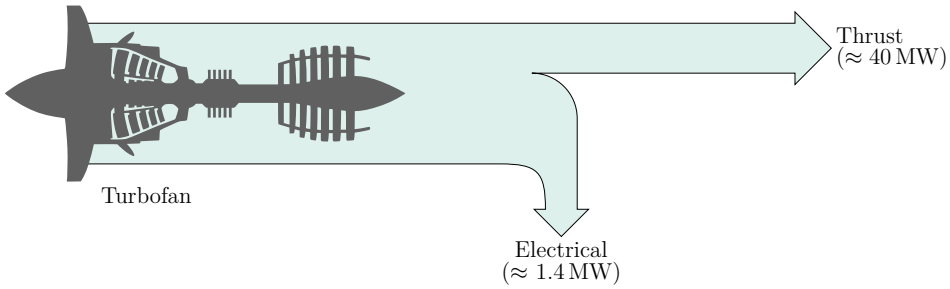

(b) More Electric Aircraft (MEA) concept

Figure 1.6: Comparison of the conventional turboelectric power distribution system with the More Electric Aircraft (MEA) concept, where mechanical, pneumatic and hydraulics are replaced by electrical actuators [23].

The shift towards MEA has significantly impacted aviation systems, influencing propulsion, actuation, taxiing, on-board generation, and fuel pump systems in aircraft [24]:

- **Propulsion**: Turboelectric propulsion can reduce fuel burn by up to 20 % compared to conventional turbofan engines [25]. Electrification introduces innovative concepts like turboelectric and hybrid propulsion, which decouple turbines from fans and utilise distributed electric motors, optimising thrust and fuel efficiency [26]. However, the low energy density of current battery technologies and the high specific power requirements remain significant constraints for electric propulsion systems [27].
- **Actuation**: Aircraft rely on primary (ailerons, rudders, elevators) and secondary control surfaces (flaps, slats) for stability and maneuverability. Electrohydraulic Actuators (EHLA) and Electrohydrostatic Actuators (EHSA) convert electric energy into hydraulic energy, and then hydraulic energy into mechanical energy via pumps and cylinders [28]. Electrifying actuation systems replaces traditional hydraulic components with Electromechanical Actuators (EMA), improving efficiency by 20 %, reducing weight, and enhancing thermal performance [29]. However, mechanical jamming risks limit the use of EMAs in primary control surfaces and landing gear systems, although they are suitable for applications like braking systems [30, 16].
- **Taxiing**: Ground movement before takeoff (taxi-out) and after landing (taxi-in) accounted for 3.3 % of CO_2 emissions during the 2022-2023 period (fig. 1.1)

[6]. Electric taxi systems integrate electric actuators into the landing gear for propulsion and steering, reducing emissions, noise, and brake wear (green taxiing) [31, 32, 33, 34] such as wheel actuators [31, 32] or electrically-powered cart [33]).

- **On-Board Generation**: Conventional aircraft rely on an Integrated Driver Generator (IDG) mechanically coupled to the engine shaft for power generation and starting. MEAs adopt Variable-Speed Constant-Frequency (VSCF) systems to improve efficiency, replacing mechanical gearboxes with electric machines and power converters (AC/DC, DC/DC, AC/AC, and DC/AC) [24, 21] to provide torque for engine startup and consistent power during flight [20].

- **Engine Fuel Pump**: Traditional fuel pumps, powered mechanically through gearboxes linked to the engine shaft, are being replaced by electric pumps [35]. These enable more precise fuel flow regulation, improving combustion efficiency and overall simplifying fuel control systems, leading to size and complexity reductions [36].

As the aviation industry continues to evolve, the integration of electric power systems is expected to be pivotal in achieving sustainable and cost-effective air transportation, since many of the long-term environmental and efficiency targets cannot be met without significant electrification. Over the past decades, major step changes in propulsion have occurred, from early turbojet engines to high-bypass turbofans, enabling substantial improvements in fuel efficiency and performance. Nevertheless, the overall aircraft configuration has remained largely unchanged for decades, and according to the Intergovernmental Panel on Climate Change (IPCC) report from 2022, it is expected to persist in this form at least until 2037 [37].

Table 1.1 summarises recent studies on electric aircraft systems undertaken by industry and academia. Most of these efforts are conceptual, assuming the availability of advanced electrical components in the future. They also differ substantially in terms of assumed aircraft size, range, electrical architecture, performance targets, and level of modelling detail. Nevertheless, they collectively contribute to the growing body of knowledge on electric aircraft, providing the reader with an overview of technological trends and benchmarks for component performance. These studies also help to delineate the potential of different electrification paths, just as in other fields such as automotion, and primarily grouped into two categories: Hybrid Electric Aircraft (HEA) and All Electric Aircraft (AEA), which are briefly introduced in this subsection.

Project	Organization	Architecture	Components	Ref.
SUGAR	NASA, Boeing	Parallel hybrid	Motors (5 kW/kg) Batteries (750 Wh/kg)	[38, 39, 40, 41]
Bauhaus	Bauhaus	Parallel hybrid	Batteries (1500 Wh/kg)	[42]
N3X	NASA	All-Electric	Generator (30 MW) Motors (14 × 2 MW)	[43]
E-Fan X	Airbus, Rolls-Royce	Parallel partial hybrid	Generator (2.5 MW) Motors (3 × 2.0 MW) Electric Motor (1 × 2.0 MW) Batteries (200 Wh/kg)	[44]
STARC-ABL	NASA	Partial turboelectric	Generator (1.45 MW) Motor (2.6 MW)	[45]

Table 1.1: Summary of electric propulsion concepts for civil aircraft [29].

All Electric Aircraft (AEA)

Turboelectric configuration is the most conventional electric type of propulsion, as it still depends on fuel to generate electrical energy that is subsequently reconverted into mechanical power (fig. 1.7a). In a partial-turboelectric configuration, electric propulsion provides only part of the propulsive power (fig. 1.7b). In contrast, fully electric systems (fig. 1.7c) rely entirely on batteries as their sole energy source for propulsion.

The defining characteristic of All Electric Aircraft (AEA) is the complete absence of combustion engines, fuel tanks, and related subsystems (fig. 1.7c). Instead, the propulsion system is powered exclusively by electrochemical storage devices (i.e. lithium-ion batteries), which feed electric motors through high-voltage power electronics. This results in a simplified architecture with fewer moving parts and no need for power generation in mid flight, potentially lower maintenance costs, and a drastic reduction of local emissions and noise.

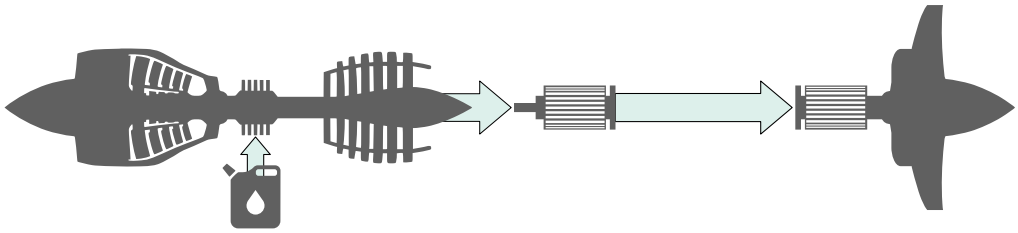

(a) Turboelectric configuration

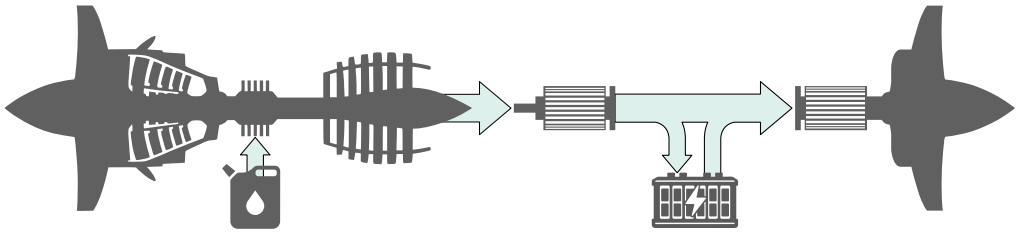

(b) Partial turboelectric configuration

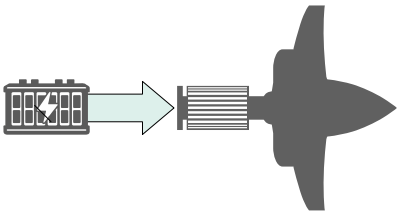

(c) All electric configuration

Figure 1.7: Schematic representation of different propulsion configurations for More Electric Aircraft (MEA), and All Electric Aircraft (AEA) with full electric propulsion [22]

However, all-electric systems are fundamentally constrained by the energy density of batteries. While current lithium-ion technologies typically achieve less than 300 Wh/kg, conventional jet fuel provides more than 12 000 Wh/kg. This energy density gap of nearly two orders of magnitude limits the range and payload of all-electric demonstrators, restricting them to short-haul missions and small passenger capacity.

Despite these limitations, research indicates that AEA could serve as a viable solution for short regional flights, commuter aircraft, and urban air mobility applications [46]. Certified examples such as the Pipistrel Velis Electro, designed as a two-seat trainer, and projects like the Eviation Alice, designed for carrying nine passengers, highlight the progress and potential of this technology [47]. Moreover, the potential of electric propulsion to decarbonise aviation is therefore significant, as all-electric aircraft could reduce direct emissions in short-range segments and complement broader strategies for sustainable aviation.

(a) Pipistrel Velis Electro

(b) Eviation Alice

Figure 1.8: Examples of commercially available All Electric Aircraft (AEA). *Image Source: Pipstrel Aircraft and Eviation*

Hybrid Electric Aircraft (HEA)

Neither lithium-ion batteries nor fuel cells currently meet the energy density requirements for AEA [25]. By integrating conventional fuel-based propulsion systems with electrical components, a practical compromise emerges similar to hybrid automotive. This is called Hybrid Electric Aircraft (HEA), and it is regarded as a more viable option in the near term [25].

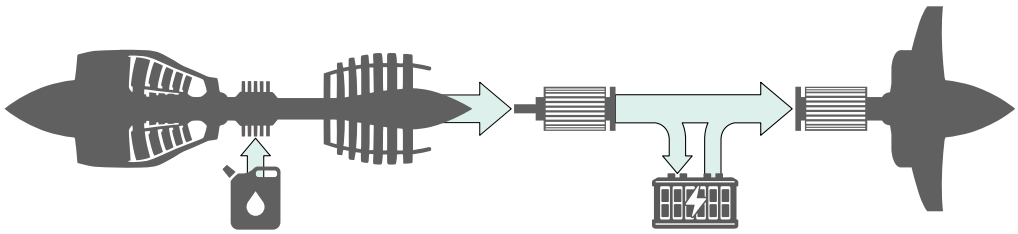

(a) Series hybrid configuration

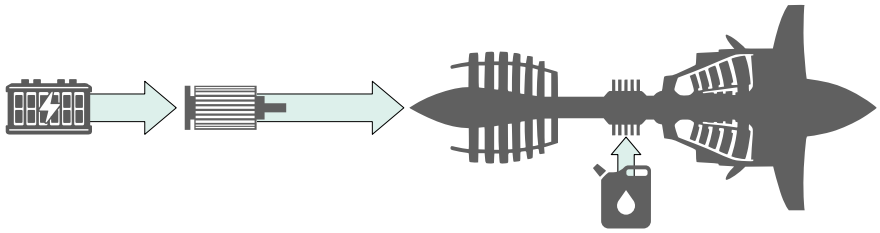

(b) Parallel hybrid configuration

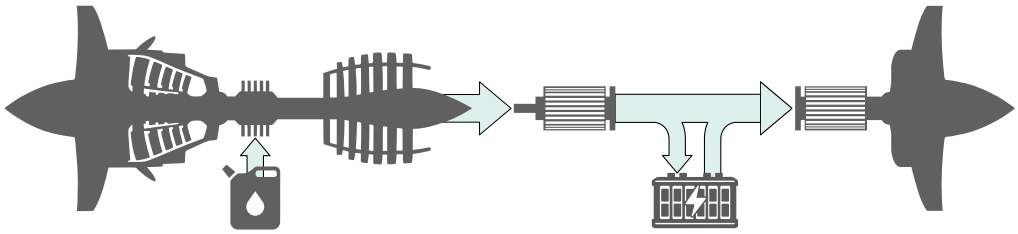

(c) Partial hybrid configuration

Figure 1.9: Schematic representation of different propulsion configurations for More Electric Aircraft (MEA), and Hybrid Electric Aircraft (HEA), showing the different hybrid configurations [22]

The term ”hybrid” have two meanings. One is related to the use of two power sources (such as turbine engine and electric motor), and the other is related to the aircraft use of a combination of more than one propulsive sources: engines, electric energy generation, fuel cells, or battery energy storage [48].

Hybrid systems use gas turbine engines for propulsion and to charge batteries; these provide energy for propulsion during one or more phases of flight. As shown in fig. 1.9b, with a parallel hybrid system, a battery-powered motor and a turbine engine are both mounted on the shaft that drives a fan, so that either or both can provide propulsion at any given time. With a series hybrid system (fig. 1.9a), only the electric motors are mechanically connected to the fans, the gas turbine is used to drive an electrical generator (driving the motors and charging the batteries).

Although discontinued in 2020, projects as the *E-Fan X* (fig. 1.10) by *Airbus*, a hybrid-electric propulsion system for regional aircraft, demonstrate the industry's interest in hybrid solutions to reduce emissions in the aviation sector [44].

Figure 1.10: E-Fan X, a conceptual example of Hybrid Electric Aircraft (HEA), particularly of parallel partial hybrid (Image source: ©Airbus Group [44])

1.2.3 Wide Bandgap (WBG) Power Devices

Although technically part of the contributors for weight, switching devices play a big role in the miniaturisation of power converters. Applications vary in voltage and power, but a particular focus in aircraft applications is the power density in both weight and volume. Wide Bandgap (WBG) power devices are enabling it to come true due to their improved efficiency and performance characteristics compared to today's Si power electronics as illustrated in fig. 1.11 [49].

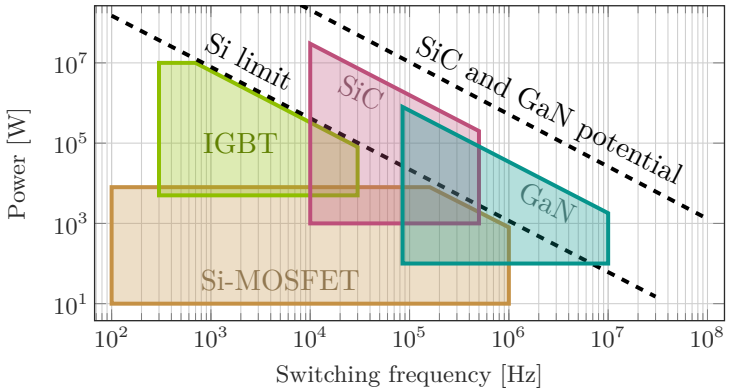

Figure 1.11: Comparison of semiconductor technologies for aircraft power electronics: Si, SiC and GaN devices. Wide bandgap devices (SiC and GaN) extend the operational envelope towards higher power and frequency, enabling compact and lightweight converters [49].

Si semiconductor technology is a mature technology, and it has been under continuous development for over half a century, enabling innovations such as the Insulated-Gate Bipolar Transistor (IGBT) and Si-based MOSFETS. These devices cover a wide operating voltage range (from a few volts up to 6.5 kV), and their reliability has been proven across countless applications. However, Si devices have everyday less margin for improvement in blocking voltage, operating temperature (below 175 °C), and switching frequency. These constraints impose limitations on further miniaturisation and efficiency improvements, particularly in aviation where high specific power is critical.

SiC devices are more reliable than silicon in commercial aircraft environments, and they are capable of reaching higher specific power (2.2 kW/kg of Si against 9 kW/kg in SiC[3]), and limited to 25 A for 270 V DC systems (for higher powered circuit protection, mechanical breakers are used) [25]. They offer superior material properties such as a higher bandgap, greater thermal conductivity, and higher critical electric field strength. These attributes translate into lower conduction and switching losses, higher allowable operating temperatures, and the possibility of using thinner drift layers, which reduce parasitic capacitances, enabling higher switching frequencies and a reduction of bulky passive components. Such advantages make SiC particularly well suited for the high-voltage, high-power, high power density converters required in the further electrification of aircraft.

GaN, another wide-bandgap material, pushes performance further by offering even lower output capacitances and extremely fast switching capabilities. This makes it ideal for high-frequency applications where reducing the size and weight of passive components is essential. Although GaN devices are today commercially available primarily at low to medium blocking voltages (40 V–650 V), their efficiency and high-frequency operation provide significant potential for future aerospace systems, especially in auxiliary power supplies and low-voltage conversion stages. Recent generations are advancing towards lower on-resistance devices, higher blocking

[3]Estimated over a 20-year period, as provided by [25].

voltages and more robustness in radiation environments [50], paving the way for broader adoption in aviation.

1.2.4 Energy Sources

Among the most promising alternatives to conventional propulsion and auxiliary systems are batteries and hydrogen fuel cells. Batteries, especially lithium-ion, have reached a high level of technological maturity, making them suitable for short-range missions and urban air mobility applications. However, their limited specific energy restricts endurance and payload capacity. In contrast, fuel cells, particularly Proton Exchange Membrane Fuel Cells (PEMFCs), harness hydrogen's high specific energy density to extend the range while reducing emissions (water vapour) [51]. Consequently, integrating both technologies into MEA architectures has become a key focus of research.

Hybrid configurations combining fuel cells and batteries are especially attractive because they exploit the complementary strengths of each technology. Batteries can deliver high instantaneous power required during take-off and climb, whereas fuel cells are better suited for sustained cruise power. Direct-hybrid architectures reduce weight and improve reliability, though they require careful sizing and control to manage variable voltage and power demands [52]. Studies on aircraft such as for the Boeing-SENASA collaboration in 2008 [53] or the more recent Cessna 172S [54] demonstrate that optimally sized hybrid systems can achieve significant reductions in total weight and hydrogen consumption while maintaining operational safety and efficiency.

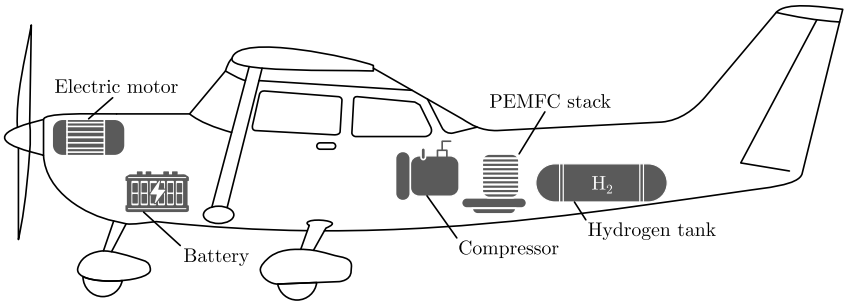

Figure 1.12: Schematic representation of the fuel cell battery hybrid propulsion system layout in Cessna 172S Aircraft [54].

Despite their potential, several technical and safety challenges remain. Batteries are susceptible to degradation, limited cycle life, and thermal runaway events, which pose critical risks in aviation environments [55]. On the other hand, fuel cells face hurdles related to hydrogen storage, volumetric density, and reduced performance at high altitudes. Furthermore, integrating these systems requires advanced power management strategies, redundancy, and lightweight components to balance performance with safety. Ongoing research aims to mitigate these limitations through improved battery chemistries, solid-state electrolytes, enhanced cooling systems, and robust hybrid architectures. If successfully implemented, the synergy of batteries and fuel cells could enable MEA to meet stringent emission targets while maintaining operational feasibility for both regional and future long-haul aircraft.

1.3 Conventional Electrical Power Distribution Inside an Aircraft

Due to the technical progress in power electronics and motor drives, the traditional electric power distribution has and will continue evolving (fig. 1.13) as it shifts towards the MEA [56, 23, 57]. The power distribution system in aircraft includes several voltage buses, many possibilities can be found for the power architecture, including DC and AC buses. Each of these buses serves specific functions and it is integral to the aircraft, for the case of commercial aircraft we distinguish:

- **AC buses**: It is used for supplying high-power traditional AC loads within the aircraft. Basically, it consists in a 115 V AC or the more recent 230 V AC, and it can operate at a constant high-frequency of 400 Hz or 360-800 Hz. The voltage generation is typically achieved through inverters that convert DC power from the aircraft's generators or other DC buses [57].

- **DC buses**: DC buses provide stable and efficient power to various subsystems. DC buses offer the advantage of reduced electromagnetic interference (compared with AC buses) and more efficient energy storage integration, making them ideal for emergency power supplies. They also optimise power flow, reduce conversion losses (high voltage distribution), and enable advanced power management strategies. Two key voltage levels are commonly used in aviation:

  - The 270 V DC bus is a high-voltage bus that facilitates efficient power distribution with reduced mass and volume. It supports high-power applications which, combined with energy storage systems (emergency backup and engine starting), provide a crucial interfacing between different voltage levels (including Alternate-Current/Direct-Current (AC/DC) converters for AC interfacing) making it ideal to manage power flow, and maintain system stability [58, 59].

  - Generated from the 270 V DC, the 28 V DC bus is commonly used for lower power loads, and it is the most traditional bus in aircraft, coming from the years of lead–acid batteries (see fig. 1.13). It is essential for powering various avionics and on-board control systems, requiring a stable and reliable low-voltage power. This bus is often used in conjunction with other voltage levels to ensure a cohesive power distribution across different systems [57].

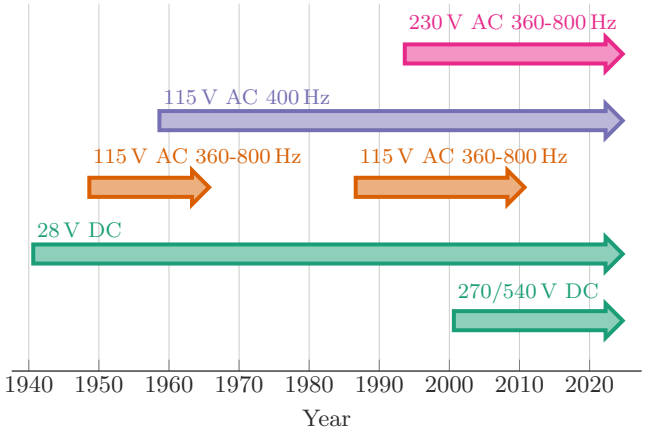

Figure 1.13: Evolution of electrical power distribution systems in aircraft, showing the transition for higher voltage levels and higher voltage systems in recent years [14]

In alignment with other standards, such as the military MIL-STD [60], additional standardised voltage levels have been established, including a power distribution voltage of ±270 V DC or ±540 V DC for future high-power aircraft. This voltage levels are currently considered the upper limit for the near future.

Higher-voltage power distribution systems in the kV range are essential for meeting the multi-megawatt power demands of future AEA. Conventional AC distribution becomes unsuitable at such power levels, making High-Voltage Direct Current (HVDC) architectures a promising alternative. Studies suggest that a DC bus voltage of approximately ±1.5 kV (3 kV total) offers advantages in terms of reduced cable weight and higher overall efficiency [49]. However, operating at these voltage levels introduces significant challenges. Insulation becomes critical in low-pressure environments due to Paschen's law, which defines the breakdown field strength as a function of altitude [43]. As illustrated in fig. 1.14, derating is typically required for semiconductor devices operating under such conditions [30]. Additional concerns include Electromagnetic Interference (EMI), exposure to cosmic radiation at high altitudes, and the development of lightweight yet reliable protection devices.

Implementing such systems requires the development of new insulation technologies, as well as revised electrical conductor spacing rules and practices [23]. National Aeronautics and Space Administration (NASA) estimated that to sustain thrust power during take-off, the phase with the highest power demand voltage levels between ±4.5 kV to 12 kV would be necessary to achieve the required power density.

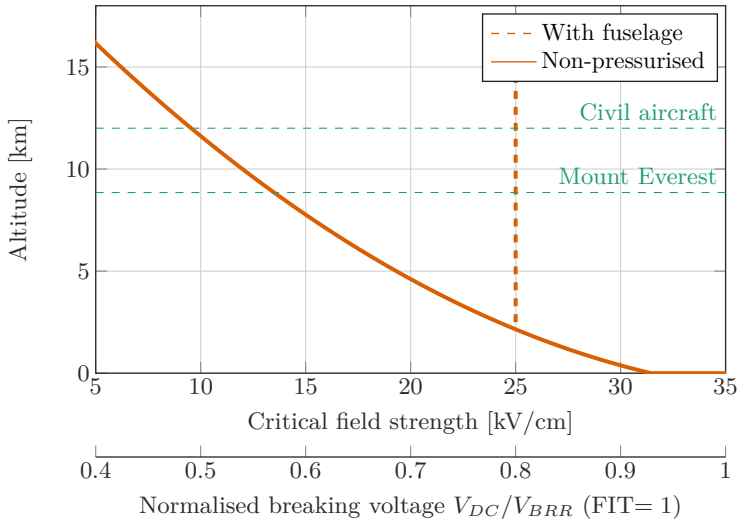

Figure 1.14: Critical field strength electric field as function of the altitude (Paschen's law) and its reduction of drain-source voltage. The normalised breaking voltage represents the typical derating needed for semiconductor devices [43, 30].

1.4 Norms and Standards for On-board Equipment

The certification and safe integration of avionics and airborne equipment into modern aircraft demand compliance with a series of rigorous international standards. These standards, developed by organisations such as the Radio Technical Commission and Test Procedures for Airborne Equipment (RTCA) or the European Organisation for Civil Aviation Equipment (EUROCAE), provide harmonised guidelines that ensure equipment reliability, interoperability, and safety under the demanding conditions of flight. They address not only environmental resilience and EMI but also the structured design assurance of complex electronic hardware and the definition of electrical power characteristics for on-board systems. Among the most widely recognised and applied are the following:

- **DO-160G and ED-14G (Environmental Conditions and Test Procedures for Airborne Equipment)**: Issued respectively by the RTCA and EUROCAE in the United States and Europe, these standards are essential for certifying and integrating airborne equipment into modern aircraft systems. They define environmental test conditions and procedures for avionics, electrical systems, and other onboard equipment across various aircraft types, from light aircraft to commercial airliners and supersonic transports. Covering a wide range of tests—including vibration, power input fluctuations, lightning strikes, and Electrostatic Discharge (ESD)—they ensure equipment reliability under harsh operational conditions. Notably, Sections 16 and 21 address radio frequency susceptibility and electromagnetic interference, ensuring compliance with regulatory requirements from authorities such as the Federal Aviation Administration (FAA) and European Union Aviation Safety Agency (EASA) [61, 62].

- **DO-254 and ED-80 (Design Assurance Guidance for Airborne Electronic Hardware)**: Issued respectively by the RTCA and EUROCAE in the United States and Europe, these standards define the development, verification, and certification requirements for airborne electronic hardware, including FPGAs, ASICs, and circuit boards. They establish a structured design assurance process to ensure the reliability and safety of complex electronic hardware used in avionics. They classify hardware components into different Design Assurance Levels (DALs) based on their impact on flight safety, (from A, catastrophic failure, to E, no effect). Compliance with these standards is required for certification by regulatory authorities such as the FAA (via AC 20-152A) and EASA (via AMC 20-152A) [63, 64].

- **MIL-STD-704F (Aircraft Electrical Power Characteristics)**: Issued by the United States Department of Defense, this standard defines the electrical power characteristics required for aircraft systems to ensure compatibility, performance, and safety. It establishes the limits for voltage, frequency, phase balance, and power quality for both AC and DC electrical systems used in military aircraft. It specifies nominal values of 115 V AC at 400 Hz and 270 V DC, with defined tolerances to accommodate variations in load conditions. Compliance with this standard ensures that airborne electrical systems can operate reliably across different aircraft platforms and meet the stringent requirements of military avionics [60].

1.5 Contributions of the Thesis

Several parts of this thesis have already been published or are being submitted in international journals or conference proceedings.

1.5.1 Conference Papers

1. **Daniel Ríos Linares** and Miroslav Vasić. "High Power Density Three-Phase LLC DC/DC Converter with Coupled Resonant Inductor and Wye-Delta Transformer for Aircraft Applications". In: *2023 IEEE Applied Power Electronics Conference and Exposition (APEC)*. 2023, pp. 1729–1736. DOI: 10.1109/APEC43580.2023.10131660

2. **Daniel Ríos Linares**, Miroslav Vasić, and Pedro Alou Cervera. "Three-Phase LLC DC/DC Converter in Stack Configuration: A Topology for High-Voltage Conversion Ratio Applications". In: *2023 IEEE Applied Power Electronics Conference and Exposition (APEC)*. 2023, pp. 1747–1752. DOI: 10.1109/APEC43580.2023.10131367

3. **Daniel Ríos Linares**, Alberto Delgado Exposito, and Miroslav Vasic. "Magnetic Optimization for Three-Phase LLC Converters". In: *PCIM Europe 2023; International Exhibition and Conference for Power Electronics, Intelligent Motion, Renewable Energy and Energy Management*. 2023, pp. 1–8. DOI: 10.30420/566091133

4. **Daniel Ríos Linares**, Miguel Astudillo Martínez, and Miroslav Vasić. "Optimal Driving Strategies for GaN HEMT: A Numerical Non-Linear Datasheet-Based Model". In: *2024 IEEE Applied Power Electronics Conference and Exposition (APEC)*. 2024, pp. 2629–2636. DOI: 10.1109/APEC48139.2024.10509318

5. Xianghao Mo, **Daniel Ríos Linares**, Regina Ramos, and Miroslav Vasić. "FPGA-based Hybrid Simulator for Real-Time 3-D Temperature Monitoring of Power Converters". In: *2025 IEEE Applied Power Electronics Conference and Exposition (APEC)*. 2025, pp. 1375–1382. DOI: 10.1109/APEC48143.2025.10977068

6. Xianghao Mo, **Daniel Ríos Linares**, Regina Ramos, and Miroslav Vasić. "Thermal Transient Digital Twin Modelling for Power Converters". In: *PCIM Europe 2024; International Exhibition and Conference for Power Electronics, Intelligent Motion, Renewable Energy and Energy Management*. 2024, pp. 2381–2388. DOI: 10.30420/566262335

7. Marta Espinosa del Pozo, Xianghao Mo, **Daniel Ríos Linares**, Regina Ramos, and Miroslav Vasić. "Cosimulación Electrotérmica en Tiempo Real con Hardware-in-the-Loop para la Creación de Gemelos Digitales en Convertidores de Potencia". In: *SAAEI'2025*. 2025

8. **Daniel Ríos Linares**, Xianghao Mo, Regina Ramos, and Miroslav Vasić. "Digital Twinning for Power Converter Temperature Monitoring". In: *Proc. IEEE International Conference on Electrical Engineering (EE)*. Novi Sad, Serbia, 2025, *Accepted (August 2025)*

1.5.2 Workshops and Seminars

1. Miroslav Vasić and **Daniel Ríos Linares**. "Mastering the Art of High-Frequency LLC Converters". PCIM Europe 2024; International Exhibition and Conference for Power Electronics. 2024

2. Miroslav Vasić and **Daniel Ríos Linares**. "Mastering the Art of High-Frequency Multi-phase LLC Converters". 2025 IEEE Applied Power Electronics Conference and Exposition (APEC). 2025

1.5.3 Journals

1. **Daniel Ríos Linares**, Alberto Delgado Expósito, and Miroslav Vasić. "High-Gain High-Frequency Three-Phase *LLC* Resonant Converter Design Based on the Wye–Delta Transformer for Aircraft Applications". In: *IEEE Transactions on Power Electronics* 39.4 (2024), pp. 4367–4383. DOI: 10.1109/TPEL.2023.3339973

2. Xianghao Mo, **Daniel Ríos Linares**, Regina Ramos, and Miroslav Vasić. "Toward Embeddable Digital Twins: A Voxel-Based Approach for Power Converter Temperature Monitoring". In: *IEEE Journal of Emerging and*

Selected Topics in Power Electronics 13.3 (2025), pp. 2781–2798. DOI: 10.1109/JESTPE.2025.3541343

3. **Daniel Ríos Linares** and Miroslav Vasić. "Detailed Description of the Three-Phase LLC Converter in Stack Configuration: A Topology for High Power Density DC/DC Conversion". In: *IEEE Transactions on Power Electronics* (2026), *To be submitted*

4. **Daniel Ríos Linares** and Miroslav Vasić. "High Output Capacitance (HOC) Model for Reconfigurable LLC Converters Design". In: *IEEE Transactions on Circuits and Systems II* (2026), *Work in progress*

1.6 Other Contributions

Some other work was not directly derived to this work and it is listed below:

1. Gabriel Luis Maldonado Roldán, **Daniel Ríos Linares**, and Miroslav Vasić. "Novel Bidirectional Capacitively Isolated Resonant Switched Capacitor DCX Topology for Voltage Reduction". In: *IEEE Transactions on Power Electronics* (2025-2026), *Submitted for review (May 2025)*

2. Gabriel Luis Maldonado Roldán, Esteban Martínez Barroeta, **Daniel Ríos Linares**, and Miroslav Vasić. "Volume Comparison of Isolated DC-DC converters for maximum power density". In: *SAAEI'2025*. 2025

1.7 Objectives

1. Topologies for high voltage step-down DC/DC converters with wide input voltage range specifically for the $270 - 28\,\mathrm{V}$ bus conversion (unidirectional loads).

2. Design of high power density DC/DC converters at high-frequency (over $1\,\mathrm{MHz}$).

3. Complete PCB-integration for converters and integrated magnetics (inductors and transformers).

1.8 Outline of the Thesis

This thesis is structured into seven chapters, which are organised as follows.

Chapter 2. Literature Review and State-of-the-Art

The second chapter surveys the state of the art in aerospace power electronics, with particular focus on the trade-offs inherent in practical aircraft converters, including electrical performance, thermal management, passive components, and semiconductor technologies. It analyses and contrasts major topologies to consistently identify the most appropriate candidates for high-power-density designs. The chapter then

provides a deeper review of the selected topology, examining controllability strategies, multi-phase implementations, stacked-cell architectures, and advances in magnetic integration, and ultimately identifies the knowledge gaps that this thesis seeks to address.

Chapter 3. Modelling and Design of High-Frequency LLC Converters

Chapter 3 establishes the theoretical framework for analysing and designing, first single-phase and then three-phase LLC converters. It develops operating principles, both in time domain and under common modelling approximations such as the FHA. A comparison between single-phase and three-phase architectures in terms of energy distribution, footprint, and scalability provides means for pursuing multi-phase high-frequency LLC converters to meet the power density expectations.

Chapter 4. Three-Phase Magnetics for LLC Converters

The fourth chapter investigates the design and integration of three-phase magnetic components, which are critical for compact and efficient LLC implementations. Strategies for transformer and inductor integration are presented, together with methods to achieve balanced three-phase operation. Key issues such as asymmetry, fringing effects, and core material selection are addressed through both geometrical and compensation techniques. The chapter also includes thermal design considerations, particularly for planar converters where power density and cooling are tightly coupled.

Chapter 5. Wye-Delta Three-Phase LLC Converters

Chapter 5 presents the main experimental contributions of the thesis: the design, optimisation, and prototyping of Wye-Delta three-phase LLC converters. Magnetic component optimisation is carried out through Pareto-front analysis, considering material properties at the MHz range of switching frequency and validating the three-port magnetic link previously analysed experimentally. The impact of geometry compensation is studied, followed by semiconductor selection and PCB layout considerations. Two architectural variants are explored: parallel inverter legs and stacked half-bridge cells, showing their progress from proof-of-concept prototypes to miniaturised designs. The chapter culminates with a final prototype achieving $20\,\mathrm{kW\,L^{-1}}$, demonstrating the feasibility of the proposed architecture for next-generation aircraft power systems.

Chapter 6. Conclusions and Future Research Lines

Chapter 6 summarises the main findings of the thesis, reflecting on the advances made in modelling, magnetic design, and the practical implementation of Wye-Delta three-phase LLC converters.

Chapter 7. Future Research Lines

The final chapter outlines several future research directions, including topology innovations, regulatory adaptation, further miniaturisation, advanced control strate-

gies, and detailed thermal modelling. These avenues provide a roadmap for continued progress in high-frequency, high-density power converters for electrified aircraft.

CHAPTER 2

Literature Review and State-of-the-Art

> We can never see past the
> choices we don't understand.
>
> — The Oracle, *The Matrix Reloaded (2003)*

Chapter 1 addressed the challenges associated with power conversion in aircraft applications. Both AC/DC and DC/DC conversions were discussed, emphasising their relevance in modern aircraft power distribution. While AC/DC conversion remains fundamental, the focus of this thesis is on DC/DC stages, as highlighted in the objectives (section 1.7), given their critical role in achieving the high step-down ratios, power density, and efficiency required in next-generation aircraft.

Building on that discussion, this chapter presents a survey of the literature, reviewing a range of DC/DC power converter solutions and their applicability to aircraft systems, with potential topologies evaluated and ranked based on their suitability under the conditions previously outlined.

To address the demands of aircraft, DC/DC converters must offer wide voltage conversion (regulation), high voltage step-down ratio for efficient energy distribution, and include features such as isolation, unidirectional power flow for auxiliary loads, high output power, compact size (power density), and high efficiency, crucial for thermal management in densely packed environments. With these considerations in mind, the requirements defined in section 1.7 for the targeted 270 V to 28 V DC/DC stage in aircraft applications can be summarised as follows:

- DC/DC power stage module.
- Wide input voltage range and fixed output voltage.
- Simple control schemes.

- Isolated.
- Low-profile PCB-integrated magnetics.
- High power density.
- Soft-switching characteristics (Electromagnetic Compatibility (EMC)).

The rising demand of such converters for efficient voltage regulation is shared among other sectors, including data centers and servers [81], industrial applications with auxiliary loads [82], and electric mobility, with electric ships [83], Electric Vehicles (EVs) [84], and aircraft in the MEA concept [85]. For this reason, and as literature directly addressing the 270 V to 28 V DC/DC conversion stage remains limited, relevant studies pursuing similar design goals in other domains are reviewed and summarised in table 2.1.

Application	Input	Output
Aircraft DC bus [85]	270 V (235-285 V)	28 V
Electric ship [83]	1000 V (850-1250 V)	68 V
Telcom [81]	240 V (100-400 V)	48 V
Server supply [81]	48 V (42-58 V)	6-12 V
Data centers [86]	48 V (40-60 V)	1.0 V (1.0-1.8 V)
Aviation microgrid [87]	48 V (36-75 V)	12 V
Automotive (EVs) [88, 89]	200 V (140-260 V)	13.6 V (10-15 V)
Industrial (auxiliar) [82]	300-430 V	12 V

Table 2.1: Summary of high-gain step-down DC/DC converter applications across different domains. Showing the shared similarities in design requirements: wide input voltage range, galvanic isolation, high power density, and high efficiency.

2.1 Trade-Offs in Practical Converters for Aircraft

Designing power converters for aircraft applications involves navigating a complex set of trade-offs. Converters must deliver high power density to minimise weight and size, yet simultaneously achieve high efficiency to reduce thermal stress and cooling demands. At the same time, they are expected to maintain robust regulation across wide input voltage ranges and dynamic load conditions.

The following subsections review these trade-offs in more detail, illustrating how electrical performance, thermal solutions, passive components, and semiconductors each impose their own constraints while shaping the achievable performance envelope of next-generation aircraft converters.

2.1.1 Electrical Performance

The list of requirements listed at the start of this chapter can be interpreted as the typical trade-offs when designing a power converter. **Power density** is often achieved at the expense of **efficiency** and **regulation** capabilities[1]. This trade-off comes from the realisation that a converter can be optimised relatively easily for a single, fixed operating point; components can be carefully selected, parasitics minimised, and parameters can be fine-tuned to maximise performance.

However, real-world applications need flexibility, they demand wide voltage operating ranges, varying loads, and output voltage stability. Meeting these requirements needs well-thought design, additional complexity, and often the inclusion of lossy elements or derating, reducing their potential efficiency in nominal conditions and increasing the size of the converter. The designer must balance these requirements, rarely achieving all three simultaneously (fig. 2.1).

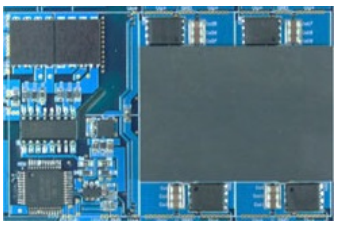

(a) Single-phase LLC with matrix transformer. 380-12 V, 97.5 % efficiency, 54 kW/L. CPES, Virginia Tech [90]

(b) DCM4623TD2H31E0y7 module. 180-420 V, 93 % efficiency, 50 kW/L. VICOR Corporation [91]

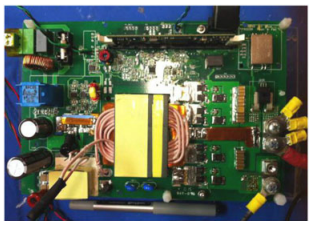

(c) DAB. 360–420 V, 98 % efficiency, 2 kW. FREEDM Systems Center, North Carolina State University [92]

Figure 2.1: Examples of commercial and academic DC/DC power converter modules illustrating the trade-off between power density, efficiency, and regulation capability

Power modules such as the one presented in [90] (fig. 2.1a) are examples of this trade-off. The LLC converter module excels in efficiency (97.5 %) and power density (54 kW/L), but it lacks regulation capabilities, as it is optimised for operating under a fixed condition (380-12 V) and does not accommodate a wide input voltage range.

Commercial DC/DC converters for aircraft applications can be found, such as VICOR's 400 W DCM4623TD2H31E0y7z (fig. 2.1b). This module supports a wide input voltage range (180-420 V) with a fixed 28 V output. However, it only achieves an efficiency of 93 %, requiring a high-performance thermal management solution. When evaluating commercial products, advertised power density figures often exclude essential external components. In this case, the module is promoted with a power density of 50 kW/L, yet requires an external output capacitor in the range of 1–10 mF to operate properly, reducing the effective power density of the system.

The final example is complementary to the previous two. In [92], a regulated DAB converter is presented (fig. 2.1c) that targets the 360–420 V input range and provides a stable 12 V output. It achieves an efficiency of 98.3 %. However, it

[1] Regulation capabilities refer to the range of operating conditions the converter must handle, such as input and output voltage variation or power output requirements.

comes at the cost of a lower power density, around 2 kW/L, highlighting the trade-off between regulation capability, efficiency, and volumetric compactness.

2.1.2 Thermal Solutions

Power converters require efficient thermal management to ensure the performance that they are advertised for. The most effective way to prevent overheating in power converters is to minimise power losses, ensure their even distribution across the system to avoid hotspots, and implement a robust thermal design [93].

Each cooling method presents unique trade-offs in terms of efficiency, complexity, and cost. The most common approaches are air cooling and liquid cooling [94]. For different power levels or system requirements, and based on a literature review table 2.2 presents a summary of the different cooling mechanisms highlighting key advantages, limitations, and typical application domains.

Mechanism	Key Advantages	Limitations	Use	Ref.
Natural convection	Simplest and lowest cost	Very limited by ambient	Low power	[95]
Forced-Air Cooling	Simple and low cost	Limited by ambient, low efficiency	Low-medium power, cost-sensitive	[96, 95]
Immersion	Extreme heat removal	Compatible and expensive fluid, insulation, weight	Ultra high-density converters	[97, 98]
Liquid Cooling	High efficiency, scalable	Complex, high cost and maintenance	High power, high density	[99, 100]
Two-Phase Cooling	Extreme heat extraction, low flow	System complexity	Systems with high performance	[101, 100]

Table 2.2: Comparison of cooling mechanisms for power converters, highlighting key advantages, limitations, and typical application domains.

Due to the limited effectiveness of forced-air cooling at high altitudes and confined aircraft environments (fuselage), forced liquid cooling has become the dominant solution in recent decades [95, 98]. As reference, [102] presents a comparison between the same design when using forced-air and liquid cooling, doubling the effective power density of the system in ground conditions.

In general, single-phase[2] cold plates are used, and depending on the available exchange surfaces for heat dissipation, a single-sided or double-sided cooling cold plate is used. In any case, the temperature level of the cooling oil is typically high[3]

[2]Single-phase in this context refers to the coolant to remain in the same state (liquid).

[3]While 90 °C may seem high for typical electronics, it is considered acceptable and even efficient, where devices are often designed to operate safely at elevated junction temperatures.

(90 °C), allowing a dissipation in the order of 1-10 W/cm^2 [95], depending on the type of cold plate structure [103].

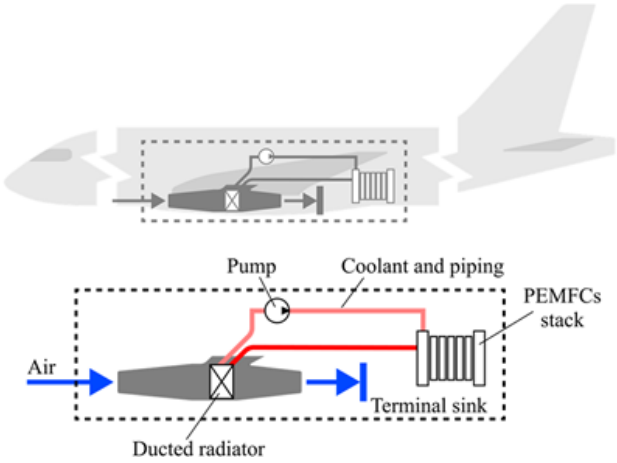

Figure 2.2: Simple schematic for the typical cooling system of an aircraft [98].

2.1.3 Passive Components: Energy and Volume

Inductors and capacitors serve as the fundamental energy storage elements in power electronic converters. Although their physical energy densities can vary dramatically depending on technology and application, capacitors generally offer much higher energy density than inductors, making them preferable in weight and space constrained applications.

This detailed view is critical because passive components typically dominate the mass and volume budget of high-performance converters. The ability to compare not just volumetric but also specific energy densities allows for more accurate and optimised component selection. It also emphasises the need to consider application-specific voltage requirements and packaging technologies when choosing between capacitor types. While inductor design is constrained by magnetic saturation, core losses, and copper windings, capacitors offer more compact and lighter alternatives under the right conditions.

When designing high power density converters, the choice of different passives is crucial to estimate the size of the converters. Volumetric energy density, typically expressed in J/mL, is a key performance metric for inductors and capacitors, and it is directly influenced by the choice of materials.

Magnetics

In the MHz-range, soft ferrites remain the default core materials for magnetics, as they combine high permeability with intrinsically high resistivity, thereby delivering a strong magnetic link with relatively low losses. The main challenge, however, lies in the rapid increase of core losses with frequency. As a result, processing techniques and compositional adjustments are specifically directed towards lowering the specific core loss while maintaining sufficient permeability and thermal stability.

After further frequency increase, a slower frequency scaling (volume reduction) will still exist, but as it approaches around 2 MHz, the trend reverses as losses outpace the thermal dissipation capacity. Figure 2.3 illustrates the estimated trend of power density versus switching frequency for typical kW-scale DC/DC converters operating at a 300 V bus voltage [104]. In these higher switching frequency ranges, conventional designs lose their effectiveness, and fully soft-switched converters with specialised magnetics become necessary.

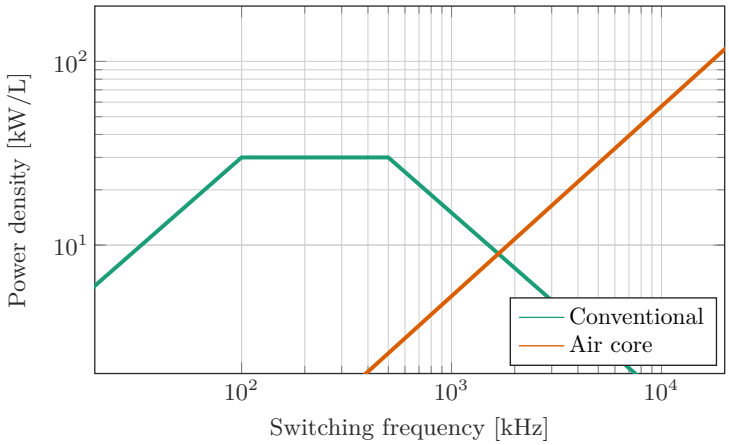

Figure 2.3: Estimate of DC/DC converter power density against switching frequency [104].

At operating frequencies around 1 MHz, magnetic components can be optimised and their power losses estimated with relative ease. Classical analytical models remain useful: Ferreira's formulations for high-frequency foil-winding losses [105, 106], Roth's model for leakage [107], fringing effects [108], and Hurley's treatment of loosely coupled inductances [109]. However, contemporary electromagnetic suites such as Ansys or FEMM often provide a more straightforward and precise estimation, with core losses evaluated independently.

In general, contemporary magnetic core materials in planar configurations can dissipate 300 mW/cm^3 without an advanced cooling technology [110], nonetheless, specific geometry and loss distribution may reduce this figure. Moreover, at higher frequencies or in very small cores, additional loss mechanisms may be significant, driven not by the intrinsic material properties but by geometric effects [111].

Multi-Layer Ceramic Capacitor (MLCC)

Capacitors are the more compact and energy-efficient electric passive components available, offering volumetric energy densities up to approximately 8 J/mL [112]. There exist many different technologies in their design, but in high power density converters, the MLCC is the most common. Its high performance stems from their internal structure: as illustrated in fig. 2.4b hundreds to thousands of thin layers of high-permittivity ceramic dielectrics are stacked within a single package, maximizing active material usage while withstanding high electric fields across each layer. This multilayer architecture enables a unique combination of high energy density, mechanical robustness, and excellent scalability for surface-mount integration in compact and high-reliability systems.

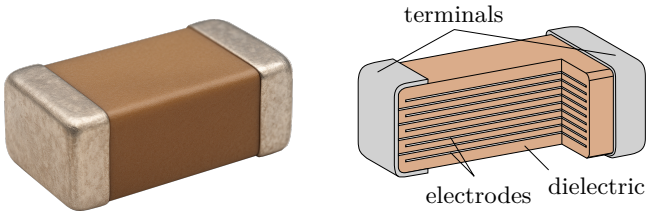

(a) 630 V 100 nF (b) Internal structure [113]

Figure 2.4: An Multi-Layer Ceramic Capacitor (MLCC) and its internal structure [114].

Despite their advantages, the energy density of these capacitors is fundamentally limited by the properties of ceramic dielectrics, particularly their breakdown strength and temperature-dependent behaviour. To accommodate different performance requirements, manufacturers utilize various dielectric classes. Class I dielectrics (such as the C0G) offer superior thermal and electrical stability, making them ideal for applications requiring consistent capacitance over wide temperature and voltage ranges. In contrast, Class II dielectrics (such as the X7R) provide significantly higher energy densities at the expense of temperature stability, varying capacitance over voltage bias, and long-term reliability due to aging [115]. This is illustrated in fig. 2.5.

Nevertheless, MLCCs continue to dominate in a wide range of power and signal applications due to their unmatched volumetric efficiency, low Equivalent Series Resistance (ESR), and automated assembly processes .

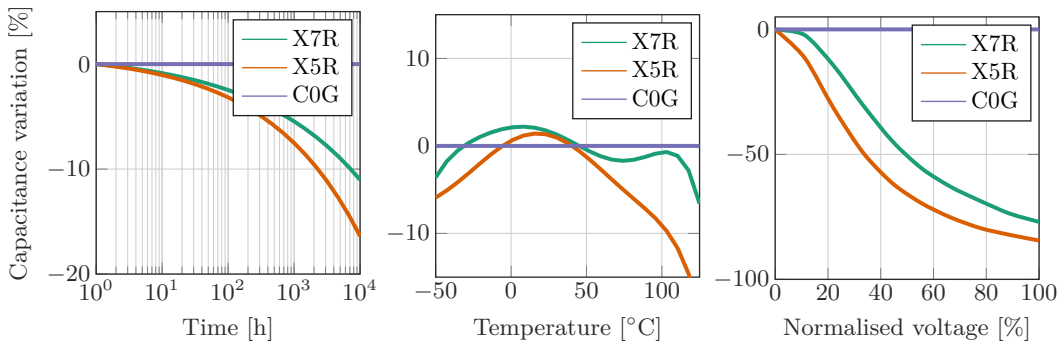

(a) Ageing of the capacitor (b) Thermal behaviour (c) Biasing effect

Figure 2.5: Typical variations of capacitance with cycles, temperature and voltage bias for different MLCC dielectrics in imperial 0805 packages [115].

In contrast with magnetics, estimating power losses in capacitors is challenging because their behaviour under real operating conditions deviates significantly from the small-signal data typically given in datasheets and that is easily measured using a network analyser. Losses are dominated by non-linear ferroelectric hysteresis effects, which are highly dependent on excitation amplitude, frequency, and DC bias, making them difficult to quantify accurately [113].

2.1.4 Semiconductors

At operating frequencies around 1 MHz and in the kilowatt power range, the choice of semiconductor devices becomes a decisive factor in achieving high efficiency and manageable thermal performance. GaN, SiC, and Si technologies each occupy a specific use defined by voltage, switching speed, and efficiency trade-offs.

At low to medium voltages applications (up to approximately 400 V), GaN HEMT devices are recognised as the most effective option for MHz operation. Their low parasitic capacitances, and absence of reverse recovery translate directly into reduced switching losses, higher efficiency, with superior dynamic behaviour compared to Si and SiC MOSFETS [116].

Nevertheless, when operating at the low voltage (60 V), Si MOSFETS can remain competitive. In such conditions, the dominant differentiator is not conduction loss but the gate-driving power required to switch devices at those high speeds. Since Si typically requires more power-hungry gate drive circuitry, its advantage may diminish, and still maintaining GaN as comparable performance at reduced driving overhead. The specific on-resistance of both technologies can be seen in fig. 2.6.

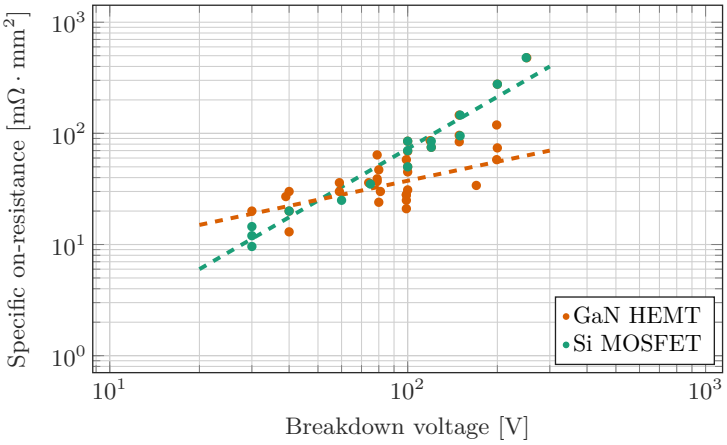

Figure 2.6: Comparison of specific on-resistance as a function of breakdown voltage for low-voltage (< 200 V) semiconductor devices, highlighting the superior figure of merit of GaN HEMT compared to conventional Si MOSFET above 100 V, but still comparable under 60 V.

For medium to high voltage applications in the 1.2 kV to 3.3 kV range, SiC devices are more suitable. They combine lower conduction and switching losses than Si with higher breakdown voltages and excellent thermal robustness. While their intrinsic switching speed is lower than GaN, SiC MOSFETS can still be operated efficiently near the MHz range when paired with soft-switching topologies to mitigate switching losses. In these cases, SiC extends MHz operation to voltage domains where GaN devices are unavailable at the current state of the technology.

In conclusion (as previously shown in fig. 1.11), at MHz operation, kilowatt power levels and voltages under 400 V, GaN HEMT is the technology of choice for low-to-medium voltage applications, offering unmatched switching performance,

compactness, and efficiency. SiC, while slower, is the most effective option for higher voltage systems, enabling MHz operation with robust thermal behaviour and high reliability. Si MOSFETS, although mature and inexpensive, are constrained to the margins of this operating space. The continuing development of WBG devices, together with advanced converter topologies, represents the most promising route for miniaturisation of power converters. A comparison of commercially available GaN transistors is presented in table 2.3. Infineon (including the former GaN Systems) leads the market above 400 V, thanks to their compact packaging and excellent thermal performance, while EPC is widely regarded as the benchmark in the low-voltage domain.

Manufacturer	Device technology	Voltage class	Integration level	$R_{DS(on)}$ [mΩ]
Infineon (CoolGaN)	e-mode lateral HEMT	> 400 V	Discrete and integrated half-bridge	25 mΩ to 150 mΩ
GaN Systems (now Infineon)	e-mode HEMT	650 V	Discrete (top and bottom cooled)	25 mΩ to 70 mΩ
GaN Systems (now Infineon)	e-mode HEMT	100 V	Discrete (top and bottom cooled)	1.5 mΩ to 10 mΩ
EPC Co.	e-mode lateral e-GaN	40-350 V	Discrete and monolithic half-bridge	0.8 mΩ to 15 mΩ
Navitas	e-mode HEMT	650 V	HEMT with integrated driver and protections	50 mΩ to 200 mΩ
Transform (Renesas SuperGaN)	Cascode d-mode GaN and Si MOSFET	650 V and 900 V	Discrete, MOSFET-like gate driving	35 mΩ to 120 mΩ

Table 2.3: Updated GaN HEMT comparison (as of August 2025).

2.2 Topology Selection

The selection of a suitable converter topology is critical to fulfil the combined requirements of wide input voltage range, high efficiency, high power output, and high power density. These demands are particularly exigent in the 270 V to 28 V aircraft electrical bus interface system, where input voltage may fluctuate significantly due to dynamic loading conditions.

Wide input voltage variations challenges the converter's ability to maintain high performance across the full operating range. Therefore, the chosen topology must inherently support a wide conversion ratio while enabling soft-switching across the entire voltage and load envelope to minimise switching losses and EMI, all within

a compact and efficient design.

To reduce design complexity and enhance robustness, multi-stage solutions involving pre-regulation have been deliberately excluded. The focus is instead on inherently isolated, single-stage or integrated topologies that deliver scalable performance and require minimal control overhead.

From all that has been discussed in this chapter so far, this section presents a comparative study of three DC/DC converter candidates: PSFB, DAB and LLC. The comparison is carried out using simplified analytical models, which allow the main characteristics and trade-offs of each topology to be highlighted without the burden of full-scale detailed simulations at this stage.

2.2.1 Phase-Shift Full-Bridge (PSFB)

The Phase-Shift Full-Bridge (PSFB) is a well-established topology commonly selected in applications requiring galvanic isolation and controllability across a wide input voltage range. Functionally, it can be seen as the isolated counterpart to the buck converter, employing Phase-Shift Modulation (PSM) to regulate the output instead of Pulse-Width Modulation (PWM).

The topology consists of a full-bridge arrangement of power semiconductors that generate a three-level high-frequency voltage across the primary of the transformer. By adjusting the phase-shift between the two inverter half-bridge legs, allows to control the effective AC voltage waveform in the secondary side that is then rectified and filtered by an output LC network to produce a DC output, maintaining output regulation.

This means that the PSFB supports current-mode control via the output inductor, and operates at a fixed switching frequency, facilitating magnetic and filter design. However, the output inductor L_f, required for energy filtering and current shaping, introduces additional losses, especially under high output current conditions. Furthermore, the square-wave nature of the current waveform leads to high harmonic content, which increases EMI, and thus requiring careful layout and filtering.

When designing for constrained conditions (high power density), extreme light-load or input conditions are detrimental to the PSFB, suffering from hard switching, which can reduce efficiency and increase switching stress. Although auxiliar circuitry composed of LC networks is typically added to the topology to aid in the soft-switching [117], adding it complicates the system and increases the volume.

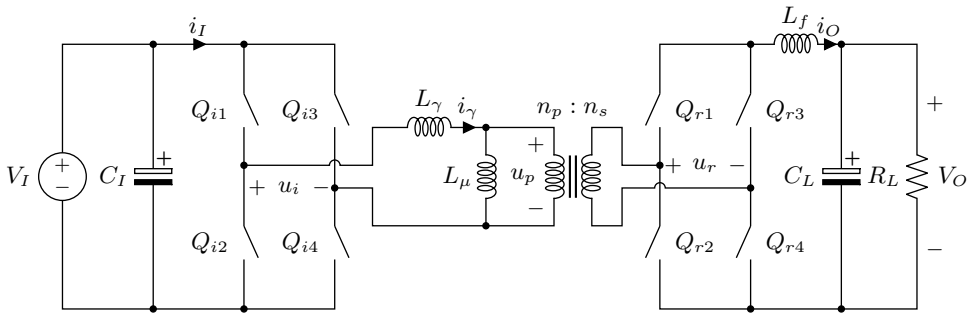

Figure 2.7: Isolated DC/DC Phase-Shift Full-Bridge (PSFB) converter.

Basic Design of a PSFB Converter

Designing a PSFB converter is straightforward. The voltage step-down is achieved through the transformer's windings turns ratio $n_n = n_p/n_s$, which provides the main voltage conversion, the rest of the conversion is performed through the modulation, typically defined with the duty-cycle equivalent $D_e = 1 - \Delta\varphi/\pi$ of the inverter:

$$n_n = \frac{n_p}{n_s} = D_e \frac{V_O}{V_I} \tag{2.1}$$

showing that it requires a lower winding turns ratio compared to other topologies.

The rest of the design focuses on four key components: the series inductance L_γ, the output filter inductance L_f, the transformer magnetising inductance L_μ, and the output capacitance C_L. The series inductance L_γ is simple to determine, as it is derived from the minimum inductance (energy) required to achieve Zero Voltage Switching (ZVS) operation, as described in [118]:

$$L_\gamma = 2C_{oss} \frac{V_I^2}{I_{ZVS}^2} \tag{2.2}$$

Note that L_γ increases significantly as the minimum switching current I_{ZVS} decreases, implying that under very light load conditions the converter may lose ZVS operation. And meaning that, at heavy loads, it results in high $\frac{\mathrm{d}v}{\mathrm{d}t}$ that can lead to high harmonic content, ultimately degrading the EMC performance. It is also important to note that the primary current must enable soft-switching of the parasitic C_{oss}, while accounting for all the parasitic elements in parallel with the transformer, this makes the use of PCB-integrated windings less suitable for achieving reliable ZVS operation as the range of power outputs expands.

Strong output current filtering is required, since the ripple in I_{ZVS} is related to the average output current I_O, further compromising soft-switching. The two filtering elements can be calculated as:

$$L_f = \frac{V_O\,(1 - D_e)}{f_S \Delta I_O} \tag{2.3a}$$

$$C_L = \frac{D_e \Delta I_O}{f_S \Delta V_O} \tag{2.3b}$$

The PSFB transformer is usually designed so it can operate in current control mode, for which the magnetising inductance can be calculated as reference [119]:

$$L_\mu \geq n\frac{V_I\,(1-D_e)}{2f_S\Delta I_O} \tag{2.4}$$

nonetheless, this design boundary is typically met, leaving the transformer design as ideal as possible. Thus, the calculation for the magnetising inductance L_μ is typically neglected as it is assumed to be much larger than the main inductance. This means that, in the case of the PSFB, the transformer is designed to be as ideal as possible, being solely limited by the magnetic core and windings, as such, we can:

$$\Phi_\mu = L_\mu \cdot \hat{I}_\mu = \hat{B}_c \cdot n_p \cdot A_c \tag{2.5a}$$

where,

$$\hat{I}_\mu = \frac{n_n V_O}{2f_S L_\mu} \tag{2.5b}$$

thus obtaining the area of the core:

$$A_c = \frac{L_\mu \hat{I}_\mu}{n_p \hat{B}_c} = \frac{V_O}{2n_s f_S \hat{B}_c} \tag{2.5c}$$

allowing to estimate the size of the core.

2.2.2 Dual Active Bridge (DAB)

The Dual Active Bridge (DAB) converter consists of two full-bridge building blocks, both actively generating square-wave voltage pulses adjustable by the duty cycles and the phase-shift (delay) between the two legs of each full-bridge. These voltages are then applied across an inductor, which can either be an external component or integrated into the transformer's leakage inductance.

Power transfer in this circuit is typically regulated by adjusting the phase-shift $\Delta\varphi$ and the amplitude of the fundamental component of the voltage applied by each bridge. Its symmetrical architecture, makes the DAB used for bidirectional power flow and naturally supports step-up and step-down voltage conversion, making it suitable for a wide range of power applications.

The DAB circuit is indicated as a possible solution for aircraft application [120] allowing to meet the requirements of high power density and low weight, as it is often used in such applications where these characteristics represent critical factors ZVS conditions [121].

Although closed-form expressions can minimize Root-Mean-Square (RMS) currents and guarantee to be designed under full ZVS conditions, they typically assume losses as negligible, and therefore fail to pinpoint truly optimal operating points. Thus, achieving optimal efficiency and weight reduction requires a careful trade-off between size, loss, and performance.

Despite these challenges, the DAB remains a compelling choice in high-performance, isolated DC/DC conversion scenarios.

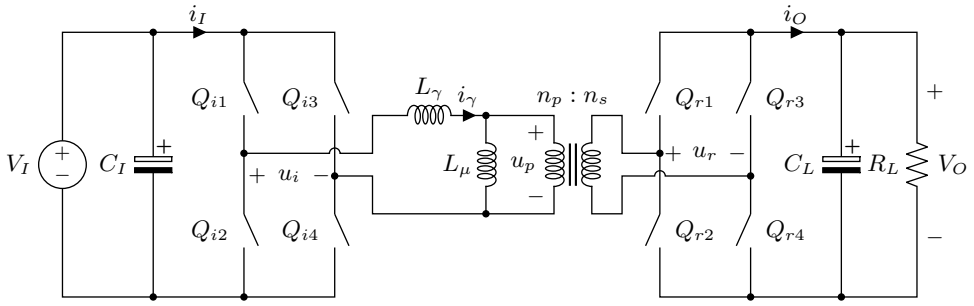

Figure 2.8: Isolated DC/DC Dual Active Bridge (DAB) converter

Basic Design of a DAB Converter

With three components to be designed (L_γ, L_μ and C_L), a basic design can be obtained, starting with the transformer's winding turns ratio, given by:

$$n_n = \frac{n_p}{n_s} = \frac{V_O}{V_I} \tag{2.6}$$

A single variable is used to control it, the phase-shift between the two bridges $\Delta\varphi$ (or its equivalent duty cycle $D_e = \Delta\varphi/\pi$). From the peak current $\hat{I}_p$, the output current I_O is then related to the phase-shift with $I_O = \hat{I}_p(1 - D_e)$. For controllability and to reduce the reactive energy, this parameter is typically set to a limit[4], and so we can calculate the main inductor L_γ as:

$$L_\gamma = n_n \frac{D_e V_I}{I_O(1 - D_e) f_S} \tag{2.7}$$

The calculation for the magnetising inductance L_μ is typically neglected as it is assumed to be much larger than the main inductance. This means that, in the case of the DAB, the transformer is designed to be as ideal as possible, being solely limited by the magnetic core and windings, as such, we can:

$$\Phi_\mu = L_\mu \cdot \hat{I}_\mu = \hat{B}_c \cdot n_p \cdot A_c \tag{2.8a}$$

where,

$$\hat{I}_\mu = \frac{n_n V_O}{2 f_S L_\mu} \tag{2.8b}$$

thus obtaining the area of the core:

$$A_c = \frac{L_\mu \hat{I}_\mu}{n_p \hat{B}_c} = \frac{V_O}{2 n_s f_S \hat{B}_c} \tag{2.8c}$$

allowing to estimate the size of the core.

This allows to calculate the output capacitance by analytically integrating the primary current (reflected to the secondary) when it surpasses the output current I_O to get the voltage ripple ΔV_O:

$$C_L = \frac{I_O(1 - D_e)}{f_S \Delta V_O} \left[D_e - \frac{D_e^3}{4} \right] \tag{2.9}$$

[4] A typical value for maximum phase-shift is 30°.

2.2.3 Single-Phase LLC

The LLC converter is a widely used topology in isolated power conversion due to its high efficiency and relatively simple operation. It uses a resonant tank composed of an inductor and a capacitor, with the resonant inductor often integrated as the transformer's leakage inductance. The converter is typically controlled by Frequency Modulation (FM), where varying the switching frequency adjusts the impedance of the resonant tank and, consequently, the voltage conversion ratio.

At frequencies above the resonance of the resonant tank, the topology acts as a step-down converter; while below resonance, the tank allows step-up behavior due to the involvement of the magnetising inductance into the resonance. This frequency-dependent behaviour makes the LLC suitable for moderate voltage variations but less efficient across a very wide conversion range.

Thanks to its soft-switching behaviour across the entire load range (ZVS on the inverter and Zero Current Switching (ZCS) on the rectifier) the LLC topology achieves excellent efficiency, particularly in high-current, high-frequency applications. However, its dependence on FM for regulation introduces challenges in applications requiring a wide voltage conversion range, as large frequency deviations significantly degrade its performance. Additionally, although the waveform harmonic content is inherently EMI-friendly (sinusoidal waveforms), the variable switching frequency complicates the design of compact EMI filters. For this reason, LLC converters are typically operated within a narrow frequency range in applications with strict EMC requirements.

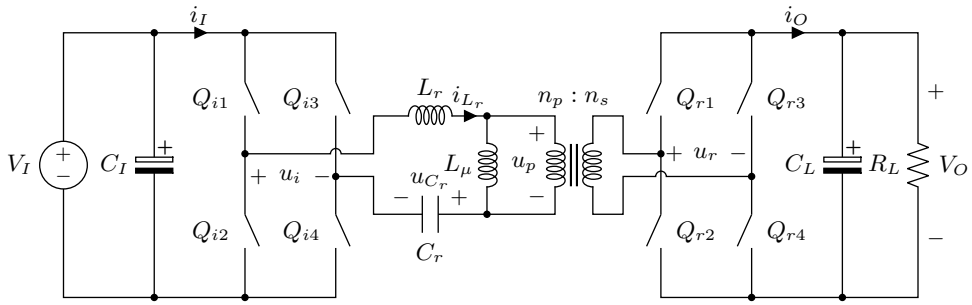

Figure 2.9: Isolated DC/DC Inductor-Inductor-Capacitor (LLC) converter

Basic Design of an LLC Converter

The LLC converter is regarded as a complex topology to design, analytical approaches include the FHA and time-domain simulation. While FHA is convenient and accurate near resonance, it becomes unreliable when operating far from unity gain, making time-domain analysis essential for precise prediction and optimisation of waveforms and operating points over a wide frequency range.

For comparison purposes, its design will be considered for a fixed condition to reflect its main features. As with the DAB, the full conversion is obtained from the transformer's winding turns ratio n_n:

$$n_n = \frac{n_p}{n_s} = \frac{V_O}{V_I} \tag{2.10}$$

Similarly to the PSFB, the magnetising inductance is designed to guarantee ZVS, in the case of the LLC converter is mostly non-dependent[5], and we can calculate it energetically with the C_{oss}:

$$L_\mu = \frac{n_n V_O}{8 f_r C_{oss} V_I^2} \tag{2.11}$$

The rest of variables, L_r and C_r require some additional assumptions, first, resonance operation is considered $f_S = f_r$, thus by neglecting the magnetising current, the maximum current through the resonant tank is given by:

$$\hat{I}_{L_r} = \frac{\pi}{2} \frac{P_O}{V_I} \tag{2.12}$$

and then if we assume a maximum voltage (rating) across the resonant capacitor $\hat{U}_{C_r}$, the resonant capacitance C_r is straightforward:

$$C_r = \frac{\hat{I}_{L_r}}{2\pi f_r \hat{U}_{C_r}} = \frac{\pi}{2} \frac{P_O}{2\pi f_r V_I \hat{U}_{C_r}} \tag{2.13}$$

and from the resonant frequency, L_r is given:

$$L_r = \frac{1}{4\pi^2 f_r^2 C_r} \tag{2.14}$$

2.3 LLC Converters in the State-of-the-art

Aircraft power electronics operate under challenging conditions with an extensive regulatory basis. The constraints on size and weight are directly linked to the requirement for high efficiency, as effective heat dissipation is inherently difficult in such compact systems. Furthermore, EMI must be tightly controlled to prevent disruption of sensitive on-board systems during flight.

A high-voltage step-down DC/DC conversion is required to supply the on-board systems, which typically operate at 28 V DC, from a wide input voltage range of 200 V to 330 V [122].

In section 2.2, three widely used isolated converter topologies for wide voltage conversion (PSFB, DAB, and LLC) were analysed, proposing a basic design under a common set of assumptions. To make an informed choice between them, a quantitative comparison is presented under a common set of assumptions (270 V to 28 V, 1 kW output power, and 500 kHz fixed switching frequency). The results are shown in fig. 2.10, showing the energy of the passives and, as previously discussed in section 2.1.3, a volume estimation.

[5]The energy required to soft-switching is independent on the frequency and load, but, as long as there is enough gain margin to avoid entering into the capacitive region, the energy stored in the transformer is independent.

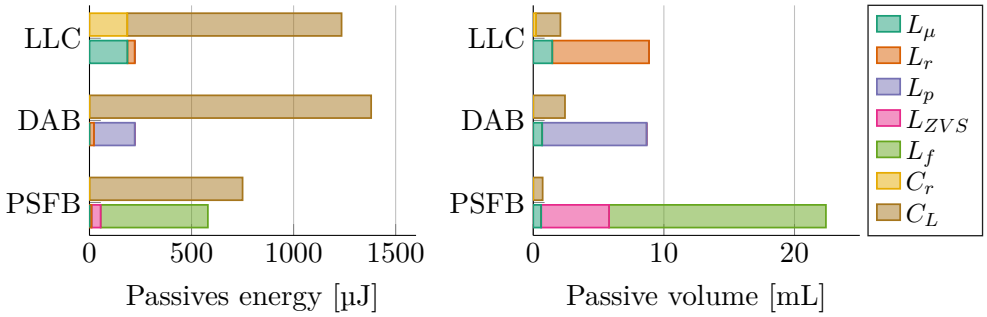

(a) Energy comparison (b) Volume comparison

Figure 2.10: Comparison of passive component energy and estimated volume for the three selected topologies: PSFB, DAB, and LLC. The analysis considers a DC/DC converter operating from 270 V to 28 V at 1 kW, with a fixed switching frequency of 500 kHz.

The PSFB converter is recognised for its structural simplicity, low cost, and inherent ZVS capability, enabled by the resonant interaction between a shim inductor and the drain-source capacitances of the primary switches. However, maintaining ZVS under light-load conditions requires a larger shim inductor, raising the $\mathrm{d}v/\mathrm{d}t$ stress during heavy-load operation [84]. Moreover, the presence of hard switching in the output rectifier further restricts high switching frequencies, limiting its miniaturisation. The conduction losses are also increased by the shim inductor and, more significantly, the output filter inductor, which is typically a high-energy component as shown in fig. 2.10, ultimately reducing the overall efficiency.

The DAB converter, in contrast, offers a symmetrical structure that enables efficient power transfer, galvanic isolation, compact integration [121] and its reconfigurability [123]. The converter allows to be operated with a constant switching frequency as well as limited switching frequency range. Nonetheless, the DAB can suffer from severe RMS current increase in deep step-down and step-up regions. These difficulties arise from the piecewise nature of the current waveforms, governed by the interaction between the bridges for different conversion ratios, thereby limiting the converter's inherent soft-switching capability. The challenge becomes even more pronounced when complex modulation schemes are employed [92]. While closed-form boundary equations have been proposed to guarantee ZVS operation under specific conditions [124], maintaining ZVS across the entire operating range remains challenging [118] but makes it possible to mitigate these drawbacks to certain extent, at the expense of a more complicated design and control of the converter. Consequently, the higher switching frequencies required to reduce magnetic component size can lead to substantial semiconductor losses due to increased switching currents [120], ultimately increasing the EMI.

The LLC resonant converter is widely recognised for its high efficiency [125], primarily due to its intrinsic soft-switching features (ZVS for the inverter switches and ZCS on the rectifier side) which remain effective across a wide range of load conditions and switching frequencies [84]. This is due to the independence of the magnetising current, which leads the main resonant current by 90°, resulting in consistently well-defined dead times and reliable high-frequency operation. Conse-

quently, both switching losses and EMI are significantly reduced. These characteristics not only enhance efficiency but also support the miniaturisation of magnetic components, increasing power density and making the LLC converter the selected topology for this work.

Numerous topologies have been proposed over the years to address these specific requirements: wide regulation, high voltage step-down, power density and high efficiency. To better understand the diversity of approaches, these techniques are categorised into four groups: controllability (modulation and morphing topologies), multi-phasing (alternative to parallelisation), stacking (inverter legs in stack for greater step-down conversion), and advanced and integrated magnetic component design.

2.3.1 Controllability of LLC Converters

The main challenge of LLC converters for wide voltage regulation lies in the control. In the literature there is a long list of possible alternatives that extend their gain possibilities. Frequency Modulation (FM) is the most classical one [126], it relies on the modulation of the total impedance of the resonant tank, by controlling the switching frequency, the voltage transfer ratio can be adjusted. For switching frequencies above resonance, the total impedance increases acquiring a step-down functionality (voltage divider). Below resonance, the series connection of the magnetising inductance starts dominating, and since the output voltage is, in truth, in parallel with the transformer, the voltage can go higher than the input voltage, allowing the converter to achieve step-up conversion.

When a wide range of step-up and step-down gains are needed, a wide switching frequency range is required, which often results in complex modulation strategies. One approach that has gained attention is the combination of a fixed-ratio DC/DC Transformer (DCX) stage with a preregulation front-end [89, 127]. This partitioning allows the designer to decouple regulation from power delivery. However, this solution is not considered in the present work, as in the kilowatt power range it typically leads to lower power density and reduced peak efficiency [128], making it less competitive for the targeted applications.

For this reason, great research effort has been put into the modulation, including:

For this reason, great research effort has been devoted to enhancing the modulation of LLC converters beyond simple frequency variation. The objective is to preserve soft-switching, extend the gain range, and maintain high efficiency across wide operating conditions. The most representative among these strategies include:

- Phase-Shift Modulation (PSM): This modulation regulates the output voltage by varying the phase angle between the inverter legs while keeping the switching frequency constant at a given load. Although the design allows easier design [129], in order to ensure ZVS operation across a wider operating condition, a combination with variable frequency control improves efficiency and reduces voltage stress. Smooth extensions of PSM are proposed in [82], where transitions between FM and PSM improve both controllability and transient response.

- Pulse-Width Modulation (PWM): Pulse-width modulation can be introduced in resonant converters to regulate output voltage at nearly constant frequency. In LLC, duty-cycle control has been combined with full-bridge or dual-bridge implementations [130], enabling additional degrees of freedom to decouple gain from frequency. The trade-off, however, is increased current stress and more complex transformer design.

- Burst Mode: At light loads, burst mode is a well-known technique to limit circulating energy and avoid excessive efficiency degradation. The converter alternates periods of normal switching and idle time, effectively reducing average switching frequency. This is attractive for low-power standby or battery-charging operation, though it introduces acoustic noise and output ripple, which require careful filtering [131].

Probably the most flexible approach is to use morphing topologies, which combine different modulation schemes and resonant tank configurations to further extend the operation of the LLC converter. Examples are abrupt transitioning from full-bridge to half-bridge [81], smooth transitioning into PSM [82] (fig. 2.12a), adding more levels [132], or simultaneously in inverter and rectifier [133] (see fig. 2.12c). Other modulations for additional modes can be added such as the quantum control [134], or the Variable Frequency Multiplier (VFX) approach, where a stacked LLC is partitioned, supplying coarse gain selection while the tank provides fine regulation and soft-switching. These morphing approaches effectively add Degrees of Freedom (DoF) to the modulation, as depicted in fig. 2.11, and allow smoother transitions across load conditions.

There are also approaches based on bridge reconfiguration, where the hardware is adapted to provide multiple equivalent converter topologies depending on the operating point, such as a hybrid dual full-bridge [135], or asymmetric resonant tanks with up to six modes of operation [136]. While these methods extend the usable gain range significantly, they add complexity in the control implementation, which limits their adoption in compact designs [137]. Other extensions include hybrid modulations, such as pulse-width and amplitude modulation [**jiang˙llc˙pwam˙control**] or capacitor-clamped multi-output variants [**ren˙capacitor˙clamped˙GaN**], which aim to integrate multiple functionalities into the same resonant platform.

A summary of all these techniques is illustrated in fig. 2.11, showing an example of achieving a desired gain for different modulations (with different frequencies). Overall, the controllability of LLC converters can be understood as a spectrum of techniques, ranging from classical frequency control to hybrid morphing and reconfigurable structures, each adding degrees of freedom to cope with the challenge of wide-range regulation. Their trade-offs in terms of complexity, efficiency, and device stress have been extensively analysed in recent works [138, 131].

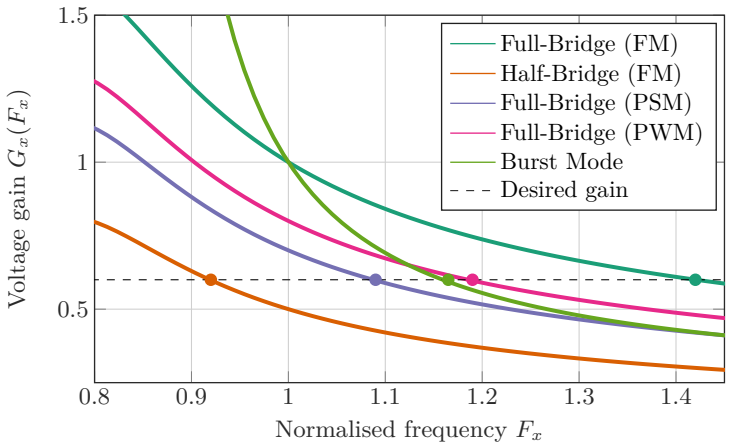

Figure 2.11: Example of different modulation strategies in an LLC converter achieving the same target voltage gain. The figure illustrates how Frequency Modulation (FM), Phase-Shift Modulation (PSM), Pulse-Width Modulation (PWM), burst mode, and the reconfiguration of the bridge (to half-bridge) shift the required normalised switching frequency F_x in order to reach the desired gain G_x.

(a) Single-phase LLC matrix transformer with two DoF (PSM and FM). 380-12 V, 96.7 % efficiency, 20 kW/L. PES Laboratory, ETH Zürich [82]

(b) 30 kW LLC DC/DC converter with reconfigurable rectifier, 98 % efficiency, 6.5 kW/L. Wolfspeed Inc. [139]

(c) T-type single-phase LLC with three DoF. 380-12 V, 97.2 % efficiency, 2 kW/L. Sakarya University [133]

Figure 2.12: Examples of academic and industry DC/DC power converter modules with morphing and reconfiguration

2.3.2 Multi-phase LLC Converters

When high output power is required, single-phase LLC converters suffer from large input and output current ripples, which demand bulky passive filters (output capacitors) to maintain the voltage ripple under specification. This becomes increasingly problematic as designs move towards higher levels of integration and miniaturisation: the output capacitance may ultimately dominate the overall converter size: in [140], a volumetric power density of 27 kW/L is reported, yet when accounting for the required output capacitance, the effective density is almost halved. Moreover, the half-sinusoidal current waveforms intrinsic to the LLC result in high RMS currents compared to other topologies with more piecewise linear current waveforms, underutilising the conduction capability of semiconductor devices. Thus,

even though switching losses are minimised by design, conduction losses can still be substantial.

Interleaving LLC Converters

To overcome these limitations, it is only natural to distribute the load among several converter phases through interleaving, much like in split-phase converters [141]. Interleaved LLC solutions are widely studied [142], including for wide input voltage ranges [137]. The idea is to connect multiple converters in parallel [143], each handling a fraction of the total current. By introducing controlled phase-shifts between them, the input and output current ripples are also attenuated, improving filtering requirements and reducing device stress.

However, balancing power among phases is not trivial. In topologies such as the buck converter, phase balance is inherently guaranteed by the PWM duty ratio. In contrast, power transfer in LLC converters is frequency-dependent; components mismatch cause each phase to exhibit slightly different resonant frequency. As a result, either one common switching frequency must be chosen (unequal power sharing) or each phase must operate at a slightly different frequency, producing low-frequency beating in the waveforms, particularly in the input and output currents. Both outcomes undermine the initial benefits of interleaving.

One partial remedy is to address tolerance-sensitive elements, particularly inductors. Coupled inductor approaches, as studied in [144], reduce but do not eliminate unbalance. Ultimately, additional circuitry or control strategies are needed to guarantee current sharing, as summarised in table 2.4, which inevitably adds complexity and reduces power density [145].

Method	Additional components	Disadvantage	Ref.
Phase-shifting	None	Controllability	[137]
Coupled magnetic	None	Partially solved	[144]
Partial processing	Auxiliary converter	Complexity	[146]
Switch-controlled resonant capacitor	IV-quadrant switch	Complexity and reliability	[147]

Table 2.4: Techniques to ensure current sharing in interleaved LLC converters.

Three-phase LLC Converters

A more elegant solution is to move from loosely interleaved phases to a fully three-phase architecture. The concept can be understood by starting with three independent single-phase LLC converters connected in parallel. Each phase processes one-third of the total power, reducing the per-phase current as well as the input and output current ripple (the same as in conventional interleaving). With a 120°

phase shift, flux cancellation occurs naturally, enabling integration of the three inductors and three transformers into a single compact magnetic structure [148, 149]. At MHz switching frequencies, this structure overcomes the bulk and complexity typically associated with multi-phase magnetics, achieving both high efficiency and exceptional power density [150].

Unlike generic interleaving, three-phase LLC converters inherently promote automatic current sharing between phases, eliminating the need for complex balancing circuits. This is guaranteed due to the resonant current coupling among phases due to the connection of the primary winding [151]. Then, by synthesising the inverter and rectifier stages in a three-phase manner (see fig. 2.13), designers can exploit additional performance benefits: ripple cancellation at the input and output [152], reduced current stress per device [151], and tighter magnetic integration for compact [153], high-efficiency designs [154]. Many of the techniques developed for single-phase LLC remain applicable: alternative rectification schemes such as phase-shift [155, 156], matrix transformer implementations [152], or further interleaving within the three-phase structure [153].

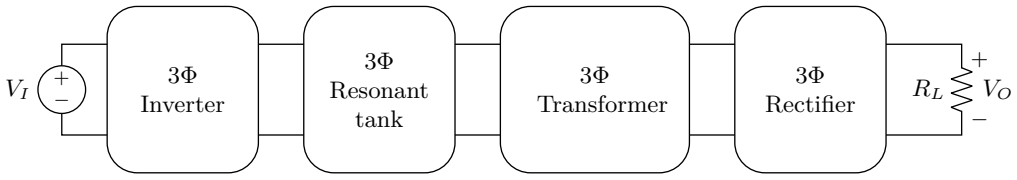

Figure 2.13: Generic schematic of the three-phase LLC converter.

Three-phase systems also offer unique benefits. Integrated three-phase inductors [157] and transformers [158] can reduce the number and volume of magnetic components. Transformer connections such as wye-delta [158], delta-wye, delta-delta [156], and wye-wye [155] are possible. Particularly interesting for this work is the wye-delta configuration as it provides an intrinsic $\sqrt{3}$ voltage step-down (current step-up), relaxing the turns ratio $n = n_p/n_s$ (less primary turns) and facilitates scaling and planar magnetics [159]. Similarly, arranging the resonant capacitors in a delta (Δ-C_r) configuration [153, 160] reduces the required capacitance per branch. Although some techniques are applicable to multi-phase LLC converters [156], dedicated methods exist for three-phase topologies [161, 162] that specifically target wide voltage regulation and light load. These features make the three-phase LLC especially attractive for high power density applications.

Finally, additional benefits can be listed. EMI further strengthens the case for three-phase topologies. Conducted emissions are a critical concern in high-frequency, planar-transformer converters. While single-phase LLC is already very competitive, the three-phase significantly reduces both Common-Mode (CM) and Differential-Mode (DM) noise [163]. The 120° displacement cancels harmonics that are not multiples of six in the CM spectrum, while current sharing reduces the DM current magnitude and shifts its fundamental harmonic to higher frequencies where filtering is easier. Moreover, distributing power among three smaller transformers lowers the effective parasitic capacitance, further reducing high-frequency coupling paths. Experimental results confirm that three-phase LLC converters achieve sub-

stantially lower emissions than single-phase equivalents, while also delivering higher efficiency [163].

Multi-phase LLC Converters

With more than three phases, multi-phase LLC resonant converters are increasingly being adopted in high-power, high-density applications due to their ability to reduce current ripple, enhance efficiency, and improve reliability. By interleaving multiple phases, these converters lower the stress further on individual devices, enabling compact and efficient power delivery [164].

Recent research has extended LLC topologies beyond the conventional three-phase configurations, with five-phase designs emerging as a promising route to achieve higher power density and lower ripple. However, increasing the number of phases may affect current unbalance due to component tolerances. To address this, both discrete coupled inductor arrays [165] (fig. 2.14) and integrated magnetic structures [166] have been proposed, enabling compact, manufacturable solutions suitable for high phase implementations [166]. These approaches improve current balancing while reducing the size and complexity of the magnetic components. For instance, a five-phase LLC converter using a discrete coupled inductor array combined with symmetrical component analysis has demonstrated excellent current sharing across all phases [167].

As in the three-phase, integrated three-phase inductors and transformers are much aligned with the philosophy of these converters, though due to the symmetry of three-phase LLC converters (one central phase and two at both sides), the advantages of increasing the phase count are limited as the integration in EE cores becomes limited [168].

A central challenge in multi-phase LLC converters is achieving robust current sharing. The passive approaches, such as common inductor [169] and common capacitor [170] schemes, connect resonant elements in parallel to enable automatic current sharing without the need for additional control. While simple and effective, these methods become increasingly sensitive to parameter mismatch as the number of phases grows [171]. In contrast, active approaches rely on control-based techniques that dynamically adjust circuit parameters such as variable magnetising inductance, variable capacitance, and partial energy processing [172].

Innovative techniques continue to push the boundaries of current sharing. For example, CLC output filters in five-phase LLC converters have been shown to suppress unbalanced currents caused by passive component tolerances [167]. Likewise, variable-capacitance schemes using ferroelectric MLCCs offer flexible and scalable current equalization suitable for converters with any number of phases [173].

State-of-the-art multi-phase LLC converters now achieve efficiencies above 97 %, high power density, and robust current sharing even under worst-case mismatches. These characteristics make them attractive for demanding applications such as datacenters, telecom power supplies, and high-performance computing [87].

Looking forward, research is focusing on further improving current sharing under severe parameter variations, developing advanced integrated magnetics, and

scaling control strategies for converters with higher phase counts. In addition, digital control, real-time monitoring, and adaptive compensation techniques are gaining attention to ensure reliable and efficient operation in practical, high-power environments [173, 166].

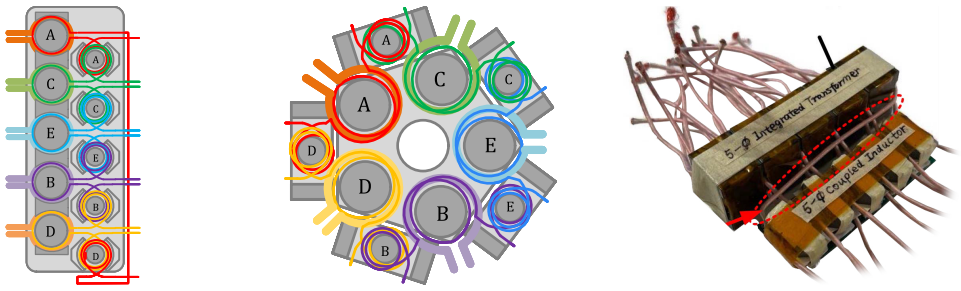

(a) Inline integration (b) Ring pentagon integration (c) Prototype

Figure 2.14: Example of a five-phase LLC converter integrated magnetics prototype with two possible integrations [165].

2.3.3 Topological Gain

There are several ways to integrate topological gain, further enabling additional modulations such as in T-type variants [133].

Nonetheless, purely topological gain is typically implemented via series stacking of switching cells embedding step-down gain into the power stage itself, prior to any contribution from modulation, transformer winding turns ratio or secondary conversion. In its most basic form, an input DC bus V_I is partitioned into N floating sub-links, each operated by a switching cell that sees only V_I/N. This enables the use of lower-voltage, higher-performance devices[6], so partitioning the bus improves conduction and switching behaviour while reducing the voltage stress. When the cells are driven in a coordinated manner, the inverter can synthesise the desired primary excitation, and the conversion gain inherits a factor of $1/N$. The overall converter can therefore reach low output voltages with a milder transformer winding turns ratio and with devices of lower voltage rating. This redistribution of electrical stress is the central attraction of stacking: improves device utilisation, unlocks faster switches with better FoM, and can relax magnetic design by keeping the isolation stage closer to unity ratio and reducing copper loss associated with extreme step-downs.

Voltage Divider

The approach has been demonstrated across single-ended stages, such as the forward active clamp [174] and bridge-based stages such as the DAB [123], that can be stacked to further improve its efficiency while shrinking the magnetics and allowing lower switching frequency operation [86]

[6]The $R_{DS(on)}$ of transistors typically scale superlinearly with breakdown voltage.

Stacking is naturally integrated in the LLC resonant family, because the resonant tank provides a low impedance AC path and, crucially, DC blocking. Probably the most successful attempt is the VFX operation in single-phase [175], a stacked front-end that introduces discrete operating modes by altering inverter drive patterns to change the effective AC gain seen by the tank [176].

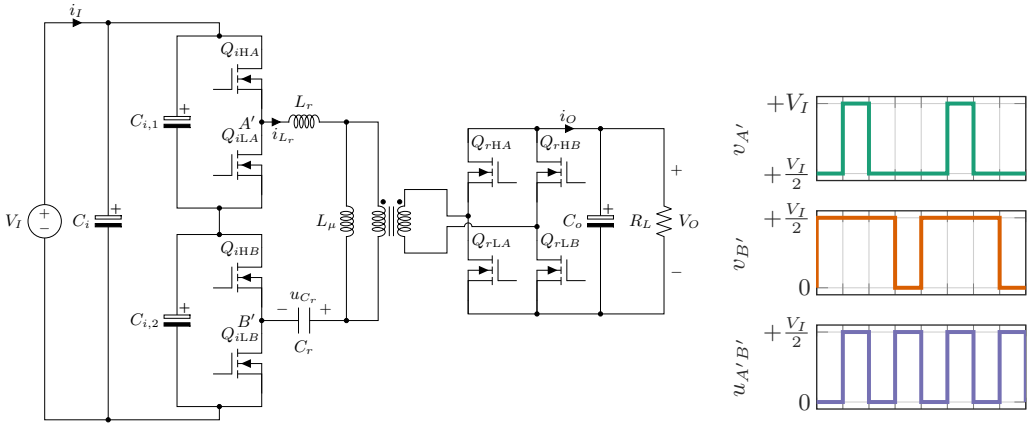

(a) Circuit schematic (b) Modulation

Figure 2.15: Variable Frequency Multiplier (VFX) topology and modulation scheme [175].

As previously mentioned, three-phase LLC converters are capable of distributing power losses equitatively among the phases, also, as the resonant capacitors block the DC common voltage, the stack configuration is only natural. This novel topology was initially proposed in [177] (see fig. 3.17), but no further optimisation was developed in this direction.

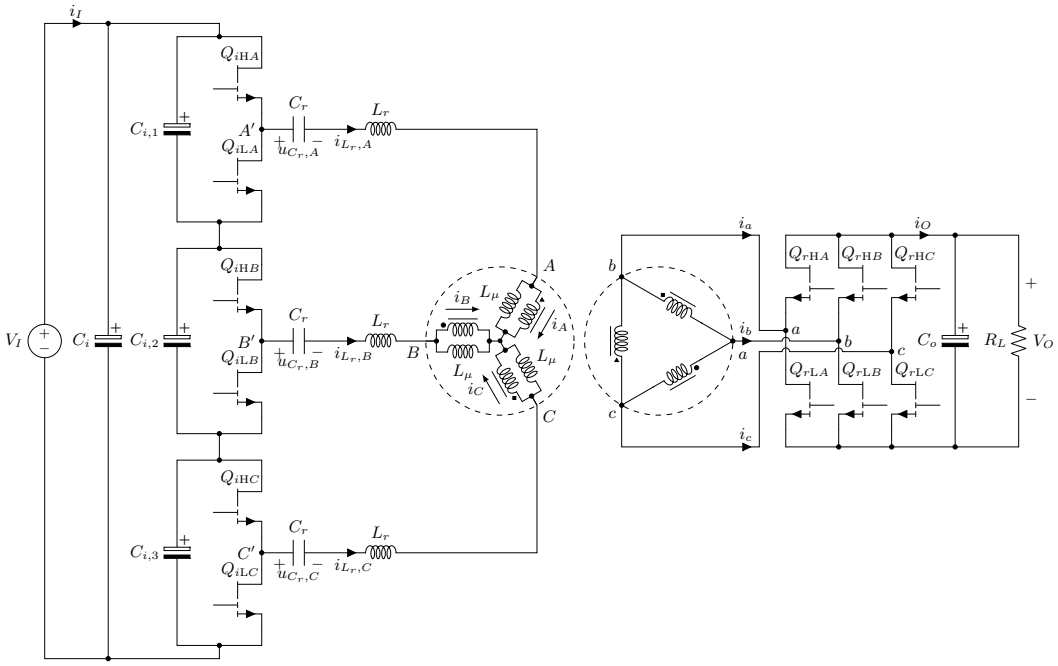

Figure 2.16: Example of a three-phase LLC converter with the inverter legs in stack [177].

Its main advantage lies in the input voltage division, which makes it particularly suitable for lower-voltage, higher-performance transistors. This feature is especially valuable when the inverter employs GaN HEMT, since commercially available devices are still relatively scarce at higher voltage ratings ($> 200\,\mathrm{V}$).

Since each cell has a different DC offset—the lower cell switching between 0 and $V_I/3$, the middle cell between $V_I/3$ and $2V_I/3$, and the upper cell between $2V_I/3$ and V_I—each resonant capacitor must withstand the corresponding DC bias. Consequently, their required voltage rating increases by $V_I/3$. This behaviour is analogous to the single-phase half-bridge LLC, demonstrating that the topology is indeed operable.

Current Multiplier

Other state-of-the-art approaches to topologically increase the overall conversion gain include a current doubler in the rectifier [84, 178] as well as a current tripler [179] for three-phase rectifiers. These extend the gain by factors of two and three, respectively. These techniques have been successfully applied in high step-down, high-current converters, improving transformer utilisation and reducing device stress. Nonetheless, they typically require additional series inductors on the rectifier side, which, under high output current conditions, can lead to significant conduction losses [128].

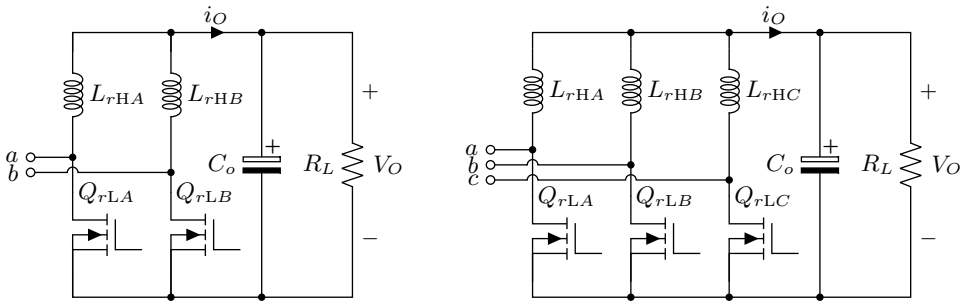

(a) Current doubler [84, 178] (b) Current tripler [179]

Figure 2.17: Current multipliers (doubler and tripler) in the rectifier.

2.3.4 Magnetic Integration

Magnetic integration in LLC converters conforms a very broad spectrum of techniques and tools for designing and integrating magnetics together to create a single magnetic structure. There are four categories in this regard: integration of multiple transformers into a single one for rectifier parallelisation, integration of multiple inductors into a single one for interleaving or multiphasing, integration of the inductor into the transformer and fractional turn transformers.

In essence, all approaches store the energy of the individuals into the same core assembly. This configuration enables the application of advanced design techniques to more effectively exploit the magnetic material, while being subject to the inherent limitations of a single component in which both functions are combined.

Integration of Multiple Inductors (Interleaving and Multiphasing)

The integration of multiple inductors has become a crucial design direction in modern split-phase, interleaving and multi-phase power converters. Coupled inductors are especially attractive since they can simultaneously reduce current ripple, improve transient response, and achieve higher power density [149]. Unified modelling frameworks allow their physical representations (inductance matrix) providing insights into current equalization and flux behaviour, which are central to reliable converters operation.

Integrating several coupled inductors in symmetric interleaving arrangements is relatively straightforward when flux balance is maintained. In such conditions, the magnetics naturally support current equalization across phases, enabling improved efficiency and reduced device stress. When the resonant inductors of all LLC phases are paralleled, allow to achieve automatic and precise passive current sharing based on a common resonant inductor without additional circuitry or complex control [180]. Integrated magnetics solutions such as dual-transformer structure for interleaved LLC converters [142], or more complex such as the double B-type integrated transformer for parallel LLC modules [148] demonstrate how magnetic integration reduces the overall volume of components, simplifies design, and enhances power density.

Further developments have also addressed the limitations of common inductor, which may be sensitive to mismatched resonant parameters. Unified methods that combines both common inductor and common capacitor approaches significantly improves current sharing even in the presence of component mismatches [145]. This highlights the importance of considering both magnetic design and passive impedance matching strategies when scaling up to multi-phase architectures.

Speaking of multi-phase and three-phase magnetics, the use of coupled inductors has been formally protected in patents, which detail configurations allowing improved current distribution in multi-phase LLC converters [144]. Recent work have demonstrated three-phase magnetic core arrangements composed of symmetrically columns, forming an equilateral triangular geometry. This design enables simplified winding, improved three-phase balance, and adaptability for both inductors and transformers, directly supporting the needs of multi-phase integration in compact and efficient power electronic systems [181]. The chain of reasoning from discrete coupled inductor arrays can be extended to any odd number of phases by applying symmetrical components analysis, enabling systematic modelling of multi-phase interleaved converters while ensuring that current sharing benefits of coupled magnetics are preserved regardless of the number of phases [182]. Thus, the integration of three-phase inductors and transformers has been investigated through magnetic core geometries. For instance, a patent from 2025 discloses techniques for integrating multi-phase windings into a unified magnetic structure that enhances balance and reduces leakage flux, thereby improving efficiency and manufacturability in high-power converters [183].

Integration of Multiple Transformers (Matrix Transformer)

Over the years, researchers have investigated different approaches to reduce the components stress for single-staged converters, with multiple transformers to reduce current stresses [184], or series-parallel multi-winding transformers [185], and even series transformers [186].

Nonetheless, traditional transformer parallelisation involves operating multiple independent transformers in parallel. In such configurations, the transformers are magnetically connected in parallel, creating multiple magnetic flux paths and causing asymmetric flux distribution in the core legs. This asymmetry results in unequal voltages induced in the secondary windings, which in turn generate unwanted circulating currents leading to increased conduction and switching losses and ultimately reducing the overall efficiency of the converter and complicating thermal management.

Initially introduced in [187] and later conceptualised in [188], the matrix transformer concept has evolved into a powerful design technique for high-density power conversion. It enables designers to decompose a single magnetic structure into multiple discrete transformer elements, improving thermal distribution and facilitating its integration into compact system architectures.

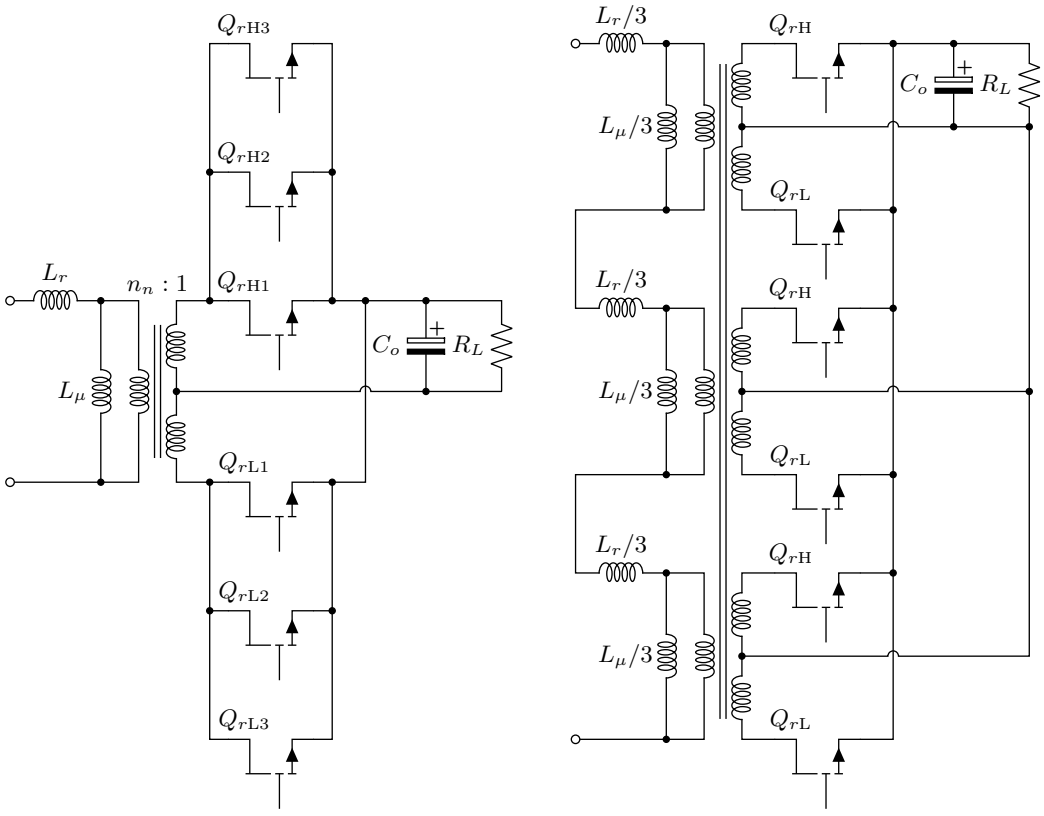

(a) Parallelisation of transistors (b) Matrix transformer

Figure 2.18: Comparison of raw classical parallelisation of transistors and the matrix transformer

Matrix transformers are increasingly employed in LLC converters (fig. 2.18) as an alternative to parallelisation, particularly in high-power, high-current applications, and have become one of the most widely adopted solutions for achieving high power density [82, 90]. Their main advantage lies in the winding configuration, where the primary windings are connected in series and the secondary windings in parallel. This arrangement not only reduces the electrical stress on each element but also inherently guarantees uniform current sharing, since the same current flows through all primary windings [189]. By contrast, with a single secondary winding, current sharing among the rectifier transistors cannot be ensured, leading to non-uniform thermal stress and higher power losses.

In LLC resonant converters, it is also common to implement matrix transformers within a unified magnetic structure comprising multiple series and parallel blocks (domino-like structure [188]), often exploiting magnetic flux cancellation [189, 190, 85]. Compared to simply paralleling transformers, this approach eliminates redundant magnetic paths that would otherwise only contribute to power losses, resulting in a more efficient and elegant design, and achieving significant reductions in both core size and volume (increased power density).

Moreover, PCB winding implementations support simple and inexpensive manufacturing processes, and the cores tend to increase their integration (windings are better confined), aiding with symmetry and helping to suppress common-mode noise, enhancing the EMC performance of the system [191].

Matrix transformers have demonstrated their practical value in state-of-the-art LLC resonant converters targeting data centers, electric vehicles, and renewable energy applications have been reported [82]. Today, the matrix approach is widely recognized as one of the most effective and scalable topologies for high-performance LLC designs, offering a unique combination of efficiency, thermal performance, and compactness [85, 90].

Integration of Multiple Transformers (Fractional Turn)

Fractional-turn transformers have emerged as a powerful enabler for high-frequency LLC resonant converters. By realising non-integer winding turns ratios such as half-turn [192] (fig. 2.19a) or quarter-turn [193] (fig. 2.19b), these structures make it possible to achieve the same voltage conversion as traditional transformers while reducing winding length and parasitic effects.

The implementation of fractional turns requires careful attention to winding structure and integration. Fractional-winding achieve the fractional ratio by dividing a full turn into equal segments. When the output capacitors clamp each segment to the same voltage, each side-leg flux is naturally balanced and the equivalent secondary turns become $1/n$ of the centre-leg turn. The only thing left is that both output positive and negative buses must be compactly routed around the outside of the core and tied to every output capacitor (equalising segment voltages/flux) while the leg reluctances must be matched to align the commutation of the synchronous rectifiers.

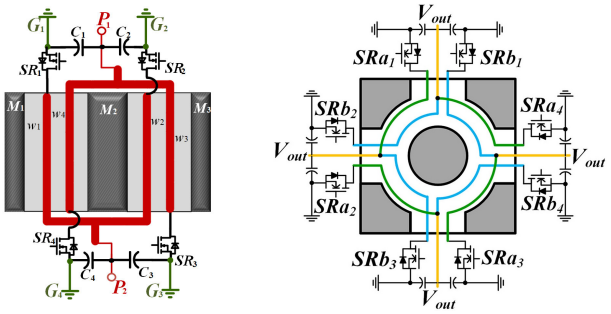

(a) Half-turn balanced symmetric structure [192]

(b) Quarter-turn balanced symmetric structure [193]

Figure 2.19: Concepts for fractional-turn transformers in the state-of-the-art used in LLC converters.

Beyond the basic fractional-winding concept, highly integrated implementations embed the synchronous rectifiers and output capacitors within the transformer window to shorten terminals and eliminate end losses, further improving density and efficiency [194]. A practical system-level advantage is that a half-turn secondary can replace multi-core matrix solutions while simplifying secondary current sharing, since all secondary segments are excited by the same primary flux [141] (fig. 2.20a).

Resonant inductor integration is also possible in this case, a magnetic-integration half-turn transformer distributes primary turns across centre and side legs so that the leakage inductance can be adjusted almost independently of the magnetising inductance, decoupling resonant design and easing ZVS design [195]. In highly integrated designs, finite-element analysis shows secondary current circulates predominantly in the segmented windings while currents in the output positive and negative buses are negligible, and keeping the air-gap away from copper reduces fringing-loss penalties [194].

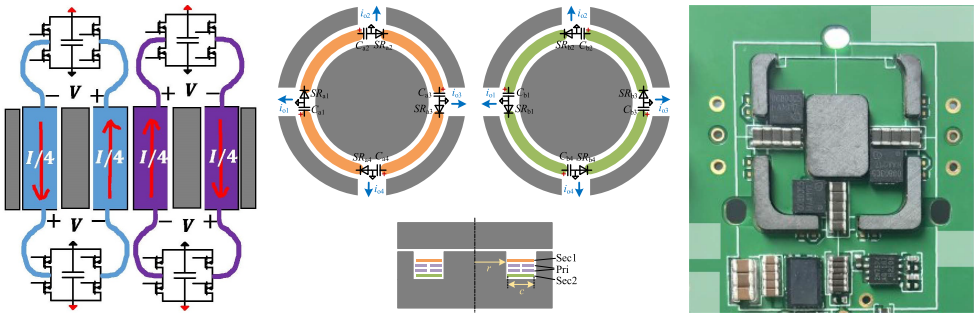

(a) Split-phase half-turn structure [141]

(b) Quarter-turn with integrated rectifier [194]

(c) Quarter-turn balanced asymmetric structure[196]

Figure 2.20: Techniques in the state-of-the-art for integrated fractional-turn transformers used in LLC converters.

One of the main benefits of fractional-turn designs is the significant improvement in power density and efficiency. Integrated fractional-turn LLC DCX hardware at

1 MHz operation achieves high efficiency with 100 W/cm^3 transformer power density and with the transformer losses reduced to 0.62 %, by shortening windings and eliminating terminal losses [194]. Quarter-turn and fractional-winding implementations at 1 MHz operation report over 97 % efficiency in the 1 kW output power with 40 W/cm^3 [193], 55 W/cm^3 [196], and 63 W/cm^3[197]. These results collectively validate that fractional turns are a practical path to higher density and efficiency in low-voltage, high-current outputs at high frequency.

Despite their advantages, fractional-turn transformers also present challenges. Uncovered primary areas (not overlapped by secondary) can suffer from R_{AC}, especially near the core and at winding terminations as R_{AC} increases with frequency and local field crowding in those regions. An example of such phenomena can be found in [198], where the coverage and leakage-layout unbalance led to current asymmetry and higher voltage spikes in the drain-source of the transistors. Accurate 3-D field and parasitic extraction remain important to verify the flux balance and reduce uneven currents due to PCB parasitics, as emphasised in quarter-turn designs [193, 197]. In fractional-winding structures the side-leg inductances participate in L_μ and directly influence the commutation of the synchronous rectifier. This means that any mismatch can make the switches to charge or discharge their output capacitance C_{oss} at different speeds, causing body-diode conduction or hard turn-on in the most extreme cases, adding local additional power losses with the degradation of soft-switching [196].

In most of this research, DCX operation is more typical as the operating conditions are fixed and easier to optimise. Looking forward, research must extend fractional-turn concepts to scalability and wide-range operation. An initial foundation for this can be to do it in two stages: adopting a highly efficient and optimised fractional-turn DCX and a second stage for regulation, the work in this regard is very limited but some effort is demonstrated in this direction as in [199].

Integration of the Inductor into the Transformer

This technique aims to intentionally combine the transformer and resonant inductor into a single magnetic structure, thereby enhancing power density, improving efficiency, and reducing overall size. This is a classical problem in power converters as many classic topologies such as the PSFB or DAB possess a series inductor with the transformer. Over the years, a variety of integration strategies have been proposed to address key challenges, including precise leakage inductance control, minimisation of core losses, and manufacturability.

Simply put, the integration of an inductor and a transformer is to share the same magnetic link, by allowing certain magnetic field to not close through the secondary.

An example of this technique is shown in fig. 2.21b, it can be seen as the addition of an extra leg into an EE-core transformer, adding certain number of additional turns [140]. In general, this requires extra care with winding losses, as strong magnetic fields are added into the window and can affect the transformer section of the windings. Typically this technique requires careful optimisation and accurate modelling of the magnetic link, usually ending up with custom magnetic cores.

This technique is most benefitial when the output voltage varies, as for the same power output, higher output voltage (higher transformer magnetisation) means lower resonant current (lower inductor magnetisation) and vice versa, making the core better used in the entire range of operation.

Splitting the magnetic core into inductor and transformer sections but without splitting the windings allows decouples the optimisation into two independent solutions [200]. Nonetheless, this type of integration is at the expense of a small reduction in energy density due to the missing core junctions.

In simple words, the integration is performed by redirecting leakage flux of the transformer by manipulating solely the windings. By separating the primary and secondary windings, less amount of flux from the primary reaches the secondary, several articles involving the positioning of primary and secondary windings (whether they are completely separated, parallel, concentric...) are in the literature [201], and although models for it can be found in [107], its effect is limited and cannot integrate larges amount of series inductance.

In practice, most integration approaches rely on working with leakage flux; however, when a high degree of controllability is required, the inductance must be increased. This implies storing a significant amount of energy in the core, which demands a high magnetic field strength and results in severe proximity losses. As illustrated in figs. 2.21c and 2.21d, the challenge is therefore to store part of the energy outside the transformer windings whenever possible. Solutions such as the extra-leg approach directly address this limitation.

For this reason, some authors increased the amount of circulating flux in the magnetic core via asymmetric winding turns ratio (additional circulating flux) [202] and, for the most constrained power density cases, unused parts of the transformer core are used as additional leakage [203].

Following the path of redirecting the leakage flux of the transformer, a magnetic shunt can be intercalated into the EE core, splitting the primary and secondary windings [204]. This technique not only further increases the leakage flux by avoiding the primary and secondary coupling [201], but also adds an additional path for the leakage fluxes of the primary and secondary, allowing better control of the leakage inductance.

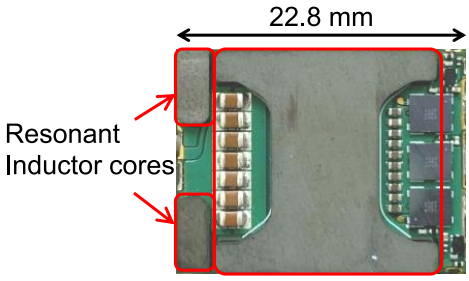

(a) Multiple resonant inductors integrated with the transformer [200]

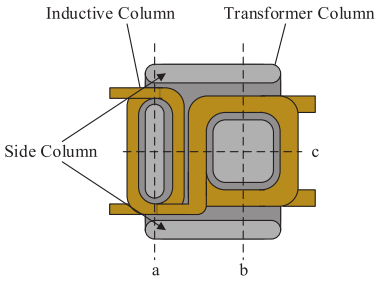

(b) Extra leg for integrated inductor [140]

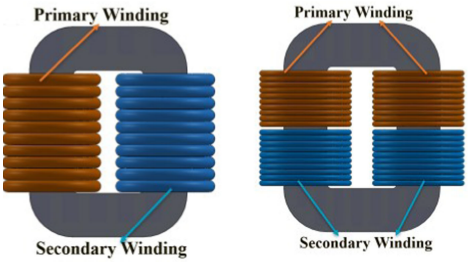

(c) Primary and secondary windings separated for leakage control [201]

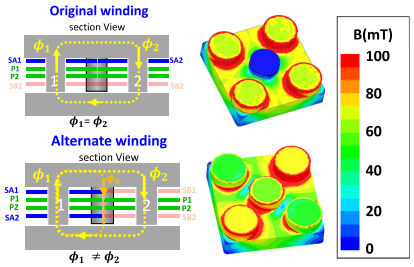

(d) Inductor into an unused area of the transformer [203]

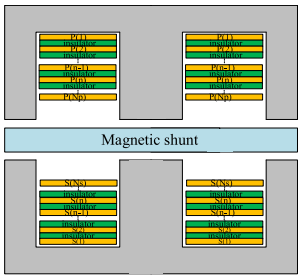

(e) Magnetic shunt for leakage inductance [204]

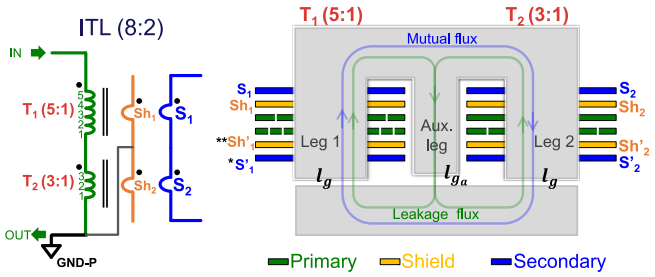

(f) Integrated inductor with asymmetric winding turns ratio [202]

Figure 2.21: Inductor and transformer integration via diverse approaches.

These techniques can be implemented alongside other techniques previously discussed such as matrix transformers, for example, in previously referenced work [205], additional to the transformer, extra legs are added to include an inductor in series.

CHAPTER 3

Modelling and Design of High-Frequency LLC Converters

> The essence of mathematics is not
> to make simple things complicated,
> but to make complicated things simple.
>
> — Stan Gutter

The core difficulty in designing LLC converters for wide voltage and current ranges lies in maintaining both high efficiency and soft-switching across the entire operating range. High power density converters demand these properties to ensure reliable operation, particularly as switching frequencies exceed the megahertz range. Under such conditions, losing ZVS leads to significant energy dissipation in the switches, and the limited physical footprint makes thermal management increasingly difficult. This, in turn, complicates the optimization of the converter, especially in the design of the switching and magnetic components.

These challenges can be effectively addressed through careful **design** and **modelling** of both the topology and its components. This chapter explores these two key aspects in detail: first, the design process, focusing on how to select the optimal operating point and component values to fulfil the specifications; and second, the modelling approach, which provides the analytical and simulation tools necessary to predict the behaviour of the converter, guide design choices, and ensure the performance.

3.1 Target Specifications

To ensure a fair comparison between the designs, the specifications of the target converter are summarised in section 3.1. These specifications were provided by Gaïa Converters, an industrial company specialising in DC/DC modules for aerospace

applications, with whom the author collaborated during the development of this thesis. They will serve as a reference throughout the remainder of the thesis whenever design decisions are discussed.

Parameter	Value	Description	
V_I	270 V 235-285 V 220-325 V	Nominal Normal Abnormal	Input voltage
V_O	28 V 26.6-29.4 V	Nominal Range	Output voltage
P_O	1 kW 0-1 kW	Nominal Range	Output power
ΔF_x	15 % 100-1000 W	Normal In range	Frequency range
V_{ins}	2250 V	Minimum	Insulation
$\hat{U}_{C_r}$	230 V	Maximum	Resonant capacitor voltage
$P_L/(w \cdot l)$ h w P_O/vol	1.4 W/m^2 12.7 mm 60 mm 20 kW/L	Dissipation Height Width Power density	Converter dimensions

Table 3.1: Specifications for the target converter, as provided by Gaïa Converters. The LLC topology, along with the operating frequency span ΔF_x, was preselected by the company based on their internal estimation of what is required to meet the applicable aerospace standards outlined in the introduction.

In section 3.1 a maximum span of $\Delta F_x = 15\,\%$ is specified. As previously explained, when wide varying step-down and step-up gains are needed, the LLC converter requires an equally wide switching frequency range, difficulting the design compact of compact EMI filters for converters with a broad spectrum of switching frequencies in an application with very strict demands for EMC [60].

The switching frequency span ΔF_x becomes a design penalty, as later in section 3.5.2 will be demonstrated that constraining the frequency variation more tightly leads to increasing design complexity

3.2 Operating Principle of Single-Phase LLC Converters

LLC designs typically rely on FM to control the current that flows through the resonant tank [206]. For simplicity, we can consider the case of a single-phase LLC converter as the one illustrated in fig. 3.1.

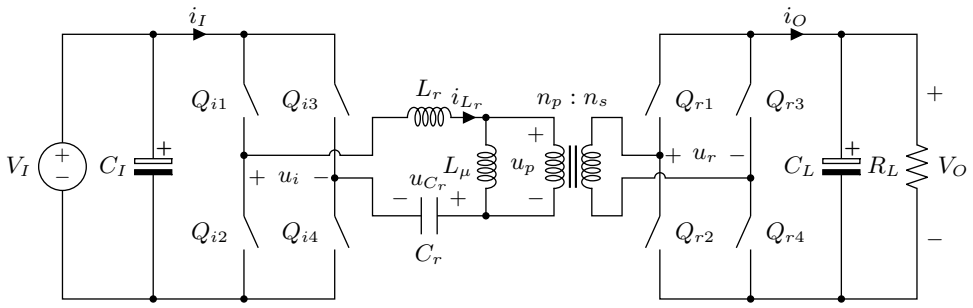

Figure 3.1: Isolated DC/DC single-phase Inductor-Inductor-Capacitor (LLC) converter.

3.2.1 Time-Domain Solution

The complexity of the operation of the LLC operation is due to its dual resonant mechanism that, besides resonance formed by

By neglecting the magnetising inductance L_μ, and as the full-bridge voltage u_{SW} excites the circuit with 50 % duty cycle, the voltage at the primary of the transformer is clamped to the output voltage $\pm nV_O$ [207]. This is the case of the Series Resonant Converter (SRC) [208].

The state variables of the resonant tank are:

$$u_{L_r}(t) = L_r \cdot \frac{\mathrm{d}i_{L_r}(t)}{\mathrm{d}t} \tag{3.1a}$$

$$i_{C_r}(t) = C_r \cdot \frac{\mathrm{d}u_{C_r}(t)}{\mathrm{d}t} \tag{3.1b}$$

and as $i_{C_r}(t) \equiv i_{L_r}(t)$, we can obtain the differential equation:

$$L_r C_r \frac{\mathrm{d}^2 u_{C_r}(t)}{\mathrm{d}t^2} + u_{C_r}(t) = u_{SW}(t) - u_p(t) \tag{3.2}$$

the solution can be expressed with the initial conditions of the resonant tank, the initial current through the inductor $i_{L_r}(0)$ and the initial voltage across the capacitor $u_{C_r}(0)$, the second-order equation time-domain solution is thus given by a combination of a sine and a cosine:

$$i_{L_r}(t) = \frac{u_{L_r}(0)}{Z_r} \cdot \sin(\omega_r t) + i_{L_r}(0) \cdot \cos(\omega_r t) \tag{3.3a}$$

$$u_{C_r}(t) = Z_r i_{L_r}(0) \cdot \sin(\omega_r t) + u_{L_r}(0) \cdot [1 - \cos(\omega_r t)] \tag{3.3b}$$

where $u_{L_r}(0) = u_{SW}(0) - u_p(0) - u_{C_r}(0)$. This solution is valid when the rectifier is conducting, this is, when the voltage at the primary is clamped. In this case, the evolution of the magnetising current is straightforward, as the state variable evolves according to:

$$u_{L_\mu}(t) = L_\mu \frac{\mathrm{d}i_{L_\mu}(t)}{\mathrm{d}t} \tag{3.3c}$$

thus,

$$i_{L_\mu}(t) = i_{L_\mu}(0) + \frac{u_p(0)}{L_\mu} t \tag{3.3d}$$

where $\omega_r = 1/\left(2\pi\sqrt{L_r C_r}\right)$ is the resonant frequency of the LLC, and $Z_r = \sqrt{L_r/C_r}$ is the characteristical impedance of the tank.

When the rectifier is not conducting, the current through the primary becomes zero, and the inductance L_r resonates together with the magnetising inductance L_μ and the resonant capacitor C_r. The solution is the same as in eq. (3.3a) and eq. (3.3b), just with lower resonant frequency:

$$i_{L_r}(t) = \frac{u_{L_r}(0) + u_{L_\mu}(0)}{Z_\mu} \cdot \sin\left(\omega_\mu t\right) + i_{L_r}(0) \cdot \cos\left(\omega_\mu t\right) \tag{3.4a}$$

$$u_{C_r}(t) = Z_\mu i_{L_r}(0) \cdot \sin\left(\omega_\mu t\right) + \left(u_{L_r}(0) + u_{L_\mu}(0)\right) \cdot \left[1 - \cos\left(\omega_\mu t\right)\right] \tag{3.4b}$$

where $Z_\mu = \sqrt{(L_r + L_\mu)/C_r}$ as now the two inductances resonate together:

$$i_{L_\mu}(t) = i_{L_r}(t) \tag{3.4c}$$

and the voltage at the primary depends on the state variable of the magnetising inductance:

$$u_{L_\mu}(t) = L_\mu \frac{\mathrm{d}i_{L_r}(t)}{\mathrm{d}t} \tag{3.4d}$$

Resonance States

We can differentiate when the rectifier conducts or not as two different states, illustrated in fig. 3.2:

- **State I**: the rectifier does conduct, and the voltage at the primary is clamped to $\pm nV_O$ with the sign given by the direction of the current through the primary.
- **State II**: the rectifier does not conduct, the voltage at the primary is given by the slope of the resonant current according to eq. (3.4d) as both L_r and L_μ resonate together at ω_μ.

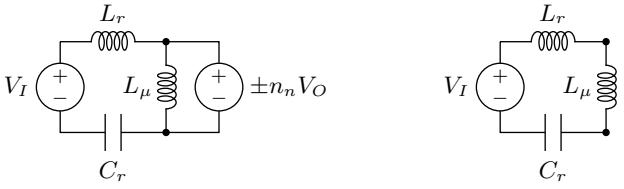

(a) State I (b) State II

Figure 3.2: Circuit representation of the two resonant states in a single-phase LLC converter.

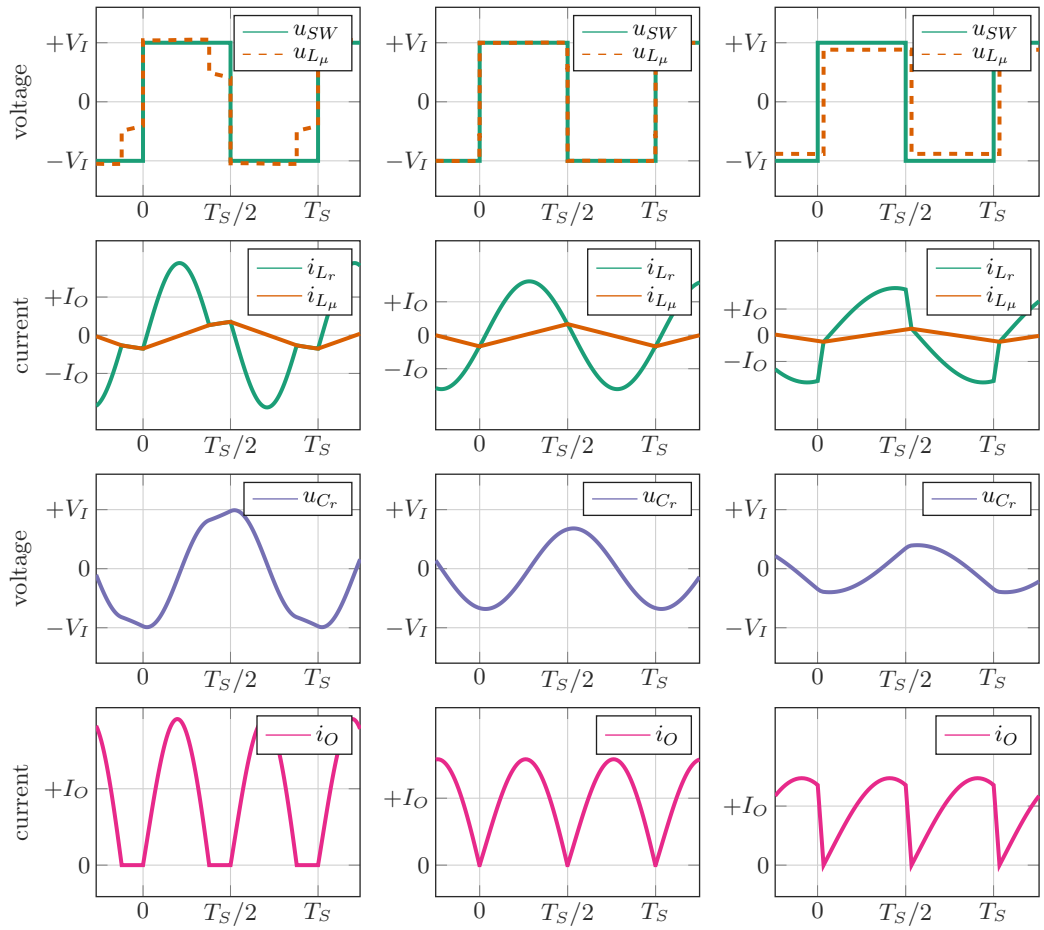

(a) Below resonance (b) At resonance (c) Above resonance

Figure 3.3: Steady-state waveforms of a single-phase LLC converter with full-bridge drive and ideal diode rectification for 1:1 winding turns ratio in the transformer, under three conditions: below, at, and above resonance. The output current I_O in each subfigure refers to that specific case.

Figure 3.3 illustrates the typical steady-state waveforms of a single-phase LLC converter under three operating conditions: below resonance, at resonance, and above resonance. It also highlights the time intervals during which the resonant tank operates in the aforementioned states I and II.

State Transitions

Transitions between the two aforementioned operating states of the single-phase LLC can only occur when the resonant and magnetising currents are equal. In state II, this condition is always satisfied as $i_{L_r}(t) \equiv i_{L_\mu}(t)$. However, in state I, the transition is defined by the intersection between the resonant current (shaped by the input voltage u_{SW} and the primary voltage u_{L_μ} via eq. (3.3d)) and the magnetising current, whose evolution is purely determined by the primary voltage (clamped on the secondary side to $\pm V_O$). The latter cannot be solved in closed form using elementary functions, as it involves a transcendental equation given by

equating 3.3a and 3.3d:

$$i_{L_r}(t) = i_{L_\mu}(t) \longrightarrow \frac{u_{L_r}(0)}{Z_r} \cdot \sin(\omega_r t) + i_{L_r}(0) \cdot \cos(\omega_r t) = i_{L_\mu}(0) + \frac{u_p(0)}{L_\mu} t \quad (3.5)$$

which corresponds to Kepler's Equation (see section B.2 for demonstration).

Let us examine the transitions in detail, as illustrated in fig. 3.4:

- **Transition I–II**: If we assume that the instant t_0 at which $i_{L_r}(t_0) = i_{L_\mu}(t_0)$ is known, further analysis is required to determine when the rectifier stops conducting, this condition depends on the voltage across the resonant capacitor. To verify if the circuit transitions to state II, we can evaluate the voltage across the magnetising inductance as if the system were already in state II. Denoting this hypothetical value as $u^*_{L_\mu}(t_0)$, it can be obtained by comparing the clamped value of u_{L_μ} to $\pm nV_O$, using 3.1a and eq. (3.3c):

$$u_{L_r}(t_0) + u_{L_\mu}(t_0) = u_{SW}(t_0) - u_{C_r}(0) \quad (3.6a)$$

$$u^{(}_{L_\mu} t_0) = \frac{L_\mu}{L_r + L_\mu} \cdot [u_{L_r}(t_0) + u_{L_\mu}(t_0)] = \frac{L_\mu}{L_r + L_\mu} \cdot [u_{SW}(t_0) - u_{C_r}(0)] \quad (3.6b)$$

  This expression depends solely on the voltage across the resonant capacitor at the transition. Thus, the transition to state II is confirmed if the condition $\left|u^*_{L_\mu}(t_0)\right| < nV_O$ is true. Otherwise, the system remains in state I, with the magnetising voltage clamped as $u_{L_\mu}(t_0) = \operatorname{sgn}\left[u^{(}_{L_\mu} t_0)\right] \cdot nV_O$[1].

- **Transition II–I**: If the LLC is in state II, its analytical solution is already known. As in the previous transition, the key is to check for the voltage across the resonant capacitor, C_r. Its time-domain evolution is given by eq. (3.4b). As before, by computing the voltage across the magnetising inductance L_μ, it can be verified when this condition is violated.

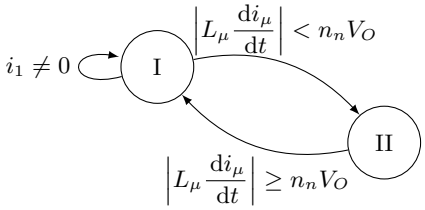

Figure 3.4: State transitions in a single-phase LLC converter.

3.2.2 Modelling with Approximations: FHA

For the LLC converters family, the Fundamental-Harmonic Approximation (FHA) is more than a widely adopted technique for modelling resonant converters [209]. It relies on the assumption that the resonant tank waveforms (voltages and currents)

[1]Here, $\operatorname{sgn}(x)$ denotes the sign function.

can be approximated as purely sinusoidal and that the power transfer is predominantly governed by the fundamental component of the switching waveform [210]. This assumption is very accurate when the converter operates near its resonant frequency $f_S \approx f_r$, since the waveforms closely resemble pure sinusoids, as illustrated in fig. 3.5.

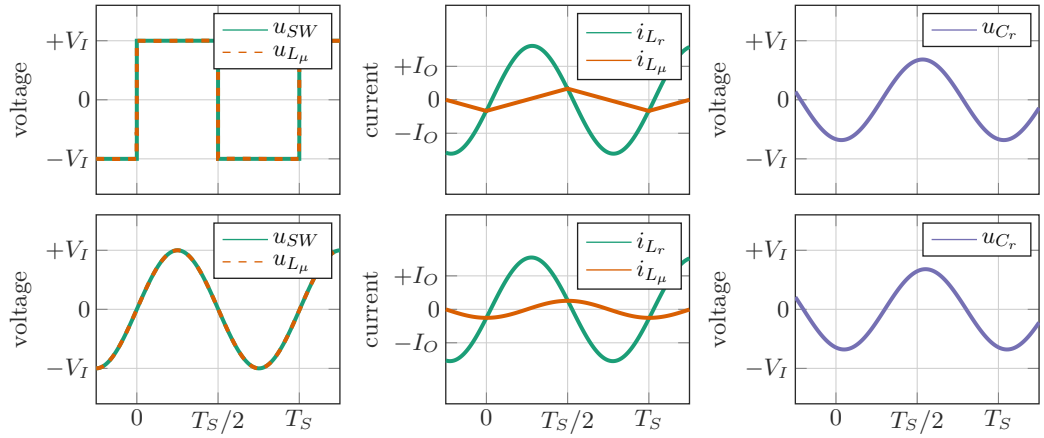

(a) Applied voltages (b) Tank currents (c) Resonant capacitor

Figure 3.5: Comparison between purely sinusoidal waveforms (FHA) and the exact solution at resonance

Building the FHA Model

Under this approximation, the inverter excitation is represented by its fundamental component, neglecting all higher-order harmonics. As a result, all waveforms are constrained to oscillate at the same frequency, enabling a simplified model suitable for linear AC small-signal analysis and the straightforward derivation of transfer functions (fig. 3.6).

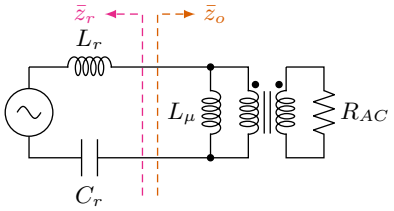

Figure 3.6: Single-phase AC equivalent circuit for a single-phase LLC

As illustrated in fig. 3.6, the FHA equivalent model of an LLC resonant converter consists of a voltage source $\bar{v}_i$, the resonant inductance L_r, the resonant capacitor C_r, and the magnetising inductance L_μ.

Since the voltage and current at the transformer secondary are purely sinusoidal due to the load resistance R_L and the bridge rectifier, and because the transformer primary voltage u_{L_μ} and current $i_p = i_{L_r} - i_{L_\mu}$ are always in phase, the load can equivalently be represented as an AC resistance R_{AC}, reflecting the actual load back to the primary side.

$$\hat{I}_p = \frac{1}{n} \cdot \hat{I}_s = \frac{1}{n} \cdot \frac{\pi}{2} I_O \tag{3.7a}$$

and the voltage is given by the fundamental voltage applied from the secondary:

$$\hat{U}_p = n \cdot \hat{U}_s = n \cdot \frac{4}{\pi} V_O \tag{3.7b}$$

obtaining the equivalent resistance R_{ac}:

$$R_{\mathrm{AC}} = \frac{\hat{U}_p}{\hat{I}_p} = n^2 \cdot \frac{8}{\pi^2} R_L \tag{3.7c}$$

where $R_L = V_O/I_O$ is the real output resistance of the converter.

Characteristical Gain $G_x(F_x)$

Thus, we can derive the voltage gain $G(\mathrm{j}\omega)$:

$$G(\mathrm{j}\omega) = n \cdot \frac{v_o(\mathrm{j}\omega)}{v_i(\mathrm{j}\omega)} = \frac{\bar{z}_o}{\bar{z}_r + \bar{z}_o} \tag{3.8a}$$

where the complex characteristical impedance is given by the series of impedances of L_r and C_r,

$$\bar{z}_r = \mathrm{j}\omega L_r + \frac{1}{\mathrm{j}\omega C_r} \tag{3.8b}$$

the output impedance by the parallel of the mutual inductance and the equivalent resistance seen from the primary,

$$\bar{z}_o = \frac{\mathrm{j}\omega L_\mu R_{ac}}{\mathrm{j}\omega L_\mu + R_{ac}} \tag{3.8c}$$

and where $R_{ac} = 8/\pi^2 \cdot n^2 R_L$, obtaining:

$$G(\mathrm{j}\omega) = \frac{(\mathrm{j}\omega)^2 \cdot L_\mu C_r}{(\mathrm{j}\omega)^3 \cdot \frac{L_\mu}{R_{ac}} L_r C_r + (\mathrm{j}\omega)^2 \cdot (L_r + L_\mu) C_r + (\mathrm{j}\omega) \cdot \frac{L_\mu}{R_{ac}} + 1} \tag{3.8d}$$

Equation (3.8d) depicts the relationship between the input and output voltages established in relation to the circuit parameters. As the current waveforms are rectified, we can calculate the DC gain with $G_x(F_x) = \sqrt{\Re\left[G(\mathrm{j}\omega/\omega_r)\right]^2 + \Im\left[G(\mathrm{j}\omega/\omega_r)\right]^2}$ from eq. (3.8d), note that the switching frequency has been normalised with $F_x = \omega/\omega_r$. Also, to write it down in a more compact form, the total inductance to resonant ratio $m = 1 + L_\mu/L_r$ and the quality factor $Q_s = \sqrt{L_r/C_r}/R_{ac}$ are defined obtaining, in canonical form:

$$G_x(F_x) = \frac{1}{n} \sqrt{\frac{1}{Q_s^2 \cdot \left(F_x - \frac{1}{F_x}\right)^2 + \left[1 + \frac{1}{m-1} - \frac{1}{(m-1) \cdot F_x^2}\right]^2}} \tag{3.9}$$

accepting the approximation as accurate allows to evaluate the gain of an LLC converter with eq. (3.9) allows to calculate the inverse solution $F_x(G_x)$ in a closed form, the derivation can be consulted in section B.1.

This analytical approach relies on simplifying assumptions, there are operating points where the resulting error can become significant, the further away from resonance. Nevertheless, the expression in eq. (3.9) provides valuable insight into the operating behaviour of the LLC converter, enabling a straightforward evaluation of design trade-offs and highlights the possibilities of the topology, making it a powerful tool for initial analysis and comparison before resorting to more detailed numerical or simulation-based methods.

3.3 Three-Phase LLC Converters

Three-phase LLC resonant converters are advanced power electronic circuits widely used in high-power applications. They offer high efficiency, soft-switching, and high power density, making them suitable for demanding environments where size, weight, and energy loss are critical concerns.

This section presents the three-phase LLC converter as an evolution of the single-phase topology, aimed at high-power applications requiring high efficiency, soft-switching operation, and improved power density. The discussion first addresses three-phase transformer connections and their influence on the effective turns ratio and voltage gain. The operating principle is then described through the characteristic waveforms and resonance behaviour under different operating points, followed by the rectifier states. Finally, the FHA modelling is extended to the three-phase case, enabling analytical evaluation of the converter gain and comparison with the single-phase counterpart.

3.3.1 Three-Phase Transformers

A particular feature in three-phase topologies is the connection of the transformer, as it adds a topological factor to the per-phase turns ratio $n_n = n_p/n_s$. Without counting the zigzag winding configuration (only wye and delta), there exist only four possibilities (fig. 3.7).

For identical n_n, the line-to-line ratio can be $|\bar{u}_{AN}/\bar{u}_{ab}| = n_n\sqrt{3}$ for wye-delta (fig. 3.7c), which acts as a natural step-down; $|\bar{u}_{AN}/\bar{u}_{ab}| = n/\sqrt{3}$ for delta-wye (fig. 3.7d), a natural step-up; and $|\bar{u}_{AN}/\bar{u}_{ab}| = n_n$ for both wye-wye (fig. 3.7a) and delta-delta (fig. 3.7b), which are topologically 1:1 with respect to the connection factor. Due to the high voltage step-down requirements of the converter, 270 V to 28 V as described in section 3.1, the wye-delta choice is the most natural as it minimises the amount of primary turns in the window of the transformer, allowing a more compact design.

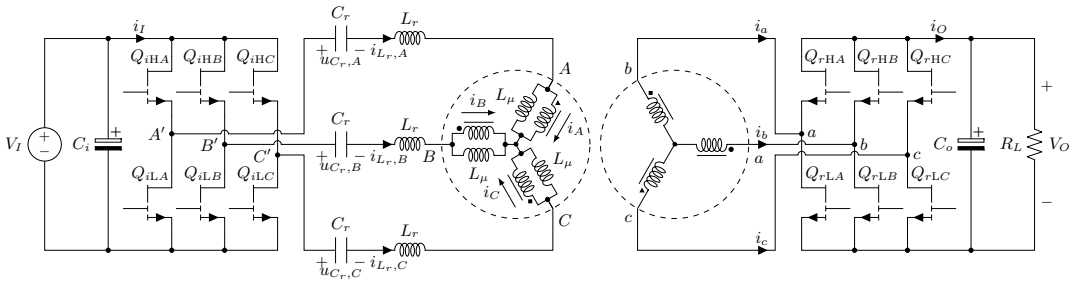

(a) Wye-wye configuration

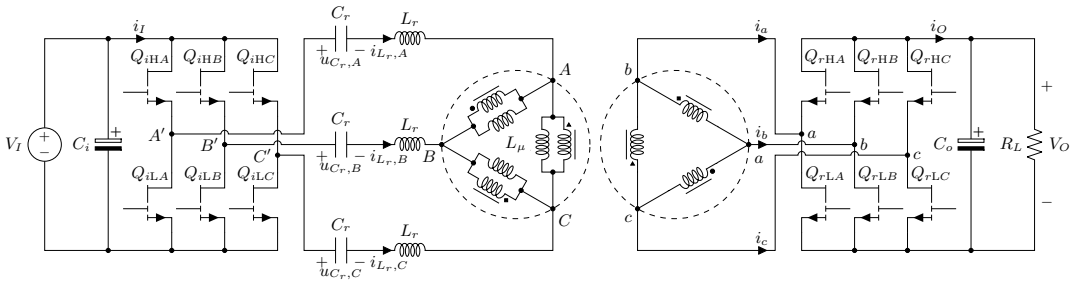

(b) Delta-delta configuration

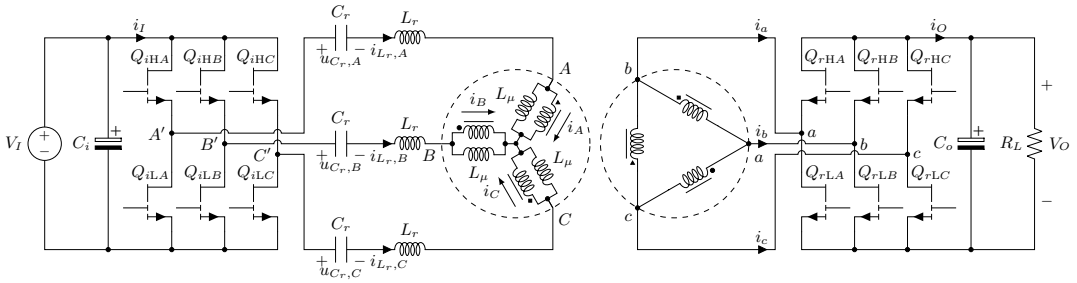

(c) Wye-delta configuration

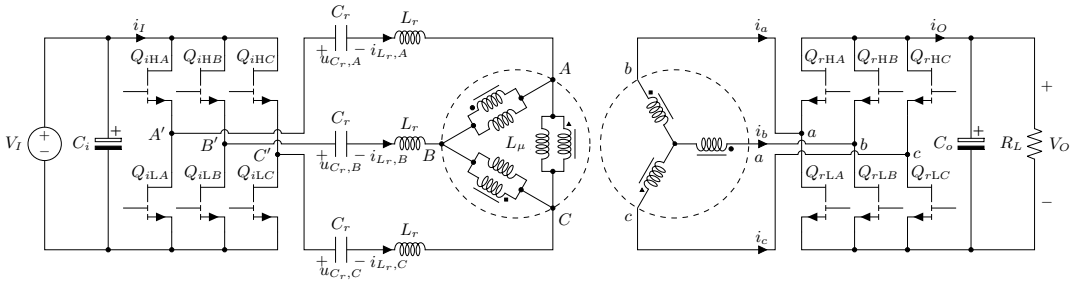

(d) Delta-wye configuration

Figure 3.7: Three-phase transformer connection options for the two types of transformer winding configurations (wye and delta) depicted in the three-phase LLC converter family

From the waveform perspective, a wye primary with a defined neutral lets, from the DC link to generate a four-level phase-to-neutral voltage, whereas a delta primary yields a three-level line waveform. Also, for mixed configurations, wye-delta and delta-wye, produce equivalent line-to-line magnitudes and introduce a characteristic phase displacement of $\pm 30°$ respectively, while same-side pairs, wye-wye and delta-delta, give corresponding waveforms with $0°$. These properties are

useful for intrinsic gain shaping, ripple management and timing in three-phase resonant converters.

3.3.2 Operating Principle of the Wye-Delta Three-Phase LLC Converter

The wye-delta connection was selected to meet more easily the step-down requirement because it provides an intrinsic line-to-line step-down, which simplifies the transformer design. For identical per-phase turns ratio $n_n = N_p/N_s$, the connection yields $|\bar{u}_{AN}/\bar{u}_{ab}| = n_n\sqrt{3}$, so a significant portion of the overall step-down is achieved topologically rather than by forcing $n_n \approx 9$; the intrinsic $\sqrt{3}$ factor lets $n_n \approx 5$ with the same conversion. This directly improves transformer window utilisation and reduces the primary turn count.

For this reason, the wye-delta configuration was chosen for practicality; now the topology can be analysed, beginning with the excitation of the inverter and rectifier, its implication in the capacitive and inductive modes of operation, and, finally, its characteristical gain $G_x(F_x)$.

Voltage Levels of the Inverter

For reference, fig. 3.8 shows a detailed view of the inverter with the primary in wye configuration, highlighting the voltage between the switching node of phase A and the neutral of the transformer N ($u_{k'N}$), which is crucial to further understand the topology operation.

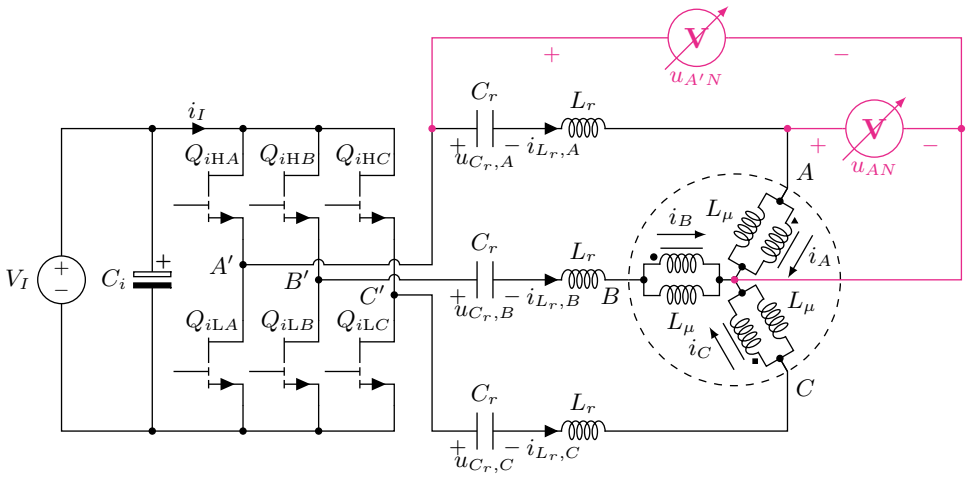

Figure 3.8: Primary of the transformer in wye configuration and its inverter in a three-phase LLC converter, highlighting the voltage between the switching node of phase A and the neutral of the transformer N ($u_{k'N}$).

The voltages across the resonant inductors L_r and capacitors C_r are given by,

$$u_{C_r,k}(t) = \frac{1}{C_r}\int_0^t i_{L_r,k}(\tau)\,\mathrm{d}\tau \tag{3.10a}$$

$$u_{L_r,k}(t) = L_r \cdot \frac{\mathrm{d}i_{L_r,k}(t)}{\mathrm{d}t} \tag{3.10b}$$

while the overall voltage across the resonant tank and primary of each phase k as $u_{k'N}$ can be calculated,

$$u_{k'N}(t) = v_{k'}(t) - u_{C_r,k}(t) - u_{L_r,k}(t) - u_{kN}(t) \tag{3.11a}$$

where $u_{kN}(t)$ is the voltage across the primary of the transformer for phase k, and it is always forced by the rectifier. The other two voltages $u_{C_r,k}(t)$ and $u_{L_r,k}(t)$ are dependant in the time-domain, but we can add the three phases together and apply the condition $i_{L_r,A} + i_{L_r,B} + i_{L_r,C} = 0$ obtaining:

$$\sum_k u_{C_k}(t) = \sum_k \left[\frac{1}{C_r} \int_0^t i_k(\tau)\,\mathrm{d}\tau \right] = \frac{1}{C_r} \cdot \sum_k \left[\int_0^t i_k(\tau)\,\mathrm{d}\tau \right] = 0 \tag{3.12a}$$

$$\sum_k u_{L_k}(t) = \sum_k \left[L_r \cdot \frac{\mathrm{d}i_k(t)}{\mathrm{d}t} \right] = L_r \cdot \sum_k \left[\cdot \frac{\mathrm{d}i_k(t)}{\mathrm{d}t} \right] = 0 \tag{3.12b}$$

this is because, even when integrating the currents in the time-domain, the initial conditions (integration constants) are also null as the initial currents also comply with $i_{L_r,A} + i_{L_r,B} + i_{L_r,C} = 0$, making the sum of the three voltages also null.

Knowing that $u_{AN} + u_{BN} + u_{CN} = 0$,

$$u_{AN}(t)+u_{BN}(t)+u_{CN}(t) = u_{A'N}(t)+u_{B'N}(t)+u_{C'N}(t)-\sum_k u_{C_k}(t)-\sum_k u_{L_k}(t) = 0 \tag{3.13}$$

and then we know the voltage of the neutral

$$\left.\begin{aligned} v_{A'}(t) - v_{B'}(t) &= u_{A'N}(t) - u_{B'N}(t) \\ v_{B'}(t) - v_{C'}(t) &= u_{B'N}(t) - u_{C'N}(t) \\ v_{C'}(t) - v_{A'}(t) &= u_{C'N}(t) - u_{A'N}(t) \\ u_{A'N}(t) + u_{B'N}(t) + u_{C'N}(t) &= 0 \end{aligned}\right\} v_N = \frac{v_{A'} + v_{B'} + v_{C'}}{3} \tag{3.14}$$

knowing the voltage at the neutral from the voltages $v_{k'}$ at the bridge for phase k, it is straightforward to calculate the voltage waveform at both sides of the resonant tank ($u_{k'N}$ and u_{kN}), **completely independently of the conditions**:

$$u_{k'N} = \frac{2v_{k'} - \sum_{j\neq k} v_{j'}}{3} \tag{3.15}$$

Note that, as shown in table 3.2, the voltage applied by the inverter to the primary $u_{k'N}$ is a four-level waveform ($+2/3\,V_I$, $+1/3\,V_I$, $-1/3\,V_I$, and $-2/3\,V_I$).

$v_{A'}$	$v_{B'}$	$v_{C'}$	$u_{A'N}$	$u_{B'N}$	$u_{C'N}$
0	0	0	0	0	0
0	0	V_I	$-1/3 \cdot V_I$	$-1/3 \cdot V_I$	$+2/3 \cdot V_I$
0	V_I	0	$-1/3 \cdot V_I$	$+2/3 \cdot V_I$	$-1/3 \cdot V_I$
0	V_I	V_I	$-2/3 \cdot V_I$	$+1/3 \cdot V_I$	$+1/3 \cdot V_I$
V_I	0	0	$+2/3 \cdot V_I$	$-1/3 \cdot V_I$	$-1/3 \cdot V_I$
V_I	0	V_I	$+1/3 \cdot V_I$	$-2/3 \cdot V_I$	$+1/3 \cdot V_I$
V_I	V_I	0	$+1/3 \cdot V_I$	$+1/3 \cdot V_I$	$-2/3 \cdot V_I$
V_I	V_I	V_I	0	0	0

Table 3.2: Operating states of the wye three-phase LLC inverter (legs in parallel).

Voltage Levels of the Rectifier

The voltage and currents in the rectifier are straightforward: the voltage across the windings are applied by the bridge directly,

$$u_{jk} = v_j - v_k \tag{3.16}$$

and the currents follow the ones from a polygon, as shown in fig. 3.9,

$$i_a = i_{ca} - i_{ab} \tag{3.17}$$

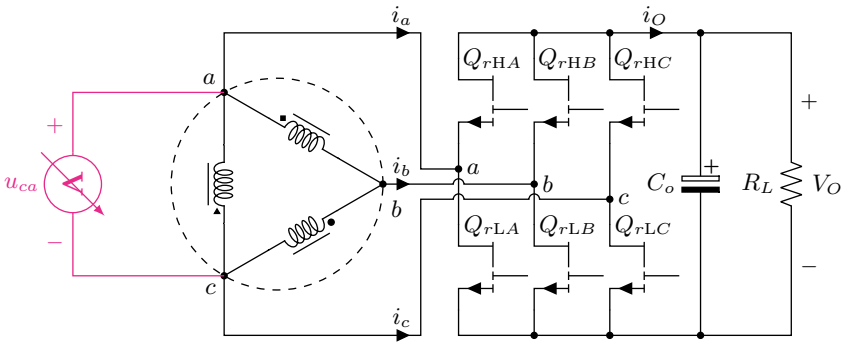

Figure 3.9: Secondary of the transformer in delta configuration and its rectifier in a three-phase LLC converter, highlighting the voltage applied to the winding of of phase ca, which will be reflected into the primary as u_{kN}.

Note that the rectifier (table 3.3) exhibits a three-level waveform as it is forced by the rectifier bridge ($+V_O$, 0, and $-V_O$) due to the delta configuration.

v_a	v_b	v_c	u_{ab}	u_{bc}	u_{ca}
0	0	0	0	0	0
0	0	V_O	0	$-V_O$	$+V_O$
0	V_O	0	$-V_O$	$+V_O$	0
0	V_O	V_O	$-V_O$	0	$+V_O$
V_O	0	0	$+V_O$	0	$-V_O$
V_O	0	V_O	$+V_O$	$-V_O$	0
V_O	V_O	0	0	$+V_O$	$-V_O$
V_O	V_O	V_O	0	0	0

Table 3.3: Operating states of the delta three-phase LLC rectifier (legs in parallel).

Main Waveforms

In fig. 3.10 the converter operates at resonance and the voltages from each switching node to the neutral u_{kN} in the primary and the voltage reflected from the secondary are in phase. When this is happening, a phase delay of $\Delta\varphi = 30°$ between the control signals at the primary and the secondary sides is present.

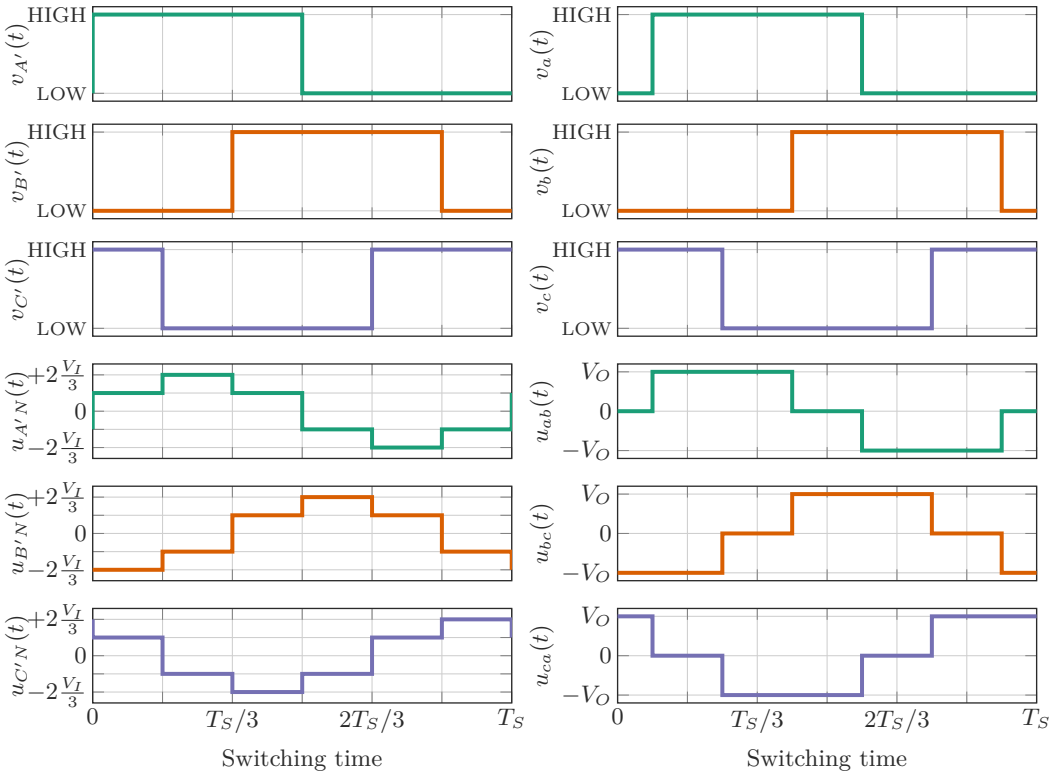

(a) Inverter switching to neutral

(b) Rectifier into the secondary

Figure 3.10: Wye-delta three-phase LLC converter: Voltages seen by the primaries and secondaries as function of the excitation (control signals).

This delay in the pulses is due to the nature of the wye/delta transformer (30° phase-shift transformer). When the converter is operating out of resonance, an additional phase delay between the inverter and rectifier has to be performed, mimicking the behaviour of a diode. Figure 3.11 shows the two most relevant cases for inductive and capacitive behaviour. In principle, six regions can be differentiated (three inductive $\Delta\varphi \in (0°,\ 180°]$ and three capacitive $\Delta\varphi \in (-180°,\ 0°]$. In normal operation, only the first two inductive regions ($\Delta\varphi \in (0°,\ 120°]$) are relevant as the third ($\Delta\varphi \in (120°,\ 180°]$) is only reached at very low power and high-frequency, while the capacitive defines the frontier for ZVS operation, being at $\Delta\varphi = 0°$ the point for ZCS.

The full analysis of the three-phase transformer and inductor will be given in-depth in section 4.1). For now, the transformer model used is derived from the consideration that it is equivalent to three independent single-phase transformers.

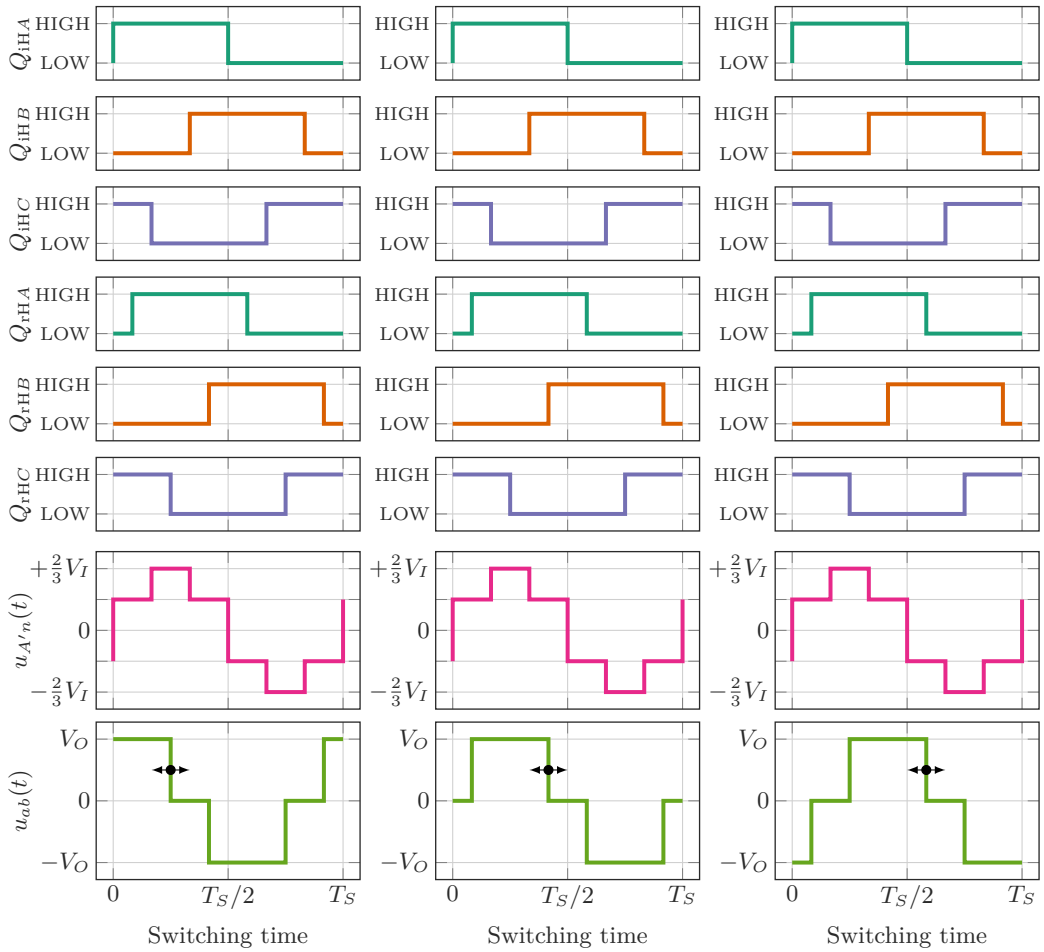

(a) Capacitive $\Delta\varphi = -30°$ (b) Inductive $\Delta\varphi = 30°$ (c) Inductive $\Delta\varphi = 60°$

Figure 3.11: Voltages at both sides of the resonant tank ($u_{A'N}$ and $u_{ab} = u_{AN}/n_n$) referred to the neutral of the primary for different load types (inductive and capacitive), demonstrating the effect of the modulation in the inverter and rectifier.

An example of the behaviour of the characteristical gain curve is shown in

fig. 3.12, where the different modes of operation areas (capacitive and inductive) are displayed, being at any point of operation under that area, represents its mode of operation.

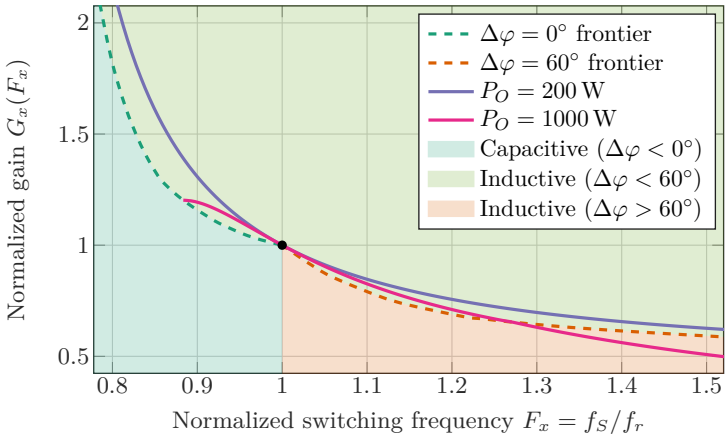

Figure 3.12: Resonant tank characteristical gain as function of the normalized switching frequency F_x highlighting the different operating areas (capacitive and inductive).

The rest of the waveforms are given in fig. 3.13 for reference. They illustrate the characteristic behaviour of the converter across the three main operating regions: below resonance, at resonance, and above resonance. The current waveforms follow a similar approach as in the single-phase LLC, with each phase resonant tank representing a second-order Ordinary Differential Equation (ODE) with the magnetising entering into the resonance with L_r and C_r when the resonant tank is not able to transmit power into the secondary (overpass the ideal diodes).

As in the single-phase LLC converter, the output current $i_O(t)$ does distort both below and above resonance due to the higher harmonics, but for narrow frequency operation we can calculate the amount of output capacitance needed by, first, calculating the average current compared to the amplitude $\hat{I}_O$ of the sine wave in a six-pulse rectifier[2] it can be obtained:

$$\frac{I_O}{\hat{I}_O} = \frac{3}{\pi} \tag{3.18}$$

and by integrating the area of the sine $i_O(t)$ over this average output current I_O, we get the charge injected into the output capacitor, and thus, from the output voltage ripple of 5 % (see section 3.1) and eq. (A.26) from chapter B we get:

$$\Delta V_O = \frac{I_O}{C_o}\left[\tan^{-1}\left(\sqrt{\left(\frac{\pi}{3}\right)^2 - 1}\right) + \sqrt{\left(\frac{\pi}{3}\right)^2 - 1}\right]. \tag{3.19}$$

[2] A full analysis in a p-pulse (being p the amount of phases) for any harmonic n is obtained, including the average, in section A.3.

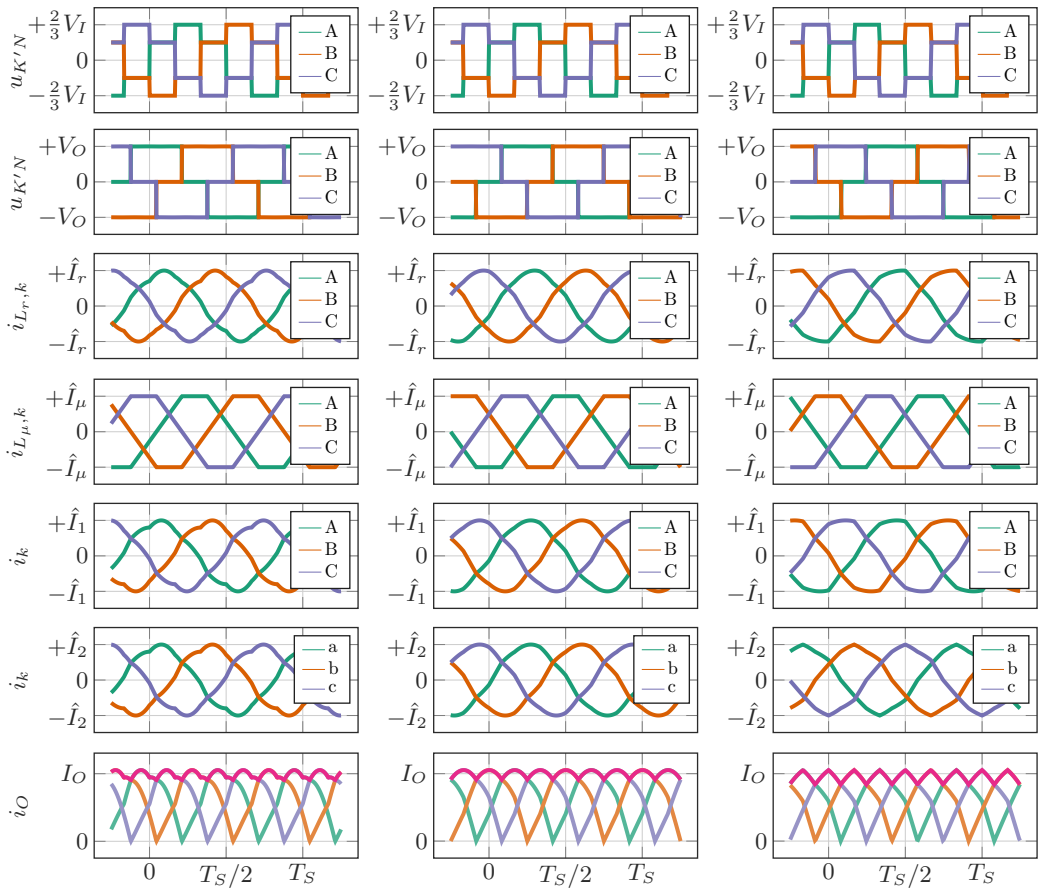

(a) Below resonance (b) At resonance (c) Above resonance

Figure 3.13: Simulation result with the main waveforms of the wye-delta three-phase LLC converter for different operating points (below resonance, at resonance, and above resonance).

3.3.3 Modelling with Approximations: FHA

Previously in section 3.2.2, a single-phase LLC converter was approximated via FHA. In it, the voltage applied by the inverter bridge was substituted by an AC voltage source, and the rectifier, as voltage and current seen from the primary of the transformer were in phase, was substituted by a pure resistive element R_{ac}.

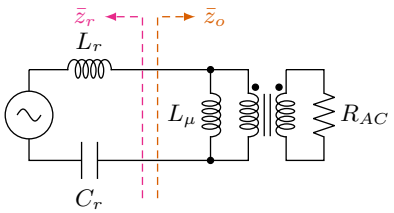

Figure 3.14: Single-phase equivalent for a three-phase LLC

In the three-phase LLC converter, the same analysis can be executed. For simplicity, an equivalent model to the single-phase LLC converter (fig. 3.14) will be

derived in this subsection for the particular case of the wye-delta three-phase LLC converter. Then, the analysis is generalised for the rest of the transformer types. As the transformer is a linear element, we only need to approximate the rest of the circuit to obtain the equivalent single-phase model.

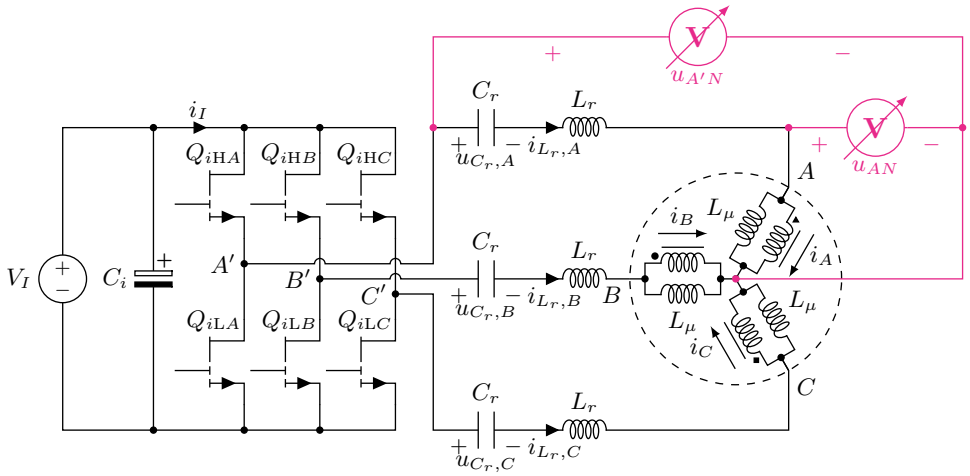

(a) Wye primary, highlighting the voltages at both sides of the resonant tank

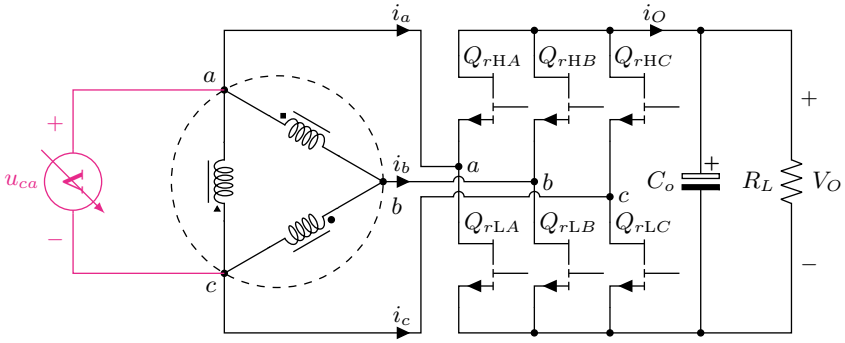

(b) Delta secondary

Figure 3.15: Wye-delta three-phase LLC converter divided into primary side (inverter) and secondary side (rectifier).

The actual analysis starts by calculating the voltage seen from the switching nodes of the inverter (A', B' and C'), and the neutral of the primary of the transformer as shown in fig. 3.15a. It is not important which phase is chosen as the single-phase equivalent is equal for the three phases.

Equivalent AC Resistance

Calculating the fundamental harmonic of the voltage across the primary winding as function of the output voltage,

$$\hat{U}_{ca} = \frac{2\sqrt{3}}{\pi} V_O \tag{3.20a}$$

and as the peak of the current as function of the output current I_O is known from eq. (3.18), the fundamental harmonic of the current is also known,

$$\hat{I}_{ca} = \frac{\pi}{6\sqrt{3}} \cdot I_O \tag{3.20b}$$

thus we can calculate the equivalent AC resistance seen from the primary winding by reflecting it from the secondary of winding *ca*:

$$R_{AC,3\phi} = n_n^2 \frac{\hat{U}_{ca}}{\hat{I}_{ca}} = n_{n,3\phi}^2 \frac{36}{\pi^2} \cdot \frac{V_O}{I_O} \tag{3.20c}$$

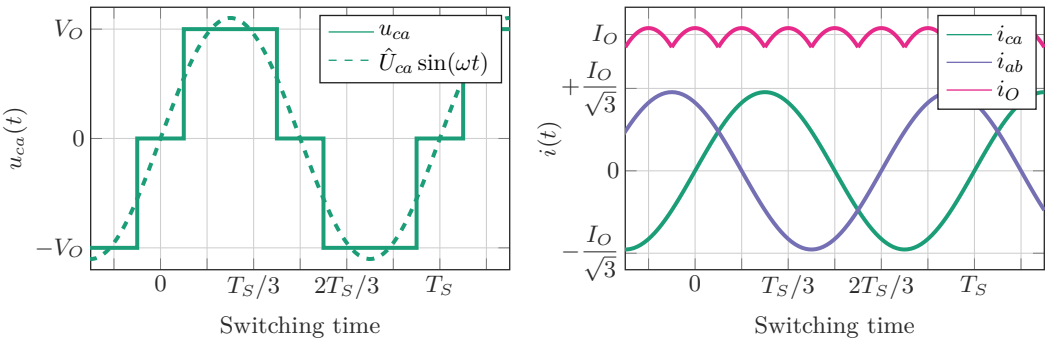

(a) Voltage at the secondary

(b) Current through the inverter

Figure 3.16: Wye-Delta Three-Phase LLC Converter: Voltages seen by the primaries and secondaries as function of the excitation (control signals).

3.4 Three-Phase LLC with Cells in Stack

As explained in , the resonant capacitors naturally enable a stacked configuration, as each cell has a distinct DC offset (from 0 to V_I, in thirds), so resonant capacitors must withstand an additional voltage rating of $V_I/3$. The main advantage is input voltage division, allowing the use of lower-voltage, high-performance transistors.

The topology starts with an input voltage capacitor divider

The first step is to take full advantage of the topology. Compared to the classical Three-Phase LLC converter with wye-wye or delta-delta configuration, the wye-delta transformer incorporates a $\sqrt{3}$ of voltage step-down conversion ratio.

The splitting of the full voltage with three cells adds an additional factor of 3, applying an equivalent factor of around 5.2, the rest of the conversion ratio will be given by the windings turn ratio of the transformer $n_n = n_p/n_s$ as well as the gain of the resonant tank (frequency modulation).

$$V_O = \frac{V_I}{3\sqrt{3}n_n} \cdot G_x(F_x) \tag{3.21}$$

where $G_x(F_x)$ is the gain of the resonant tank for a switching frequency of $F_x \cdot f_r$.

Moreover, the blocking voltage of the inverter transistors is also divided by three, allowing to choose from a wider range of lower on-resistance transistors, building a compromise between this and the fact that the RMS current increases.

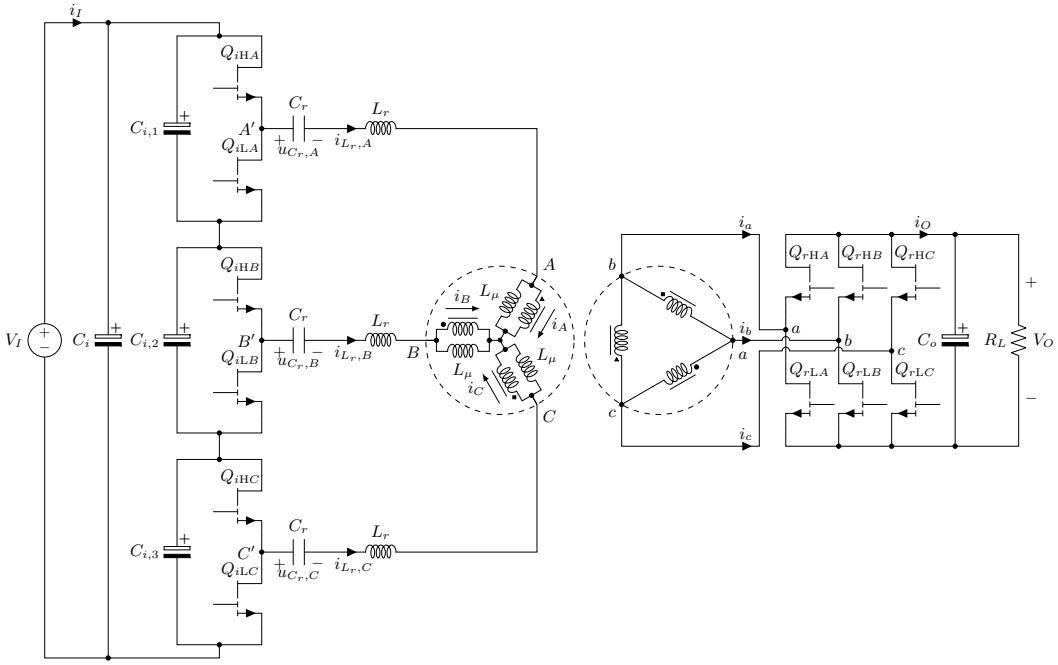

Figure 3.17: Wye-delta three-phase LLC converter with inverter legs in stack.

3.4.1 Voltage Divider Stability

In stacked converter architectures, the input voltage is divided among multiple floating cells connected in series. Ideally, each cell sustains an equal share of the total stress, preserving electrical margin and device reliability. In practice, however, this division is not guaranteed: static mismatches in parasitics, capacitances, inductances, magnetic coupling, or gate timing can bias the average voltage of a section, while dynamic events such as start-up, load transients, or mode changes can inject net charge into a floating link and drift the distribution. Such unbalance is critical because overstressed sections may exceed safe operating limits, while understressed ones contribute less effectively to power transfer, leading to unequal loss, thermal runaway, and eventual failure.

Ensuring stable voltage division is therefore a central design task, requiring mechanisms that act over different timescales to suppress fast imbalances, restore equilibrium during steady operation, and supervise behaviour during start-up or mode changes. Balance is therefore addressed on several timescales:

- **Fast timescale (a few switching periods):** When all primary windings are tightly and symmetrically coupled, the induced voltages across stacked sections are constrained to be similar and the switching waveforms tend to self-centre. This argues for integrated or co-wound primaries and carefully mirrored layouts to equalise parasitics, making magnetic coupling and sym-

metry desirable, and requires symmetric magnetic behaviour that will be explained later in section 4.1.

- **Medium timescale (milliseconds to seconds):** Passive equalisation with high-value bleed resistors across each floating link provides a gentle restoring force that corrects slow drift with negligible switching penalty. The time constants are chosen long compared to the switching period but short compared to operating-mode dwell times.

- **Slow/supervisory timescale:** Active trimming can be introduced by sensing each link voltage (via capacitive dividers and isolated measurement) and injecting a small bias in duty, phase, or dwell to cancel residual error. Such loops need only modest bandwidth and can remain dormant in steady conditions, waking during start-up and after mode changes.

Start-up sequencing deserves separate attention. As the links are floating, an uncontrolled pre-charge can leave one section over-energised. A symmetrical pre-charge path into each sub-link, released simultaneously, prevents such unbalance. Holding the tank at a fixed, conservative frequency (usually over resonance to use the reactive energy) during this phase helps to slow-down the transition and ensure equal voltage distribution.

Similar care is required when changing modes if morphing topologies are employed. Transitions should include hysteresis to avoid chatter and should slew internal timing parameters so that the average leg voltages during the handover do not impart a net DC bias. If a mode change alters the average of the applied waveforms, a brief, scripted re-centring burst in the more favourable mode can remove accumulated offset before normal regulation resumes.

A second complication is current sharing and leakage management, when multiple windings or integrated leakage elements are used to shape energy transfer. Intentional leakage is an effective means to control resonant or quasi-resonant behaviour, but it must be proportioned evenly so that each stacked section sees similar commutation conditions. This is best handled by designing the magnetic structure with an explicit inductance-matrix target and validating it by finite-element analysis; symmetry in gaps and window utilisation is more important than absolute inductance value, as symmetry governs sharing and balance. On the secondary side, if paralleled paths exist, the reduced per-section current in a stacked design eases sharing, but layout symmetry and small series ballast remain effective tools to mitigate residual imbalance.

Finally, stacking introduces additional CM $\mathrm{d}v/\mathrm{d}t$ paths and more complex fault management. Multiple floating midpoints increase the number of nodes that can capacitively couple to chassis; disciplined placement of shield windings, symmetric parasitic capacitances to a quiet reference, and careful return routing mitigate the resultant emissions. Protection should be coordinated so that an over-voltage or over-current in one section triggers a system-level response that prevents the remaining sections from driving an unbalanced structure.

3.5 Designing LLC Converters

Careful definition of the gains that meet the requirements for every input/output voltage combination is needed in steady-state. Figure 3.18 shows the generalized DC/DC converter with wide input/output voltage ranges. These specifications might be more relaxed when designing more restricted situations such as a voltage regulator (constant output voltage), and even more in a DCX, with a constant input/output voltage switching at resonance.

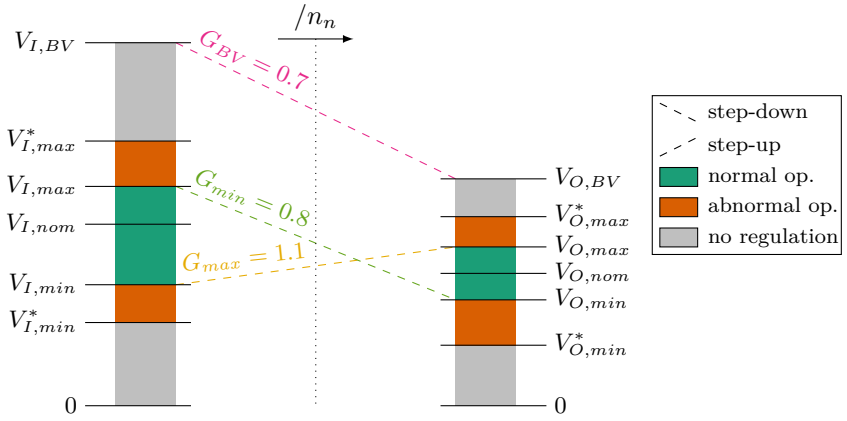

Figure 3.18: Illustrative DC/DC voltage conversion with an input and output voltage range of operation, highlighting the minimum and maximum gains.

Each parameter is related to certain constraints in the design, apart from the winding turns ratio n_n, there are two triplets of parameters equivalent between them that can be used to design: at component level (L_r, C_r and L_μ), representing the electrical model of the converter, or at system level (ω_r, Z_r and m) that represent the normalised behaviour of the converter. In general, the latter set is used as ω_r is typically a prior design choice.

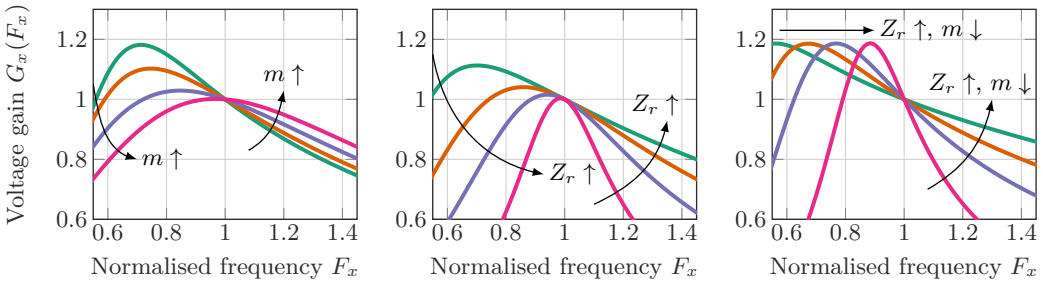

(a) m sweep (b) Q_s sweep (c) m and Z_r sweep

Figure 3.19: Influence of the design parameters m and Q_s on the gain characteristic of an LLC resonant converter

Figure 3.19 illustrates the influence of the resonant tank parameters on the characteristical gain of an LLC converter. In fig. 3.19a, increasing m while keeping Z_r constant flattens the gain curve, requiring a wider switching frequency range for

the same gain variation, this means that the maximum boost gain G_{max} is reduced. A similar effect occurs when increasing Q_s at a fixed m, as shown in fig. 3.19b. The different sensitivity of the gain function G_x to m and Q_s provide a degree of flexibility in shaping the gain profile. This is exemplified in fig. 3.19c, where m and Z_r are swept simultaneously so that a maximum gain is maintained. As a result, the operating frequency span can be narrowed or widened while preserving the gain limit, highlighting how a family of m, Z_r pairs can yield the same gain characteristics to specific design objectives.

3.5.1 Fundamental-Harmonic Approximation (FHA)

The parameters m and Z_r are widely used by LLC converter designers to compare the selectivity of the filter. The analysis of these converters is typically initiated using the FHA, as it provides a straightforward method to describe the converter gain as a function of the switching frequency. The simplicity of the FHA model makes it attractive for initial design stages and for comparing topologies, since the gain of the converter can be evaluated close to the resonant frequency $f_S \approx f_r$.

Despite these advantages, the limitations of the FHA become apparent when the operating frequency deviates significantly from resonance. Its single-harmonic representation does not capture the multi-resonant nature of the LLC tank (L_μ resonance), leading to inaccuracies in predicting the amplitude under below-resonance conditions as seen in fig. 5.17. As a consequence, designs based on FHA are very conservative, designing larger resonant inductors than necessary.

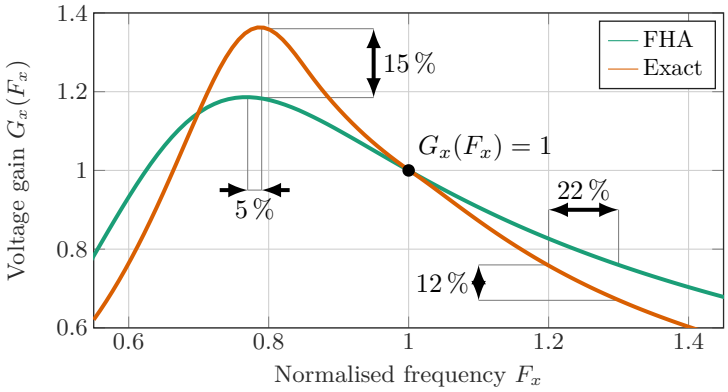

Figure 3.20: Generic characteristical gain $G_x(F_x)$ comparison between an FHA ($Q_s = 1$, $m = 3$) with an exact solution (simulated in PLECS)

In essence, any modelling effort based on linearised equations, such as the FHA, aims to approximate the fundamentally non-linear behaviour of the LLC converter. The main benefits of the method can be summarised as:

- Providing a considerable amount of insight into the converter's resonant behaviour and voltage gain.
- Enabling AC small-signal analysis, which is particularly useful for control design.

- Allowing simple, step-by-step design procedures derived from the analytical $F_x(G_x)$ relationship.

When the operating frequency moves further from resonance, the contribution of higher-order harmonics becomes non-negligible, reducing accuracy. To address this, several extensions of the FHA have been proposed. Some approaches replace the equivalent resistive load with a more complex impedance model that reflects the combined capacitive and resistive behaviour of the tank. Others employ direct time-domain analysis of the converter's switching intervals to compute the gain without relying exclusively on harmonic approximations. More advanced methods incorporate superposition or Fourier series expansion to selectively include higher-order harmonics, thereby improving accuracy.

It is also important to note that while the FHA provides valuable insights into the resonant characteristics of the converter, it does not fully capture the switching dynamics. In particular, conditions for ZVS in the inverter switching components and ZCS in the rectifier are only partially represented. The FHA can establish necessary, but not sufficient, conditions for soft-switching, and further refinements or complementary models are usually required to guarantee accurate prediction of switching behaviour. For this reason, a different design methodology, based on numerical solutions and simulations, is presented in this section.

3.5.2 Generalised Method for Designing LLC Converters

The translation of the specifications of a converter, such as the one in this work (section 3.1), needs to be first translated into gain requirements as in fig. 3.18. The complete workflow is illustrated in fig. 3.21, and it will be explained in detail in the rest of this subsection.

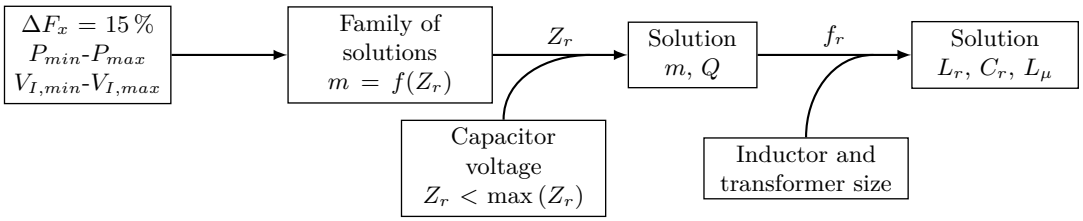

Figure 3.21: Generalised workflow for designing LLC converters

Design Steps for LLC Converters

The first variable of the procedure is to decide the winding turns ratio n_n, which, in general, it becomes as the relationship between the input and output voltage at resonance, or more generally, at nominal voltage. The specific decision can be analysed depending on the balance between power losses. In this case, the choice for n_n is taken as the closest to nominal operation

$$\frac{V_I}{V_O} = \frac{270\,\mathrm{V}}{28\,\mathrm{V}} \approx 9 \tag{3.22}$$

the decision for n_n depends on the topology chosen, for example, for the case of the selected wye-delta three-phase LLC converter, the $\sqrt{3}$ factor makes $n_{n,\mathrm{par}-3\phi} = 5\text{-}6$

for the case of the inverter in parallel and $n_{n,\text{sta}-3\phi}$ = 1-2 in the case of the stacked version. For reference, the single-phase LLC converter makes for $n_{n,\text{HB}-1\phi}$ = 9-10 for the case of a full-bridge inverter, and $n_{n,\text{HB}-1\phi}$ = 5-6.

Once n_n is decided, the second step is the core of the design of the converter as it involves the evaluation of the real characteristical gain $G_x(F_x)$ to comply with the frequency span ΔF_x. This needs to be guaranteed for two operating points:

- The maximum gain G_{max} (maximum step-up) is limited by the minimum input voltage $V_{I,min}$ and maximum output voltage $V_{O,max}$ at the maximum output power $P_{O,max}$.
- The minimum gain G_{min} (maximum step-down) is limited by the maximum input voltage $V_{I,min}$ and minimum output voltage $V_{O,max}$ at the minimum output power $P_{O,max}$.

These can be calculated with the $F_x(G_x)$ function derived in section B.1. No matter what model is employed, as long as the model delivers a monotonous function, **only one solution exist** for each ΔF_x. In fig. 3.22 an example that illustrates this uniqueness[3].

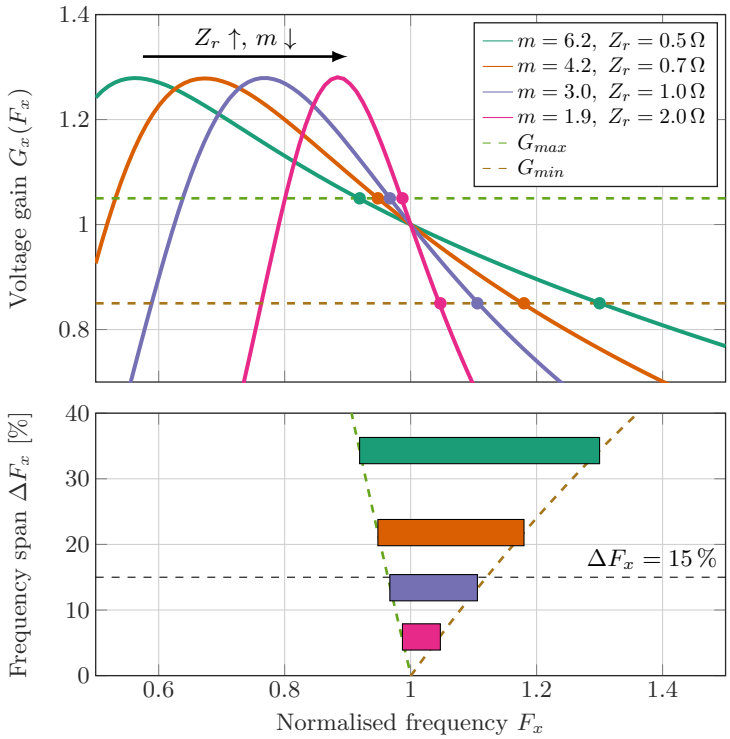

Figure 3.22: Influence of the design parameters m and Q_s on the characteristical gain for constant gain range ΔG_x at different frequency span ΔF_x.

[3]Only one solution exist independently of whether the resonant frequency falls in the $F_{x,min}$ and $F_{x,max}$ range or not (maximum or minimum gain both over or below the gain at resonance).

As fig. 3.22 illustrates, the narrower the ΔF_x, naturally the more sensitivity of the gain function with the switching frequency F_x, the gain margin above the maximum gain requirement gives a margin in the switching current, as close to the peak of the gain, zero switching current exist.

The designs are made for the four alternatives (single-phase LLC for both half-bridge and full-bridge, as well as the two three-phase topologies, with the inverter in parallel and in stack as shown in table 3.4), the gain margin was set to 10 %, the switching frequency was set to 1 MHz and, for specification, the maximum voltage in the resonant capacitor was set to 230 V (see section 3.1). All of the designs led to low values of m factor, making L_r and L_μ comparable, and that there will be a lot of reactive enregy circulating in the converter, penalizing the efficiency. This goes in line with the experience that the controlability is normally paid with efficiency.

Topology	f_r [MHz]	Z_r [Ω]	m	L_r [µH]	C_r [nF]	L_μ [µH]
Single-phase LLC (half-bridge)	1 MHz	25 Ω	2.2	4.2 µH	6 nF	5.2 µH
Single-phase LLC (full-bridge)	1 MHz	100 Ω	2.2	16.8 µH	1.5 nF	21.0 µH
Three-phase LLC (parallel bridge)	1 MHz	54 Ω	2.25	8.50 µH	3.00 nF	10.6 µH
Three-phase LLC (stacked bridge)	1 MHz	15 Ω	2.25	2.35 µH	10.8 nF	3.0 µH

Table 3.4: Equal designs for different topologies of LLC converters compared.

3.6 Meeting Power Density Expectations

Note that in the previous section, no mention of the resonant switching frequency f_r was done, this is because it is not directly related to the characteristical gain of the converter, instead, it is more of a practical implementation, defining the size of the passive components from the mathematical representation m and Z_r.

In this section, two topologies from the LLC family of converters are considered as the potential candidates to meet the power density targets set for this converter in section 3.1. Simple calculations for sizing the key components are explained, starting from the transistors and moving through the resonant elements and magnetics.

3.6.1 Losses in the Switches

To simplify the analysis, we assume the same total amount of transistor material by conceptually dividing the half-bridge of the single-phase LLC converter into three parallel single-phase half-bridges. In this equivalent representation, each transistor has $3R_{DS(on)}$ and $E_{off}/3$[4].

[4]This approximation will be revisited in section 5.2, where it will be shown that such transistors are typically constructed from multiple identical dies connected in parallel.

Since magnetising current is required in both the single-phase and three-phase cases to achieve soft-switching, and each of the three phases must provide it, the current handled by each transistor in the three-phase topology is reduced. Consequently, the circulating energy in the tank decreases according to the RI^2 law, thereby lowering the energy requirements of the resonant inductor.

3.6.2 Passives Size

Table 3.4 summarises the passive component values (L_r, C_r, and L_μ) for the different topologies under the same specifications (section 3.1). This enables a fair comparison between single-phase and three-phase LLC converters.

As discussed in section 2.1.3, the energy and volume of passive components are closely related. Since m and Z_r are known from table 3.4, the actual values of L_r, C_r, and L_μ can be determined for any resonant frequency f_r. The transformer size is relatively straightforward to estimate, as it mainly depends on the applied voltage in the secondary, and is limited by the maximum dimensions of 60 mm in width and 12.7 mm in height (section 3.1).

The inductor footprint, on the other hand, is more flexible. An optimisation was carried out assuming a maximum air-gap length of 200 µm, under the constraint of constant volumetric core losses of 300 mW cm^{-3}. This figure, introduced in section 2.1.3, corresponds to the ML91S material [211], which at the time of optimisation offered the best performance.

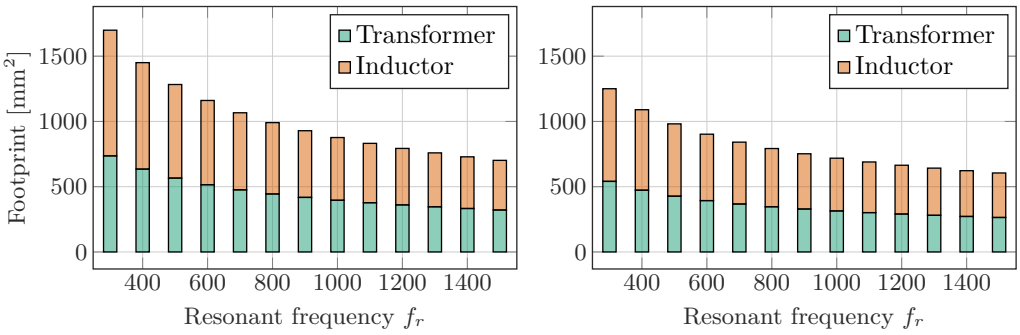

(a) Single-phase LLC (b) Three-phase LLC

Figure 3.23: Transformer and inductor footprints for the single-phase and three-phase cases.

The resulting trends are presented in fig. 3.23, which shows the variation of magnetic component footprint (inductor and transformer) as a function of resonant frequency. At lower frequencies, both components occupy larger volumes. As the frequency increases, the required magnetic volume decreases rapidly at first, since higher-frequency operation allows smaller values of resonant inductance L_r and magnetising inductance L_μ. Beyond approximately 800 kHz to 1000 kHz, however, the reduction in footprint slows down, revealing a saturation trend where further frequency increase yields diminishing benefits. This behaviour, consistent with the scaling laws shown in fig. 2.3, indicates an optimal design window around 1 MHz,

where substantial volume reduction is achieved without incurring the drawbacks of excessively high-frequency operation.

At the vicinity of 1 MHz, in terms of energy, the three-phase topology shows an improvement of about 10 % to 20 % in the inductor compared to the single-phase case.

3.6.3 Input and Output Capacitance

As previously discussed, the rectifier in LLC converters can be synthetised as full-wave rectification, where any negative time-domain current (sinusoidal) is rectified to obtain ZCS. Extended into three-phase, six-pulse rectification is obtained. This is illustrated in fig. 3.24b for both the single-phase and three-phase LLC.

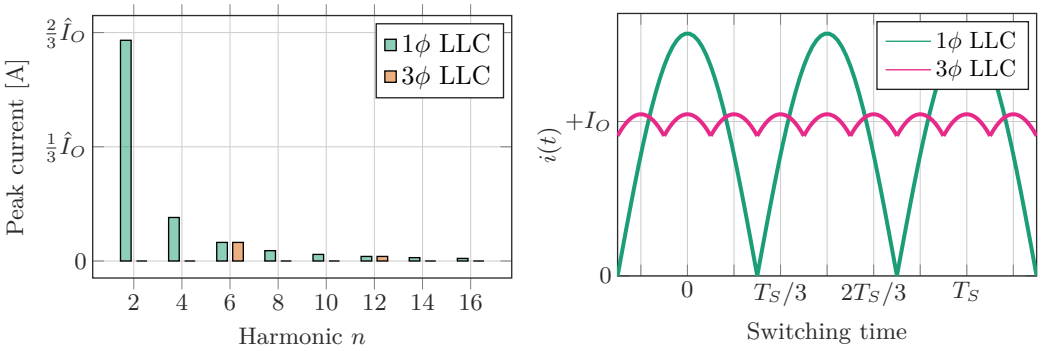

(a) Harmonic contents

(b) Temporal visualisation

Figure 3.24: Input current harmonic content of both single-phase and three-phase LLC converter with a time-domain representation of the rectified current for reference.

Any harmonic component can be obtained from eq. (A.22) for the input current (from the DC input supply) and the output current (to the load). The comparison between these two cases is shown in fig. 3.24a. In the three-phase LLC, only harmonics that are multiples of six are present, which reduces the current stress and losses in the input EMI filter and enables a smaller filter. The same effect appears at the output, and by using eq. (A.26) (see section A.3), the ripple reduction achieved by the three-phase approach can be estimated as

$$\Delta V_O(p) = \frac{I_O}{\omega_S C_o} \cdot \frac{1/\xi}{2\cos^{-1}(\xi)} \int_{-\cos^{-1}(\xi)}^{+\cos^{-1}(\xi)} \left[\cos(\omega t) - \xi\right] \mathrm{d}(\omega t) \tag{3.23}$$

where ξ is the relationship between the DC component and the peak of the sine wave, which depends on the number of phases $\xi(p) = \hat{I}_O/I_O$. In section A.3 the p-pulse sinusoidal rectification for an arbitrary number of phases p and harmonic index n is derived. For $p = 3$ (three-phase, six-pulse rectification) and $p = 1$ (single-phase, full-wave rectification), the DC component ($n = 0$) of the rectified current follows from eq. (A.24): specifically, $I_O/\hat{I}_O = 2/\pi$ for the single-phase and $I_O/\hat{I}_O = 3/\pi$ for the three-phase case.

From eq. (3.23), and for the same output voltage ripple ΔV_O, switching frequency ω_S, and average output current I_O, we can solve for the required output

capacitance C_o and obtain,

$$\frac{C_o(p=3)}{C_o(p=1)} \equiv \frac{\Delta V_O(p=3)}{\Delta V_O(p=1)} \approx 8.4\,\% \tag{3.24}$$

which implies a large reduction in the required output capacitance C_o for the three-phase case (about $-91.6\,\%$ in capacitance, and thus, in volume).

3.6.4 Nonidealities in the Design of LLC Converters

In practice, the characteristical gain of LLC converters deviates from the exact model (simulator-grade design) due to several non-idealities. Dead times introduced in the switching bridges reduce the amplitude of the fundamental, leading to gain shifts at resonance. In addition, conduction and switching losses in the semiconductor devices, together with parasitic effects in the passive components, further reduce the achievable gain and efficiency. These effects must be taken into account to obtain an accurate prediction of the converter behaviour and to ensure robust design margins.

Figure 3.22 shows how for each m, only one Z_r exist that matches the same maximum gain where a margin of $20\,\%$ was given for the maximum of the $G_x(F_x)$ for illustrative purposes. In reality, this margin will be given to guarantee ZVS and depending on the dead times required for both the inverting and rectifying switches as it reduces the amplitude of the fundamental harmonic. This effect increases with switching current and frequency, making it complex to initially estimate it but still possible.

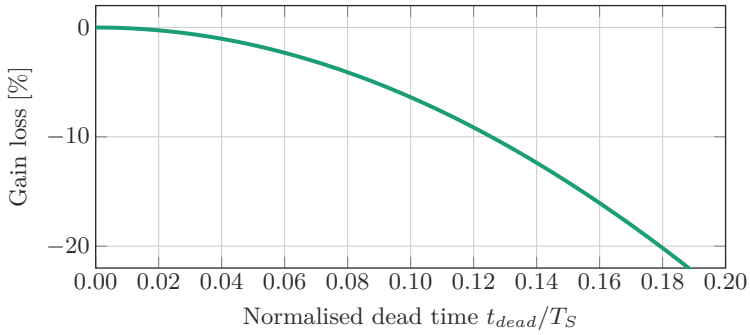

Figure 3.25: Gain loss (reduction in the amplitude of the fundamental) due to the dead time in the bridge for soft-switching.

Another source of error is the power losses, switching losses in the inverter are directly given by the input, so no effect is derived from them other than the related to dead time (fig. 3.25), nonetheless, any upstream sources of losses has an effect:

- Conduction losses: Any source of losses that is related with a purely resistive element can be seen as a drop voltage (gain reduction as a voltage divider), giving additional step-down to the characteristical gain, these are: the ESR of the inductor and transformer and the $R_{DS(on)}$ of both the inverter and rectifier.

- Switching losses of the rectifying transistors: as the rectifier is a purely resistive element, any power loss inside behaves as additional loading to the output, as these power losses depend non-linearly with output voltage and current, if those vary, so it will the equivalent resistive element.
- Core losses: These losses are typically modelled as an Equivalent Parallel Resistance (EPR) to the primary and secondary winding as the magnetisation of the core depends on the voltage applied (and frequency) and not the current, completely reflecting it into the output load.

In summary, the characteristic gain of LLC converters is strongly affected by non-idealities that arise both in the switching network and in the passive components. Dead times reduce the effective fundamental amplitude, while conduction, switching, and core losses introduce additional gain degradation that can be modelled as equivalent resistive elements or reflected impedances. Although these effects complicate the analytical prediction of the gain curves, their impact is systematic and must be considered during design. Accounting for them ensures that sufficient margin is reserved for ZVS operation and that the expected efficiency and regulation performance are preserved under realistic operating conditions.

CHAPTER 4

Three-Phase Magnetics for LLC Converters

No symmetry,
no beauty.

— Hermann Weyl

In the previous chapter, the design methodology for LLC converters was established, with particular emphasis on the selection of the resonant inductance L_r and the magnetising inductance L_μ as key parameters defining the characteristical gain and frequency span.

While these results relied on lumped models of the passives, their practical implementation requires the synthesis of magnetic structures that simultaneously define the transformer and the resonant inductor within strict dimensional and thermal constraints. In three-phase architectures, this task is further complicated by the need to ensure balanced flux distribution among phases, mitigate circulating energy caused by asymmetries, and minimise high-frequency losses.

This chapter addresses these challenges by analysing the integration of three-phase magnetics, developing models for balanced operation, and proposing geometrical compensation techniques that enable compact, low-profile, and efficient transformer and inductor realisations for next-generation aircraft power systems.

4.1 Integration of Three-Phase Magnetics

The LLC converter includes two magnetic components: an inductor and a transformer. Any ideal, purely inductive [1] n-port component can be described using an inductance matrix $\mathbf{L}$, which relates the port voltages and currents:

[1] In this context, "purely inductive" implies that both resistive and capacitive effects are neglected, and only the magnetic (inductive) interactions between windings are considered.

$$\mathbf{u}(t) = \mathbf{L} \cdot \frac{\mathrm{d}}{\mathrm{d}t}\mathbf{i}(t) \tag{4.1}$$

This subsection derives the conditions required for achieving balanced three-phase magnetic components in both the inductor and the transformer. The analysis is generalised using the three coupled windings shown in fig. 4.1.

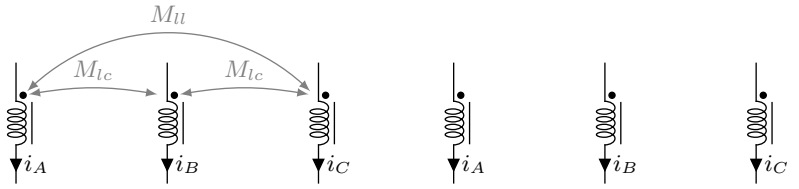

(a) Three coupled windings (b) Three independent windings

Figure 4.1: Illustration of the target uncoupled magnetic representation and the coupled model for three magnetically linked windings, highlighting the mutual couplings

These coupled elements can be described using an unified inductance matrix $\mathbf{L}$ that captures the voltage and current interactions among multiple windings, enabling equivalent circuit-level representation of the electrical interactions. Thus, the inductance matrix for the generalised case shown in fig. 4.1a, becomes:

$$\mathbf{L} = \begin{bmatrix} L_{AA} & M_{AB} & M_{AC} \\ M_{BA} & L_{BB} & M_{BC} \\ M_{CA} & M_{CB} & L_{CC} \end{bmatrix} \tag{4.2}$$

where M_{jk} is the coupling between windings j and k and L_{jj} represents the self-inductance of the winding j. The voltage and current vectors, consistent with the winding arrangement in fig. 4.1, are given respectively by:

$$\mathbf{u}^T(t) = \begin{bmatrix} u_A(t) & u_B(t) & u_C(t) \end{bmatrix} \tag{4.3a}$$

$$\mathbf{i}^T(t) = \begin{bmatrix} i_A(t) & i_B(t) & i_C(t) \end{bmatrix} \tag{4.3b}$$

The targeted behaviour of three single-phase windings (as in fig. 4.1b)

$$\mathbf{L} = \begin{bmatrix} L_{AA} & 0 & 0 \\ 0 & L_{BB} & 0 \\ 0 & 0 & L_{CC} \end{bmatrix} \tag{4.4}$$

This configuration guarantees that no coupling exists between different phases, allowing each to operate independently as three single-phase components represented by L_{jj}. To derive eq. (4.4) from eq. (4.2) we must guarantee two conditions:

1. The mutual between any two phases is the same ($M_{jk} \equiv M$ for any $j \neq k$).

2. The sum of the currents is zero ($i_A + i_B + i_C = 0$).

The first condition can be applied to eq. (4.4), enabling the matrix $\mathbf{L}$ to be split in two, the equivalent inductance matrix (denoted by $\mathbf{L}^*$) is:

$$\mathbf{L}^* = \begin{bmatrix} L_{AA} - M & 0 & 0 \\ 0 & L_{BB} - M & 0 \\ 0 & 0 & L_{CC} - M \end{bmatrix} + \begin{bmatrix} M & M & M \\ M & M & M \\ M & M & M \end{bmatrix} \tag{4.5}$$

In order to apply the second condition, we must calculate the flux contribution of all windings from the current eq. (4.3b):

$$\mathbf{\Phi}(t) = \begin{bmatrix} \Phi_A(t) \\ \Phi_B(t) \\ \Phi_C(t) \end{bmatrix} = \mathbf{L}^* \cdot \mathbf{i}(t) = \begin{bmatrix} (L_{AA} - M)\, i_A(t) \\ (L_{BB} - M)\, i_B(t) \\ (L_{CC} - M)\, i_C(t) \end{bmatrix} + \begin{bmatrix} M & M & M \\ M & M & M \\ M & M & M \end{bmatrix} \cdot \begin{bmatrix} i_A(t) \\ i_B(t) \\ i_C(t) \end{bmatrix} \tag{4.6}$$

if we apply the second condition, the constant matrix full of M multiplied by the current $\mathbf{i}(t)$ returns a null vector, allowing us to rewrite $\mathbf{L}^*$ as an equivalent diagonal matrix. Also, due to conservation of flux, the overall contribution of the inductive link must guarante that $\Phi_A(t) + \Phi_B(t) + \Phi_C(t) = 0$,

$$\begin{aligned} &\Phi_A(t) + \Phi_B(t) + \Phi_C(t) = \\ &\quad = (L_{AA} - M)\, i_A(t) + (L_{BB} - M)\, i_B(t) + (L_{CC} - M)\, i_C(t) = 0 \end{aligned} \tag{4.7}$$

the only non-trivial[2] solution is that $L_{AA} \equiv L_{BB} \equiv L_{CC} = L$. Finally, as long as the two conditions apply, the equivalent inductance matrix $\mathbf{L}^*$ is:

$$\mathbf{L}^* = \begin{bmatrix} L & M & M \\ M & L & M \\ M & M & L \end{bmatrix} \tag{4.8}$$

For simplicity, eq. (4.8) was derived for three independent windings (a three-phase inductor), for a transformer it can be easily extended. Consider the block matrix representing $\mathbf{L}^*_{pp}$ the primary windings, $\mathbf{L}^*_{ss}$ the secondary windings, and $\mathbf{M}^*_{ps} \equiv \mathbf{M}^*_{sp}$ the mutual blocks between primary and secondary windings:

$$\mathbf{L}^* = \begin{bmatrix} \mathbf{L}^*_{pp} & \mathbf{M}^*_{ps} \\ \mathbf{M}^*_{sp} & \mathbf{L}^*_{ss} \end{bmatrix} \tag{4.9}$$

we can recalculate the total flux by multiplying by their respective current vectors:

$$\mathbf{\Phi}(t) = \begin{bmatrix} \mathbf{\Phi}_p(t) \\ \mathbf{\Phi}_s(t) \end{bmatrix} = \begin{bmatrix} \mathbf{L}^*_{pp} & \mathbf{M}^*_{ps} \\ \mathbf{M}^*_{sp} & \mathbf{L}^*_{ss} \end{bmatrix} \cdot \begin{bmatrix} \mathbf{i}^*_p \\ \mathbf{i}^*_s \end{bmatrix} = \begin{bmatrix} \mathbf{L}^*_{pp} \cdot \mathbf{i}^*_p + \mathbf{M}^*_{ps} \cdot \mathbf{i}^*_s \\ \mathbf{M}^*_{sp} \cdot \mathbf{i}^*_p + \mathbf{L}^*_{ss} \cdot \mathbf{i}^*_s \end{bmatrix} \tag{4.10}$$

[2]Non-trivial solution in this context means that at least two of the currents $i_A(t)$, $i_B(t)$, $i_C(t)$ are not constant and that $L_{AA} - M \neq 0$, $L_{BB} - M \neq 0$ and $L_{CC} - M \neq 0$

the overall flux of both $\mathbf{L}^*_{pp} \cdot \mathbf{i}^*_p$ and $\mathbf{L}^*_{ss} \cdot \mathbf{i}^*_s$ terms have been demonstrated to be null as long as the conditions used for deriving eq. (4.8) are met: the sum of the currents in primary and secondary are independently zero and the mutual inductances are equal.

For the other two terms we can apply the same two conditions, arriving at the conclusion that the matrices $\mathbf{M}^*_{ps}$ and $\mathbf{M}^*_{sp}$ have the same form as eq. (4.8) so that the net flux is zero:

$$\mathbf{M}^* = \begin{bmatrix} L & M & M \\ M & L & M \\ M & M & L \end{bmatrix} \tag{4.11}$$

This conclusion means that any two different set of three windings can be coupled together.

4.2 Design of Balanced Three-Phase Components

In order to reduce the solution size, an integrated structure for the three single-phase inductors is desired. Unlike the resonant capacitor which voltage and current ratings as well as its capacitance are known and can be found in a parametric search, the design and optimization of L_r and L_μ requires a lot of calculation and simulation effort, even when the nominal lumped-model values are known.

Within the behaviour of three-phase magnetics, and more predominantly, in planar magnetics, the potential for phase unbalance increases. These phenomenon impacts significantly the performance of power converters, requiring the development of compensation techniques to mitigate their effects.

This phenomenon manifests as voltage and current dependance between phases. When the synchronous rectifier forces the voltage across the secondary windings, if unbalanced, results in an uneven storage of magnetizing energy among the phases. Consequently, an unbalance becomes apparent during operation. The issue worsens in a three-phase inductor for the same unbalance, rather than the transformer. This is due to an additional series coupling between two phases. For instance, the current flowing through phase k will induce an additional series voltage in the other phases, which should be 120° apart from phase k, unbalancing the system.

This is because of the non-symmetry of the typical three-phase magnetic core (equal columns in a EE core), where one of the columns (central) presents a shorter magnetic path length to the merging point compared with the other columns (laterals). To overcome this, in this section, a comprehensive analysis is made to address non-symmetrical magnetic core structures and achieve optimal performance.

4.2.1 Gapped Three-Port Asymmetric Magnetic Core

Three-phase core architectures require to have three independent magnetic paths, and this is translated into an architecture with three winding positions usually refered to as three ports.

In general, it is desirable that balanced three-phase magnetic components are built upon symmetric structures such as delta or wye cores [212] (see fig. 4.2), as this enables current sharing among multiple phases [213]. This is also often called as Inverse-Coupled Resonant Inductor (ICRI), where the phase windings are inversely coupled so that mutual fluxes oppose each other, shaping the inductance matrix of a multi-phase magnetic link to improve current sharing.

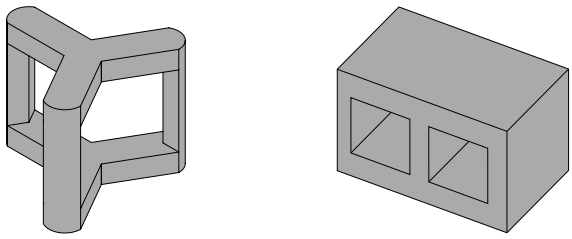

(a) Wye-core (b) EE-core

Figure 4.2: Three-leg core geometries: an example of a wye core (symmetrical) and an EE core (asymmetrical).

Nonetheless, these structures have higher volume and inconvenient terminations for the windings in a linear downstream circuit topology (fig. 4.2), and non-symmetrical magnetic cores may lead to magnetic components with different coupling between phases, detrimental to the balancing of the phases.

In the case of the three-phase LLC converter, each phase has its current shifted, unbalancing the soft-switching of the inverter (different switching currents in the bridge risking losing ZVS) and the currents in the secondary (quasi-ZCS). Altogether, a symmetric magnetic component in a three-phase system minimises the unbalance between phases, reducing the power losses and improving its thermal stability.

In [157] (fig. 4.3a), a three-column EE-core was built with two different soft materials to compensate the magnetic coupling between columns. Other authors such as in [213] (fig. 4.3b), exploit the outer magnetic fields from the corners of the magnetic core.

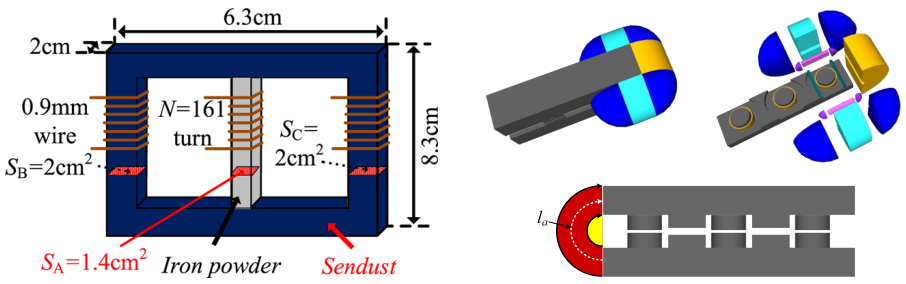

(a) Multiple materials [157] (b) Air magnetic field modelling [213]

Figure 4.3: Known techniques for compensation of asymmetric magnetic cores for three-phase inductors in the literature.

4.2.2 Geometrical Design for Asymmetric Magnetic Cores

The techniques shown in fig. 4.3 have demonstrated to be effective when compensating the flux unbalance in asymmetric magnetic cores. Nonetheless, this same effect can be accomplished by narrowing the central column respect to the laterals as the equivalent reluctance seen from the null flux singular point of the core is compensated, leading to a custom geometry core as will be shown in this section, simplifying the analysis and manufacturing, while reducing the leakage flux of the core.

In this subsection, the geometry compensation is derived for two three-port core geometries: the EE-core and the EI-core. The core dimensioning is shown in fig. 4.4.

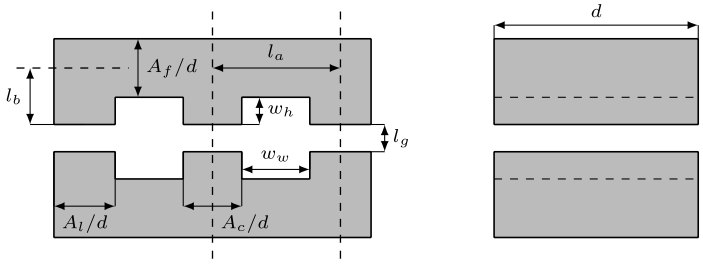

(a) Front view (b) Side view

Figure 4.4: EE-core dimensioning

The mathematical analysis is performed for the magnetostatic problem for which Ampère's Law (4.12) and the Magnetic Flux Conservation Law (4.13) are used,

$$\oint_L H \,\mathrm{d}l = \oiint_S J \,\mathrm{d}S \tag{4.12}$$

$$\oiint_S B \,\mathrm{d}S = 0 \tag{4.13}$$

all the analysis is made considering the fringing, by using σ_l and σ_c correction factors, reserved for future analysis in this subsection.

To simplify the analysis and make it more comprehensible, an approach regarding the winding layout in this section was adopted. Instead of detailing the winding layout for each individual phase, the winding arrangement was considered as one phase for each column. Figure 4.5 provides a visual representation of this simplified winding layout, illustrating how we treated the windings as a single phase within each column, highlighting the connections and relationships that are relevant to our analysis and design.

Note that from fig. 4.5, only the current through the windows is needed, as the subtraction of the two shared windings in the window (fig. 4.6). Evaluating the H-loops defined in fig. 4.6 with (4.12) we obtain the first two equations,

$$\left(\frac{l_g}{\sigma_l} + \frac{2l_b}{\mu_r}\right)\frac{B_1}{\mu_0} + \frac{2l_a}{\mu_r}\frac{B_{12}}{\mu_0} - \left(\frac{l_g}{\sigma_c} + \frac{2l_b}{\mu_r}\right)\frac{B_2}{\mu_0} = I_1 - I_2 \tag{4.14}$$

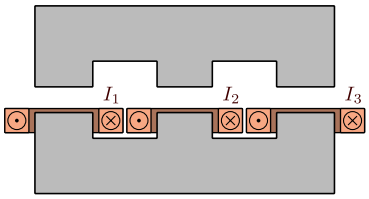

Figure 4.5: Winding layout

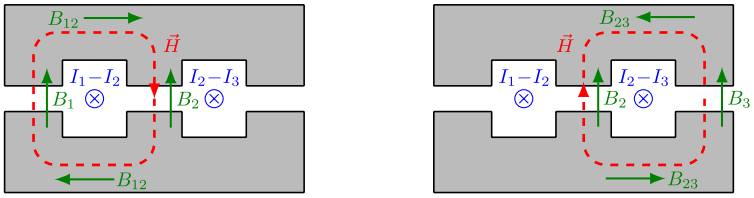

(a) Left current loop (b) Right current loop

Figure 4.6: H-field loops and the current through the window.

$$\left(\frac{l_g}{\sigma_l}+\frac{2l_b}{\mu_r}\right)\frac{B_3}{\mu_0}+\frac{2l_a}{\mu_r}\frac{B_{23}}{\mu_0}-\left(\frac{l_g}{\sigma_c}+\frac{2l_b}{\mu_r}\right)\frac{B_2}{\mu_0}=I_2-I_3 \tag{4.15}$$

to complete the system, we apply (4.13) to the paths between columns,

$$B_{12}=B_1\cdot\frac{A_l}{A_f} \tag{4.16a}$$

$$B_{23}=B_3\cdot\frac{A_l}{A_f} \tag{4.16b}$$

and to the singular spot where the three magnetic fluxes of the columns meet,

$$B_1\cdot A_l+B_2\cdot A_c+B_3\cdot A_l=0 \tag{4.16c}$$

Equation (4.16) can be substituted into (4.14) and (4.15). Together with (4.16c), a system of three linear equations with B_1, B_2 and B_3 (B-field for each column) is obtained,

$$\mathbf{A}\mathbf{x}=\mathbf{b}\longrightarrow\mathbf{x}=\mathbf{A}^{-1}\cdot\mathbf{b} \tag{4.17a}$$

$$\begin{cases} a_{11}=\dfrac{1}{\mu_0}\left[\dfrac{l_g}{\sigma_l}+\dfrac{2l_b}{\mu_r}+\dfrac{2l_a}{\mu_r}\dfrac{A_l}{A_f}\right] \\ a_{23}=a_{11} \\ a_{12}=\dfrac{l_g}{\sigma_c}+\dfrac{2l_b}{\mu_r} \\ a_{22}=a_{12} \end{cases} \tag{4.17b}$$

$$\mathbf{A}=\begin{bmatrix} a_{11} & a_{12} & 0 \\ 0 & a_{22} & a_{23} \\ A_l & A_c & A_l \end{bmatrix},\ \mathbf{x}=\begin{bmatrix} B_1 \\ B_2 \\ B_3 \end{bmatrix},\ \mathbf{b}=\begin{bmatrix} I_1-I_2 \\ I_2-I_3 \\ 0 \end{bmatrix} \tag{4.17c}$$

The B-field now is completely defined and solved with (4.17a). To fill the inductance matrix $\mathbf{L}$ of (4.18) for a three-column, single-turn magnetic component

we define the flux on each column j (ϕ_{ij}) and divide it by the current I_i that causes it, obtaining (4.19).

$$\mathbf{L}_t = \begin{bmatrix} L_{ll} & M_{lc} & M_{ll} \\ M_{lc} & L_{cc} & M_{lc} \\ M_{ll} & M_{lc} & L_{ll} \end{bmatrix} \tag{4.18}$$

$$L_{ll} = \left.\frac{\phi_1}{I_1}\right|_{\substack{I_2=0 \\ I_3=0}} \approx +\mu_0 \frac{A_l(A_c + A_l)}{l_g(2A_l + A_c)} \tag{4.19a}$$

$$L_{cc} = \left.\frac{\phi_2}{I_2}\right|_{\substack{I_1=0 \\ I_3=0}} \approx +\mu_0 \frac{2A_cA_l}{l_g(2A_l + A_c)} \tag{4.19b}$$

$$M_{ll} = \left.\frac{\phi_1}{I_3}\right|_{\substack{I_2=0 \\ I_3=0}} \approx -\mu_0 \frac{A_l^2}{l_g(2A_l + A_c)} \tag{4.19c}$$

$$M_{lc} = \left.\frac{\phi_1}{I_2}\right|_{\substack{I_1=0 \\ I_3=0}} \approx -\mu_0 \frac{A_cA_l}{l_g(2A_l + A_c)} \tag{4.19d}$$

This approximation represents the effect of an ideal magnetic core ($\mu_r \to +\infty$). The complete solution to (4.17a) can be solved to get $M_{lc} = M_{ll}$, for which the corrected area of the lateral column A_l^* is given by:

$$A_l^* = A_c \cdot \frac{A_f\left(2\frac{l_b}{\mu_c} + \frac{l_g}{\sigma_l}\right)}{A_f\left(2\frac{l_b}{\mu_c} + \frac{l_g}{\sigma_c}\right) - 2A_c\frac{l_a}{\mu_c}} \tag{4.20}$$

Note that, as all parameters are geometrical (non-negative), the fraction that multiplies is always lesser than one, indicating that A_l must always shrink. Also, a minimum air-gap length is required and can be extracted from nulling of the denominator in (4.20):

$$l_g \geq \sigma_c \cdot \frac{2}{\mu_r}\left(\frac{A_c}{A_f}l_a - l_b\right) \tag{4.21}$$

When (4.20) is satisfied, we can calculate the exact solution for (4.19):

$$L_{ll} = \left.\frac{\phi_1}{I_1}\right|_{\substack{I_2=0 \\ I_3=0 \\ A_l=A_l^*}} = +\mu_0 \frac{2}{3} \frac{A_c}{\frac{l_g}{\sigma_c} + \frac{2l_b}{\mu_c}} \tag{4.22a}$$

$$L_{cc} = \left.\frac{\phi_2}{I_2}\right|_{\substack{I_1=0 \\ I_3=0 \\ A_l=A_l^*}} = +\mu_0 \frac{2}{3} \frac{A_c}{\frac{l_g}{\sigma_c} + \frac{2l_b}{\mu_c}} \tag{4.22b}$$

$$M_{ll} = \left.\frac{\phi_1}{I_3}\right|_{\substack{I_2=0 \\ I_3=0 \\ A_l=A_l^*}} = -\mu_0 \frac{1}{3} \frac{A_c}{\frac{l_g}{\sigma_c} + \frac{2l_b}{\mu_c}} \tag{4.22c}$$

$$M_{lc} = \left.\frac{\phi_1}{I_2}\right|_{\substack{I_1=0\\ I_3=0\\ A_l=A_l^*}} = -\mu_0 \frac{1}{3} \frac{A_c}{\frac{l_g}{\sigma_c} + \frac{2l_b}{\mu_c}} \tag{4.22d}$$

4.2.3 Compensating the Fringing Effect

An accurate representation of the air-gap effect in the coupling of the windings is essential when designing the components. For such task, two correction factors were introduced previously into the analysis made in the present paper denoted by σ_l and σ_c for the lateral and central columns respectively.

In [214], a simplified method for calculating the reluctance of the air-gap was described based on the Schwarz-Christoffel transformation for infinitely long magnetic cores (2-D). A similar approach was taken in [215] were the afore-mentioned work is extrapolated into both directions of the cross-section of the air-gap.

For the three possible cases, the side view σ_{yk} is identical (type I), while for the front view σ_{xk} corresponds to the air-gap types I, II and III as shown in [215]. In the case of an EE core, the effective air gap in the central limb corresponds to:

$$\sigma_{xc} = \frac{a_c \cdot \pi}{a_c \cdot \pi + 2l_g \cdot \left(1 + \ln\left(\pi \frac{2l_b - a_f}{4l_g}\right)\right)} \tag{4.23a}$$

$$\sigma_{yc} = \frac{d \cdot \pi}{d \cdot \pi + 2l_g \cdot \left(1 + \ln\left(\pi \frac{2l_b + a_f}{4l_g}\right)\right)} \tag{4.23b}$$

$$\sigma_c = \sigma_{xc} \cdot \sigma_{yc} \tag{4.23c}$$

in the lateral columns:

$$\sigma_{xl} = \frac{a_l \cdot \pi}{a_l \cdot \pi + 2l_g \cdot \left(1 + \ln\left(\pi \frac{2l_b - a_f}{4l_g}\right)\right)} \tag{4.24a}$$

$$\sigma_{yl} = \frac{d \cdot \pi}{d \cdot \pi + 2l_g \cdot \left(1 + \ln\left(\pi \frac{2l_b + a_f}{4l_g}\right)\right)} \tag{4.24b}$$

$$\sigma_l = \sigma_{xl} \cdot \sigma_{yl} \tag{4.24c}$$

and for the case of the central column in an EI core:

$$\sigma_{xt} = \frac{a_c \cdot \pi}{a_c \cdot \pi + 4l_g \cdot \left(1 + \ln\left(\pi \frac{2l_b - a_f}{8l_g}\right)\right)} \tag{4.25a}$$

$$\sigma_{yt} = \frac{d \cdot \pi}{d \cdot \pi + 2l_g \cdot \left(1 + \ln\left(\pi \frac{2l_b + a_f}{4l_g}\right)\right)} \tag{4.25b}$$

Once compensated via eq. (4.20) and with $\sigma_t = \sigma_{xt} \cdot \sigma_{yt}$ from eq. (4.24c) and eq. (4.25b), fig. 4.7 shows the comparison between the self-inductances L_{lc} and L_{ll} and the mutual inductances M_{lc} and M_{ll} for the case shown in table 4.1 according to fig. 4.4 and sweeping the air-gap l_g, showing the predictive capability of the model.

Parameter	Value	Description
w_w	6.00 mm	Window width
w_h	4.10 mm	Window height
A_f/d	4.25 mm	Junction column width
A_c/d	4.25 mm	Central column width
A_l/d	4.60 mm	Lateral column width

Table 4.1: Three-column EI-core dimensions

The simulations were carried in Ansys Maxwell 3D with minimal track width to discard the effect of the inductance added by the windings. Even though the error between the compensated calculation case and the simulated for the same corrected column area has a difference over 16 % in relative terms, it does succeed in compensating the coupling obtaining $L_{ll} \approx L_{cc}$ and $M_{ll} \approx M_{lc}$, narrowing it down to under 3 % between each pair.

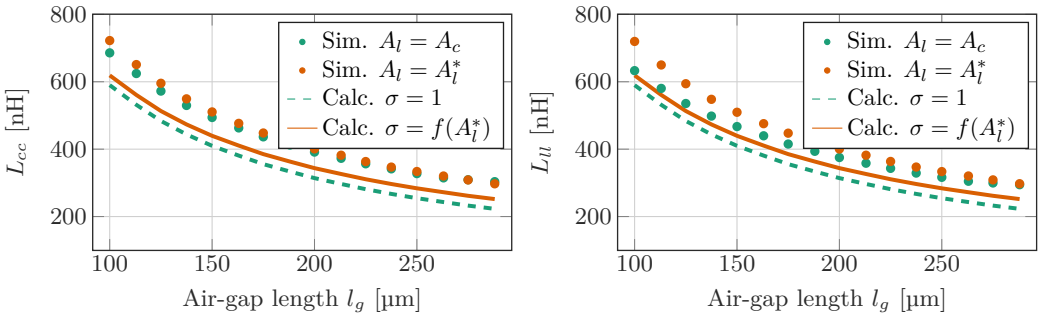

(a) Central self-inductance L_{cc}

(b) Lateral self-inductance L_{ll}

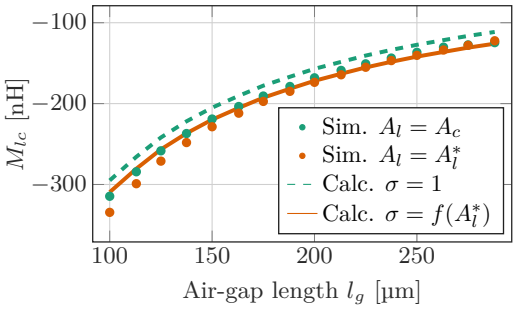

(c) Lateral-central M_{lc}

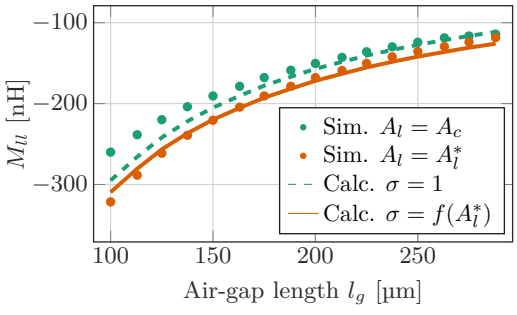

(d) Lateral-lateral M_{ll}

Figure 4.7: Comparison of the inductance matrix components calculated with (4.20) and the obtained in a magnetostatic Ansys simulation sweeping $A_l^* = f(l_g)$ and $A_l = A_c$.

CHAPTER 5

Wye-Delta Three-Phase LLC Converters

> If you can't measure it,
> you can't improve it.
>
> — Peter Drucker

Without clear metrics, it becomes impossible to ensure that efforts are effective, and how to adjust them for better results. For this purpose, previous chapters have provided a comprehensive examination of the design and theoretical analysis of three-phase LLC resonant converters, focusing on their operating principles, modulation strategies, and expected performance characteristics.

With the design phase now complete, the focus shifts to their practical implementation and experimental iteration in hardware. This involves, not only the physical assembly and validation of the power stage, but also the development of the different components including magnetics, PCB layout, thermal management, and overall system miniaturisation. Each of these aspects is critical for achieving the desired performance targets and ensuring reliable operation. The implementation process further serves to uncover the practical challenges in the converter development.

5.1 Optimisation of Magnetic Components

5.1.1 Magnetic Materials at 1 MHz

At switching frequencies around 1 MHz, the volumetric energy density of magnetic components emerges as a key constraint in the miniaturisation and efficiency of power electronic converters. Inductors and transformers typically rely on ferrite or powdered metal cores, which, despite their effectiveness in storing and transferring magnetic energy, offer comparatively low energy densities relative to other passive elements. This limitation originates mainly from the frequency-dependent nature of

core losses, which restrict both the maximum usable flux density and the achievable operating frequency.

Consequently, the design of magnetic components requires careful trade-offs among inductance value, core size, saturation limits, and AC loss characteristics. While advancements in materials and core geometries have enabled progress in high-frequency operation and improved thermal behaviour, magnetics still account for a significant portion of the overall volume in compact power converters.

Magnetic core materials for application below the 1 MHz switching frequency have been well-established for many years, being the most popular TDK's N49, N95. Recent developments in commercial Mn-Zn ferrites have shown that low-temperature sintering, when combined with carefully tailored additives, can produce fine-grain, high-density materials [211]. These materials are specifically optimised for the critical 0.5-2 MHz range in power applications, where both low core loss and reliable thermal performance are essential. A series of plots with the volumetric core losses of three different materials (Hitachi's ML91S [211], DMEGC's DMR51W [216], and TDG's TP5H [217]) is shown in fig. 5.1 for reference, though there are more such as Ferroxcube's 3F46 or the TDK's N49.

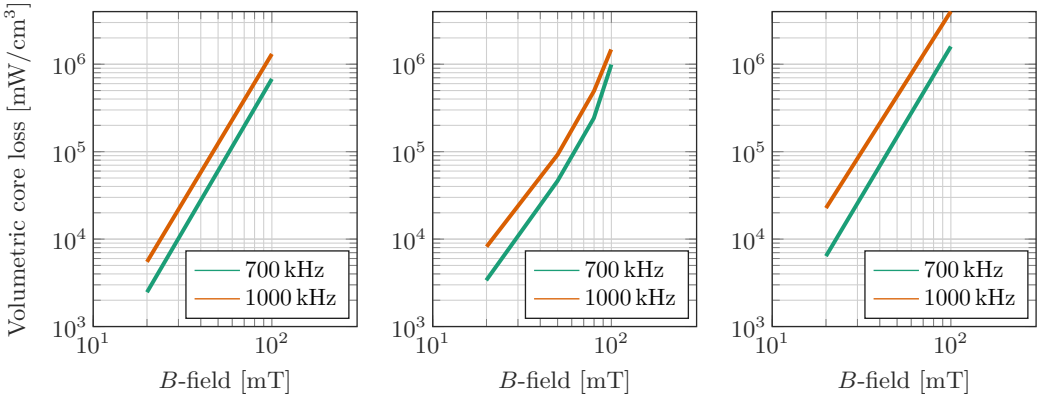

(a) Hitachi's ML91S (b) DMEGC's DMR51W (c) TDG's TP5H

Figure 5.1: Volumetric core losses of different soft ferrite magnetic materials (Mn-Zn) in the 1 MHz switching operation under sinusoidal excitation.

As the magnetic core needs to be customised (to compensate for the magnetic coupling), due to the constraints in manufacturing geometries, cost and manufacturing time, the TDG's TP5H was the material of choice, even being the most lossy of the three (three times as much as the ML91S and five times as much as the DMEGC DMR51W).

Either way, volumetric losses shown in fig. 5.1 is only for sinusoidal excitation. From considerations of accuracy, the Improved Generalised Steinmetz Equation (IGSE) is generally used to estimate core losses, as it accommodates non-sinusoidal flux waveforms, where, from the Steinmetz Equation:

$$P_V = k \cdot f^{\alpha} \hat{B}^{\beta} \tag{5.1}$$

the IGSE for non-sinusoidal operation is given by:

$$P_V = \frac{1}{T_S} \int_0^{T_S} k_i \left| \frac{\mathrm{d}B}{\mathrm{d}t} \right|^{\alpha} \cdot \Delta B^{\beta-\alpha} \, \mathrm{d}t \tag{5.2}$$

with k_i given by the integral:

$$k_i = \frac{k}{(2\pi)^{\alpha-1} \int_0^{2\pi} |\cos(\theta)|^{\alpha} \cdot 2^{\beta-\alpha} \, \mathrm{d}\theta} \tag{5.3}$$

Nonetheless, to better represent the core losses, measurements at different excitations were performed with the setup from [218] for sinusoidal excitation (fig. 5.2) being the case of the resonant current, as well as for the trapezoidal excitation (fig. 5.3), which is the magnetising flux waveform for the case of the transformer.

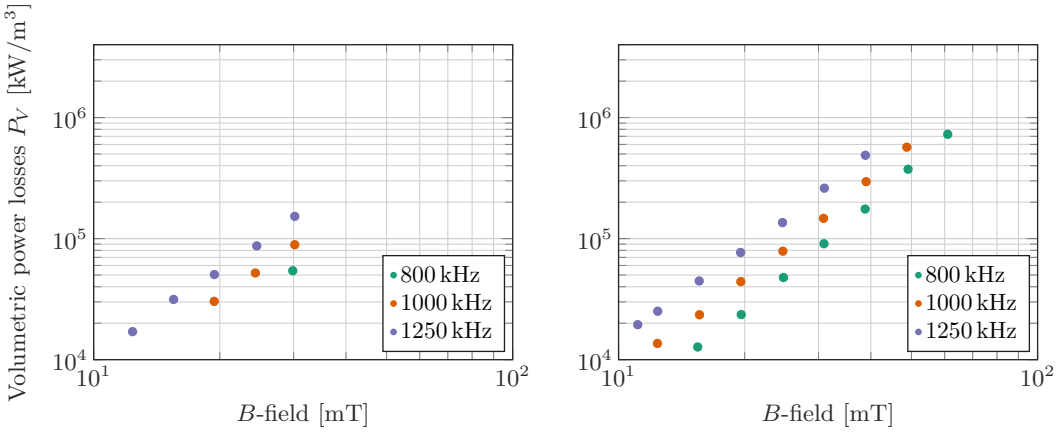

(a) TDK's 3F46 (b) TDG's TP5H

Figure 5.2: Experimental core losses for the TDK's 3F46 and TDG's TP5H under a trapezoidal B-field excitation at 90 °C [218].

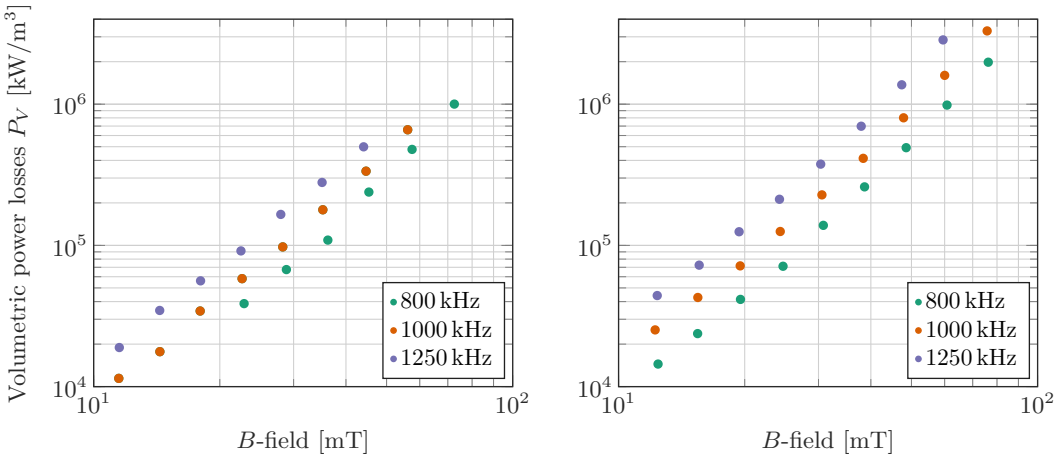

(a) TDK's 3F46 (b) TDG's TP5H

Figure 5.3: Experimental core losses for the TDK's 3F46 and TDG's TP5H under a trapezoidal B-field excitation at 90 °C [218].

5.1.2 Pareto-Front Optimal

The design is carried out based on the target specifications discussed in section 3.1. In section 4.2, a three-port magnetic core was analysed, demonstrating that it enables the integration of three single-phase magnetics (inductor and transformer) into a single three-phase magnetic structure.

In this section, the optimisation of the inductor and transformer for both topologies analysed in section 3.3 is carried out. An EI-core was taken as reference to calculate the main design parameter of a three-phase planar transformer, this is because an EE-core and an EI-core are equivalent, allowing to use the same equation by making the equivalence and choosing the appropiate fringing correction factors, for the central column (EE core).

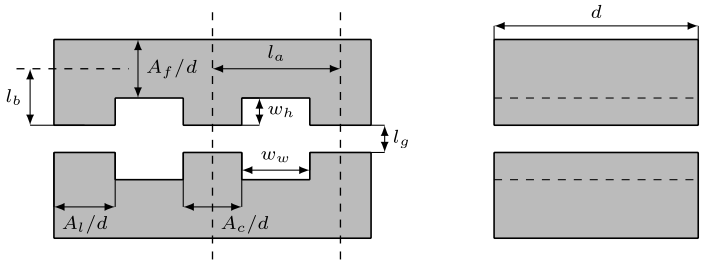

(a) Front view (b) Side view

Figure 5.4: EE-core dimensioning

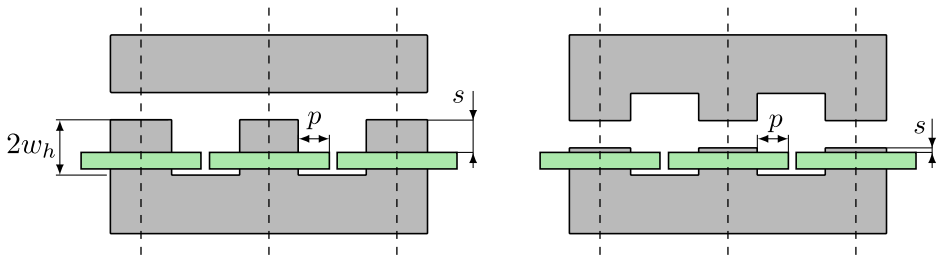

(a) EI-core (b) EE-core

Figure 5.5: Extra design space parameters of the design.

Design Space Parameters

Due to the highly constrained design space, all optimisations have been carried out using a brute-force approach. In these cases, the constraints tend to simplify the optimisation problem rather than complicate it, as less degrees of freedom are allowed. The mandatory constraints of the design are:

- **Central column shrinkage:** eq. (4.20) defines the relationship between the lateral and central columns as a function of l_g.
- **Thermal dissipation capability:** This constraint defines the maximum permissible B-field in the column, based on the core power losses. Estimation

is non-trivial, as it requires accurate models (typically simulations) validated against experimental results. A reasonable starting point for planar magnetics with forced air convection is $300\,\mathrm{mW/cm^3}$ [110].

- **Inductance:** The air-gap is determined by eq. (4.19d), and later compensated by the lateral column compensation in eq. (4.20) bounded by the maximum air-gap given in eq. (4.21).
- **Width of the prototype:** As the converter is set for limits in width, a geometrical constrained is added into the designing of the core and winding sets.

From the previously defined geometry of the custom magnetic core (fig. 4.4), displayed again in fig. 5.4 for clarity, it can be shown that the design has six degrees of freedom. Each parameter influences the implementation differently, resulting in a complex trade-off:

- **Depth of the core** d: A deeper core makes longer windings through the window but shortens the columns.
- **Width of the window** w_w: A wider window allows for wider windings (reducing R_{DC}) and generally mitigates fringing effects. However, it also increases the footprint (without any advantage) and core losses.
- **Height of the window** $2w_h$: With a minimum height determined by the thickness of a PCB winding (typically 1.6 mm), this dimension allows windings to be positioned further away from the air-gap. This is particularly beneficial for large air-gaps, where fringing-induced losses become more significant, but it also results in thinner column bridges, stretching the size of the converter.
- **Area of the central column** $A_c = a_c \cdot d$: This is primarily determined by the air-gap length, as it sets both the inductance and the thermal constraints.
- **Area of the lateral column** $A_l = a_l \cdot d$: Governed by the compensation requirement discussed in eq. (4.20). In general, increasing the air-gap length enables greater utilisation of the material, as $A_l > A_c$.
- **Air-gap length** l_g: This directly controls the inductance and it is a source of fringing fields. It should therefore be kept as short as possible.

With six degrees of freedom and four fixed constraints, the remaining parameters from fig. 5.4, along with the additional parameter for the winding in fig. 5.5, are swept during optimisation:

- **Air-gap proximity to the windings** s: Shorter windows increase winding losses due to the fringing field from the gap, whereas increasing s requires a deeper core, which proportionally lengthens the windings and increases winding losses.
- **Air-gap** l_g: Discretised according to the available air-gap spacers.
- **Width of the window** w_w.

Transformer Winding Strategy

At high-frequency, skin and proximity effects contribute significantly in the power loss distribution, particularly in regions with strong magnetic fields, such as those near the air-gap. A distributed air-gap can help reduce localised fringing flux, but due to the mechanical constraints, cost of manufacturing (low-profile magnetics) and increased manufacturing complexity, single air-gaps are analysed in this work. Alternatively, simply placing the conductors further from the air-gap for example, using an EI-core instead of an EE-core can significantly reduce fringing fields and, consequently, winding losses.

For interleaving, the usual approach is to divide the secondary winding into n_p parts, which equalises the current and compensates for the increased H-field generated by the primary turns. However, the asymmetry of this arrangement makes the winding more susceptible to external magnetic fields. This can be mitigated by splitting the secondary into $n_p - 1$ parts instead.

To prevent fringing field interference with the windings, the EI-core structure is advantageous, as its geometry allows for a greater distance between the conductors and the air-gap. In this case, the design space can be reduced to three main parameters: the air-gap length l_g, the spacing between the air-gap and the winding s, and the winding width p.

Although an initial approximation can be obtained for foil conductors (PCB tracks) with analytical equations [106], fringing losses play a big role in the optimization of the winding losses. Efforts in the fringing power losses estimation are discussed in the literature for planar magnetics [108]. Nonetheless, the highest accuracy is returned by Finite Element Method (FEM) simulations.

When comparing different interleaving strategies, results show that the PSPSP-SPSP arrangement performs better as the fringing effect becomes more pronounced within the winding window (i.e., as the influence of the air-gap increases).

In planar magnetic cores in high-frequency applications, solid wire solutions become inconvenient as the current stress required in the windings increases in amplitude and harmonic content. The skin effect alone makes the maximum wire diameter to be AWG36 at 1 MHz (127 µm in diameter), requiring a high number of wires in parallel leading into higher proximity and worsening the termination effect [219].

Although Litz wire is a good solution due to its performance at high-frequency, it compromises the economic viability of the converter. PCB windings are less expensive, easily customizable and ideal to create interleaving structures within the winding. For the converter presented, a 5:1 windings turns ratio for the transformer has to be implemented, for which PCB windings are chosen.

In order to make interleaving, the secondary turn is split into five to obtain the same current density. Nonetheless, due to the asymmetry of this arrangement, this makes it more susceptible to external fields. Instead, the secondary can be split into four leaving two primary turns enveloping with the top and bottom layers the rest of the winding turns in the PCB.

With high-frequency currents, skin and proximity effects contribution gain weight in the power losses breakdown. This is especially important in regions of strong magnetic fields (proximity to the air-gap). A set of simulations were run varying the air-gap with a fringing effect close to the top layer of the PCB. This is made for two strategies (PSPSPSPSPS and PSPSPSPSP) defining the order of the primary (P) and secondary (S) layers. The result depends heavily on the size of the gap and the distance from the winding to it as shown in fig. 5.7, where the frontier between the two strategies is highlighted. A more detailed example is shown in fig. 5.6, where the two strategies are compared varying the air-gap length.

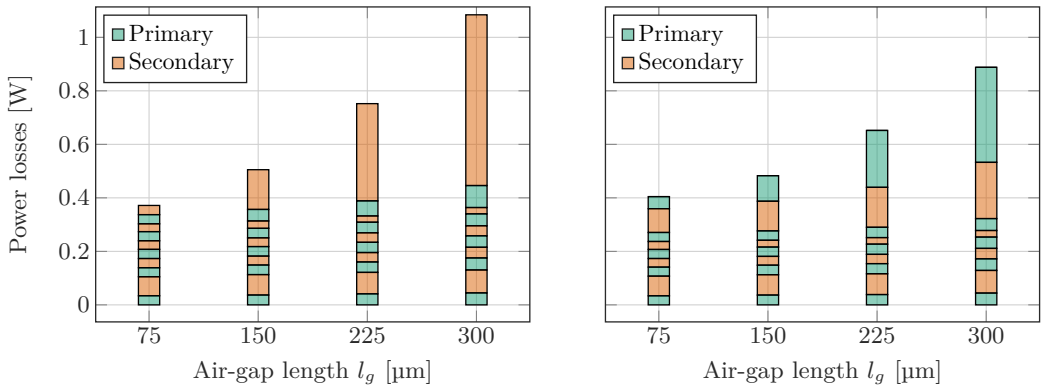

(a) PSPSPSPSPS (b) PSPSPSPSP

Figure 5.6: Winding losses for the same EE-core depending on the winding strategy at 1 MHz. The bar stack represents the layers of the PCB. The simulations has been performed in Ansys Maxwell 3D.

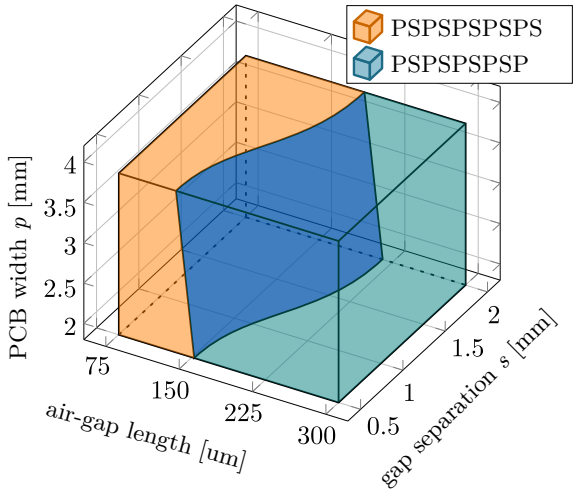

Figure 5.7: Optimal interleaving winding strategy design space for the transformer for the case of the inverter in parallel. The simulations has been performed in Ansys Maxwell 3D.

Pareto-Optimal Magnetic Designs

With the parameters previously discussed, the design space is optimised. The optimisation is performed with Ansys Maxwell 3D for both the topology with the inverter in parallel (fig. 5.8) and in stack (fig. 5.9).

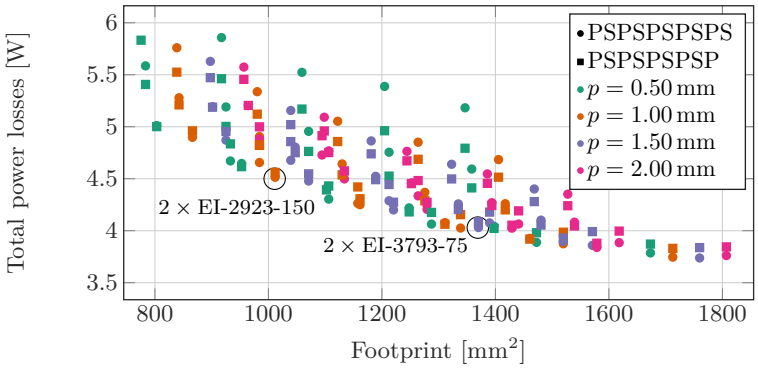

(a) Transformer pareto front

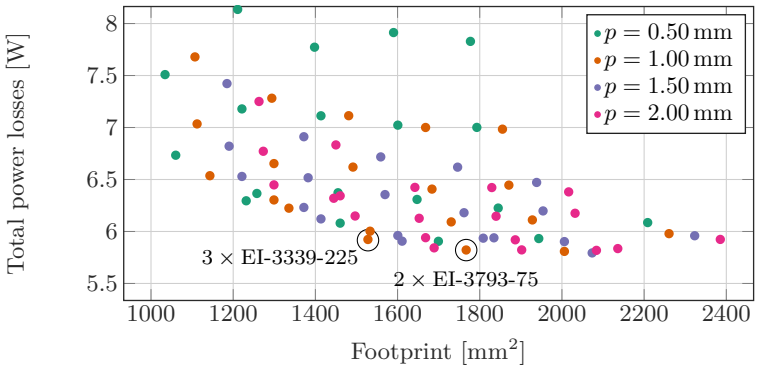

(b) Inductor pareto front

Figure 5.8: Pareto-front of the three-phase inductor and three-phase transformer with an EE-core (inverter in parallel). The highlighted solutions are selected for later experimental validation. The simulations has been performed in Ansys Maxwell 3D.

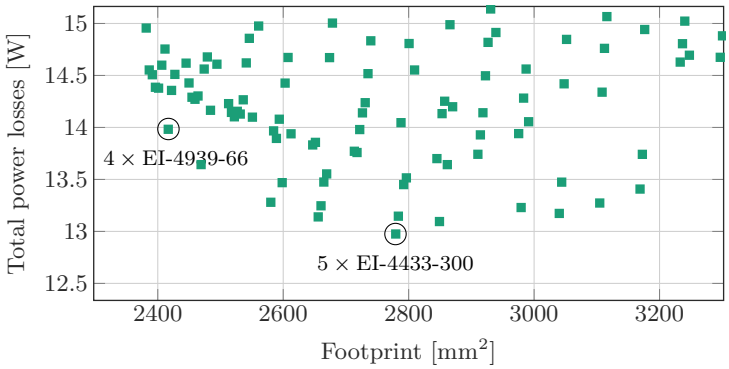

Figure 5.9: Pareto-front of the three-phase inductor and three-phase transformer with an EE-core (inverter in stack). The highlighted solutions are selected for later experimental validation. The simulations has been performed in Ansys Maxwell 3D.

5.1.3 Validating the Magnetic Link

To validate experimentally the analysis of the magnetic modelling chapter, in particular in section 4.2.2, where a compensated geometry was proposed, we need to verify that the lateral-to-lateral M_{ll} and lateral-to-central M_{lc} couplings are equivalent. For this, the process is illustrated in fig. 5.10: the self-inductance is straightforward, as each winding j only needs to be excited by a sinusoidal current i_x and measure the potential u_x as shown in fig. 5.10a, obtaining the main diagonal of the inductance matrix $\mathbf{L}$; the mutual inductances require to know the self-inductances beforehand as now two windings are connected in series as exemplified in fig. 5.10b with windings 1 and 2, note that $i_1 = i_2 = i_x$ and $u_1 + u_2 = u_x$, so we can derive it from the definition of $\mathbf{L}$:

$$\mathbf{U} = \begin{bmatrix} u_1 \\ u_2 \end{bmatrix} = \mathbf{L} \cdot \dot{\mathbf{I}} = \begin{bmatrix} L_{11} & M_{12} \\ M_{21} & L_{22} \end{bmatrix} \cdot \begin{bmatrix} \dot{i}_1 \\ \dot{i}_2 \end{bmatrix} = \begin{bmatrix} L_{11} & M_{12} \\ m_{21} & L_{22} \end{bmatrix} \cdot \begin{bmatrix} \dot{i}_x \\ \dot{i}_x \end{bmatrix} = \begin{bmatrix} L_{11} \cdot \dot{i}_x + M_{12} \cdot \dot{i}_x \\ M_{21} \cdot \dot{i}_x + L_{22} \cdot \dot{i}_x \end{bmatrix} \tag{5.4a}$$

$$u_x = u_1 + u_2 = (L_{11} + L_{22} + 2M_{12}) \cdot \dot{i}_x \tag{5.4b}$$

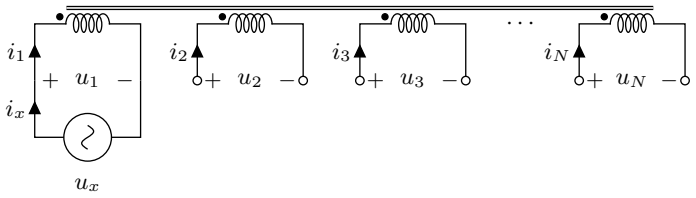

(a) Self-inductance of winding 1

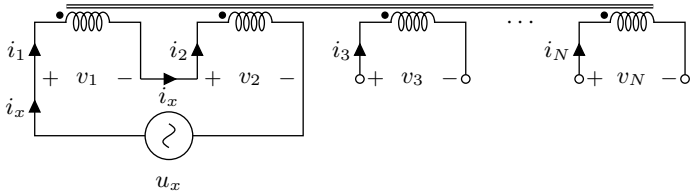

(b) Mutual inductance of windings 1 and 2

Figure 5.10: Example that illustrates how to measure self-inductances and mutual inductances for windings coupled together in the same lumped model.

Having to switch between different windings constantly is inconvenient, thus, the accessory shown in fig. 5.11 was built so that the Device under Test (DuT) is soldered once onto a small daughterboard that plugs into a motherboard, avoiding repeated solder and desolder cycles and guaranteeing a repeatable mechanical reference.

The measurement protocol consisted of a calibration of the impedance analyser E4990A from Keysight [220], followed by a second calibration consisting on short-circuiting each windings in the accessory to obtain the reference of each connection. Then, the measurement procedure is started by reconfiguring the connections of the accessory. In order to extract accurate measurements, all measurements were performed at 1 MHz.

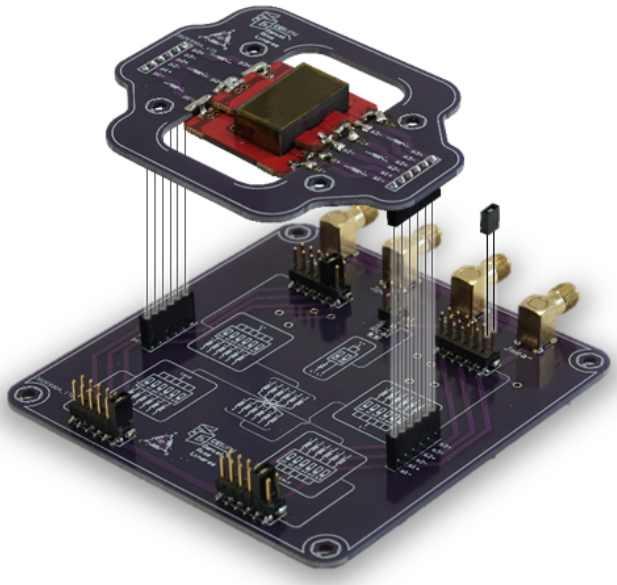

Figure 5.11: Custom-made experimental platform for small-signal impedance analysis compatible with the E4990A.

Table 5.1 reports the extracted inductance matrices for the geometries chosen from the Pareto-front optimal cores performed in section 5.1.2 with a single core part in parallel and a single turn. The calculation of the relative error $\Delta\mathbf{L}$ was evaluated as the relative difference of each term with the mean value of the upper and lower diagonals of the $\mathbf{L}$ matrix (mutual inductances),

$$\Delta\mathbf{L}_{ij} = \frac{\mathbf{L}_{ij} - \sum_{j\neq k}\mathbf{L}_{i'j'}}{\sum_{j\neq k}\mathbf{L}_{i'j'}}, \quad \forall i \neq j \tag{5.5a}$$

and, similarly, for the main diagonal (self-inductances),

$$\Delta\mathbf{L}_{ij} = \frac{\mathbf{L}_{ij} - \sum_{j=k}\mathbf{L}_{i'j'}}{\sum_{j=k}\mathbf{L}_{i'j'}}, \quad \forall i = j \tag{5.5b}$$

The compensation is consistent with the analytical prediction in section 4.2 as shown in the $\Delta\mathbf{L}$ column of table 5.1. The residual asymmetry is attributed to parasitic capacitances and gap-spacer tolerances[1].

The construction of an uncompensated magnetic core with equal column width (EE-2270-150) was made to prove the need for the compensation proposed. As expected, the core exhibits a clear unbalance with a maximum of $|\Delta\mathbf{L}| = 17\,\%$ with the ideal target. By contrast, the constructed compensated EI variants have a median value of less than 1 % with the highest error of around 7 % for the smallest air-gap length case.

[1]The discrete gap-spacers used were measured to be 25 µm, 70 µm and 100 µm.

Geometry [mm]	Photography	Air-gap	**L** [nH]	**ΔL** [%]
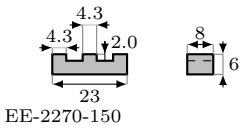 EE-2270-150		150 µm	$\begin{bmatrix} 522 & 292 & 219 \\ 293 & 585 & 285 \\ 220 & 285 & 508 \end{bmatrix}$	$\begin{bmatrix} -3.0 & +10 & -18 \\ +10 & +8.7 & +7.4 \\ -17 & +7.2 & -5.6 \end{bmatrix}$
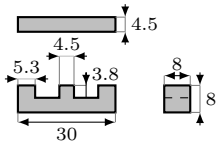 EI-2923-150		150 µm	$\begin{bmatrix} 172 & 63 & 64 \\ 64 & 172 & 63 \\ 65 & 63 & 170 \end{bmatrix}$	$\begin{bmatrix} +0.3 & -0.6 & +0.4 \\ 0.0 & +0.6 & -1.1 \\ +2.0 & -0.6 & -0.9 \end{bmatrix}$
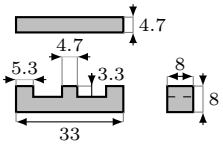 EI-3339-225	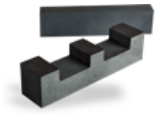	225 µm	$\begin{bmatrix} 240 & 106 & 100 \\ 106 & 242 & 109 \\ 101 & 109 & 238 \end{bmatrix}$	$\begin{bmatrix} +0.2 & +0.9 & -5.0 \\ +1.1 & +0.7 & +3.6 \\ -4.2 & +3.6 & -0.8 \end{bmatrix}$
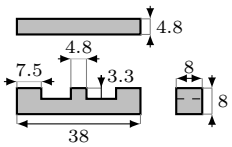 EI-3793-75	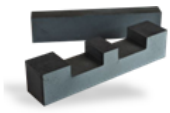	75 µm	$\begin{bmatrix} 170 & 66 & 63 \\ 68 & 172 & 66 \\ 64 & 67 & 170 \end{bmatrix}$	$\begin{bmatrix} -0.3 & +1.3 & -4.4 \\ +3.0 & +0.6 & +1.0 \\ -2.7 & +1.6 & -0.3 \end{bmatrix}$
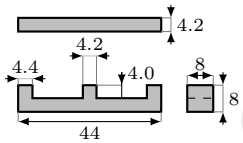 EI-4433-300		300 µm	$\begin{bmatrix} 185 & 76 & 74 \\ 77 & 193 & 80 \\ 75 & 81 & 186 \end{bmatrix}$	$\begin{bmatrix} -1.6 & -1.5 & -4.1 \\ -0.2 & +2.7 & +3.7 \\ -2.8 & +5 & -1.1 \end{bmatrix}$
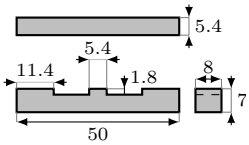 EI-4939-66	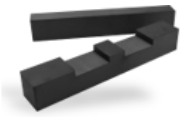	66 µm	$\begin{bmatrix} 258 & 116 & 128 \\ 117 & 247 & 126 \\ 130 & 127 & 262 \end{bmatrix}$	$\begin{bmatrix} -1.6 & +0.4 & -7.5 \\ +1.8 & +2.7 & +5.7 \\ -7.5 & +7.0 & -1.1 \end{bmatrix}$

Table 5.1: Measurement results obtained at 1 MHz using the experimental hardware analyser and the custom accessory shown in fig. 5.11 for a single core, single turn. The measurement hardware platform was manually calibrated.

In simulation, geometric compensation in the proposed three-phase magnetics reduced mutual-inductance unbalance to 3 %. This sets the design expectation for balanced operation, in hardware, residual mismatch once compensated typically fall within the 5 % to 7 %, with many measurements under the 5 %.

Note that these measurements were performed with single-turn windings made from very thin conductors to minimize the wire self-inductance. The following subsection experimentally validates the geometric compensation on a practical inductor and quantifies how the resulting percentage errors propagate to the current unbalance, using the same inductor later employed for the full power converter tests.

5.1.4 Effect of the Geometry Compensation

With the help of an impedance analyzer, the **L** matrix was measured for both the transformers and inductors obtaining an error not greater than a 5 %, being the sensitivity of the μ_c of the material, the windings parasitic capacitances, and the tolerance of the air-gap the sources subject to uncertainty.

The experimental inductance matrices **L** where measured with the accessory in fig. 5.11, for the case of the parallel prototype:

$$\mathbf{L}_{T_x} = \begin{bmatrix} 12.90 & 2.56 & 7.00 & -1.44 & 5.16 & -1.07 \\ 2.55 & 0.52 & -1.43 & 0.29 & -1.06 & 0.22 \\ 7.00 & -1.43 & 14.56 & 2.88 & 6.80 & -1.40 \\ -1.44 & 0.29 & 2.88 & 0.59 & -1.40 & 0.29 \\ 5.15 & -1.06 & 6.80 & -1.40 & 12.68 & 2.50 \\ -1.07 & 0.22 & -1.40 & 0.28 & 2.50 & 0.51 \end{bmatrix} \mu\text{H} \tag{5.6a}$$

$$\mathbf{L}_{L_r} = \begin{bmatrix} 5.85 & -2.50 & -2.31 \\ -2.49 & 5.81 & -2.53 \\ -2.31 & -2.53 & 5.93 \end{bmatrix} \mu\text{H} \tag{5.6b}$$

Based on the data in eq. (5.8a), we can calculate the coupling factor of each of the individual phases coupling factors by extracting 2×2 matrices between each primary and secondary, first for the version with inverter legs in parallel (fig. 5.12):

$$\mathbf{L}_{AA} = \begin{bmatrix} 12.90 & 2.56 \\ 2.55 & 0.52 \end{bmatrix} \mu\text{H} \longrightarrow k_A = \frac{2.56}{\sqrt{12.90 \cdot 0.52}} = 0.988 \tag{5.7a}$$

$$\mathbf{L}_{BB} = \begin{bmatrix} 14.56 & 2.88 \\ 2.88 & 0.59 \end{bmatrix} \mu\text{H} \longrightarrow k_B = \frac{2.88}{\sqrt{14.56 \cdot 0.59}} = 0.983 \tag{5.7b}$$

$$\mathbf{L}_{CC} = \begin{bmatrix} 12.68 & 2.50 \\ 2.50 & 0.51 \end{bmatrix} \mu\text{H} \longrightarrow k_C = \frac{2.50}{\sqrt{12.68 \cdot 0.51}} = 0.988 \tag{5.7c}$$

and also for the inverter cells in stack:

$$\mathbf{L}_{T_x} = \begin{bmatrix} 1668 & 1110 & 686 & -456 & 668 & -444 \\ 1110 & 737 & -460 & 301 & -442 & 296 \\ 690 & -464 & 1739 & 1160 & 717 & -483 \\ -462 & 312 & 1156 & 776 & -483 & 322 \\ 674 & -449 & 729 & -490 & 1671 & 1119 \\ -451 & 304 & -483 & 324 & 1118 & 747 \end{bmatrix} \text{nH} \tag{5.8a}$$

$$\mathbf{L}_{L_r} = \begin{bmatrix} 1851 & -764 & -737 \\ -767 & 1931 & -799 \\ -754 & -812 & 1861 \end{bmatrix} \text{nH} \tag{5.8b}$$

Both the inductor and the transformer were integrated into a proof-of-concept inverter and rectifier, as will be shown later in section 5.4. When the switches are operated as previously described (fig. 3.13), the resulting three-phase currents satisfy the neutral connection condition ($i_A + i_B + i_C = 0$).

The experimental response in fig. 5.13b matches expectations: the three currents are piecewise sinusoidal, and the three phases are identical except for a 120° phase shift. In contrast, when a non-compensated structure is tested, the waveforms become sinusoidal, but the 120° phase separation is lost and the amplitudes are unequal (see fig. 5.13a). The prototype was constructed using the EE-2270-150 magnetic core shown in table 5.1, wound with sufficient turns to resonate at 1 MHz, resulting in a max $(|\Delta\mathbf{L}|) < 17\,\%$ of error.

(a) Transformer (2 × EI-3793-75) (b) Inductor (3 × EI-3339-225)

Figure 5.12: Prototyped inductor and transformer for the wye-delta three-phase LLC converter with inverter legs in parallel.

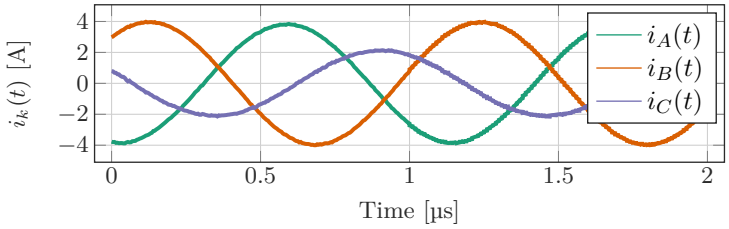

(a) Uncompensated inductor and transformer with the three legs equal with a maximum error of max $(|\Delta\mathbf{L}|) < 17\,\%$

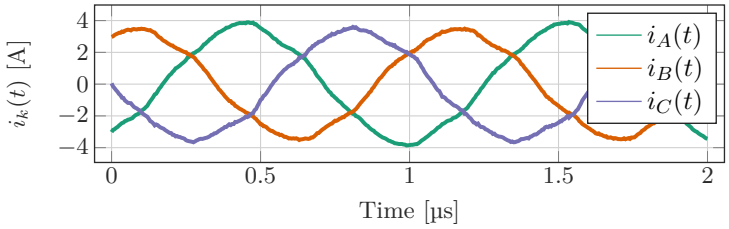

(b) Compensated inductor and transformer manufactured according to eq. (4.20) with a maximum error of max $(|\Delta\mathbf{L}|) < 5\,\%$

Figure 5.13: Effect of the geometric compensation in the magnetics in the inductor currents (nominal voltage conditions: 270 V to 28 V, and 730 W of output power).

This effect is more pronounced in the inductor, since the transformer is forced by the synchronous rectifier. Experimentally, only a minor influence was observed on the transformer behaviour.

With the compensated magnetic structure fig. 5.14b, temperatures are not only even but also lower. As shown in fig. 5.14a, the temperature is uneven in the windings, reaching 64 °C in phase A and down to 50 °C, this is confirmed by the current waveforms as the peak of the current in that phase is lower than in the other two. Moreover, as ZVS is lost, the temperature of the transistors is higher than in the case of compensated

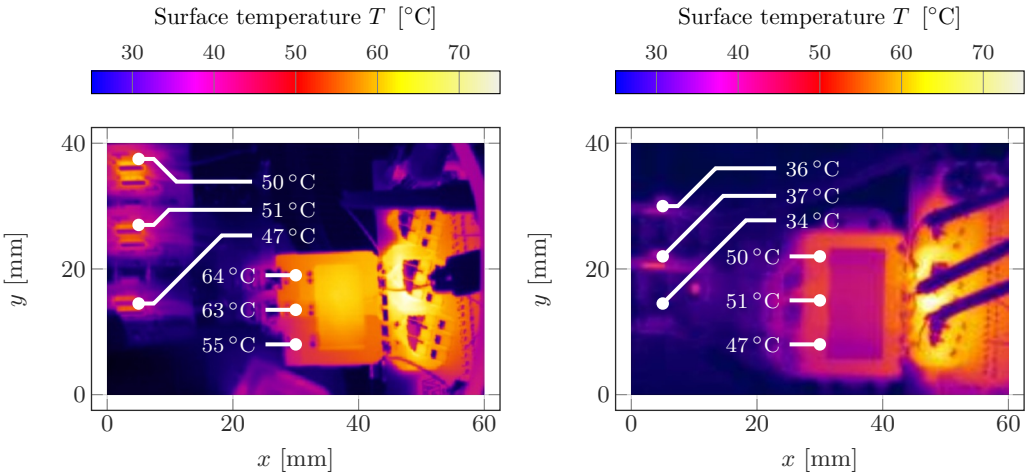

(a) Non-compensated structure

(b) Compensated structure

Figure 5.14: Effect of the geometric compensation in the magnetics in the thermal response of the converter (nominal voltage conditions: 270 V to 28 V, and 730 W of output power).

5.2 Semiconductor Selection

The three-phase LLC in this work targets 1 MHz switching to compress magnetics and passive energy. At these frequencies, any frequency-related mechanisms (input and output parasitic capacitances, reverse recoveries, package parasitics...) dominate over pure conduction ($R_{DS(on)}$). This tends to favour WBG devices when choosing devices for both the inverter and rectifier.

Calculating the switching losses in Si and even SiC devices is straightforward and a lot of literature exist in that matter [221], although some models also exist for GaN [116], their accuracy is low as the assumptions do not match reality. This is complicated even more due to the variable switching frequency nature of the converter and the varying current during the switcing cycle.

5.2.1 Inverter Transistors

For the inverter transistors, 650 V enhancement-mode GaN HEMTs were chosen for the three-phase inverter as the inverter operates in the range of 1 MHz of switching

frequency, driving more by switching terms than by $R_{DS(on)}I^2$. The key advantages that made GaN the winner are:

- **Very low gate charge and drive loss.** Driver dissipation scales as $P_{dr} = Q_G \cdot V_{dr} \cdot f_S$, and nowadays typical GaN is a few tens (typically 1 nC to 20 nC at 5 V), which is an order of magnitude below comparable Si MOSFETS (typically 100 nC to 300 nC at 10 V).
- **Zero reverse recovery charge ($Q_{rr} \approx 0$).** The LLC operates largely under ZVS on the primary, yet commutation still processes the devices' body diode charge. GaN removes this penalty and widens the ZVS window, requiring less magnetising current needed to guarantee soft-switching, reducing circulating energy and core/copper losses in the magnetic link.
- **Lower C_{oss} energy and faster transitions.** The energy E_{oss} and the high f tail of $C_{oss}(V_{DS,max})$ dominate turn-on and turn-off overlap at 1 MHz. GaN devices exhibit small E_{oss} and package inductance, allowing short dead-times (5 ns to 20 ns) and minimizing circulating current.
- **Package parasitics.** The inverter loop inductance sets the over/undershoot and ringing. Low-inductance GaN packages (no wire bonds, short source loops) are critical at 1 MHz where even 0.5 nH to 1 nH changes the commutation dynamics.

Picture	Manufacturer's part name	Breakdown voltage [V]	On-resistance $R_{DS(on)}$ [Ω]	Power losses [W]	Package	Ref.
	GS66506T (GaN Systems)	650 V	67 mΩ	2.55 W 3.99 W 0.12 W	GaNPX 5 × 7 mm	[222]
	GS66508T (GaN Systems)	650 V	50 mΩ	1.72 W 5.35 W 0.18 W	GaNPX 4 × 5 mm	[223]
	EPC2308 (EPC Co.)	150 V	6.0 mΩ	3.52 W 3.40 W 0.35 W	QFN 3 × 5 mm	[224]
	EPC2307 (EPC Co.)	200 V	10.0 mΩ	5.68 W 2.50 W 0.30 W	QFN 3 × 5 mm	[225]

Table 5.2: Comparison of transistors for the inverter, the losses were calculated for full power at 100 °C and are displayed as total in the rectifier (from top to bottom: conduction, switching and driving losses).

As with the inductor and transformer, the choice of semiconductor devices for the inverter stage was guided by the specific requirements of the two proposed configurations for the inverter: with legs in parallel (classical) and with three cells in stack. To make a more informed decision and from the table table 5.2, the thermal-cost FoM from fig. 5.15 is employed. This results in the initial choice of the

GS66508T from GaN Systems for a proof-of-concept, but eventually substituted in the miniaturisation by the GS66506T, also from GaN Systems due to its reduced size. For the stacked-cell configuration, the EPC2308 from EPC Co. was adopted due to its compact package and low parasitics making it ideal for this operation, contributing to the miniaturisation and high power density targets of the topology.

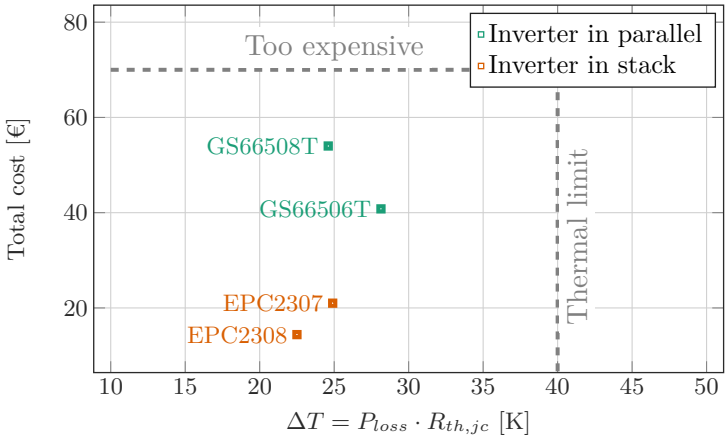

Figure 5.15: Comparison of high-voltage side transistors (inverter) for both configurations (legs in parallel and cells in stack) compared with a thermal-cost FoM

In fig. 5.16, the family of 650 V from the Infineon (formerly GaN Systems) is shown, including the internal die structure [226, 227], notice how for the GS66502B, GS66504B, GS66506T, and GS66508T, the structure is equivalent to parallelising die units, matching the on-resistance, making it easy to estimate the switching power losses once it is known for one of the cases. In [228], the GS66508T was thoroughly tested, allowing to fill the data in table 5.2.

(a) GS66502B 2 die units 200 mΩ

(b) GS66504B 4 die units 100 mΩ

(c) GS66506T 6 die units 67 mΩ

(d) GS66508T 8 die units 50 mΩ

(e) GS66516T 6 die units 25 mΩ

Figure 5.16: Die units of the 650 V line of Infineon (formerly GaN Systems) [226, 227]

Ensuring ZVS in the Inverter

When designing converters very tightly specified for minimised energy in the passives, the current during the switching transient can be vary considerably. This time-dependance in the current waveform is particularly pronounced when the transistor speed is comparable with the switching period, as to meet the ZVS condition, constant switching current cannot be considered.

An initial approximation (fig. 5.17) in this regard is a linear switching current, denoted as $I_{SW}(t)$ and reducing the problem to two variables: the initial current $I_{SW}(0)$, and the slope at the zero-current crossing $\omega\hat{I}_{SW}$ given by the zero-crossing first derivative of a sinusoidal current of amplitude $\hat{I}_{SW}$ at a frequency ω.

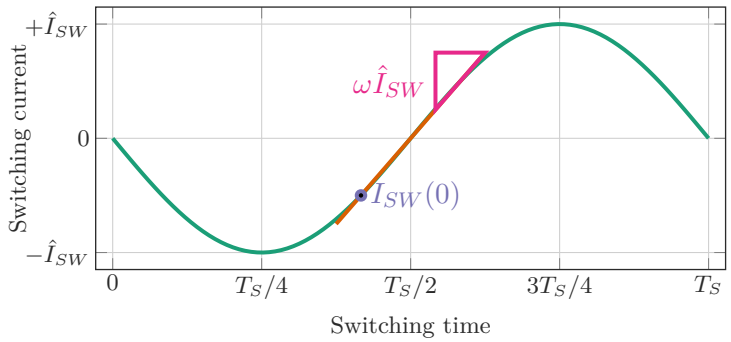

Figure 5.17: Current waveform at the switching instant, highlighting the varying nature of the resonant current.

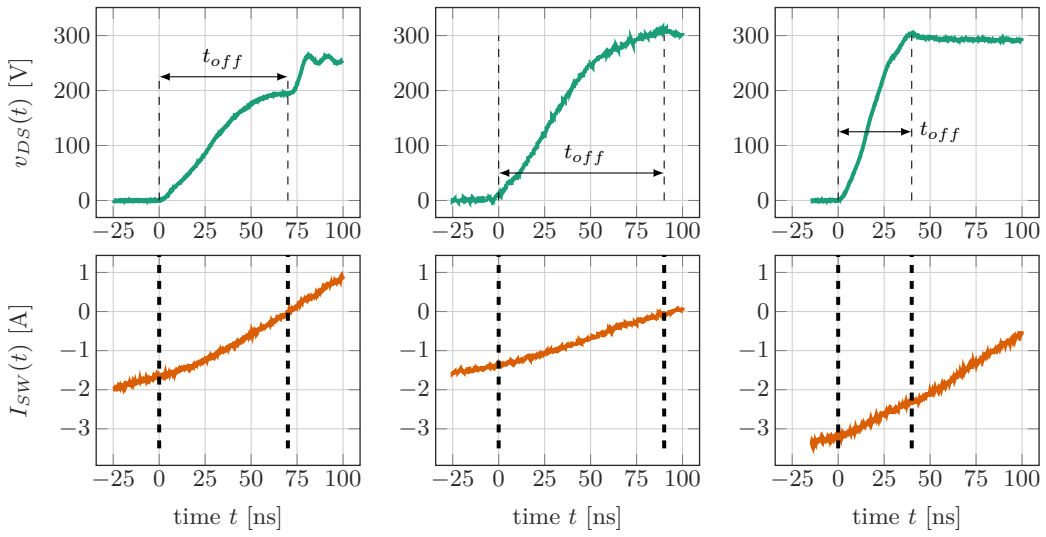

(a) Partial ZVS (b) Ideal ZVS (c) Non-Ideal ZVS

Figure 5.18: Experimental waveforms for a half-bridge in various ZVS conditions (partial, ideal and non-ideal)

5.2.2 Rectifier Transistors

On the rectifier side the voltage rating is much lower than in the inverter and the current is much higher, as the output voltage is 28 V. The initial choice was Si MOSFETS in the 40 V class for two reasons:

1. **Minimum conduction loss.** State-of-the-art Si offers very competitive $R_{DS(on)}$ in the 0.6 mΩ to 1.8 mΩ range in compact packages, which is hard to beat in pure $R_{DS(on)}I^2$.

2. **Cost and availability.** For the proof-of-concept, Si parts and gate drivers were used for comparable performance to the GaN HEMTs.

The comparison of different devices is shown in table 5.3, including an estimation of the breakdown of power losses (conduction, switching and driving losses) at 100 °C.

Picture	Manufacturer's part name	Breakdown voltage [V]	On-resistance $R_{DS(on)}$ [Ω]	Power losses [W]	Package	Ref.
	BSZ018N04LS6 (Infineon)	40 V	1.80 mΩ (3 per switch)	1.53 W 2.30 W 5.58 W	TSDSON-8 3.3 × 3.3 mm	[229]
	IQE013N04LM6 (Infineon)	40 V	1.35 mΩ (2 per switch)	1.72 W N/A 4.92 W	PG-TTFN-9 3.3 × 3.3 mm	[230]
	TPWR8004PL (Toshiba)	40 V	0.65 mΩ (1 per switch)	1.72 W 2.00 W 6.18 W	DSOP Adv. 5.0 × 6.0 mm	[231]
	NVMFS5C410N (Onsemi)	40 V	0.92 mΩ (1 per switch)	2.44 W 4.80 W 5.16 W	DFN5 SO-8 5.0 × 6.0 mm	[232]
	EPC2302 (EPC Co.)	100 V	1.80 mΩ (1 per switch)	5.72 W 0.50 W 0.27 W	QFN 3.0 × 5.0 mm	[233]
	EPC2361 (EPC Co.)	100 V	1.00 mΩ (1 per switch)	3.18 W N/A 0.25 W	QFN 3.3 × 5.0 mm	[234]
	EPC2366 (EPC Co.)	40 V	0.80 mΩ (1 per switch)	2.55 W N/A 0.16 W	QFN 3.3 × 3.3 mm	[235]
	EPC2367 (EPC Co.)	100 V	1.20 mΩ (1 per switch)	3.82 W N/A 0.16 W	QFN 3.3 × 3.3 mm	[236]

Table 5.3: Comparison of transistors for the rectifier, the losses were calculated for full power at 100 °C and are displayed as total in the rectifier (from top to bottom: conduction, switching and driving losses).

5.3 PCB Layout

A detailed analysis of the power and driving loops is fundamental to ensure high efficiency in modern power converters. WBG devices, particularly GaN HEMTs, switch at very high speeds, which amplifies the impact of parasitic inductances and capacitances from both the package and the PCB layout.

These parasitics introduce overshoots, crosstalk and false triggering, all of which increase switching losses and compromise system reliability. The minimisation of

these loop inductances, including their mutual coupling, enables ideal switching behaviour and allows optimisation of PCB layouts to mitigate such effects.

Equally critical is the optimisation of terminations and magnetic connections in high-current, high-frequency designs. Winding terminations and copper track geometries strongly influence the conduction losses in the PCB, responsible not only of lower efficiency but of higher temperatures.

5.3.1 Power Loops

In high-frequency power converters, the inductance of PCB tracks can cause voltage overshoot, current ringing, and additional stress on semiconductor devices, which increases switching losses and compromises soft-switching conditions, ultimately reducing both efficiency and reliability.

To mitigate these issues, careful PCB layout strategies such as flux cancellation and current interleaving are employed to minimise stray loop inductance as well as AC resistance [89]. By arranging parallel opposing current paths in close proximity, the associated magnetic fields cancel out, thereby minimising effective loop inductance.

Once the layout is optimised to minimise proximity effect, the skin effect becomes the dominant—and unavoidable—source of conduction losses in PCB tracks. Its impact can be significant, and PCB design must balance shortened current paths, sufficient copper cross-section, and thermal considerations.

Fortunately, for foil conductors (equivalent to PCB tracks) a set of analytical equations for skin effect is derived in [106]. The fundamental equation is given by:

$$P_{skin} = R_{DC} \cdot F_F \cdot \hat{I}^2 \tag{5.9a}$$

where F_F is a correction factor for skin effect:

$$F_F = \frac{\nu}{4} \cdot \frac{\sinh(\nu) + \sin(\nu)}{\cosh(\nu) - \cos(\nu)} \tag{5.9b}$$

with $\nu = t/\delta$ being the fraction of the skin depth δ compared to the thickness of the PCB tracks t.

To demonstrate the applicability of this equation, a simulation in Ansys Maxwell 3-D was conducted, obtaining the current density $J(x, y)$ as in fig. 5.19a. Due to the low output voltage compared to the input, the rectifier stage carries high-frequency, high-amplitude currents. At these current levels, charge tends to concentrate at the edges of the PCB tracks because of the strong internal electromagnetic fields, which increases the RMS current and consequently the conduction losses.

Since the rectifier is three-phase, a reasonable first approximation is to assume that two phases conduct simultaneously, this is, we can assume that two switches are active at any given time (one state), which yields approximately 4.53 W of losses according to electromagnetic simulations. Evaluating eq. (5.9a) at 1 MHz with a peak current $\hat{I} = 36\,\text{A}$ through an equivalent, intuitive length of copper track, a theoretical loss of 4.5 W is obtained.

To validate this estimation, an experimental characterisation was performed by exploiting the built-in resonant tank to generate the large signal three-phase currents required for excitation. Two tests were carried out:

- Short-circuiting the rectifier transistors and allowing the current to flow freely into the rectifier stage.
- Short-circuiting the three output terminals of the transformer secondary windings.

In both cases, the short-circuit current is naturally limited by the impedance of the rectifier board and transformer windings. To prevent destructive overcurrents, the experiment was conducted at an equivalent condition of full load, corresponding to 36 A on the secondary side. This way, the rectifier board experienced the same current stress as in nominal operation, while the power losses of the inverter, resonant tank, and transformer were excluded once the experiment with shorted secondaries was performed, leaving the difference as the conduction losses of the rectifier PCB.

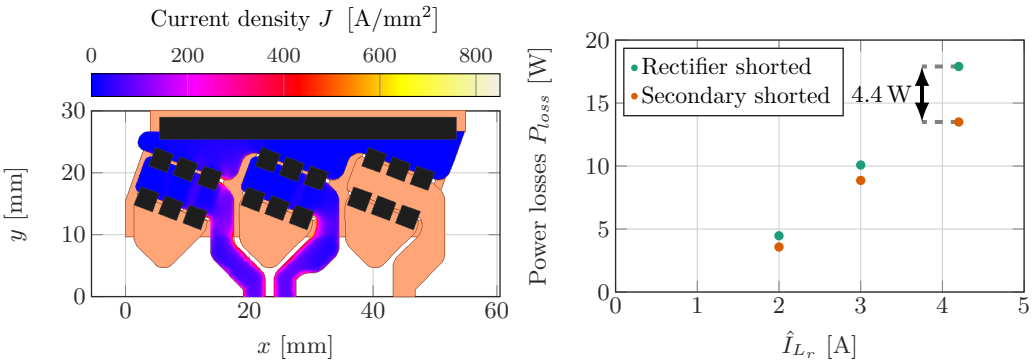

(a) Simulation of the current density profile in the rectifier (Ansys Maxwell 3-D) at full load

(b) Experimental PCB losses as function of a three-phase against the peak of the current

Figure 5.19: Experimental and simulated PCB losses as a function of the peak of the three-phase injected sinusoidal current at 1 MHz into the rectifier at full load (1 kW).

This operation is shown in fig. 5.19b, the measured loss of 4.4 W from fig. 5.19 is close with both the analytical prediction from eq. (5.9a) (around 2.8 % error) and the electromagnetic simulation in fig. 5.19a (3 % error). Notice that these conduction losses already account for approximately 0.75 % efficiency reduction at 1 kW output power once extrapolated to the actual peak current (5.2 A).

5.3.2 Driving Loops

The gate driver and the input of the transistor (gate-source terminals) form an LC-series resonant tank. This is because, the network includes the transistor internal gate inductance L_G, the Equivalent Series Inductance (ESL) of the supply capacitor,

as well as the gate driver pull-up or pull-down internal inductances, and the high-frequency equivalent effect of the interconnections between the components.

With this in mind, and to minimise switching time, it is best to minimise the overall resistance of this loop as much as possible, nonetheless, due to the inductive and capacitive nature of the loop, some resistance is always needed to avoid voltage overshoot at the gate-source as it does increase the EMI and it degrades the transistor over time. This can be achieved by adding an external damping resistance in series R_{ext},

$$R_{ext} \geq \sqrt{\frac{4L_{GG}}{C_{iss}}} \tag{5.10}$$

This results that the best way is to minimise the equivalent driving loop inductance L_{GG} through layout techniques for minimal gate inductance.

Nonetheless, the parasitic inductances of the main loop are not all, the Common-Source Inductance (CSI) L_{SS} which includes the intrinsic inductance of its source and its contact with the PCB and it is shared between the driving and power loops. During fast $\mathrm{d}i/\mathrm{d}t$ transitions, it induces a voltage that can, at best, reduce the switching speed and, at worst, overdriving the gate-source voltage of the transistor, potentially reducing the lifespan of the device and ultimately damaging it. This effect is specially more pronounced in GaN devices due to their smaller input capacitance C_{iss}. Even values of 100 pH can translate into a few volts due to the very fast transitions. Minimising L_{CS} requires careful package choice (preferably with a dedicated Kelvin source) and PCB layout practices that separate power and gate returns and exploit magnetic field cancellation.

The second key parasitic is the **gate loop inductance** L_{GG}, together with the input capacitance C_{iss}, this forms an LC resonant tank, as already described, that may cause gate voltage overshoot and oscillations if not properly damped. Minimisation of L_{GG} is best achieved by short and wide traces, placing the driver close to the switching device, and, when available, dedicated Kelvin connections. A small external resistor R_{ext} in series with the gate is typically added to damp the loop, balancing switching speed and voltage stability.

The parasitic capacitances also may play a decisive role, the input capacitance C_{iss} sets the fundamental gate charge requirements. The reverse transfer capacitance C_{rss} (or C_{gd}) couples the drain voltage to the gate, leading to Miller-induced oscillations, especially in high dv/dt environments. Although C_{rss} in GaN devices is smaller than in Si MOSFETs, the much higher dv/dt levels typical of GaN circuits make its influence still critical. Careful selection of driver strength and the use of split-gate resistors (separate turn-on and turn-off resistances) are effective countermeasures.

Finally, the ESL of the driver supply capacitor also contributes to gate loop ringing. This inductance, although usually less dominant than the rest, can inject noise and reduce gate drive effectiveness at high frequency. Placing high-quality ceramic capacitors (C0G) with low ESL as close as possible to the driver supply pins is essential to mitigate this effect.

Table 5.4 shows a list of gate drivers used for all components, which are specially designed for GaN HEMT driving so that can provide fast switching speeds and ultimately reduce switching losses.

Picture	Manufacturer's part name	Features	Package	Ref.
	Si8271 (Skyworks Inc.)	Isolation, split output (sink and source)	SOIC-8	[237]
	LM5114 (Texas Instruments)	Split output (sink and source)	SOTC	[238]
	LMG1210 (Texas Instruments)	Isolation, half-bridge	SOIC-8	[239]

Table 5.4: Off-the-shelf commercially-available gate drivers considered for driving of both the inverter and rectifier.

The calculation of the self and mutual inductances of complex circuit structures can be estimated [240, 241, 242]. Although they provide means to control the PCB layout, contemporary Finite Element Analysis (FEA) tools such as Ansys HFSS, Q3D or Keysight's PathWave ADS can be employed to accurately represent the interactions between the electrical conductors that composes the circuit layout directly from the routing software.

The definition of the different conductor paths to complete the desired circuit connections is shown in fig. 5.20, where partial current paths are bounded by key net points in the circuit (G, D, S, M, N, O, P, Q) to accurately evaluate the entire circuit. This returns three different inductive partial paths (OG, OD and SO) and three capacitive coupling (GS, DS and GD).

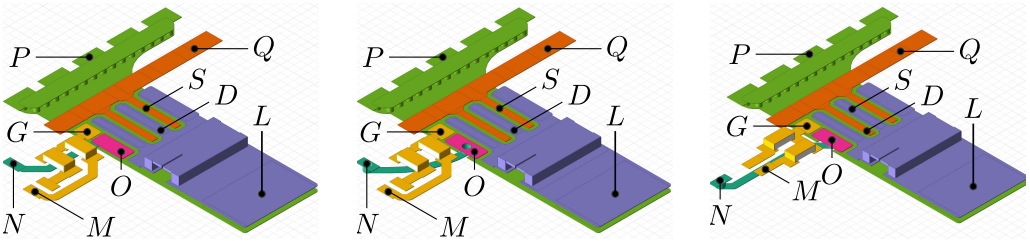

(a) Single layer meander (b) Two layer meander (c) Two layer straight

Figure 5.20: Study cases for different go-and-return driving loops modelled in Ansys HFSS 2023 with a 0.4 mm PCB board thickness.

To analyse the driving-loop inductance, its effect on the power losses and its realisation in the PCB layout, two conventional approaches to the driving loops are presented for comparison. These are named "meander" and "straight" for reference,

depending on the alignment of the go-and-return from the driver, the R_{on} and R_{off} resistors and the gate and source terminals of the transistor. These two approaches can be distinguished in fig. 5.20a, fig. 5.20b and fig. 5.20c respectively. The rest of the dependance is entirely given by the package of the components.

The numerical solution of the three cases is shown in table 5.5, the three solutions are very comparable. The major difference of the three cases is given by L_{GG}, being the 1-layer meander case significantly lower than the other cases without compromising the rest of the inductive coupling, improving it slightly or maintaining it. This effect is not translated into more time delay as the time constant of the equivalent RLC circuit of the driving loop is dominated by the RC ($R_G C_{iss} > L_G/R_G$).

L_{ij} [pH]	OG	OD	OS
OG	2735.3	-30.6	0.38
OD	-30.6	4509.7	-5.1
OS	0.38	-5.1	172.3

C_{ij} [pF]	
GS	0.069
DS	0.551
GD	0.061

R_{ij} [mΩ]	
OG	4.5
OD	2.1
OS	0.1

(a) 1-layer meander

L_{ij} [pH]	OG	OD	OS
OG	3784.6	-48.58	0.62
OD	-48.58	4506.8	-5.1
OS	0.62	-5.1	171.4

C_{ij} [pF]	
GS	0.069
DS	0.463
GD	0.057

R_{ij} [mΩ]	
OG	4.8
OD	2.1
OS	0.1

(b) 2-layer meander

L_{ij} [pH]	OG	OD	OS
OG	3276.4	-29.89	0.41
OD	-29.89	4524.6	-5.2
OS	0.41	-5.2	172.1

C_{ij} [pF]	
GS	0.073
DS	0.543
GD	0.047

R_{ij} [mΩ]	
OG	5.4
OD	2.2
OS	0.1

(c) 2-layer straight

Table 5.5: PCB layout simulated circuit coupling (inductive and capacitive) and resistive at 1 MHz

The low capacitance obtained in simulation compared to the parasitic capacitances of the EPC2302, particularly in the context of the C_{rss} (reverse transfer capacitance) from the typical 7 pF of the transistor to 0.057 pF of the PCB, evidencing a minor role in the performance of the overall system. This is not neccesarily the case if bigger copper areas are required for better thermal dissipation and must be taken into consideration.

Meticulous optimization of the PCB layout and careful consideration of the arrangement of conductors, their proximity, and routing to minimize unwanted coupling lead to a negligible effect of the coupling between driving and power loops in the power losses. Despite this apparently efficient optimization of the PCB

layout, it is still crucial to consider the effect of the coupling between when larger packaging is employed. In such cases, increased parasitic elements may lead to more significant effects such as power losses [243] or crosstalk [244] and the false turn-on of the device.

5.3.3 Transformer Loops

The remaining connections in the PCB layout are those to the inductors and transformers. Three connections must be made: the link between the inductor and the transformer, the wye connection on the primary side, and the delta connection on the secondary side.

The wye connection is straightforward, as the windings simply join three points together at the neutral. For the delta, however, two options are possible, as shown in fig. 5.21. The configuration named Yd1 (fig. 5.21a) is the most symmetric, since each path has equal connection length. Nevertheless, it complicates the layout and prevents the use of two-layer PCBs. For this reason, the Yd11 configuration (fig. 5.21b) is adopted.

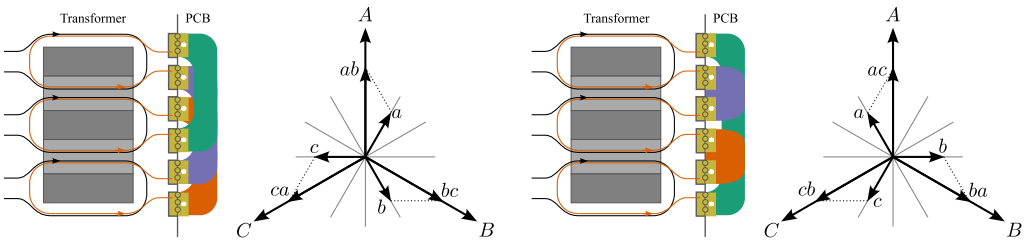

(a) Symmetric solution (transformer Yd1) (b) Asymmetric solution (transformer Yd11)

Figure 5.21: Transformer terminal connections for the secondary (delta configuration)

Both approaches were analysed and physically implemented, showing no noticeable differences in waveforms or overall performance. Consequently, most of the prototypes did employ the Yd11 configuration as shown in fig. 5.22.

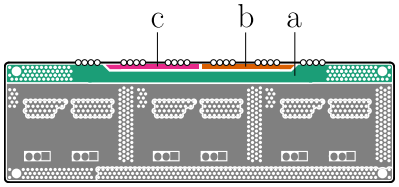

Figure 5.22: Rectifier board (Mid Layer 1) highlighting the switching nodes connections for the delta transformer.

5.4 Wye-Delta Three-Phase LLC with Inverter Legs in Parallel

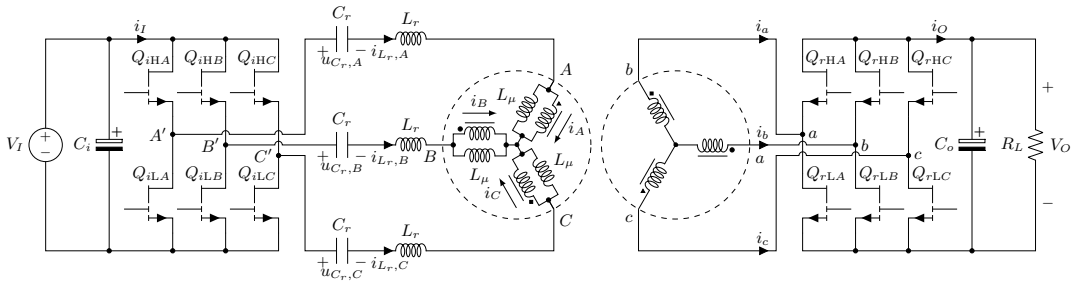

Figure 5.23: Basic circuit schematic of the wye-delta three-phase LLC converter with inverter legs in parallel

5.4.1 Proof-of-concept

In order to demonstrate current sharing between legs, the consequent preservation of soft-switching, the accuracy of the gain control across the specified input voltage and load ranges, and to learn as much as possible from specific layout techniques and the topology, the proof-of-concept platform in fig. 5.24 was assembled.

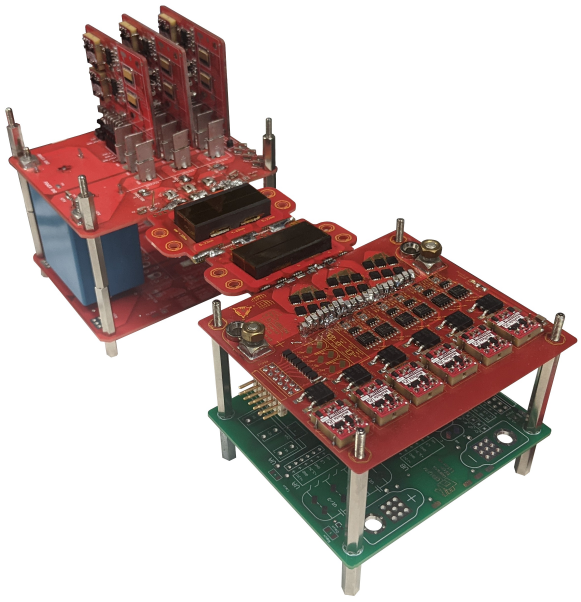

(a) Full prototype

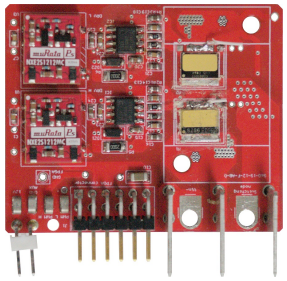

(b) Inverter card

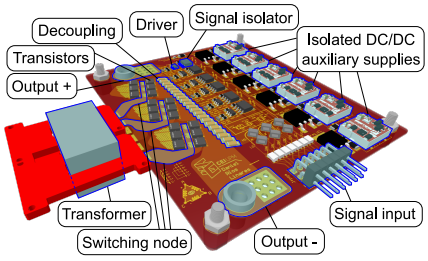

(c) Rectifier

Figure 5.24: Proof-of-concept prototype for the wye-delta three-phase LLC converter with inverter legs in parallel.

The most representative waveforms are shown in fig. 5.25, note that the resonant current zero crossings are aligned with the commanded switching events. The efficiency vs. load sweep is shown in fig. 5.26 peaking around 96 % efficiency with 95 % at full load (50 W of power losses).

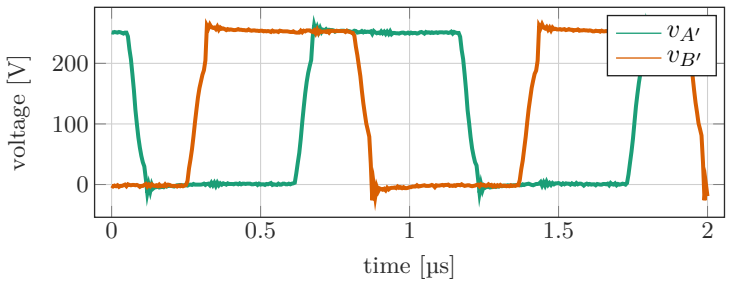

(a) Voltage at the switching nodes (resonant tank input)

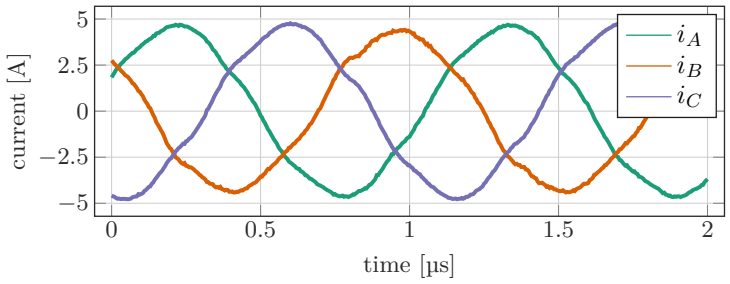

(b) Currents through the resonant tank

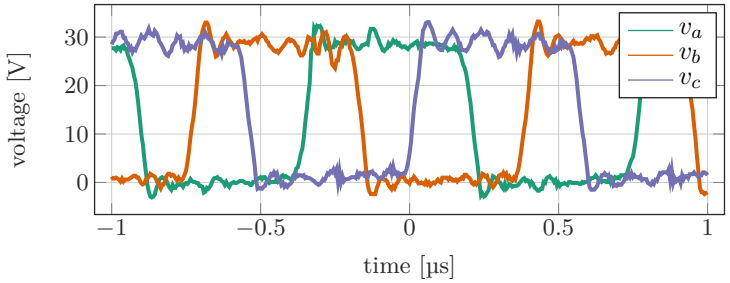

(c) Voltage at the switching nodes (delta terminals)

Figure 5.25: Experimental waveforms for 250-28 V for 1 kW switching at 870 kHz.

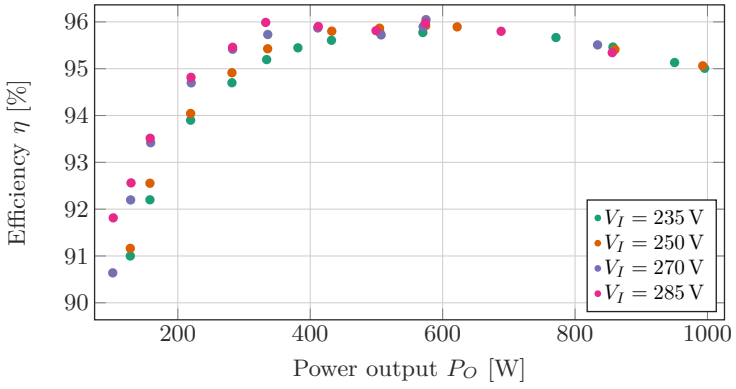

Figure 5.26: Measured efficiency for 235-285 V of input voltage and the 100-1000 W output power range (Proof-of-concept of the three-phase LLC with the inverter in parallel).

5.4.2 Miniaturisation

Building on the functional demonstrator, the converter was condensed to the form factor shown in fig. 5.27. The reduced volume was achieved by integrating the three-phase transformer and inductor in a stacked planar assembly and by compressing the commutation loops vertically using interleaved power and return planes.

The assembly (without auxiliar supplies) achieved a measured power density of approximately 15 kW/L. Efficiency measurements in fig. 5.28 confirm that the miniaturisation did degrade performance; the peak efficiency remains within 0.5 % of the proof-of-concept, translating into a full-load temperature rise not within the thermal stability. The soft-switching window was obtained within the 15 % sufficient to regulate the output.

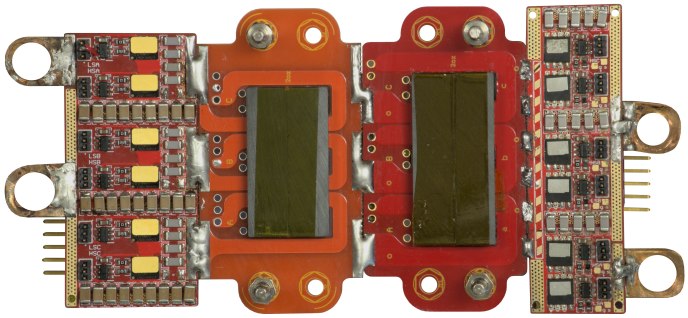

(a) Top view

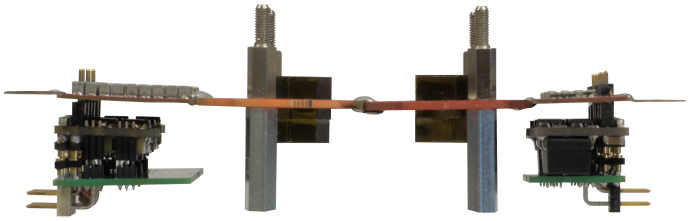

(b) Side view

Figure 5.27: Miniaturisation prototype platform for waveform demonstration and magnetics with miniaturised parts (including inverter and rectifier).

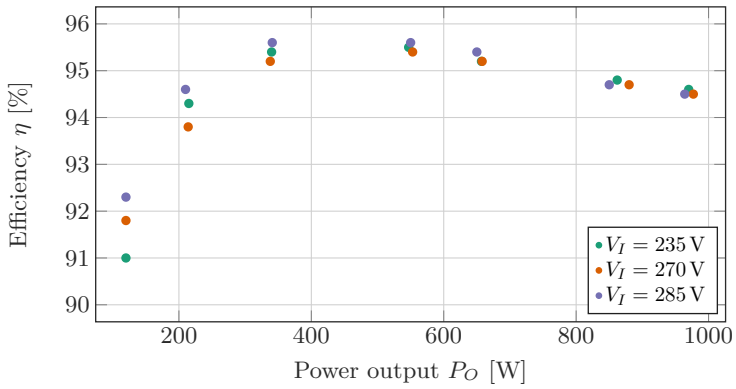

Figure 5.28: Measured efficiency for 235-285 V of input voltage and the 100-1000 W output power range (Miniaturised three-phase LLC with the inverter in parallel).

Two rectifiers were constructed. The first one, made with Si transistors as shown in fig. 5.29 was compatible with two transistors of similar performance, the TPWR8004PL from Toshiba [231] and the NVMFS5C410N from On-semiconductor [232]. The power losses were estimated in both cases as a full-bridge (two phases) and a resonant tank in the middle, emulating the behaviour of the converter and allowing to estimate the power losses for switching by discriminating the losses of the passive components and the conduction from the datasheet, the figure is shown in the table from the rectifier selection table 5.3.

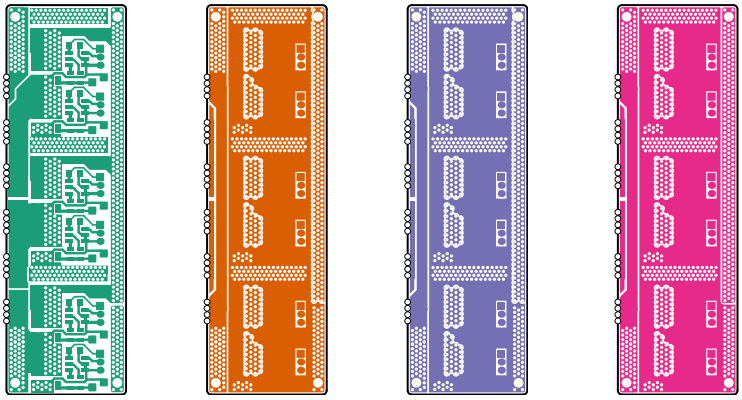

(a) Top layer (b) Mid layer 1 (c) Mid layer 2 (d) Bottom layer

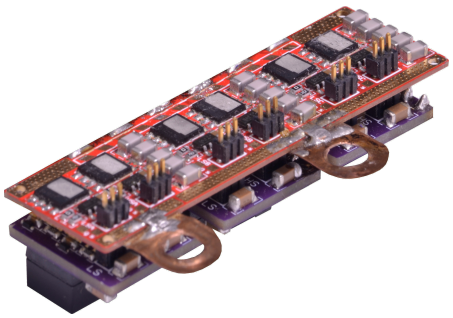

(e) Power board

Figure 5.29: PCB layout of the three-phase rectifier compatible with TPWR8004PL and NVMFS5C410N.

A similar approach was made for the second prototype (fig. 5.29), this time with GaN HEMTs, particularly the EPC2302 from EPC Co. [233], exhibiting better performance than the proof-of-concept. Due to the unstability of the converter hardware, the actual efficiency measurements are left in the final prototype later in this chapter.

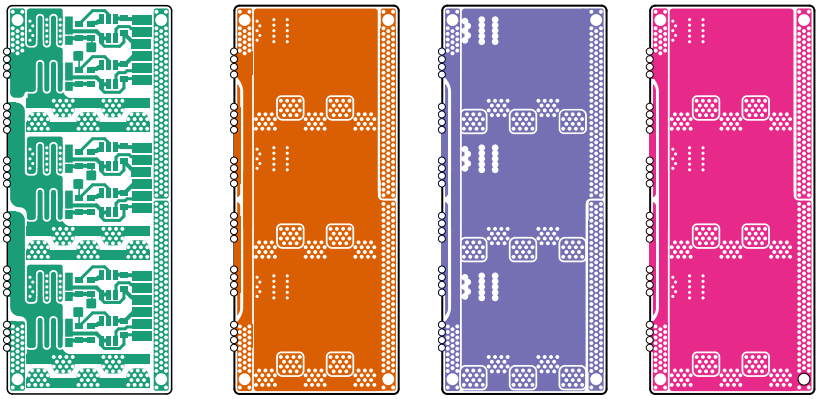

(a) Top layer (b) Mid layer 1 (c) Mid layer 2 (d) Bottom layer

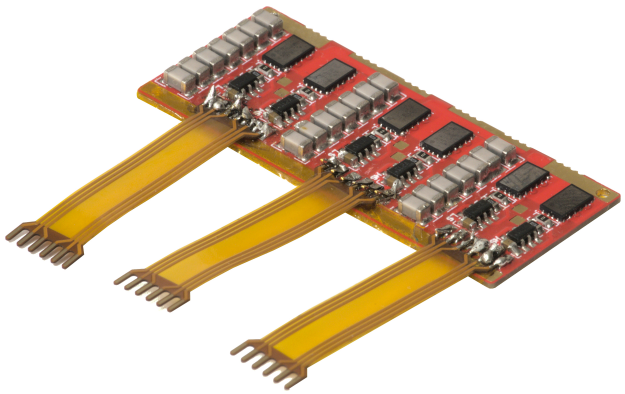

(e) Power board

Figure 5.30: PCB layout of the three-phase rectifier compatible with EPC2302 and EPC2361.

5.5 Wye-Delta Three-Phase LLC with Half-Bridge Inverter Cells in Stack

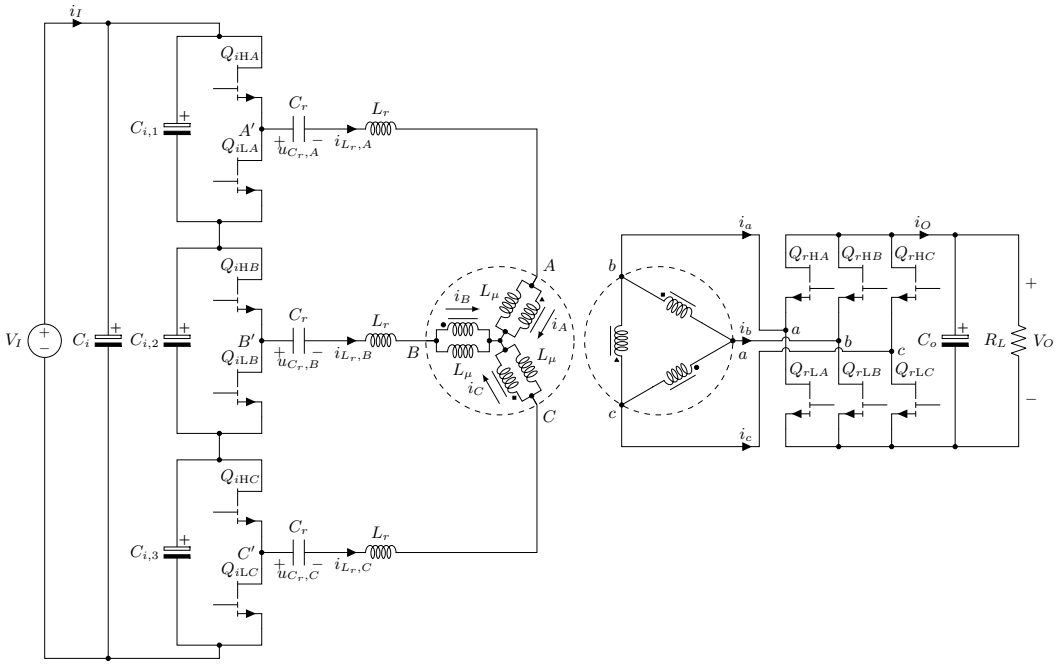

Figure 5.31: Basic circuit schematic of the wye-delta three-phase LLC converter with half-bridge cells in series (stack)

5.5.1 Proof-of-concept

The stacked-cell topology in fig. 5.31 was validated with a laboratory platform aimed at confirming correct voltage sharing and timing across the series half-bridges.

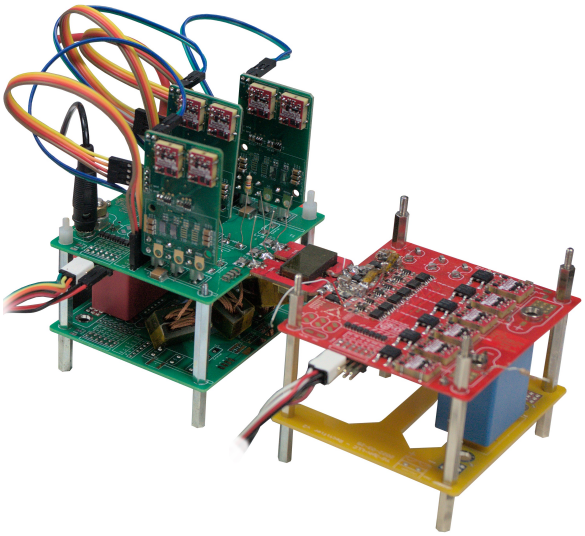

(a) Full prototype

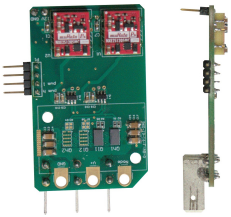

(b) Inverter card

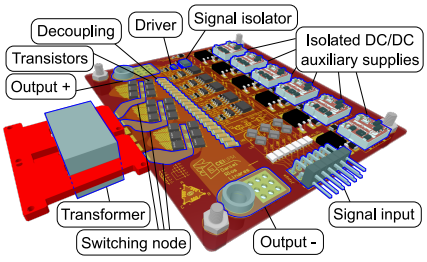

(c) Rectifier

Figure 5.32: Proof-of-concept prototype platform for waveform demonstration and magnetics of the wye-delta three-phase LLC converter with inverter legs in stack

During steady-state operation at resonance, the average potentials of the intermediate nodes were measured to be within 1 % of the ideal fractions of the input voltage, with no observable drift over several minutes. Switch-node waveforms showed the expected six-state sequence and the primary phase-to-neutral voltages retained their symmetry, which is crucial to avoid DC bias in the transformer.

The measured efficiencies in fig. 5.33 are consistent with the use of lower-voltage devices with reduced $R_{DS(on)}$, while the ZVS margin remained adequate across the mapped operating region.

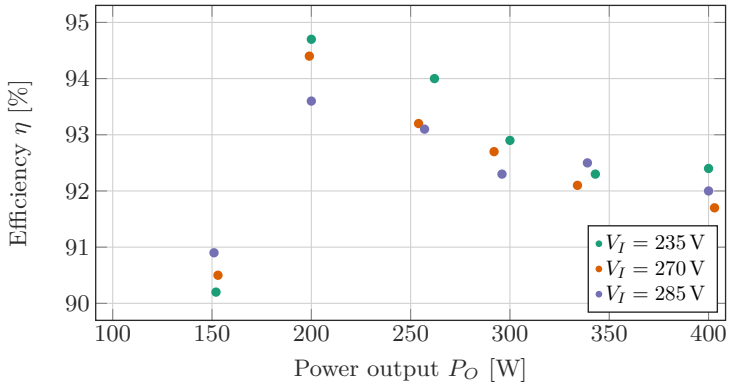

Figure 5.33: Measured efficiency for 235-285 V of input voltage and the 100-400 W output power range (Proof-of-concept of the three-phase LLC with the inverter in stack).

5.5.2 Miniaturisation

A compact implementation of the stacked topology was then developed, targeting a nominal density of 14 kW/L. The reduction in footprint was enabled by folding the three half-bridges along a common heat spreader and by co-locating the DC-link capacitors in a low-inductance busbar arrangement.

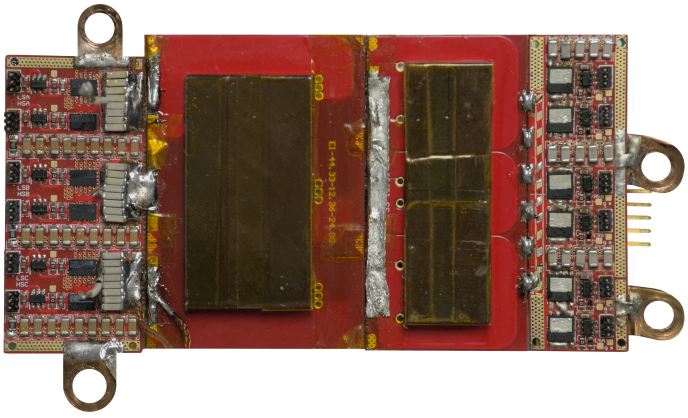

Figure 5.34: Proof-of-concept prototype platform for waveform demonstration and magnetics of the topology with the inverter in stack.

Experimental characterisation verified that device temperatures remained within specification and that the voltage sharing held across the full operating map. The

efficiency curve in fig. 5.35 shows identical peak efficiency within measurement repeatability and a marginally better part-load performance due to reduced circulating energy in the tank, the same analysis could have been performed as in the inverter in parallel version for the rectifier, nonetheless, to further miniaturise the converter, a new set of experiments were designed to achieve higher power density and efficiency as the last section of this chapter follows.

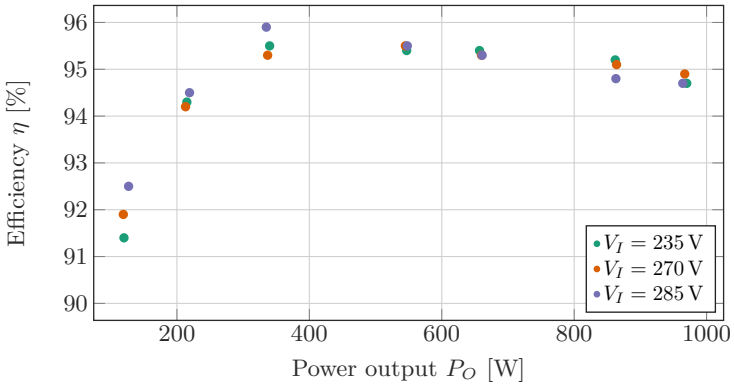

Figure 5.35: Measured efficiency for 235-285 V of input voltage and the 100-1000 W output power range (Miniaturised the three-phase LLC with the inverter in stack).

5.5.3 Final Prototype 20 kW/L

The final prototype, shown in fig. 5.36, consolidates the stacked-cell architecture and the compensated three-phase magnetics into a tightly integrated assembly meeting a power density of approximately 20 kW/L.

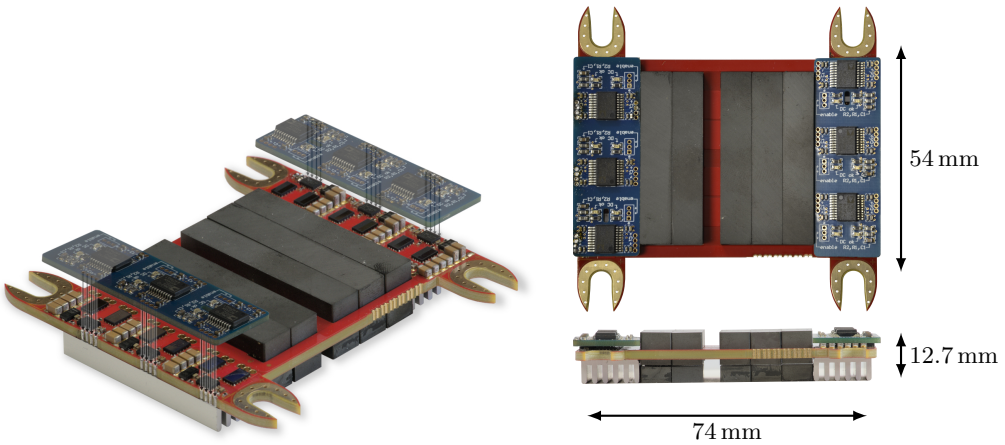

(a) Isometric view of the full power converter showing the auxiliar supply with 50 % transparency

(b) Front and side view of the full power converter showing its dimensions

Figure 5.36: Final prototype platform for waveform demonstration and magnetics.

The prototype was constructed with a different auxiliar supply, up until now, the power density of the converters was measured without the inclusion of the auxiliar supply, this is because of the driving power losses in Si transistors and the

generalisation of the auxiliar PCB board. Due to the reduced power requirements of the GaN HEMTs, a new auxiliar supply composed by the ADUM6210ARZ [245], a small isolated converter that is able to give 5 V at the output as well as two digital signals (employed for PWM) for each phase for both the inverter and rectifier.

The operating converter was recorded at 270 V and up to 400 W due to time constraints, including efficiency as shown in fig. 5.37, reaching 96.5 % efficiency, and confirming that the frequency range was confined to 10 % to 15 %.

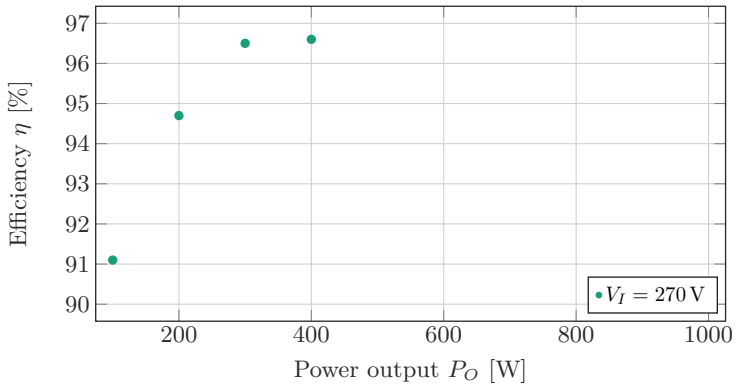

Figure 5.37: Measured efficiency for 235-285 V of input voltage and the 100-1000 W output power range (Miniaturised of the three-phase LLC with the inverter in stack for 20 kW/L).

CHAPTER 6

Conclusions

Advice is a dangerous gift.

— Gandalf the Grey, *The Lord of the Rings*

This thesis examined the design, optimisation, and experimental validation of three-phase wye-delta LLC converters targeted at the demanding requirements of next-generation aircraft power systems. The work addressed system-level architecture, resonant tank design, planar magnetics, high-frequency layout strategies, and architectural extensions such as stacked configurations. The proposed methods have been substantiated through analytical modelling, finite-element simulations, and prototype implementation, providing a comprehensive basis for scalable, compact, and efficient MHz-class conversion stages.

6.1 Summary of the Approach

1. System architecture. The wye-delta three-phase configuration was adopted to intrinsically reduce input and output ripple, thereby lowering the requirements for EMI filtering and output capacitance. The transformer connection introduced an additional conversion factor, reducing turns ratio and copper utilisation, while enabling low-profile, planar integration of magnetic components.

2. Tank design methodology. A design flow was developed by combining fundamental harmonic approximation with exact time-domain analysis, ensuring ideal rectifier behaviour even under off-resonant operation. The methodology constrained frequency deviation to around 10 %–15 % across the specified input and load ranges, thereby enabling practical MHz-class operation with manageable thermal stress and magnetic design.

3. Three-phase planar magnetics. The intrinsic asymmetry of three-port EE/EI cores was analytically studied and compensated through a redistribution of

magnetic column areas. Closed-form models with fringing corrections were established and validated by finite-element simulations, achieving mutual inductance equalisation and containing residual imbalance to only a few percent for realistic air gaps.

4. High-frequency layout and copper-loss control. PCB windings were dimensioned with attention to skin effect in foil conductors, and termination losses were mitigated by optimised pad and return current arrangements. The layout of secondary windings prioritised orthogonality between layers and minimised loop inductance, achieving compatibility with conventional planar manufacturing processes.

5. Architectural variants and stacking. Beyond parallel inverter legs, stacked half-bridge arrangements were introduced to extend the operating voltage range while preserving the three-phase magnetic integration. Simplified single-phase models and AC resistance derivations were presented for this variant, along with measures for maintaining voltage balance across different dynamic time scales.

6.2 Principal Contributions

- The proposal of a scalable wye-delta three-phase LLC converter as a modular building block for aircraft DC/DC conversion, achieving reduced filter demands and lower turns ratios while remaining compatible with low-profile, PCB-based magnetics.
- The development of a resonant tank design methodology that combines frequency-domain synthesis with exact time-domain modelling, constraining the switching-frequency excursion to about 10 %–15 % while still covering the full operating envelope.
- The establishment of a topology-aware three-phase magnetics design method, including analytical expressions for self and mutual inductances with fringing compensation, and a geometric compensation strategy for balancing flux, supported by FEM verification.
- The derivation of layout rules tailored for MHz-class PCB windings, addressing skin, proximity, and termination losses, and applicable across different magnetic families.
- The exploration of stacked-cell three-phase LLC variants, supported by analytical modelling and balancing guidelines, extending the usable design space while maintaining soft-switching operation.

6.3 Experimental Validation and Results

A 1 kW prototype operating at approximately 1 MHz, with a single-turn secondary and integer-turn primary, demonstrated the practical feasibility of the proposed methods. The hardware:

- Preserved soft-switching across the defined operating space,
- Delivered a regulated 28 V output with minimal ripple,
- Reached peak efficiencies close to 96 %,
- Confined the switching-frequency excursion to around 10 %–15 %,
- Achieved a volumetric density of about 20 kW/L.

Measured input and output currents confirmed the anticipated ripple reduction, thereby reducing the filtering burden. Thermal imaging showed balanced temperature distribution with no termination hot-spots, validating both the compensated magnetics and layout strategy. Comparisons with phase-shift full-bridge and dual-active-bridge baselines indicated that the proposed architecture delivers higher efficiency over a wide operating range, lower filter volume, and improved magnetic utilisation under the same constraints.

CHAPTER 7

Future Research Lines

Las ideas no duran mucho,
hay que hacer algo con ellas.

— Santiago Ramon y Cajal

7.1 Topologies

7.1.1 Fewer Cells in Stack

Traditional three-phase inverter bridge cells use six switches as shown so far in this work. In the patent in [246], a four-switch, three-phase DC/DC resonant converter aimed at reducing the number of active semiconductor devices compared to conventional three-phase resonant converters. This topology achieves full three-phase operation using only four switches arranged in two half-bridges, similarly to the VFX [175].

The circuit consists of a first half-bridge and a second half-bridge, each providing one output phase. A third connection is obtained by appropriately controlling the switching pattern with a phase shift. In the baseline embodiment, the phase-shift between the half-bridges is 60°. By phase-shifting each half-bridge leg, the outputs form a balanced three-phase system.

The switching circuit is directly connected to a three-phase resonant tank. Each output node of the half-bridges provides one phase signal to the resonant tank, which shapes the voltage and current waveforms for efficient power transfer. The resonant stage is followed by a three-phase transformer, which provides galvanic isolation and voltage scaling. The secondary side employs a three-phase rectifier bridge and output filtering to produce the DC output.

The main innovation lies in reducing the inverter stage from six switches to four, lowering the number of active devices, gate drivers, and control complexity. This provides lower cost, improved efficiency, and higher reliability.

Nonetheless, when operated in this way, ZVS is not achieved in all switches due to the voltage phase shift between the bridges. To solve it, an additional inductor or even a resonant tank can be placed in the switching node to compensate for that, but this way, defeats the purpose of a more compact integrated topology, thus, as a future research line, the development of a geometrically-compensated three-phase magnetic structure that is able to operate 120° of phase-shift (the traditional), while maintaining balanced, three-phase currents is proposed.

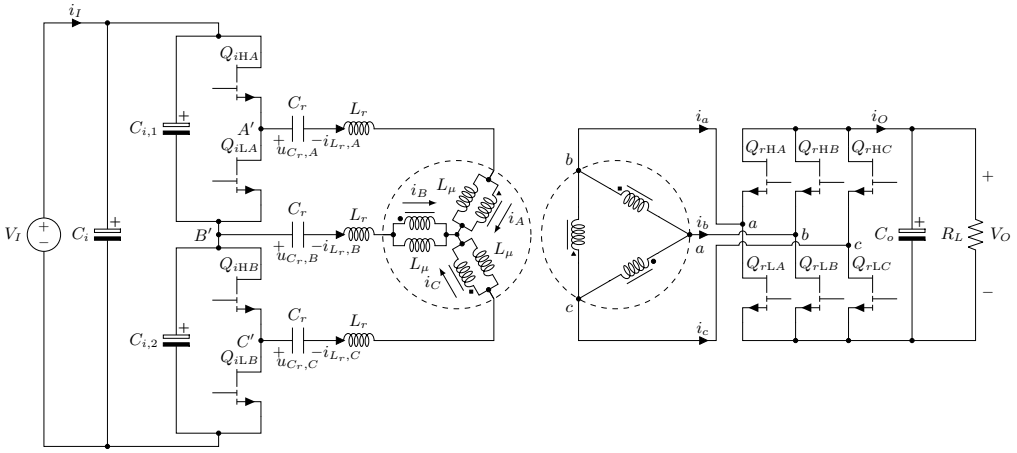

Figure 7.1: Wye-delta three-phase LLC converter with a novel inverter with two legs in stack.

An experimental confirmation of this proposal was quickly tested in the three cells stack by always shorting the middle cell, showing promising results when the three-phase inductor is not compensated (not operating as three independent inductors) and operating at resonance (operating as a DCX), nonetheless, further characterisation and analysis needs to be performed.

7.1.2 Half-Wave Rectifiers

Apart from the centre-tap rectifier configuration—which doubles the required voltage rating of the rectifying transistors (still within the limits of the employed GaN devices such as the EPC2302 and EPC2361)—and the resulting optimisation of the transformer secondary windings and PCB decoupling layout, half-wave rectification can further improve the system's power density. However, this approach triples the voltage stress on the rectifying transistors and increases the converter gain by a factor of 1.5 compared to full-wave rectification, while also introducing Discontinuous Conduction Mode (DCM) operation at light loads, which severely distorts the characteristic gain curve. Several control techniques have been proposed to mitigate this issue; for instance, PWM control of the input voltage duty cycle can partially compensate for the DCM behaviour.

7.1.3 Matrix Transformer

Matrix transformers in three-phase LLC converters are not a new concept. However, their ability to improve magnetic core utilisation is particularly relevant in

three-phase systems, where the return current converges at a neutral point. This characteristic makes the topology a strong candidate for high output current applications.

7.2 Reliability in Cells in Stack

In converter with stacked cells, short-circuit conditions can occur if one or more switching devices fail short. Because the cells are connected in series, a short in a single cell effectively bypasses its voltage contribution and distorts the balance of voltage and current sharing among the others. This can force neighbouring cells to operate outside their designed voltage window, leading to stress on semiconductors, unbalance in resonant currents, and a potential collapse of the regulated DC bus.

1. **Cell Short-Circuit Events:** A shorted cell disturbs the resonant condition and shifts the operating frequency away from its designed point. This may generate circulating currents through the remaining healthy cells, overstress the resonant tank and the bulk capacitor, and trigger uncontrolled bus voltage drift. In severe cases, a cascade failure may occur as other devices are forced to carry unintended fault currents, resulting in the loss of soft-switching and increased switching losses.

2. **Cell Open-Circuit or Disconnection:** An open-circuited cell reduces the effective turns ratio and introduces output voltage imbalance. This causes asymmetry in current sharing, decreases efficiency, and may drive the magnetic components into saturation due to distorted flux balance.

3. **Component Parameter Mismatch:** Tolerances in magnetising inductance, resonant capacitance, or transformer leakage inductance can affect the gain symmetry across cells. This may lead to unequal current distribution, circulating currents, reduced power density, and difficulties in maintaining ZVS under all load conditions.

4. **Thermal Imbalance:** Unequal heat dissipation between stacked devices can create localised hot-spots, accelerating the ageing of GaN/SiC transistors. This raises the risk of thermal runaway in one branch, thereby compromising the overall converter reliability.

5. **Control and Synchronisation Issues:** Mismatched phase shifts between cells can cause duty cycle distortion, harmonic cancellation loss, and increased EMI. This necessitates highly accurate synchronisation and balancing control loops.

6. **Fault Propagation and Protection:** Without redundancy, the failure of a single cell may result in a complete shutdown of the converter. The lack of fast fault detection can exacerbate fault energy dissipation. Future research should address advanced protection schemes such as active current balancing, fault isolation, and redundant cell inclusion.

7. **System-Level Interactions:** Under fault conditions, unfiltered currents may be injected into the three-phase source, potentially compromising galvanic isolation and stressing EMI filters and bus capacitors. This calls for a deeper analysis of interactions between the stacked cells and system-level components.

Future work should therefore focus on the systematic study of these failure modes, the development of fault-tolerant modulation strategies, the design of redundant or reconfigurable cell architectures, and the integration of advanced protection schemes. Reliability testing under accelerated ageing and abnormal operating conditions is also required to validate the robustness of three-cell stack LLC converters in demanding applications.

7.3 Miniaturisation

Miniaturisation in power converters is ultimately constrained by several factors: switching frequency, efficiency, and thermal management. Increasing frequency allows the reduction of passive component size, yet it can also amplify losses and thermal stress. The selection of core materials and semiconductor technology therefore plays a crucial role in enabling further reductions in volume without compromising reliability. The same thing happens with transistors, newer generations of GaN HEMT technology have demonstrated their advantages over traditional Si transistors.

Future research in miniaturisation is structured around three complementary directions: the adoption of new magnetic materials, the integration of better transistors, and the development of better heat extraction mechanisms.

7.3.1 New Magnetic Materials

In this thesis, the TP5H ferrite material from TDG was employed, providing a good compromise between loss characteristics, manufacturability and cost. However, more advanced materials such as the DMR51W, from DMEGC, have since become available and exhibit superior performance in terms of reduced core loss at high frequency.

The adoption of such materials could directly increase the achievable power density, particularly in three-phase LLC converters where magnetic integration is pivotal. Although not accessible at the time of the optimisation process, future prototypes should incorporate these next-generation materials to fully exploit the benefits of high-frequency operation, potentially increasing the power density up to 28 kW/L at 2 MHz switching frequency, a concept of this prototype is shown in fig. 7.2.

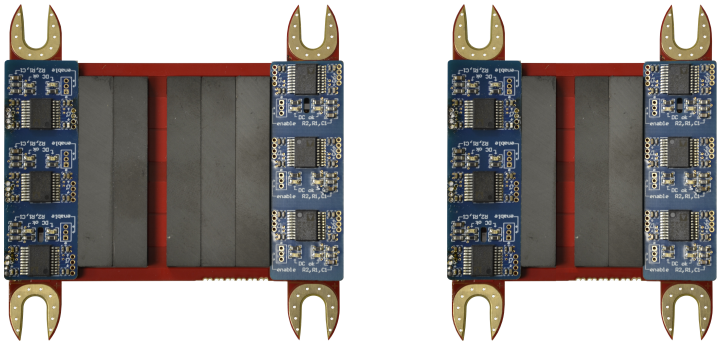

(a) Actual final miniaturised prototype at 20 kW/L

(b) Conceptual 2 MHz at 28 kW/L

Figure 7.2: Conceptual prototype for 2 MHz switching frequency operation.

7.3.2 Improved Switching Models

The continuous evolution of GaN technology opens the path to higher switching frequencies, which directly support further miniaturisation. Since the selection of devices for this thesis, newer generations of GaN HEMTs, such as the EPC2361, EPC2366, and EPC2367, have been released. These transistors exhibit lower parasitic capacitances and reduced $R_{DS(on)}$, making them highly suitable for MHz-range DC/DC converters. Compared to the devices employed in this work, their superior characteristics would permit operation at frequencies beyond 2 MHz while maintaining soft-switching and manageable efficiency.

Having higher performance transistors available allows to improve the efficiency of the converters, but smart use of them also allows to improve it. Existing datasheet-based models often oversimplify the non-linearities of GaN HEMTs, leading to the overestimation of power losses in this technology by a factor of 2 to 5. When miniaturising converters, every watt must be carefully predicted in order to optimise properly.

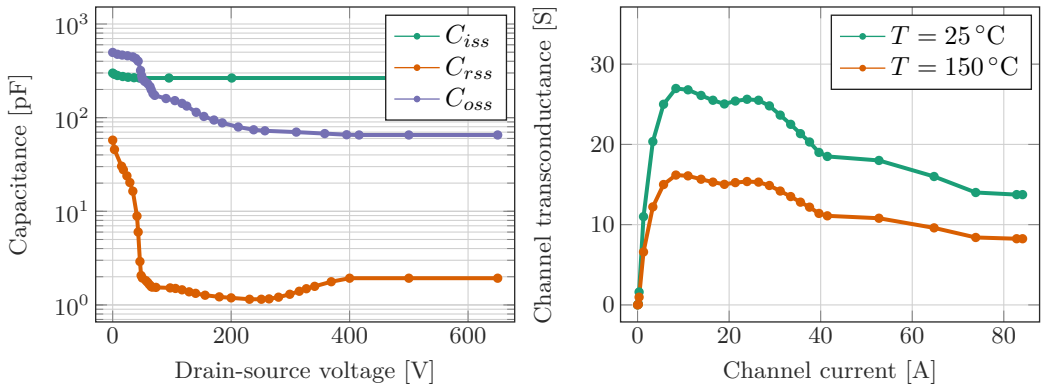

(a) Parasitic capacitances

(b) Channel transconductance

Figure 7.3: Representative transistor characteristics implemented in the simulator-grade solver (parasitic capacitances and transconductance).

Although there are a lot of parameters that can be extracted from the datasheet, the two most important are the ones that model the transient: the parasitic capacitances, and the transconductance (fig. 7.3)

Numerical Solver

The numerical solver proposed by the authors in [68] as part of this thesis, demonstrates how a universal approach can be derived from datasheet parameters, accounting for parasitics, capacitance non-linearities, and PCB-induced coupling.

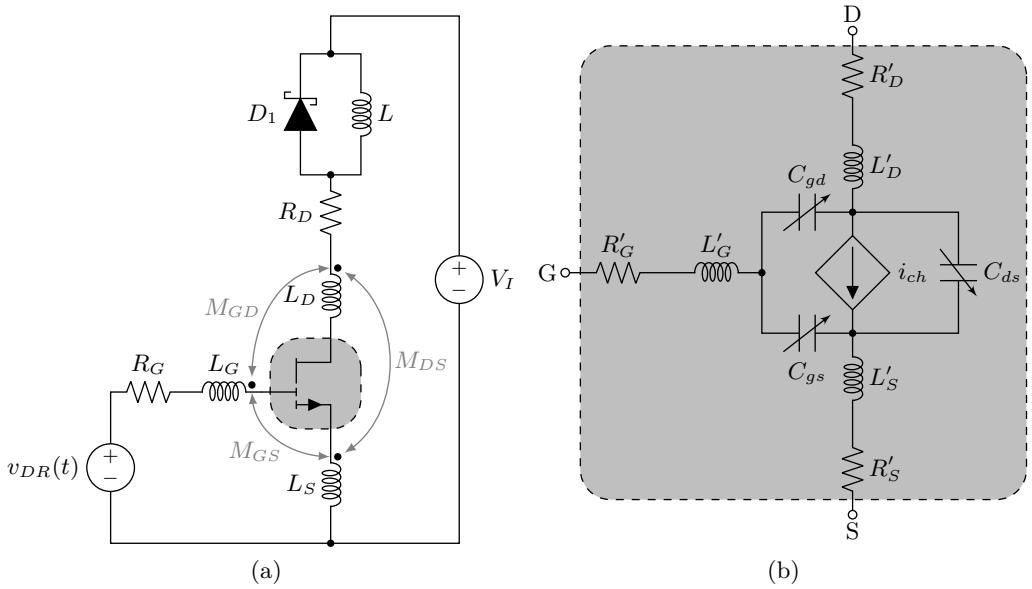

Figure 7.4: Example of a setup for switching losses testing: DPT.

Equation (7.1) shows how the DPT circuit in fig. 7.4 is modelled in the state space $\dot{\mathbf{x}} = \mathbf{A} \cdot \mathbf{x} + \mathbf{b}$.

$$\begin{bmatrix} 0 & 0 & L_{dr} & L_{dp} \\ 0 & 0 & L_{dp} & L_{pw} \\ 2C_{rss} - C_{iss} & C_{rss} & 0 & 0 \\ C_{rss} & -C_{oss} & 0 & 0 \end{bmatrix} \begin{bmatrix} \dot{v}_{GS} \\ \dot{v}_{DS} \\ \dot{i}_G \\ \dot{i}_D \end{bmatrix} + \begin{bmatrix} 1 & 0 & R_{GG} + R_{SS} & R_{SS} \\ 0 & 1 & R_{SS} & R_{DD} + R_{SS} \\ 0 & 0 & 1 & 0 \\ 0 & 0 & 0 & 1 \end{bmatrix} \begin{bmatrix} v_{GS} \\ v_{DS} \\ i_G \\ i_D \end{bmatrix} = \begin{bmatrix} V_{DR} \\ V_{DC} \\ 0 \\ i_{ch} \end{bmatrix} \tag{7.1}$$

where L_{dr}, L_{dp} and L_{pw} are the inductance coupling link between the loops of the system: L_G, L_D and L_S; and the current through the channel i_{ch} is time-dependent and is calculated through the previously plotted transconductance g_m in fig. 7.3b as:

$$i_{ch} = \begin{cases} 0 & v_{GS} \leq V_{th} \\ g_m \cdot (v_{GS} - V_{th}) & V_{th} < v_{GS} \leq V_{pl} \\ \dfrac{v_{DS}}{r_{ON} - R_{DD} - R_{SS}} & v_{GS} > V_{pl} \end{cases} \tag{7.2}$$

To simplify the analysis, previous work explored the possibility of separately model the stages [247, 248]. This method implies that the transistor cannot reenter

prior stages due to oscillations of the state variables. Instead, the full system of non-linear differential equations is used for all stages.

With the system of non-linear differential equations discussed as well as its initial state, a numerical method for solving it needs to be chosen. An analysis of various numerical methods, including Euler, Heun, Runge-Kutta 4 and Dormand-Prince, was performed to determine the most suitable method for the system. Euler and Heun, although computationally efficient, exhibited low accuracy, requiring a very small time step. Both the Runge-Kutta 4 and Dormand-Prince, demonstrated superior accuracy, making it the preferred choice for our study. At the end, Runge-Kutta 4 was employed due to its high accuracy and relatively low computational cost for which equations (7.3) and (7.4) are employed for the matrices $\mathbf{A}_k$ and $\mathbf{B}_k$ evaluated with $\mathbf{x}_k$.

$$\mathbf{x}_{k+1} = \mathbf{x}_k + \frac{h}{6}\left(\mathbf{k}_1 + 2\mathbf{k}_2 + 2\mathbf{k}_3 + \mathbf{k}_4\right) \tag{7.3}$$

where h is the time step and the different $\mathbf{k}_i$ are given by:

$$\mathbf{k}_1 = \mathbf{A}_k \cdot \mathbf{x}_k + \mathbf{B}_k \tag{7.4a}$$

$$\mathbf{k}_2 = \mathbf{A}_k \cdot \left(\mathbf{x}_k + \frac{h}{2} \cdot \mathbf{k}_1\right) + \mathbf{B}_k \tag{7.4b}$$

$$\mathbf{k}_3 = \mathbf{A}_k \cdot \left(\mathbf{x}_k + \frac{h}{2} \cdot \mathbf{k}_2\right) + \mathbf{B}_k \tag{7.4c}$$

$$\mathbf{k}_4 = \mathbf{A}_k \cdot \left(\mathbf{x}_k + h \cdot \mathbf{k}_3\right) + \mathbf{B}_k \tag{7.4d}$$

Solver Results

The solver proposed have demonstrated to be more fitting to experimental data, for example, the experimental DPT data from [228] has been use to fit in the model as shown in fig. 7.5.

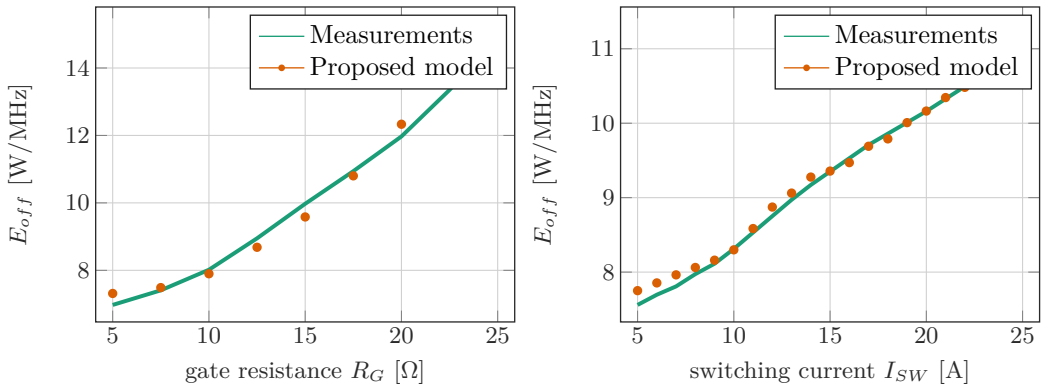

(a) R_{off} sweep, $I_{SW} = 15\,\mathrm{A}$ (b) I_{SW} sweep, $R_{off} = 1\,\Omega$

Figure 7.5: Experimental and modelled switching losses (GS66508T) with $V_{DC} = 400\,\mathrm{V}$ and $h = 0.1\,\mathrm{ns}$ [228]

Such tools not only allow for accurate design-phase optimisation but also enable digital twin implementations for real-time monitoring and health prediction. Incorporating these universal models into the design workflow of resonant converters would significantly enhance predictive accuracy and robustness, ultimately improving the performance of the converters.

7.4 Thermal Performance

Future work will extend beyond traditional FEM thermal verification to the development of real-time digital twins for high-density converters. While this thesis has validated the feasibility of heat extraction at 1.4 W/cm^2 through simulations in Ansys IcePak (fig. 7.6), the next step is to integrate predictive thermal models capable of running alongside the physical prototype.

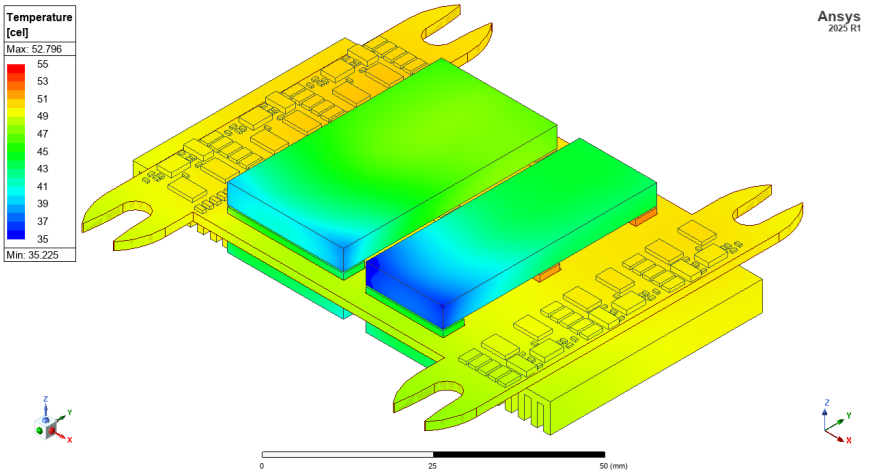

Figure 7.6: Thermal simulation performed in Ansys IcePak 2025 for the miniaturised 20 kW/L power converter at 400 W, with an estimated power loss of 15 W in total (96.2 % efficient) and forced air convection from one side.

Recent contributions co-authored by the author of this work [69, 70, 71, 72, 76] have demonstrated the potential of voxel-based solvers to implement compact and efficient thermal models. These models exploit a Finite-Difference Time-Domain (FDTD) formulation with adaptive meshing, enabling accurate three-dimensional temperature mapping of power converters with reduced computational cost. When executed on Graphics Processing Unit (GPU) platforms such as the Nvidia A30, implemented in PyTorch, the simulator achieves orders-of-magnitude faster computation compared to conventional FEM tools. Furthermore, embedded implementations on Field-Programmable Gate Array (FPGA) platforms have shown promise for deploying real-time digital twins with accuracy better than 5 %.

As a future research direction, coupling these voxel-based thermal solvers with the converters presented in this thesis would allow continuous monitoring of junction and hotspot temperatures, early detection of thermal anomalies, and long-term tracking of degradation. Unlike traditional lumped-parameter Foster or Cauer networks, the voxel approach explicitly accounts for geometry, material properties, and

inter-component coupling, thereby offering a more faithful representation of the thermal dynamics. This integration could evolve into a framework for condition-based maintenance and predictive reliability assessment in next-generation high-density aerospace converters, where thermal management is one of the primary design bottlenecks.

7.5 Control and Modelling

7.5.1 Closed Loop Operation

Up until now, the converters in this work have been tested fully in an open-loop manner. The control of three-phase LLC converters presents unique challenges compared to their single-phase counterparts. In conventional LLC topologies, regulation is primarily achieved through frequency modulation, where the switching frequency is varied around resonance to adjust the output voltage. Extending this principle to the three-phase domain introduces additional degrees of freedom, such as the relative phase shift between phases, which can be exploited to enhance performance but also complicates the design of robust control schemes.

One of the main difficulties arises from the nonlinear dynamics of the resonant tank, which become more pronounced when three interleaved tanks interact. Accurate small-signal modelling across the entire operating range is nontrivial, as the resonant frequency shifts with load and component tolerances. Furthermore, the presence of multiple resonant paths and circulating currents requires the controller to maintain phase balance and ensure that zero-voltage switching (ZVS) is preserved under varying load conditions.

Digital control has emerged as the most promising approach for this topology. Modern digital controllers, typically based on high-performance DSPs or FPGAs, enable fine-grained management of both frequency and phase-shift modulation. They also provide the flexibility to implement advanced algorithms, such as adaptive frequency tracking, phase balancing, and nonlinear gain compensation, which are necessary to stabilise the converter under wide input–output variations. However, this comes at the cost of increased computational demand, precise clock synchronisation, and the need for low-latency measurement and actuation.

The control requirements are particularly stringent in applications such as aerospace power electronics, where the three-phase LLC is envisioned. Besides high efficiency and compactness, these systems must guarantee stability across extreme temperature variations, rapid dynamic response to pulsed or unbalanced loads, and compliance with electromagnetic compatibility regulations. Consequently, the control system must integrate not only power regulation functions but also supervisory and diagnostic features, ensuring fault tolerance and long-term reliability.

7.5.2 High Output Capacitance (HOC) Modelling

Up until now, the analytical equations have been presented in section 3.2.1. The next step is to leverage them into a generalised simulator capable of automatically

solving the converter states, thus relieving the designer from the need to derive time-domain expressions for each operating condition.

The High Output Capacitance (HOC) model assumes a quasi-static output voltage due to a high output capacitance, effectively decoupling the resonant tank (L_r and C_r), the magnetising inductance (L_μ), and the output capacitance (C_L). Under this approximation, the behaviour of the LLC converter can be described with recursive piecewise equations that account for the non-linear transitions of the rectifier. The approach builds on the governing differential equations of the converter, which are reformulated into a state-transition problem solvable with matrix inversion techniques (e.g. Moore–Penrose pseudoinverse). The solver distinguishes two resonant states—L_r–C_r resonance when the rectifier conducts, and L_r–L_μ–C_r resonance when it is blocked—as shown in figs. 7.7 and 7.8.

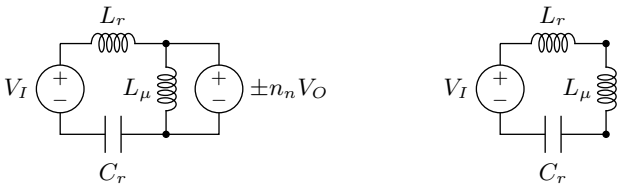

(a) State I (b) State II

Figure 7.7: Circuit representation of the two resonant states in a single-phase LLC converter.

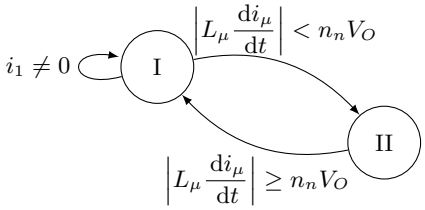

Figure 7.8: State transitions in a single-phase LLC converter.

Compared to the FHA, which only provides an averaged steady-state solution and often underestimates the maximum gain, the HOC model achieves simulation-grade accuracy. It tracks the converter's state variables ($i_{L_r}, v_{C_r}, i_{L_\mu}$) across switching periods, using recursive subintervals to capture the diode transitions. Although the transitions involve transcendental equations (similar to Kepler's equation), iterative numerical methods (bisection or secant) can be applied efficiently within each interval. This way, the solver yields the same accuracy as circuit-level simulators while retaining analytical tractability as compared in fig. 7.9, by only calculating the most critical time instants for the state transitioning in fig. 7.8, and automatically integrating the current to the output rectifier (only during state I).

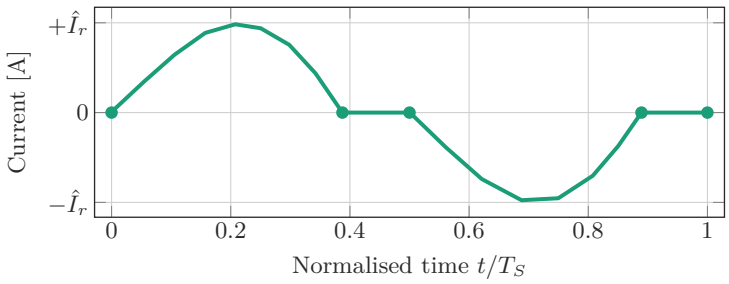

(a) Resonant tank currents

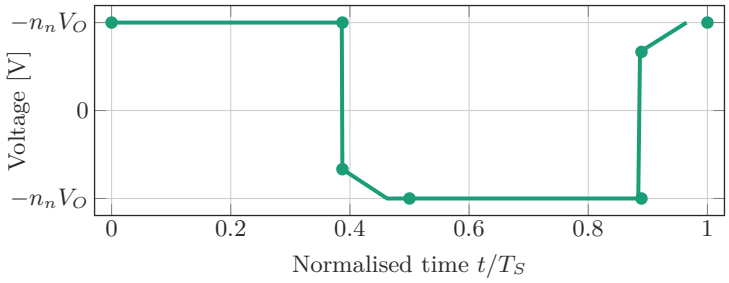

(b) Voltage at the primary winding

Figure 7.9: Example of time-domain solution in steady-state for a single-phase LLC converter, highlighting the most important time instants needed for solving it.

Another path is the generalisation of the model towards multi-phase resonant topologies, including the three-phase LLC converters. Some effort in this direction has been already developed by defining the possible states of the three-phase, eight in total for the inverter and the rectifier (see table 3.2 and table 3.3), implementing an early version that is able to work above resonance, but additional effort is needed before publication [78].

Future research should aim for the recursive solver to be adapted to handle parallel and interleaved resonant tanks, paving the way for a standardised design methodology applicable to a wide class of resonant converters. Ultimately, the HOC model could serve as a unifying framework, bridging analytical design, numerical simulation, and advanced control strategies in the pursuit of highly efficient and reliable power conversion systems.

Moreover, extending the HOC methodology beyond steady-state prediction can be useful, one promising direction is its integration into Optimised Trajectory Control (OTC), a technique that has demonstrated excellent performance for very fast load transients, specially important in very low-voltage Point of Load (PoL) applications [249]. The proposed recursive solver provides single-period accurate predictions of the converter response under sudden disturbances, such as load transients [250, 251], input voltage variations, or mode changes and morphing topologies (half-bridge to full-bridge) as described in section 2.3.1. By embedding the solver into the control loop, it becomes possible to compute feed-forward optimal trajectories, improving dynamic performance.

7.6 Regulations

Three-phase LLC converters are generally considered advantageous in terms of EMI performance, primarily due to the inherent cancellation of CM noise [252]. While recent studies have investigated this aspect from a theoretical and modelling perspective [163], experimental validation is still lacking, particularly for miniaturised prototypes. This gap is especially relevant given that one of the main claims of the three-phase LLC topology is its ability to meet the stringent electromagnetic compatibility requirements imposed in the aerospace sector, where compactness and compliance are critical.

APPENDIX A

Fourier Transformations

The Fourier transform are fundamental tools for analysing signals in the frequency domain. They provide a systematic way to decompose a time-domain waveform into a series of orthogonal sinusoids, thereby revealing its harmonic content. This appendix summarises the theoretical foundations and demonstrates the derivation of Fourier coefficients for various waveforms relevant to this work.

A.1 Basic Fourier Transformation

A periodic signal $x(\omega t)$ with period 2π can be expressed as a Fourier series of the form

$$x(\omega t) = \frac{a_0}{2} + \sum_{n=1}^{\infty} \left[a_n \cos(n\omega t) + b_n \sin(n\omega t) \right], \tag{A.1}$$

where the Fourier coefficients a_n and b_n are given by

$$a_n = \frac{1}{\pi} \int_{\omega t_0}^{\omega t_0 + 2\pi} x(\omega t) \cdot \cos(n\omega t) \, \mathrm{d}(\omega t), \tag{A.2}$$

$$b_n = \frac{1}{\pi} \int_{\omega t_0}^{\omega t_0 + 2\pi} x(\omega t) \cdot \sin(n\omega t) \, \mathrm{d}(\omega t). \tag{A.3}$$

These coefficients describe the projection of the original waveform onto the orthogonal basis $\{\cos(n\omega t), \sin(n\omega t)\}$. In practice, many engineering signals are piecewise continuous, which allows their Fourier decomposition to be derived by segments.

A.2 Piecewise Waveforms

For piecewise linear functions, we can formalise the problem by defining two vectors of $M \geq 2$ terms:

$$\mathbf{x} = [x_1, \ldots, x_i, \ldots, x_M], \tag{A.4}$$

$$\mathbf{y} = [y_1, \ldots, y_i, \ldots, y_M], \tag{A.5}$$

where y_i represents the value of the waveform at x_i, and the periodicity condition $\max(\mathbf{x}) - \min(\mathbf{x}) = 2\pi$ must hold for this analysis.

The Fourier coefficients for harmonic $n = 1, 2, \ldots$ are obtained by summing the integrals of each linear segment (x_m, x_{m+1}):

$$a_n = \frac{1}{\pi} \sum_{m=1}^{M-1} \int_{x_m}^{x_{m+1}} \left[y_m + \frac{y_{m+1} - y_m}{x_{m+1} - x_m} (x - x_m) \right] \cos(n \cdot x) \, \mathrm{d}x, \tag{A.6}$$

$$b_n = \frac{1}{\pi} \sum_{m=1}^{M-1} \int_{x_m}^{x_{m+1}} \left[y_m + \frac{y_{m+1} - y_m}{x_{m+1} - x_m} (x - x_m) \right] \sin(n \cdot x) \, \mathrm{d}x, \tag{A.7}$$

where a_0 represents the average value of the signal:

$$a_0 = \frac{1}{\pi} \int_{\omega t_0}^{\omega t_0 + 2\pi} x(\omega t) \, \mathrm{d}(\omega t). \tag{A.8}$$

This formulation allows systematic treatment of triangular, trapezoidal, and hybrid waveforms as shown in the following cases.

A.2.1 Triangular Waveform

Consider a symmetric triangular waveform consisting of two linear sections: one rising from -1 to $+1$, and one falling from $+1$ to -1. Using the piecewise vector definitions:

$$\mathbf{x} = [0, 1, 3, 4] \cdot \frac{2\pi}{4}, \tag{A.9}$$

$$\mathbf{y} = [0, +1, -1, 0], \tag{A.10}$$

the resulting Fourier coefficients are

$$a_n = 0, \tag{A.11}$$

$$b_n = \frac{8}{\pi^2} \cdot \frac{1}{n^2} \cdot \sin\left(\frac{n\pi}{2}\right). \tag{A.12}$$

As the function is odd and has zero average, only sine terms (b_n) are present.

A.2.2 Trapezoidal Waveform

A trapezoidal waveform can be decomposed into four linear sections: two constant plateaus and two linear ramps. Defining the piecewise samples as

$$\mathbf{x} = [0, 2, 3, 5, 6] \cdot \frac{2\pi}{6}, \tag{A.13}$$

$$\mathbf{y} = [-1, +1, +1, -1, -1], \tag{A.14}$$

we obtain

$$a_n = 0, \tag{A.15}$$

$$b_n = \frac{6\sqrt{3}}{\pi^2} \cdot \frac{1}{n^2} \cdot \sin^2\left(\frac{n\pi}{2}\right) \cdot \frac{2\sqrt{3}}{3} \sin\left(\frac{n\pi}{3}\right). \tag{A.16}$$

As with the triangular case, the waveform is odd with zero DC component, leaving only sine harmonics.

A.2.3 Superposition of a Trapezoidal and a Triangular Waveform

The superposition principle can be applied directly by summing piecewise functions. Defining the $\mathbf{x}$,

$$\mathbf{x} = [0, 1, 3, 5, 6, 7, 9, 11, 12] \cdot \frac{2\pi}{12}, \tag{A.17}$$

and $\mathbf{y}$,

$$\mathbf{y} = \left[0, +\frac{1}{2}, +1, +\frac{1}{2}, 0, -\frac{1}{2}, -1, -\frac{1}{2}, 0\right], \tag{A.18}$$

the Fourier coefficients are

$$a_n = 0, \tag{A.19}$$

$$b_n = \frac{\pi}{3} \cdot \frac{1}{n^2} \cdot \sin^2\left(\frac{n\pi}{2}\right) \cdot \operatorname{sgn}\left[\sin\left(\frac{\pi n}{6}\right)\right]. \tag{A.20}$$

Here, the sign function $\operatorname{sgn}(x)$ ensures correct alternation of harmonic polarity, and it has been directly derived from the tan function[1].

A.3 p-Pulse Sinusoidal Rectification

Fourier analysis can also be applied to rectified sinusoidal signals. For a p-pulse rectifier, the harmonic content is periodic with multiples of p.

The cosine Fourier coefficients are

$$a_n = \frac{1}{\pi} \sum_{k=1-p}^{p} \int_{-\frac{\pi}{2p}+k\frac{\pi}{p}}^{+\frac{\pi}{2p}+k\frac{\pi}{p}} \cos\left(\omega t - k \cdot \frac{\pi}{p}\right) \cdot \cos(n \cdot \omega t)\, \mathrm{d}(\omega t), \tag{A.21}$$

which after simplification yields

$$\begin{aligned} a_n = \frac{(-1)^n}{2\pi} \sum_{k=1-p}^{p} \Bigg\{ & \frac{1}{n+1}\Big[\sin\Big(\frac{(2k+1)\cdot n+1}{2p}\pi + n\pi\Big) - \sin\Big(\frac{(2k-1)\cdot n-1}{2p}\pi + n\pi\Big)\Big] \\ & + \frac{1}{n-1}\Big[\sin\Big(\frac{(2k+1)\cdot n-1}{2p}\pi + n\pi\Big) - \sin\Big(\frac{(2k-1)\cdot n+1}{2p}\pi + n\pi\Big)\Big]\Bigg\}, \end{aligned} \tag{A.22}$$

with

$$b_n = 0, \tag{A.23}$$

and the DC component

$$a_0 = \frac{p}{\pi} \int_{-\frac{\pi}{2p}}^{+\frac{\pi}{2p}} \cos(\omega t)\, \mathrm{d}(\omega t) = \frac{2p}{\pi} \sin\left(\frac{\pi}{2p}\right). \tag{A.24}$$

[1] A continuous definition is $\operatorname{sgn}(x) = \frac{2}{\pi}\left[\tan^{-1}(x) + \tan^{-1}(1/x)\right]$.

A.4 Voltage Ripple

The harmonic decomposition enables analytical evaluation of output ripple in rectifiers and filters. The peak-to-peak voltage ripple can be expressed as

$$\Delta V_O = \frac{I_O}{C_o} \int_{-\cos^{-1}\left(\frac{3}{\pi}\right)}^{+\cos^{-1}\left(\frac{3}{\pi}\right)} \left[\hat{I}_O \cos(\omega t) - I_O\right] \mathrm{d}(\omega t) \approx \frac{4 I_O}{C_o} \sqrt{\left(\frac{\pi}{3}\right)^2 - 1}, \tag{A.25}$$

approximated due for displaying purposes with less than a 5 % error, the complete solution is given by:

$$\Delta V_O = \frac{I_O}{C_o} \left[\tan^{-1}\left(\sqrt{\left(\frac{\pi}{3}\right)^2 - 1}\right) + \sqrt{\left(\frac{\pi}{3}\right)^2 - 1}\right]. \tag{A.26}$$

These expressions illustrate the direct link between harmonic distortion of rectified waveforms and the output voltage ripple.

APPENDIX B

Demonstrations

B.1 Fundamental-Harmonic Approximation $F_x(G_x)$

The FHA assumes that only the first harmonic of the switching waveform contributes significantly to the resonant tank behaviour. The normalised gain $G_x(F_x)$ can then be expressed as

$$G_x(F_x) = \frac{1}{n}\sqrt{\frac{1}{Q_s^2 \cdot \left(F_x - \frac{1}{F_x}\right)^2 + \left[1 + \frac{1}{m-1} \cdot \left(1 - \frac{1}{F_x^2}\right)\right]^2}}. \tag{B.1}$$

By squaring and inverting both sides, we obtain a polynomial of order six in F_x with null odd coefficients, i.e. a bicubic in F_x^2. This allows closed-form solutions for the inductive and capacitive regions of operation. Rewriting as

$$(F_x^2)^3 + c_2 \cdot (F_x^2)^2 + c_1 \cdot (F_x^2) + c_0 = 0,$$

the coefficients are

$$\begin{aligned} c_0 &= \frac{1}{(m-1)^2 \cdot Q_s^2}, \\ c_1 &= 1 - 2\frac{\sqrt{c_0} + c_0}{Q_s^2}, \\ c_2 &= \frac{-3Q_s^2 + c_2 + 1 - \frac{1}{G_x^2}}{Q_s^2}. \end{aligned} \tag{B.2}$$

By performing the variable change $t = (F_x^2) + c_2/3$ to obtain the depressed cubic $t^3 + pt + q = 0$, we define

$$p = c_1 - \frac{1}{3}c_2^2, \qquad q = \frac{2c_2^3 - 9c_2c_1 + 27c_0}{27}. \tag{B.3}$$

The inductive and capacitive solutions are then

$$F_{x,ind} = \sqrt{\frac{(-\mathrm{j}\sqrt{3}+1)\cdot\left(\sqrt{81q^2+12p^3}-9q\right)^{\frac{2}{3}}+2\sqrt[3]{12}\cdot p}{(\mathrm{j}\sqrt{3}+1)\cdot\sqrt[3]{18\sqrt{81q^2+12p^3}-162q}}+\frac{c_2}{3}}, \tag{B.4}$$

$$F_{x,cap} = \sqrt{\frac{(-\mathrm{j}\sqrt{3}-1)\cdot\left(\sqrt{81q^2+12p^3}-9q\right)^{\frac{2}{3}}-2\sqrt[3]{12}\cdot p}{(\mathrm{j}\sqrt{3}-1)\cdot\sqrt[3]{18\sqrt{81q^2+12p^3}-162q}}+\frac{c_2}{3}}. \tag{B.5}$$

Both solutions become complex once the maximum achievable gain is exceeded.

B.2 Kepler's Equation Eccentricity of an LLC Converter

The transition between resonant states occurs when the resonant current equals the magnetising current,

$$i_{L_r}(\Delta t) - i_{L_\mu}(\Delta t) = 0. \tag{B.6}$$

With initial conditions $i_{L_r}(0)$ and $u_{L_r}(0)$, the resonant current is

$$i_{L_r}(\Delta t) = \frac{u_{L_r}(0)}{Z_r}\sin(\omega_r \Delta t) + i_{L_r}(0)\cos(\omega_r \Delta t), \tag{B.7}$$

while the magnetising current is

$$i_{L_\mu}(\Delta t) = i_{L_\mu}(0) + \int_0^{\omega_r \Delta t} \frac{u_{L_\mu}(\varphi)}{Z_r(m-1)}\,\mathrm{d}\varphi. \tag{B.8}$$

By rearranging and defining constants, this equation reduces to Kepler's form

$$M = E - e\sin(E), \tag{B.9}$$

with

$$M = \tan^{-1}\left[Z_r\frac{i_{L_r}(0)}{u_{L_r}(0)}\right] - Z_r\frac{i_{L_\mu}(0)}{u_{L_\mu}(0)}(m-1), \tag{B.10}$$

$$e = \frac{Z_r(m-1)}{u_{L_\mu}(0)}\sqrt{\frac{u_{L_r}(0)^2}{Z_r^2}+i_{L_r}(0)^2}, \tag{B.11}$$

$$E = \omega_r \Delta t + \tan^{-1}\left[Z_r\frac{i_{L_r}(0)}{u_{L_r}(0)}\right]. \tag{B.12}$$

Here M is the mean anomaly, e the eccentricity, and E the eccentric anomaly, confirming the analogy with celestial mechanics.

B.3 Equivalent Waveforms Between Winding Configurations

To compare different transformer connections (wye–wye, delta–delta, wye–delta, delta–wye), the problem is simplified to two reference cases: wye–wye and wye–delta. The harmonic content of the reflected voltages determines the amplitude of the fundamental magnetising current.

B.3.1 Star–Star Configuration

From eq. (A.20), the first harmonic amplitude is

$$b_1 = \frac{6\sqrt{3}}{\pi^2}. \tag{B.13}$$

Thus, the peak of the magnetising current fundamental is

$$\hat{I}_\mu = G_r \frac{V_O}{\omega L_\mu} \cdot \frac{4\sqrt{3}}{3\pi} \approx 0.735 \cdot G_r \frac{V_O}{\omega L_\mu}. \tag{B.14}$$

B.3.2 Star–Polygon Configuration

In this case, evaluating eq. (A.16) gives

$$b_1 = \frac{\pi}{3}. \tag{B.15}$$

The corresponding magnetising current fundamental is

$$\hat{I}_\mu = G_r \frac{V_O}{\omega L_\mu} \cdot \frac{\pi^2}{9\sqrt{3}} \approx 0.633 \cdot G_r \frac{V_O}{\omega L_\mu}. \tag{B.16}$$

Bibliography

Aircraft Review

[1] Fei Gao. *Decentralised control and stability analysis of a multi-generator based electrical power system for more electric aircraft*. Dec. 2016. URL: https://eprints.nottingham.ac.uk/37955/.

[2] Hannah Ritchie. "What share of global CO_2 emissions come from aviation?" In: *Our World in Data* (2024). https://ourworldindata.org/global-aviation-emissions.

[3] International Energy Agency (IEA). *CO_2 Emissions in 2023*. Licence: CC BY 4.0. Accessed: 2025-01-25. Paris, 2024. URL: https://www.iea.org/reports/co2-emissions-in-2023.

[4] International Energy Agency (IEA). *CO_2 Emissions in 2009*. Licence: CC BY 4.0. Accessed: 2025-01-25. Paris, 2010. URL: https://www.iea.org/reports/co2-emissions-in-2010.

[5] International Council on Clean Transportation. *CO2 emissions from commercial aviation, 2018*. [Online; accessed 04-Jan-2020]. 2018. URL: https://theicct.org/publications/co2-emissions-commercial-aviation2018.

[6] Performance Review Commission. *Eurocontrol performance review report 2023: An assessment of air traffic management in Europe*. Tech. rep. PRR 2023. Accessed: 2025-01-22. EUROCONTROL, 2024. URL: https://www.eurocontrol.int/air-navigation-services-performance-review.

[7] R. Vaia. "Aerospace materials 2030: challenges and opportunities". In: 11591 (2021), p. 1159102. DOI: 10.1117/12.2582257.

[8] P. Jaramillo, S. Kahn Ribeiro, P. Newman, S. Dhar, O. E. Diemuodeke, T. Kajino, D. S. Lee, S. B. Nugroho, X. Ou, A. Hammer Strømman, and J. Whitehead. "Transport". In: *Climate Change 2022: Mitigation of Climate Change. Contribution of Working Group III to the Sixth Assessment Report of the Intergovernmental Panel on Climate Change*. Ed. by P. R. Shukla, J. Skea, R. Slade, A. Al Khourdajie, R. van Diemen, D. McCollum, M. Pathak, S. Some, P. Vyas, R. Fradera, M. Belkacemi, A. Hasija, G. Lisboa, S. Luz, and J. Malley. Cambridge, UK and New York, NY, USA: Cambridge University Press, 2022. DOI: 10.1017/9781009157926.012.

History of Aircraft

[9] Trent J. Carroll and T. Carroll. "Wright Brothers' Invention of 1903 Propeller and Genesis of Modern Propeller Theory". In: *Journal of Aircraft* 42 (2005), pp. 218–223. DOI: 10.2514/1.6361.

[10] R. Smith. "Marrying Airframes and Engines in Ground Test Facilities: An Evolutionary Revolution". In: *Journal of Aircraft* 33 (1996), pp. 649–679. DOI: 10.2514/3.47001.

[11] S. Bozhko, Tao Yang, Jean-Marc Le Peuvedic, P. Arumugam, M. Degano, A. La Rocca, Zeyuan Xu, M. Rashed, W. Fernando, C. Hill, C. Eastwick, S. Pickering, C. Gerada, and P. Wheeler. "Development of Aircraft Electric Starter–Generator System Based on Active Rectification Technology". In: *IEEE Transactions on Transportation Electrification* 4 (2018), pp. 985–996. DOI: 10.1109/TTE.2018.2863031.

[12] Knezevic Dragutin. "Application of Fluidic Elements and Systems for Aircraft, Missiles and Spacecrafts," in: (1971).

Aircraft Electrification

[13] Junhyung Bae. "A Review of Electric Actuation and Flight Control System for More/All Electric Aircraft". In: *2021 24th International Conference on Electrical Machines and Systems (ICEMS)*. 2021, pp. 1943–1947. DOI: 10.23919/ICEMS52562.2021.9634663.

[14] Vincenzo Madonna, Paolo Giangrande, and Michael Galea. "Electrical Power Generation in Aircraft: Review, Challenges, and Opportunities". In: *IEEE Transactions on Transportation Electrification* 4.3 (2018), pp. 646–659. DOI: 10.1109/TTE.2018.2834142.

[15] B. Sarlioglu and Casey T. Morris. "More Electric Aircraft: Review, Challenges, and Opportunities for Commercial Transport Aircraft". In: *IEEE Transactions on Transportation Electrification* 1 (2015), pp. 54–64. DOI: 10.1109/TTE.2015.2426499.

[16] Ashkan Barzkar and Mona Ghassemi. "Electric Power Systems in More and All Electric Aircraft: A Review". In: *IEEE Access* 8 (2020), pp. 169314–169332. DOI: 10.1109/ACCESS.2020.3024168.

[17] Fei Wang, Ruirui Chen, and K. Rajashekara. "Wide Bandgap Semiconductor-Based Power Electronics for Aviation". In: *IEEE Power Electronics Magazine* 9 (2022), pp. 26–36. DOI: 10.1109/MPEL.2022.3194225.

[18] Kartik Shreenath Bohra and Yoshita S. Dharmadhikari. "History of Fly by wire, The Tech That Expanded Human Horizons in Aviation". In: *2023 8th IEEE History of Electrotechnology Conference (HISTELCON)*. 2023, pp. 46–51. DOI: 10.1109/HISTELCON56357.2023.10365861.

[19] Yi Wei Lin. "The Development and Challenges of More Electric Aircraft". In: *Highlights in Science, Engineering and Technology* (2022). URL: https://api.semanticscholar.org/CorpusID:255289629.

[20] S. Bozhko, Tao Yang, Jean-Marc Le Peuvedic, P. Arumugam, M. Degano, A. La Rocca, Zeyuan Xu, M. Rashed, W. Fernando, C. Hill, C. Eastwick, S. Pickering, C. Gerada, and P. Wheeler. "Development of Aircraft Electric Starter–Generator System Based on Active Rectification Technology". In: *IEEE Transactions on Transportation Electrification* 4 (2018), pp. 985–996. DOI: 10.1109/TTE.2018.2863031.

[21] J.A. Rosero, J.A. Ortega, E. Aldabas, and L. Romeral. "Moving towards a more electric aircraft". In: *IEEE Aerospace and Electronic Systems Magazine* 22.3 (2007), pp. 3–9. DOI: 10.1109/MAES.2007.340500.

[22] Engineering National Academies of Sciences and Medicine. *Commercial Aircraft Propulsion and Energy Systems Research: Reducing Global Carbon Emissions*. Washington, DC: The National Academies Press, 2016. ISBN: 978-0-309-44096-7. DOI: 10.17226/23490. URL: https://nap.nationalacademies.org/catalog/23490/commercial-aircraft-propulsion-and-energy-systems-research-reducing-global-carbon.

[23] Pat Wheeler and Sergei Bozhko. "The More Electric Aircraft: Technology and challenges". In: *IEEE Electrification Magazine* 2.4 (2014), pp. 6–12. DOI: 10.1109/MELE.2014.2360720.

[24] Ehab Sayed, Mohamed Abdalmagid, G. Pietrini, Nicole-Marie Sa'adeh, A. Callegaro, C. Goldstein, and A. Emadi. "Review of Electric Machines in More-/Hybrid-/Turbo-Electric Aircraft". In: *IEEE Transactions on Transportation Electrification* 7 (2021), pp. 2976–3005. DOI: 10.1109/TTE.2021.3089605.

[25] Committee Emissions, Aeronautics Board, Division Sciences, and National Medicine. *Commercial aircraft propulsion and energy systems research: Reducing global carbon emissions*. Sept. 2016, pp. 1–122. ISBN: 9780309440967. DOI: 10.17226/23490.

[27] Xiaolong Zhang, Cheryl L. Bowman, Tim C. O'Connell, and Kiruba Sivasubramaniam Haran. "Large electric machines for aircraft electric propulsion". In: *Iet Electric Power Applications* 12 (2018), pp. 767–779. URL: https://api.semanticscholar.org/CorpusID:117133503.

[28] Jianming Li, Zhiyuan Yu, Yuping Huang, and Zhiguo Li. "A review of electromechanical actuation system for more electric aircraft". In: Oct. 2016, pp. 490–497. DOI: 10.1109/AUS.2016.7748100.

[29] Bulent Sarlioglu and Casey T. Morris. "More Electric Aircraft: Review, Challenges, and Opportunities for Commercial Transport Aircraft". In: *IEEE Transactions on Transportation Electrification* 1 (2015), pp. 54–64. URL: https://api.semanticscholar.org/CorpusID:12815419.

[30] A. Boglietti, A. Cavagnino, A. Tenconi, S. Vaschetto, and Politecnico di Torino. "The safety critical electric machines and drives in the more electric aircraft: A survey". In: *2009 35th Annual Conference of IEEE Industrial Electronics*. 2009, pp. 2587–2594. DOI: 10.1109/IECON.2009.5415238.

[31] M. Galea, Z. Xu, C. Tighe, T. Hamiti, C. Gerada, and S. Pickering. "Development of an aircraft wheel actuator for green taxiing". In: *2014 International Conference on Electrical Machines (ICEM)*. 2014, pp. 2492–2498. DOI: 10.1109/ICELMACH.2014.6960537.

[32] Fabian Kelch, Yinye Yang, Berker Bilgin, and Ali Emadi. "Investigation and design of an axial flux permanent magnet machine for a commercial mid-size aircraft electric taxiing system". In: *IET Electrical Systems in Transportation* 8.1 (2018), pp. 52–60. DOI: https://doi.org/10.1049/iet-est.2017.0039. eprint: https://ietresearch.onlinelibrary.wiley.com/doi/pdf/10.1049/iet-est.2017.0039. URL: https://ietresearch.onlinelibrary.wiley.com/doi/abs/10.1049/iet-est.2017.0039.

[33] Daniel Rohacs and Jozsef Rohacs. "Magnetic levitation assisted aircraft take-off and landing (feasibility study – GABRIEL concept)". In: *Progress in Aerospace Sciences* 85 (2016), pp. 33–50. ISSN: 0376-0421. DOI: https://doi.org/10.1016/j.paerosci.2016.06.001. URL: https://www.sciencedirect.com/science/article/pii/S0376042116300070.

[35] Wenping Cao, Barrie C. Mecrow, Glynn J. Atkinson, John W. Bennett, and David J. Atkinson. "Overview of Electric Motor Technologies Used for More Electric Aircraft (MEA)". In: *IEEE Transactions on Industrial Electronics* 59.9 (2012), pp. 3523–3531. DOI: 10.1109/TIE.2011.2165453.

[37] P. Jaramillo, S. Kahn Ribeiro, P. Newman, S. Dhar, O. E. Diemuodeke, T. Kajino, D. S. Lee, S. B. Nugroho, X. Ou, A. Hammer Strømman, and J. Whitehead. "Transport". In: *Climate Change 2022: Mitigation of Climate Change. Contribution of Working Group III to the Sixth Assessment Report of the Intergovernmental Panel on Climate Change*. Ed. by P. R. Shukla, J. Skea, R. Slade, A. Al Khourdajie, R. van Diemen, D. McCollum, M. Pathak, S. Some, P. Vyas, R. Fradera, M. Belkacemi, A. Hasija, G. Lisboa, S. Luz, and J. (eds.) Malley. Cambridge, UK, and New York, NY, USA: Cambridge University Press, 2022. Chap. 10. DOI: 10.1017/9781009157926.012. URL: https://www.ipcc.ch/report/ar6/wg3/downloads/report/IPCC_AR6_WGIII_Chapter10.pdf.

[38] M. K. Bradley and C. K. Droney. *Subsonic Ultra Green Aircraft Research: Phase I Final Report*. Tech. rep. NASA CR-2011-216847. s.l.: NASA, 2011.

[39] M. Bradley and C. K. Droney. *SUGAR Phase II: N+4 Advanced Concept Development*. Tech. rep. NASA/CR-2012-217556. s.l.: NASA, 2012.

[40] M. K. Bradley and C. K. Droney. *Subsonic Ultra Green Aircraft Research: Phase II. Volume II: Hybrid Electric Design Exploration*. Tech. rep. NASA/CR–2015-218704/Volume II. Huntington Beach, California: Boeing Research and Technology, 2015.

[41] Neal A. Harrison, Krishna Hoffman, David S. Lazzara, Eric Y. Reichenbach, Anthony J. Sclafani, and Christopher K. Droney. *Subsonic Ultra Green Aircraft Research: Phase IV Final Report – Volume I, Mach 0.80 Transonic Truss-Braced Wing High-Speed Design Report*. Technical Report. Huntington Beach, CA; St. Louis, MO; Long Beach, CA: Boeing Research and Technology, 2023.

[42] C. Pornet, C. Gologan, P. C. Vratny, A. Seitz, O. Schmitz, A. T. Isikveren, and M. Hornung. "Methodology for Sizing and Performance Assessment of Hybrid Energy Aircraft". In: *Journal of Aircraft* 52.4 (2015). Published Online: 5 Feb 2015, pp. 1150–1164. DOI: 10.2514/1.C032716. URL: https://doi.org/10.2514/1.C032716.

[43] Mona Ghassemi, Ashkan Barzkar, and Mohammadreza Saghafi. "All-Electric NASA N3-X Aircraft Electric Power Systems". In: *IEEE Transactions on Transportation Electrification* (Mar. 2022), pp. 1–1. DOI: 10.1109/TTE.2022.3158186.

[44] Airbus. *E-Fan X*. Accessed: 2025-01-23. 2025. URL: https://www.airbus.com/en/innovation/low-carbon-aviation/hybrid-and-electric-flight/e-fan-x.

[45] NASA Glenn Research Center. *STARC-ABL: A Hybrid Electric Aircraft Concept*. NASA Website. Accessed: 2025-01-31. 2023. URL: https://www1.grc.nasa.gov/aeronautics/eap/airplane-concepts/starc-abl/.

[46] J. J. Sachs-Wetstone, S. J. Bianco, J. L. Kratz, D. E. Culley, H. E. Buescher, M. A. Horning, J. R. Saus, and J. W. Connolly. "Hybrid-Electric Aero-Propulsion Controls Testbed Results". In: 2023.

[47] B. Kish, M. Wilde, Isaac Silver, B. Wheeler, Alexandra Cleveland, and Kristjana Reppen. "Flight Test Comparison of Three Air Vehicles Flying Urban Air Mobility Mission Trajectories". In: *2022 IEEE Aerospace Conference (AERO)* (2022), pp. 1–9. DOI: 10.1109/AERO53065.2022.9843555.

[48] Cheryl Bowman. *Visions of the Future: Hybrid Electric Aircraft Propulsion*. Tech. rep. Available at: https://ntrs.nasa.gov/archive/nasa/casi.ntrs.nasa.gov/20170002633.pdf, archived as: https://perma.cc/2L2P-WJYL. National Aeronautics and Space Administration (NASA), 2016.

[49] Hendrik Schefer, Leon Fauth, Tobias H. Kopp, Regine Mallwitz, Jens Friebe, and Michael Kurrat. "Discussion on Electric Power Supply Systems for All Electric Aircraft". In: *IEEE Access* 8 (2020), pp. 84188–84216. DOI: 10.1109/ACCESS.2020.2991804.

[50] K. Boomer, L. Scheik, and A. Hammoud. *Body of Knowledge (BOK): Gallium Nitride (GaN) Power Electronics for Space Applications*. Accessed: Jul. 7, 2020. NASA Electronic Parts and Packaging (NEPP). 2020. URL: https://nepp.nasa.gov/workshops/etw2019/talks/0619WED/1300%20-%20GaN%20BOK%20NEPP%20ETW%20Presentation7.pdf.

[51] Gianluca Marinaro, Giuseppe Di Lorenzo, and Antonio Pagano. "From a Battery-Based to a PEM Fuel Cell-Based Propulsion Architecture on a Lightweight Full Electric Aircraft: A Comparative Numerical Study". In: *Aerospace* 9.408 (2022). DOI: 10.3390/aerospace9080408.

[52] Tobias Graf, Robin Fonk, Christiane Bauer, Josef Kallo, and Caroline Willich. "Optimal Sizing of Fuel Cell and Battery in a Direct-Hybrid for Electric Aircraft". In: *Aerospace* 11.176 (2024). DOI: 10.3390/aerospace11030176.

[53] Elena Bataller-Planes, Nieves Lapena-Rey, Jonay Mosquera, Fortunato Orti, J. A. Oliver, O. Garcia, F. Moreno, J. Portilla, Y. Torroja, M. Vasic, S.C. Huerta, M. Trocki, P. Zumel, and J.A. Cobos. "Power balance of a hybrid power source in a power plant for a small propulsion aircraft". In: *2008 IEEE Power Electronics Specialists Conference*. 2008, pp. 295–301. DOI: 10.1109/PESC.2008.4591944.

[54] Oguz Kagan Keles, Ibrahim Hakyemez, Mustafa Bagriyanik, and Ozcan Kalenderli. "A Study on Power System Retrofit for Cessna-172S Aircraft by Using Hydrogen Fuel Cell and Battery Hybrid". In: *IEEE Access* 13 (2025), pp. 6089–6105. DOI: 10.1109/ACCESS.2025.3526633.

[55] Shashank Sripad, Alexander Bills, and Venkatasubramanian Viswanathan. "A review of safety considerations for batteries in aircraft with electric propulsion". In: *MRS Bulletin* 46 (2021), pp. 435–446. DOI: 10.1557/s43577-021-00097-1.

[56] Reyad Abdel-Fadil, Ahmad Eid, and Mazen Abdel-Salam. "Electrical distribution power systems of modern civil aircrafts". In: Feb. 2013.

[57] C. Yang, Min-Ze Lu, and C. Liaw. "Development of an Aircraft Electric Power Architecture With Integrated Ground Power Unit". In: *IEEE Transactions on Aerospace and Electronic Systems* 58 (2022), pp. 3446–3459. DOI: 10.1109/taes.2022.3151582.

[58] F. Khera, S. Bozhko, and Patrick Wheeler. "Design Analysis of SiC-MOSFET Based Bidirectional SSPC for Aircraft High Voltage DC Distribution Network". In: *IEEE Access* 11 (2023), pp. 113900–113912. DOI: 10.1109/ACCESS.2023.3323599.

[59] A. Lamantia, F. Giuliani, and A. Castellazzi. "Power Scalable Bi-Directional DC-DC Conversion Solutions for Future Aircraft Applications". In: *Energies* (2020). DOI: 10.3390/en13205470.

[87] Lei Wang, Donglai Zhang, Jinpei Duan, and Yangyang Hao. "High-Frequency 12 V Regulated LLC Bus Converter With Integrated Multiphase Inverse Coupled Resonant Inductor". In: *IEEE Transactions on Power Electronics* 38.5 (2023), pp. 5742–5762. DOI: 10.1109/TPEL.2022.3232893.

[88] Hiroaki Matsumori, Takashi Kosaka, Kisho Sekido, Kitae Kim, Takashi Egawa, and Nobuyuki Matsui. "Isolated DC-DC Converter utilizing GaN power device for Automotive Application". In: *2019 IEEE Applied Power Electronics Conference and Exposition (APEC)*. 2019, pp. 1704–1709. DOI: 10.1109/APEC.2019.8722097.

[122] Mohd Tariq, Ali I. Maswood, Chandana Jayampathi Gajanayake, and Amit K. Gupta. "Modeling and Integration of a Lithium-Ion Battery Energy Storage System With the More Electric Aircraft 270 V DC Power Distribution Architecture". In: *IEEE Access* 6 (2018), pp. 41785–41802. ISSN: 2169-3536. DOI: 10.1109/ACCESS.2018.2860679.

Aircraft Standards

[60] United States Department of Defense. *MIL-STD-704F: Aircraft Electric Power Characteristics*. Latest revision as of 2004. Washington, D.C.: U.S. Department of Defense, 2004.

[61] RTCA. *DO-160G: Environmental Conditions and Test Procedures for Airborne Equipment*. Revised December 2021. Washington, D.C.: RTCA, Inc., 2021.

[62] EUROCAE. *ED-14G: Environmental Conditions and Test Procedures for Airborne Equipment*. Revised December 2021. Paris, France: EUROCAE, 2021.

[63] RTCA. *DO-254: Design Assurance Guidance for Airborne Electronic Hardware*. RTCA Standard for airborne electronic hardware certification. Washington, D.C.: RTCA, Inc., 2000.

[64] EUROCAE. *ED-80: Design Assurance Guidance for Airborne Electronic Hardware*. Equivalent to RTCA DO-254. Paris, France: EUROCAE, 2000.

State-of-the-Art

[82] Gustavo C. Knabben, Grayson Zulauf, Jannik Schäfer, Johann W. Kolar, Matthias J. Kasper, Jon Azurza Anderson, and Gerald Deboy. "Conceptualization and Analysis of a Next-Generation Ultra-Compact 1.5-kW PCB-Integrated Wide-Input-Voltage-Range 12V-Output Industrial DC/DC Converter Module". In: *Electronics* 10.17 (2021). ISSN: 2079-9292. DOI: 10.3390/electronics10172158. URL: https://www.mdpi.com/2079-9292/10/17/2158.

[83] Byeong-Mun Song, R. McDowell, and A. Bushnell. "A three-level DC-DC converter with wide-input voltage operations for ship-electric-power-distribution systems". In: *Digest of Technical Papers. PPC-2003. 14th IEEE International Pulsed Power Conference (IEEE Cat. No.03CH37472)*. Vol. 2. 2003, 1309–1312 Vol.2. DOI: 10.1109/PPC.2003.1278055.

[84] Jiangheng Lu and Alireza Khaligh. "1kW, 400V/12V high step-down DC/DC converter: Comparison between phase-shifted full-bridge and LLC resonant converters". In: (2017), pp. 275–280. DOI: 10.1109/ITEC.2017.7993284.

[85] Aurora de Juan, Diego Serrano, Pedro Alou, Jean-Noël Mamousse, Romain Deniéport, and Miroslav Vasic. "High-Frequency LLC Converter with Narrow Frequency Variations for Aircraft Applications". In: *2022 IEEE Applied Power Electronics Conference and Exposition (APEC)*. 2022, pp. 2098–2105. DOI: 10.1109/APEC43599.2022.9773409.

[86] Branko Majmunović and Dragan Maksimović. "400–48-V Stacked Active Bridge Converter". In: *IEEE Transactions on Power Electronics* 37.10 (2022), pp. 12017–12029. DOI: 10.1109/TPEL.2022.3160413.

[89] Yuliang Cao, Minh Ngo, Ning Yan, Dong Dong, Rolando Burgos, and Agirman Ismail. "Design and Implementation of an 18-kW 500-kHz 98.8% Efficiency High-Density Battery Charger With Partial Power Processing". In: *IEEE Journal of Emerging and Selected Topics in Power Electronics* 10.6 (2022), pp. 7963–7975. DOI: 10.1109/JESTPE.2021.3108717.

[90] Chao Fei, Fred C. Lee, and Qiang Li. "High-Efficiency High-Power-Density LLC Converter With an Integrated Planar Matrix Transformer for High-Output Current Applications". In: *IEEE Transactions on Industrial Electronics* 64.11 (2017), pp. 9072–9082. DOI: 10.1109/TIE.2017.2674599.

[91] VICOR Corporation. *DC-DC Converter DCM4623TD2H31E0y7z - Datasheet*. Datasheet, accessed on 2025-07-26. 2020. URL: https://www.vicorpower.com/products/dcm/dcm4623td2h31e0y7z.

[92] Fei Xue, Ruiyang Yu, and Alex Q. Huang. "A 98.3% Efficient GaN Isolated Bidirectional DC–DC Converter for DC Microgrid Energy Storage System Applications". In: *IEEE Transactions on Industrial Electronics* 64.11 (2017), pp. 9094–9103. DOI: 10.1109/TIE.2017.2686307.

[116] Alex Lidow, Michael de Rooij, Johan Strydom, David Reusch, and John Glaser. *GaN Transistors for Efficient Power Conversion*. 3rd. Hoboken, NJ: John Wiley & Sons, 2020. ISBN: 9781119594147.

[117] Zhiqiang Guo, Deshang Sha, Xiaozhong Liao, and Jiankun Luo. "Input-Series-Output-Parallel Phase-Shift Full-Bridge Derived DC–DC Converters With Auxiliary LC Networks to Achieve Wide Zero-Voltage Switching Range". In: *IEEE Transactions on Power Electronics* 29.10 (2014), pp. 5081–5086. DOI: 10.1109/TPEL.2014.2309342.

[123] Rose A. Abramson, Samantha J. Gunter, David M. Otten, Khurram K. Afridi, and David J. Perreault. "Design and Evaluation of a Reconfigurable Stacked Active Bridge DC–DC Converter for Efficient Wide Load Range Operation". In: *IEEE Transactions on Power Electronics* 33.12 (2018), pp. 10428–10448. DOI: 10.1109/TPEL.2018.2801306.

[126] George W. Oughton and Glenn J. Smollinger. "Series Resonant Battery Charger and Control Therefor". Pat. US4200830A (United States). United States Patent and Trademark Office. Apr. 29, 1980. URL: https://patents.google.com/patent/US4200830A.

[127] Dominik Neumayr, Matthias Vöhringer, Nikolaos Chrysogelos, Gerald Deboy, and Johann W. Kolar. "P^{3}DCT—Partial-Power Pre-Regulated DC Transformer". In: *IEEE Transactions on Power Electronics* 34.7 (2019), pp. 6036–6047. DOI: 10.1109/TPEL.2018.2879064.

[128] Jinghai Zhou. "High Frequency, High Current Density Voltage Regulators". PhD thesis. 2005. URL: https://api.semanticscholar.org/CorpusID:61504708.

[142] Shahid Iqbal. "Interleaved LLC resonant converter with integrated dual transformer for PV power systems". In: *8th IET International Conference on Power Electronics, Machines and Drives (PEMD 2016)*. 2016, pp. 1–6. DOI: 10.1049/cp.2016.0209.

[143] Guangcan Li and Xinke Wu. "A 98.4% 380V-12V DCX With 1.3kW/in3 Power Density Using Low NFoM Devices and Resonant Drive Transformer". In: *IEEE Transactions on Power Electronics* 37.10 (2022), pp. 12346–12356. DOI: 10.1109/TPEL.2022.3178162.

[145] Zhifeng Sun, Qin Wang, Qunfang Wu, Lan Xiao, Jinbo Li, Zhitian Liu, and Junlin Zhu. "A Unified Common Inductor and Common Capacitor Current Sharing Method for Multiphase LLC Converter". In: *IEEE Transactions on Power Electronics* 37.10 (2022), pp. 12182–12196. DOI: 10.1109/TPEL.2022.3178497.

[174] Shivangi Sinha, Branko Majmunović, and Dragan Maksimović. "48V to 1V Active-Clamp Stacked Direct Forward Converter". In: *2023 IEEE 24th Workshop on Control and Modeling for Power Electronics (COMPEL)*. 2023, pp. 1–8. DOI: 10.1109/COMPEL52896.2023.10221063.

[175] Wardah Inam, Khurram K. Afridi, and David J. Perreault. "Variable Frequency Multiplier Technique for High-Efficiency Conversion Over a Wide Operating Range". In: *IEEE Journal of Emerging and Selected Topics in Power Electronics* 4.2 (2016), pp. 335–343. DOI: 10.1109/JESTPE.2015.2461615.

[176] Lei Gu, Wei Liang, Max Praglin, Sombuddha Chakraborty, and Juan Rivas-Davila. "Universal line input power factor preregulator using VFX technique". In: *2017 IEEE Applied Power Electronics Conference and Exposition (APEC)*. 2017, pp. 1810–1815. DOI: 10.1109/APEC.2017.7930944.

[177] Shota Kimura, Kimihiro Nanamori, Mostafa Noah, and Masayoshi Yamamoto. "A novel llc resonant dc-dc converter with integrated transformer". In: *2017 IEEE International Telecommunications Energy Conference (INTELEC)*. 2017, pp. 506–510. DOI: 10.1109/INTLEC.2017.8214186.

[178] Ke-Ming Chen, Tsorng-Juu Liang, Shih-Ming Chen, and Shih-Wen Tsai. "Design and implementation of a half-bridge dual LLC converter with symmetrical autotransformer". In: *2014 IEEE Energy Conversion Congress and Exposition (ECCE)*. 2014, pp. 4735–4741. DOI: 10.1109/ECCE.2014.6954049.

[180] Hongliang Wang, Yang Chen, Yan-Fei Liu, Jahangir Afsharian, and Zhihua Yang. "A Passive Current Sharing Method With Common Inductor Multiphase LLC Resonant Converter". In: *IEEE Transactions on Power Electronics* 32.9 (2017), pp. 6994–7010. DOI: 10.1109/TPEL.2016.2626312.

[184] Bor-Ren Lin and Huei-Yuan Shih. "ZVS Converter With Parallel Connection in Primary Side and Series Connection in Secondary Side". In: *IEEE Transactions on Industrial Electronics* 58.4 (2011), pp. 1251–1258. DOI: 10.1109/TIE.2010.2042422.

[185] Bor-Ren Lin and Jia-Yu Dong. "ZVS Resonant Converter With Parallel–Series Transformer Connection". In: *IEEE Transactions on Industrial Electronics* 58.7 (2011), pp. 2972–2979. DOI: 10.1109/TIE.2010.2077612.

[186] Bor-Ren Lin and Shin-Feng Wu. "ZVS Resonant Converter With Series-Connected Transformers". In: *IEEE Transactions on Industrial Electronics* 58.8 (2011), pp. 3547–3554. DOI: 10.1109/TIE.2010.2089946.

[208] Robert William Johnson. "Resonant power inverter and method of operation thereof". Patent EP0041360A2. Expired — filed May 27, 1981; priority May 29, 1980. Dec. 1981. URL: https://patents.google.com/patent/EP0041360A2/en.

Thermal Solutions

[94] Ali Moghassemi, S. I. Rahman, Gokhan Ozkan, C. Edrington, Zheyu Zhang, and P. Chamarthi. "Power Converters Coolant: Past, Present, Future, and a Path Toward Active Thermal Control in Electrified Ship Power Systems". In: *IEEE Access* 11 (2023), pp. 91620–91659. DOI: 10.1109/ACCESS.2023.3308523.

[95] Yi-Gao Lv, Gao-Peng Zhang, Qiu-Wang Wang, and Wen-Xiao Chu. "Thermal Management Technologies Used for High Heat Flux Automobiles and Aircraft: A Review". In: *Energies* 15.21 (2022). ISSN: 1996-1073. DOI: 10.3390/en15218316. URL: https://www.mdpi.com/1996-1073/15/21/8316.

[96] S. M. Imrat Rahman, Ali Moghassemi, Ali Arsalan, Laxman Timilsina, Phani Kumar Chamarthi, Behnaz Papari, Gokhan Ozkan, and Christopher S. Edrington. "Emerging Trends and Challenges in Thermal Management of Power Electronic Converters: A State of the Art Review". In: *IEEE Access* 12 (2024), pp. 50633–50672. DOI: 10.1109/ACCESS.2024.3385429.

[97] Reza Ilka, Yiju Wang, JiangBiao He, Ronak Ali, Aaron Swartz, Zhi Chen, Ning Ren, Z. George Zhang, Gefei Wu, and Roger England. "Multi-Physics Modeling of Power Electronic Converters with Liquid Immersion Cooling". In: *2023 IEEE Energy Conversion Congress and Exposition (ECCE)*. 2023, pp. 4698–4704. DOI: 10.1109/ECCE53617.2023.10362241.

[98] W. Canders, J. Hoffmann, and M. Henke. "Cooling Technologies for High Power Density Electrical Machines for Aviation Applications". In: *Energies* (2019). DOI: 10.3390/en12234579.

[99] Chunrong Zhao, Matthew Clarke, Hagen Kellermann, and Dries Verstraete. "Liquid Cooling Systems for Batteries of Electric Vertical Takeoff and Landing Aircraft". In: *Journal of Aircraft* (2024). DOI: 10.2514/1.c037404.

[100] S.M. Sohel Murshed and C.A. Nieto de Castro. "A critical review of traditional and emerging techniques and fluids for electronics cooling". In: *Renewable and Sustainable Energy Reviews* 78 (2017), pp. 821–833. ISSN: 1364-0321. DOI: https://doi.org/10.1016/j.rser.2017.04.112. URL: https://www.sciencedirect.com/science/article/pii/S1364032117305944.

[101] N. E. Lima Baschera, A. Lidozzi, G. Zummo, L. Saraceno, F. Riccardi, F. Ortenzi, M. di Benedetto, and L. Solero. "Advances in Two-Phase Cooling for Next Power Electronics Converters". In: *IEEE Open Journal of Industry Applications* 5 (2024), pp. 381–390. DOI: 10.1109/OJIA.2024.3451990.

[102] Martin Pavlovsky, Sjoerd Walter Hero de Haan, and Jan Abraham Ferreira. "Reaching High Power Density in Multikilowatt DC–DC Converters With Galvanic Isolation". In: *IEEE Transactions on Power Electronics* 24.3 (2009), pp. 603–612. DOI: 10.1109/TPEL.2008.2008650.

[103] Ekaterina Abramushkina, Assel Zhaksylyk, Thomas Geury, Mohamed El Baghdadi, and Omar Hegazy. "A Thorough Review of Cooling Concepts and Thermal Management Techniques for Automotive WBG Inverters: Topology, Technology and Integration Level". In: *Energies* 14.16 (2021). ISSN: 1996-1073. DOI: 10.3390/en14164981. URL: https://www.mdpi.com/1996-1073/14/16/4981.

Capacitor Technology

[112] Ziming Cai, Hongxian Wang, Peiyao Zhao, Lingling Chen, Chaoqiong Zhu, Kezhen Hui, Long-tu Li, and Xiao-hui Wang. "Significantly enhanced dielectric breakdown strength and energy density of multilayer ceramic capacitors with high efficiency by electrodes structure design". In: *Applied Physics Letters* (2019). DOI: 10.1063/1.5110527.

[113] Yunlei Jiang, Borong Hu, Yanfeng Shen, Xufu Ren, Steve Sandler, Stephan Hofmann, and Teng Long. "Loss Characterization and Modeling of Class II Multilayer Ceramic Capacitors: A Synergistic Material-Microstructure-Device Approach". In: *IEEE Transactions on Power Electronics* 38.11 (2023), pp. 13535–13554. DOI: 10.1109/TPEL.2023.3286818.

[114] David Menzi, Dominik Bortis, Grayson Zulauf, Morris Heller, and Johann W. Kolar. "Novel iGSE-C Loss Modeling of X7R Ceramic Capacitors". In: *IEEE Transactions on Power Electronics* 35.12 (2020), pp. 13367–13383. DOI: 10.1109/TPEL.2020.2996010.

[115] Robert Lu. *Temperature, Bias and Ageing Impact to Capacitance Stability of MLCC Ceramic Capacitors*. Accessed on 8 September 2025. Jan. 2023. URL: https://passive-components.eu/temperature-bias-and-ageing-impact-to-capacitance-stability-of-mlcc-ceramic-capacitors/.

Semiconductor Technology

[221] Anliang Hu and Jürgen Biela. "Fast and Accurate Data Sheet Based Analytical Switching Loss Model for a SiC MOSFET and Schottky Diode Half-Bridge". In: *IEEE Open Journal of Power Electronics* 5 (2024), pp. 1684–1696. DOI: 10.1109/OJPEL.2024.3485891.

[226] Elena Barbarini. *Reverse Technology and Cost Report*. Available: https://www.slideshare.net/Yole_Developpement/gan-on-si-hemt-vs-sjmosfet-technology-and-cost-comparison-teardown-reverse-costingreport-published-by-yole-developpement. 2016. URL: https://www.slideshare.net/Yole_Developpement/gan-on-si-hemt-vs-sjmosfet-technology-and-cost-comparison-teardown-reverse-costingreport-published-by-yole-developpement.

[227] Yanfeng Shen, Huai Wang, Zhan Shen, Yongheng Yang, and Frede Blaabjerg. "A 1-MHz Series Resonant DC–DC Converter With a Dual-Mode Rectifier for PV Microinverters". In: *IEEE Transactions on Power Electronics* 34.7 (2019), pp. 6544–6564. DOI: 10.1109/TPEL.2018.2876346.

[228] Edward A. Jones, Fred Wang, Daniel Costinett, Zheyu Zhang, Ben Guo, Bo Liu, and Ren Ren. "Characterization of an enhancement-mode 650-V GaN HFET". In: *2015 IEEE Energy Conversion Congress and Exposition (ECCE)*. 2015, pp. 400–407. DOI: 10.1109/ECCE.2015.7309716.

[247] Xudong Wang, Zhengming Zhao, Kai Li, Yicheng Zhu, and Kainan Chen. "Analytical Methodology for Loss Calculation of SiC MOSFETs". In: *IEEE Journal of Emerging and Selected Topics in Power Electronics* 7.1 (2019), pp. 71–83. DOI: 10.1109/JESTPE.2018.2863731.

[248] Dong Yan, Lijun Hang, Yuanbin He, Zhen He, and Pingliang Zeng. "An Accurate Switching Transient Analytical Model for GaN HEMT under the Influence of Nonlinear Parameters". In: *Energies* 15.1 (2022), p. 2966. DOI: 10.3390/en15082966.

Control Schemes

[81] Milan M. Jovanović and Brian T. Irving. "On-the-Fly Topology-Morphing Control—Efficiency Optimization Method for LLC Resonant Converters Operating in Wide Input- and/or Output-Voltage Range". In: *IEEE Transactions on Power Electronics* 31.3 (2016), pp. 2596–2608. DOI: 10.1109/TPEL.2015.2440099.

[82] Gustavo C. Knabben, Grayson Zulauf, Jannik Schäfer, Johann W. Kolar, Matthias J. Kasper, Jon Azurza Anderson, and Gerald Deboy. "Conceptualization and Analysis of a Next-Generation Ultra-Compact 1.5-kW PCB-Integrated Wide-Input-Voltage-Range 12V-Output Industrial DC/DC Converter Module". In: *Electronics* 10.17 (2021). ISSN: 2079-9292. DOI: 10.3390/electronics10172158. URL: https://www.mdpi.com/2079-9292/10/17/2158.

[129] S. M. Showybul Islam Shakib and Saad Mekhilef. "A Frequency Adaptive Phase Shift Modulation Control Based LLC Series Resonant Converter for Wide Input Voltage Applications". In: *IEEE Transactions on Power Electronics* 32.11 (2017), pp. 8360–8370. DOI: 10.1109/TPEL.2016.2643006.

[130] Xiaofeng Sun, Xiaohua Li, Yanfeng Shen, Baocheng Wang, and Xiaoqiang Guo. "Dual-Bridge LLC Resonant Converter With Fixed-Frequency PWM Control for Wide Input Applications". In: *IEEE Transactions on Power Electronics* 32.1 (2017), pp. 69–80. DOI: 10.1109/TPEL.2016.2530748.

[131] Yuqi Wei, Quanming Luo, and H. Alan Mantooth. "An LLC Converter With Multiple Operation Modes for Wide Voltage Gain Range Application". In: *IEEE Transactions on Industrial Electronics* 68.11 (2021), pp. 11111–11124. DOI: 10.1109/TIE.2020.3029474.

[132] Il-Oun Lee and Gun-Woo Moon. "Analysis and Design of a Three-Level LLC Series Resonant Converter for High- and Wide-Input-Voltage Applications". In: *IEEE Transactions on Power Electronics* 27.6 (2012), pp. 2966–2979. DOI: 10.1109/TPEL.2011.2174381.

[133] Kemal Kalayci, Onur Demirel, Ugur Arifoglu, and Halime Hizarci. "Analysis of Three-Level T-Type LLC Resonant Isolated Bidirectional DC–DC Converter Under Three-Degrees-of-Freedom Modulation". In: *IEEE Access* 11 (2023), pp. 60605–60625. DOI: 10.1109/ACCESS.2023.3285265.

[134] G.B. Joung, C.T. Rim, and G.H. Cho. "Modeling of quantum series resonant converters-controlled by integral cycle mode". In: *Conference Record of the 1988 IEEE Industry Applications Society Annual Meeting*. 1988, 821–826 vol.1. DOI: 10.1109/IAS.1988.25156.

[135] Yuqi Wei, Quanming Luo, and H. Alan Mantooth. "A Novel LLC Converter With Topology Morphing Control for Wide Input Voltage Range Application". In: *IEEE Journal of Emerging and Selected Topics in Power Electronics* 10.2 (2022), pp. 1563–1574. DOI: 10.1109/JESTPE.2020.3044207.

[136] Cheng Li and Haoyu Wang. "A Wide Gain Range LLC Resonant Converter Based on Reconfigurable Bridge and Asymmetric Resonant Tanks". In: *2019 IEEE Applied Power Electronics Conference and Exposition (APEC)*. 2019, pp. 3281–3286. DOI: 10.1109/APEC.2019.8722214.

[137] Philipp Rehlaender, Frank Schafmeister, and Joachim Böcker. "Interleaved Single-Stage LLC Converter Design Utilizing Half- and Full-Bridge Configurations for Wide Voltage Transfer Ratio Applications". In: *IEEE Transactions on Power Electronics* 36.9 (2021), pp. 10065–10080. DOI: 10.1109/TPEL.2021.3067843.

[138] Hao Tong, Zheyu Miao, Huipin Lin, Wenxi Yao, Wuhua Li, and Zhengyu Lu. "A Three-Level LLC Converter With Flexible Variable-Mode Control for Wide Gain Range Application". In: *IEEE Transactions on Power Electronics* 38.4 (2023), pp. 4503–4519. DOI: 10.1109/TPEL.2022.3232365.

[139] Wolfspeed, Inc. *CRD-30DD12N-K: 30kW Three-phase Interleaved LLC DC/DC Converter*. https://www.wolfspeed.com. [Online; accessed 27-Jul-2025]. 2022.

[146] Hui Chen, Xinke Wu, and Shuai Shao. "A Current-Sharing Method for Interleaved High-Frequency LLC Converter With Partial Energy Processing". In: *IEEE Transactions on Industrial Electronics* 67.2 (2020), pp. 1498–1507. DOI: 10.1109/TIE.2019.2896102.

[147] Zhiyuan Hu, Yajie Qiu, Laili Wang, and Yan-Fei Liu. "An Interleaved LLC Resonant Converter Operating at Constant Switching Frequency". In: *IEEE Transactions on Power Electronics* 29.6 (2014), pp. 2931–2943. DOI: 10.1109/TPEL.2013.2273939.

[156] R. Mirzahosseini and F. Tahami. "A phase-shift three-phase bidirectional series resonant DC/DC converter". In: *IECON 2011 - 37th Annual Conference of the IEEE Industrial Electronics Society*. 2011, pp. 1137–1143. DOI: 10.1109/IECON.2011.6119468.

[249] Ahmed Nabih, Mohamed Ahmed, Qiang Li, and Fred. C. Lee. "Simplified Optimal Trajectory Control for 1 MHz LLC Converter with Wide Input Voltage Range". In: *2019 IEEE Applied Power Electronics Conference and Exposition (APEC)*. 2019, pp. 212–219. DOI: 10.1109/APEC.2019.8722275.

[250] Weiyi Feng, Fred C. Lee, and Paolo Mattavelli. "Simplified Optimal Trajectory Control (SOTC) for LLC Resonant Converters". In: *IEEE Transactions on Power Electronics* 28.5 (2013), pp. 2415–2426. DOI: 10.1109/TPEL.2012.2212213.

[251] Chao Fei, Fred C. Lee, and Qiang Li. "Light load efficiency improvement for high frequency LLC converters with Simplified Optimal Trajectory Control (SOTC)". In: *2015 IEEE Energy Conversion Congress and Exposition (ECCE)*. 2015, pp. 1653–1659. DOI: 10.1109/ECCE.2015.7309893.

Topology Operation

[118] Matthias Kasper, Ralph M. Burkart, Gerald Deboy, and Johann W. Kolar. "ZVS of Power MOSFETs Revisited". In: *IEEE Transactions on Power Electronics* 31.12 (2016), pp. 8063–8067. DOI: 10.1109/TPEL.2016.2574998.

[119] Texas Instruments. *Phase-Shifted Full-Bridge Design Guide*. https://www.ti.com/lit/ug/tidu248/tidu248.pdf. Accessed: 2025-08-03. 2015. (Visited on 08/03/2025).

[120] M. Coppola, A. Dannier, and A. Del Pizzo. "Loss Analysis of Dual Active Bridge DC-DC Converter for Aircraft Application". In: *2020 International Symposium on Power Electronics, Electrical Drives, Automation and Motion (SPEEDAM)* (2020), pp. 769–773. DOI: 10.1109/SPEEDAM48782.2020.9161950.

[121] Alberto Rodríguez, Aitor Vázquez, Diego G. Lamar, Marta M. Hernando, and Javier Sebastián. "Different Purpose Design Strategies and Techniques to Improve the Performance of a Dual Active Bridge With Phase-Shift Control". In: *IEEE Transactions on Power Electronics* 30.2 (2015), pp. 790–804. DOI: 10.1109/TPEL.2014.2309853.

[124] J. Everts. "Closed-Form Solution for Efficient ZVS Modulation of DAB Converters". In: *IEEE Transactions on Power Electronics* 32 (2017), pp. 7561–7576. DOI: 10.1109/TPEL.2016.2633507.

[125] S. Mukherjee, Ashish Kumar, and S. Chakraborty. "Comparison of DAB and LLC DC–DC Converters in High-Step-Down Fixed-Conversion-Ratio (DCX) Applications". In: *IEEE Transactions on Power Electronics* 36 (2021), pp. 4383–4398. DOI: 10.1109/TPEL.2020.3019796.

Magnetics

[104] John S. Glaser, Jeffrey Nasadoski, and Richard Heinrich. "A 900W, 300V to 50V Dc-dc Power Converter with a 30MHz Switching Frequency". In: *2009 Twenty-Fourth Annual IEEE Applied Power Electronics Conference and Exposition*. 2009, pp. 1121–1128. DOI: 10.1109/APEC.2009.4802804.

[105] J. A. Ferreira. "Eddy Currents in Conductors". In: *Electromagnetic Modelling of Power Electronic Converters*. Boston, MA: Springer US, 1989, pp. 49–65. ISBN: 978-1-4757-2014-3. DOI: 10.1007/978-1-4757-2014-3_4.

[106] Marian Kazimierczuk. *High-Frequency Magnetic Components: Second Edition*. Nov. 2013, pp. 1–729. ISBN: 9781118717790. DOI: 10.1002/9781118717806.

[107] R. Schlesinger. "Analytical Transformer Leakage Inductance Modelling". Doctoral Thesis. ETH Zurich, 2023. URL: https://www.research-collection.ethz.ch/handle/20.500.11850/644945.

[108] Rouhollah Shafaei, Maria Celeste Garcia Perez, and Martin Ordonez. "Planar Transformers in LLC Resonant Converters: High-Frequency Fringing Losses Modeling". In: *IEEE Transactions on Power Electronics* 35.9 (2020), pp. 9632–9649. DOI: 10.1109/TPEL.2020.2971424.

[109] W.G. Hurley and M.C. Duffy. "Calculation of self and mutual impedances in planar magnetic structures". In: *IEEE Transactions on Magnetics* 31.4 (1995), pp. 2416–2422. DOI: 10.1109/20.390151.

[110] Alex J. Hanson, Julia A. Belk, Seungbum Lim, Charles R. Sullivan, and David J. Perreault. "Measurements and Performance Factor Comparisons of Magnetic Materials at High Frequency". In: *IEEE Transactions on Power Electronics* 31.11 (2016), pp. 7909–7925. DOI: 10.1109/TPEL.2015.2514084.

[111] Marcin Kacki. "Investigation of the High-Frequency Effects in MnZn Ferrites for EMI Filter Applications". PhD. Thesis submitted for the degree of Doctor of Philosophy, Department of Electrical and Electronic Engineering. PhD thesis. Cork, Ireland: University College Cork, National University of Ireland, 2022.

[140] Lei Li, Feng Hong, Minggang Chen, and Qinsong Qian. "A high power density magnetically integrated scheme of LLC converter". In: *IET Power Electronics* 18.1 (2025), e70006. DOI: https://doi.org/10.1049/pel2.70006. eprint: https://ietresearch.onlinelibrary.wiley.com/doi/pdf/10.1049/pel2.70006. URL: https://ietresearch.onlinelibrary.wiley.com/doi/abs/10.1049/pel2.70006.

[141] Mike Kavian Ranjram and David John Perreault. "A 380-12 V, 1-kW, 1-MHz Converter Using a Miniaturized Split-Phase, Fractional-Turn Planar Transformer". In: *IEEE Transactions on Power Electronics* 37.2 (2022), pp. 1666–1681. DOI: 10.1109/TPEL.2021.3103434.

[144] Y.-F. Liu and Z. Hu. "Interleaved resonant converter". Patent WO2014/040170A1. 2014.

[148] Nenghong Xia, Shuang Yan, Huaqi Ma, Xike Mao, and Mengqi Chen. "Double B-type magnetic integrated transformer based input-parallel output-parallel LLC resonant converter modules". In: *Frontiers in Energy Research* (2024). DOI: 10.3389/fenrg.2024.1343247.

[149] Minjie Chen and Charles R. Sullivan. "Unified Models for Coupled Inductors Applied to Multiphase PWM Converters". In: *IEEE Transactions on Power Electronics* 36.12 (2021), pp. 14155–14174. DOI: 10.1109/TPEL.2021.3088083.

[152] Jing-Yuan Lin, Hsuan-Yu Yueh, Yi-Feng Lin, and Pin-Hsien Liu. "Analysis and Design of Three-Phase LLC Resonant Converter with Matrix Transformers". In: *Energies* (2022). DOI: 10.3390/en15041315.

[157] Hiroaki Matsumori, Toshihisa Shimizy, Koushi Takano, and Hitoshi Ishii. "Three-Phase AC Filter Inductor Design for Three-Phase PWM Inverter for Conversion Efficiency Improvement at Low Load". In: *Electrical Engineering in Japan* 203.1 (2018), pp. 37–49. DOI: https://doi.org/10.1002/eej.23053.

[158] Mostafa Noah, Shota Kimura, Jun Imaoka, Wilmar Martinez, Shun Endo, Masayoshi Yamamoto, and Kazuhiro Umetani. "Magnetic Design and Experimental Evaluation of a Commercially Available Single Integrated Transformer in Three-Phase LLC Resonant Converter". In: *IEEE Transactions on Industry Applications* 54.6 (2018), pp. 6190–6204. DOI: 10.1109/TIA.2018.2856631.

[168] Yu-Chen Liu, Chen Chen, Yu-Chen Chung, Meng-Chi Tsai, and Katherine A. Kim. "Integrated magnetics optimization process for an interleaved three-phase buck converter at 500 kHz". In: *IET Power Electronics* 16.10 (2023), pp. 1743–1753. DOI: https://doi.org/10.1049/pel2.12338. eprint: https://ietresearch.onlinelibrary.wiley.com/doi/pdf/10.1049/pel2.12338. URL: https://ietresearch.onlinelibrary.wiley.com/doi/abs/10.1049/pel2.12338.

[181] "Three-phase transformer, three-phase inductor, and magnetic core". CN215183430U. Chinese Utility Model Patent. Dec. 2021.

[182] Xiang Zhang, S. Pan, and P. Jain. "A Discrete Coupled Multiphase Interleaved LLC Converter With Symmetrical Components Analysis". In: *IEEE Transactions on Power Electronics* 38 (2023), pp. 14150–14165. DOI: 10.1109/TPEL.2023.3279822.

[183] "Multiphase Three-Phase Integrated Inductor and Transformer". US12212247B2. U.S. Patent. Jan. 2025.

[187] Edward Herbert. "Flat Matrix Transformer". Patent US4665357A (United States). United States Patent and Trademark Office. May 1987.

[188] Edward Herbert. "Design and Application of Matrix Transformers and Symmetrical Converters". In: *Fifth International High-Frequency Power Conversion Conference*. Santa Clara, California: FMTT, May 11, 1990.

[189] Yong Li, Junyang Bao, Bangyin Liu, and Shanxu Duan. "Design and Optimization of Vertically Integrated Four-Leg Matrix Transformer for Bidirectional LLC Converter". In: *IEEE Transactions on Industrial Electronics* 72 (2025), pp. 3840–3850. DOI: 10.1109/TIE.2024.3454449.

[190] Yuyang Jiang, X. Ruan, Renxi Dong, and Ye Xu. "A DCX-LLC Resonant Converter with High Input-Output Voltage Ratio Based on an Integrated Matrix Transformer". In: *IECON 2022 – 48th Annual Conference of the IEEE Industrial Electronics Society* (2022), pp. 1–5. DOI: 10.1109/IECON49645.2022.9968663.

[192] Siqi Li, Enguo Rong, Qingyun Min, and Sizhao Lu. "A Half-Turn Transformer With Symmetry Magnetic Flux for High-Frequency-Isolated DC/DC Converters". In: *IEEE Transactions on Power Electronics* 33.8 (2018), pp. 6467–6470. DOI: 10.1109/TPEL.2018.2789939.

[193] Yu-Chen Liu, Kai-De Chen, Chen Chen, Yong-Long Syu, Guan-Wei Lin, Katherine A. Kim, and Huang-Jen Chiu. "Quarter-Turn Transformer Design and Optimization for High Power Density 1-MHz LLC Resonant Converter". In: *IEEE Transactions on Industrial Electronics* 67.2 (2020), pp. 1580–1591. DOI: 10.1109/TIE.2019.2902821.

[194] Kangping Wang, Qingyuan Gao, Gaohao Wei, and Xu Yang. "Integrated Fractional-Turn Planar Transformer for MHz and High-Current Applications". In: *IEEE Transactions on Power Electronics* 38.6 (2023), pp. 7374–7384. DOI: 10.1109/TPEL.2023.3244846.

[195] Siqi Li, Qingyun Min, Enguo Rong, Rui Zhang, Xiao Du, and Sizhao Lu. "A Magnetic Integration Half-Turn Planar Transformer and its Analysis for LLC Resonant DC-DC Converters". In: *IEEE Access* 7 (2019), pp. 128408–128418. DOI: 10.1109/ACCESS.2019.2939274.

[196] Kangping Wang, Qingyuan Gao, Kexin Zhao, Hongchang Li, and Xu Yang. "Planar Fractional-Winding Transformer With Flexible Asymmetric Structure". In: *IEEE Transactions on Power Electronics* 39.8 (2024), pp. 9943–9952. DOI: 10.1109/TPEL.2024.3400833.

[197] Yu-Chen Liu, Chen Chen, Kai-De Chen, Yong-Long Syu, Wen-Hao Xue, Yun-Yan Chen, Katherine A. Kim, and Huang-Jen Chiu. "Design and development of a fractional-turn transformer for high power density LLC resonant converters". In: *2021 IEEE Applied Power Electronics Conference and Exposition (APEC)*. 2021, pp. 335–342. DOI: 10.1109/APEC42165.2021.9487397.

[198] Yu-Chen Liu, Meng-Chi-Tsai, and Phuc-Dinh Nguyen. "Analysis of Winding Coverage in Planar Transformers with Fractional Turns for High Frequency LLC Resonant Converters". In: *2022 International Power Electronics Conference (IPEC-Himeji 2022- ECCE Asia)*. 2022, pp. 1179–1184. DOI: 10.23919/IPEC-Himeji2022-ECCE53331.2022.9807080.

[199] Xiaobin Li, Hongbo Ma, and Zhongcai Qiu. "Half-Turn LLC-DCX Based Two-Stage DC-DC Converter for Wide Input Voltage Range Applications". In: *2024 IEEE 7th International Electrical and Energy Conference (CIEEC)*. 2024, pp. 1396–1400. DOI: 10.1109/CIEEC60922.2024.10583250.

[200] Michael A. de Rooij, Alejandro Pozo Arribas, and John S. Glaser. "High Power-Density, Bi-Directional, 48 V to 12 V Converter using eGaN FETs for Next Generation BEV's". In: *PCIM Europe 2023; International Exhibition and Conference for Power Electronics, Intelligent Motion, Renewable Energy and Energy Management*. 2023, pp. 1–8. DOI: 10.30420/566091095.

[201] Zhicheng Guo, Ruiyang Yu, Wei Xu, Xianyong Feng, and Alex Q. Huang. "Design and Optimization of a 200-kW Medium-Frequency Transformer for Medium-Voltage SiC PV Inverters". In: *IEEE Transactions on Power Electronics* 36.9 (2021), pp. 10548–10560. DOI: 10.1109/TPEL.2021.3059879.

[202] Ahmed Nabih. "Efficient Planar Integrated Transformer-Inductor with High PCB Utilization and Optimized Core". In: *TechRxiv* (Mar. 2023). DOI: 10.36227/techrxiv.22213780.v1. URL: https://doi.org/10.36227/techrxiv.22213780.v1.

[203] Ahmed Nabih, Qiang Li, and Fred C. Lee. "Magnetic Integration of Four-Transformer Matrix with High Controllable Leakage Inductance using a Five-Leg Magnetic". In: *2022 IEEE Applied Power Electronics Conference and Exposition (APEC)*. 2022, pp. 693–700. DOI: 10.1109/APEC43599.2022.9773575.

[204] Mingxiao Li, Ziwei Ouyang, and Michael A. E. Andersen. "High-Frequency LLC Resonant Converter With Magnetic Shunt Integrated Planar Transformer". In: *IEEE Transactions on Power Electronics* 34.3 (2019), pp. 2405–2415. DOI: 10.1109/TPEL.2018.2842029.

[205] Ahmed Nabih and Qiang Li. "A Method to Embed Resonant Inductor Into PCB Matrix Transformer for High-Density Resonant Converters". In: *IEEE Transactions on Power Electronics* 39.2 (2024), pp. 2385–2400. DOI: 10.1109/TPEL.2023.3330974.

[212] Veda Samhitha Duppalli and Scott Sudhoff. "Power density comparison of three-phase AC inductor architectures". In: *2017 IEEE Electric Ship Technologies Symposium (ESTS)*. 2017, pp. 217–224. DOI: 10.1109/ESTS.2017.8069284.

[213] Lei Wang, Donglai Zhang, Jinpei Duan, and Yangyang Hao. "High-Frequency 12 V Regulated LLC Bus Converter With Integrated Multiphase Inverse Coupled Resonant Inductor". In: *IEEE Transactions on Power Electronics* 38.5 (2023), pp. 5742–5762. DOI: 10.1109/TPEL.2022.3232893.

[214] A. Balakrishnan, W.T. Joines, and T.G. Wilson. "Air-gap reluctance and inductance calculations for magnetic circuits using a Schwarz-Christoffel transformation". In: *IEEE Transactions on Power Electronics* 12.4 (1997), pp. 654–663. DOI: 10.1109/63.602560.

[218] Haoran Li, Seungjae Ryan Lee, Min Luo, Charles R. Sullivan, Yuxin Chen, and Minjie Chen. "MagNet: A Machine Learning Framework for Magnetic Core Loss Modeling". In: *2020 IEEE 21st Workshop on Control and Modeling for Power Electronics (COMPEL)*. 2020, pp. 1–8. DOI: 10.1109/COMPEL49091.2020.9265869.

[219] Mike K. Ranjram, Pedro Acosta, and David J. Perreault. "Design Considerations for Planar Magnetic Terminations". In: *2019 20th Workshop on Control and Modeling for Power Electronics (COMPEL)*. 2019, pp. 1–8. DOI: 10.1109/COMPEL.2019.8769642.

Three-Phase LLC Converters

[150] Chao Fei, Rimon Gadelrab, Qiang Li, and Fred. C. Lee. "High-Frequency Three-Phase Interleaved LLC Resonant Converter With GaN Devices and Integrated Planar Magnetics". In: *IEEE Journal of Emerging and Selected Topics in Power Electronics* 7 (2019), pp. 653–663. URL: https://api.semanticscholar.org/CorpusID:139808233.

[151] Enrico Orietti, Paolo Mattavelli, Giorgio Spiazzi, Claudio Adragna, and Giuseppe Gattavari. "Current sharing in three-phase LLC interleaved resonant converter". In: *2009 IEEE Energy Conversion Congress and Exposition*. Sept. 2009, pp. 1145–1152. DOI: 10.1109/ECCE.2009.5316510.

[152] Jing-Yuan Lin, Hsuan-Yu Yueh, Yi-Feng Lin, and Pin-Hsien Liu. "Analysis and Design of Three-Phase LLC Resonant Converter with Matrix Transformers". In: *Energies* (2022). DOI: 10.3390/en15041315.

[153] Rimon Gadelrab, Ahmed Nabih, Fred C. Lee, and Qiang Li. "LLC Resonant Converter with 99 Efficiency for Data Center Server". In: *2021 IEEE Applied Power Electronics Conference and Exposition (APEC)*. 2021, pp. 310–319. DOI: 10.1109/APEC42165.2021.9487423.

[154] Yucen Li, Shuai Shao, Hui Chen, Junming Zhang, and Kuang Sheng. "High-gain high-efficiency IPOS LLC converter with coupled transformer and current sharing capability". In: *CPSS Transactions on Power Electronics and Applications* 5.1 (2020), pp. 63–73. DOI: 10.24295/CPSSTPEA.2020.00006.

[156] R. Mirzahosseini and F. Tahami. "A phase-shift three-phase bidirectional series resonant DC/DC converter". In: *IECON 2011 - 37th Annual Conference of the IEEE Industrial Electronics Society*. 2011, pp. 1137–1143. DOI: 10.1109/IECON.2011.6119468.

[158] Mostafa Noah, Shota Kimura, Jun Imaoka, Wilmar Martinez, Shun Endo, Masayoshi Yamamoto, and Kazuhiro Umetani. "Magnetic Design and Experimental Evaluation of a Commercially Available Single Integrated Transformer in Three-Phase LLC Resonant Converter". In: *IEEE Transactions on Industry Applications* 54.6 (2018), pp. 6190–6204. DOI: 10.1109/TIA.2018.2856631.

[159] Anup Anurag, Sayan Acharya, Subhashish Bhattacharya, Todd R. Weatherford, and Andrew A. Parker. "A Gen-3 10-kV SiC MOSFET-Based Medium-Voltage Three-Phase Dual Active Bridge Converter Enabling a Mobile Utility Support Equipment Solid State Transformer". In: *IEEE Journal of Emerging and Selected Topics in Power Electronics* 10.2 (2022), pp. 1519–1536. DOI: 10.1109/JESTPE.2021.3069810.

[160] Jiajia Guan, Zongheng Wu, Teng Liu, Jin Wen, Wenzhe Xu, Cai Chen, and Yong Kang. "A High Efficiency Δ-Lr-Y Type Three-Phase Interleaved LLC Converter With Less Transformer Loss". In: *IEEE Transactions on Power Electronics* 38.9 (2023), pp. 11152–11168. DOI: 10.1109/TPEL.2023.3283391.

[161] Sayed Abbas Arshadi, Martin Ordonez, Wilson Eberle, Mohammad Ali Saket, Marian Craciun, and Chris Botting. "Unbalanced Three-Phase *LLC* Resonant Converters: Analysis and Trigonometric Current Balancing". In: *IEEE Transactions on Power Electronics* 34.3 (2019), pp. 2025–2038. DOI: 10.1109/TPEL.2018.2846526.

[162] Sayed Abbas Arshadi, Martin Ordonez, Wilson Eberle, Marian Craciun, and Chris Botting. "Three-Phase LLC Battery Charger: Wide Regulation and Improved Light-Load Operation". In: *IEEE Transactions on Power Electronics* 36.2 (2021), pp. 1519–1531. DOI: 10.1109/TPEL.2020.3006422.

[168] Yu-Chen Liu, Chen Chen, Yu-Chen Chung, Meng-Chi Tsai, and Katherine A. Kim. "Integrated magnetics optimization process for an interleaved three-phase buck converter at 500 kHz". In: *IET Power Electronics* 16.10 (2023), pp. 1743–1753. DOI: https://doi.org/10.1049/pel2.12338. eprint: https://ietresearch.onlinelibrary.wiley.com/doi/pdf/10.1049/pel2.12338. URL: https://ietresearch.onlinelibrary.wiley.com/doi/abs/10.1049/pel2.12338.

[179] Virginia Tech Intellectual Properties Inc. "Multi-phase interleaving isolated DC/DC converter". Patent US6944033B1 (United States). Filed: 2002-06-14, Issued: 2005-09-13. Sept. 2005. URL: https://patents.google.com/patent/US6944033B1/en.

[181] "Three-phase transformer, three-phase inductor, and magnetic core". CN215183430U. Chinese Utility Model Patent. Dec. 2021.

[183] "Multiphase Three-Phase Integrated Inductor and Transformer". US12212247B2. U.S. Patent. Jan. 2025.

[246] Grover Torrico-Bascope, Cicero Postiglione, and Ltd. Huawei Technologies Co. "Four-switch three phase DC-DC resonant converter". WO2018006961A1. International Publication under the PCT. Jan. 2018. URL: https://patentscope.wipo.int/search/en/detail.jsf?docId=WO2018006961.

Multi-Phase LLC Converters

[164] Taotao Jin and Keyue Smedley. "Multiphase LLC Series Resonant Converter for Microprocessor Voltage Regulation". In: *Conference Record of the 2006 IEEE Industry Applications Conference Forty-First IAS Annual Meeting*. Vol. 5. 2006, pp. 2136–2143. DOI: 10.1109/IAS.2006.256838.

[165] Xiang Zhang, S. Pan, and P. Jain. "A Discrete Coupled Multiphase Interleaved LLC Converter With Symmetrical Components Analysis". In: *IEEE Transactions on Power Electronics* 38 (2023), pp. 14150–14165. DOI: 10.1109/TPEL.2023.3279822.

[166] R. Gadelrab and F. Lee. "PCB-Based Magnetic Integration and Design Optimization for Three-Phase LLC". In: *IEEE Transactions on Power Electronics* 38 (2023), pp. 14037–14049. DOI: 10.1109/TPEL.2023.3285652.

[167] J. Wang, W. Pei, Jiawen Hu, Shuang Zhao, and Jiacai Zhuang. "Five-Phase LLC Resonant DC/DC Converter Utilizing CLC Filter for Current Sharing". In: *IEEE Transactions on Industrial Electronics* 70 (2023), pp. 8634–8644. DOI: 10.1109/TIE.2022.3215456.

[169] Hongliang Wang, Yang Chen, Yanfei Liu, J. Afsharian, and Z. Yang. "A Passive Current Sharing Method With Common Inductor Multiphase LLC Resonant Converter". In: *IEEE Transactions on Power Electronics* 32 (2017), pp. 6994–7010. DOI: 10.1109/TPEL.2016.2626312.

[170] Zhifeng Sun, Qin Wang, Qunfang Wu, Lan Xiao, Jinbo Li, Zhitian Liu, and Junlin Zhu. "A Unified Common Inductor and Common Capacitor Current Sharing Method for Multiphase LLC Converter". In: *IEEE Transactions on Power Electronics* 37 (2022), pp. 12182–12196. DOI: 10.1109/TPEL.2022.3178497.

[171] Hanjing Dong and Xiaogao Xie. "Review of Current-Sharing Schemes for Multiphase LLC Resonant Converter". In: *IEEE Transactions on Power Electronics* 40 (2025), pp. 1322–1345. DOI: 10.1109/TPEL.2024.3447047.

[172] Yue-Lin Lee, Han-Hsiang Chen, and Kuo-Ing Hwu. "Applying a Current Sharing Method Based on Partial Energy Processing to Multiphase LLC Resonant Converters". In: *Energies* (2024). DOI: 10.3390/en17153859.

[173] Yue-Lin Lee and Kuo-Ing Hwu. "Multiphase LLC DC-Link Converter with Current Equalization Based on CM Voltage-Controlled Capacitor". In: *Energies* (2024). DOI: 10.3390/en17112793.

Electromagnetic Compatibility

[163] Mohammadreza Pashaei, Mohammadhesam Hasanisadi, and Farzad Tahami. "Comprehensive Conducted Emission Analysis of the Three-Phase and Single-Phase LLC Resonant Converters for EV Application". In: *IEEE Transactions on Electromagnetic Compatibility* 65.5 (2023), pp. 1556–1564. DOI: 10.1109/TEMC.2023.3280362.

[191] Shuo Wang, Fred C. Lee, and Qiang Li. "Improved Balance Technique for Common-Mode Noise Suppression of PCB-Based PFC". In: *IEEE Transactions on Power Electronics* 37.4 (2022), pp. 4174–4182. DOI: 10.1109/TPEL.2021.3124505.

[252] Tyler McGrew, Xingyu Chen, and Qiang Li. "PCB Inductor With Integrated Shielding to Contain Switching Electric Field and Reduce CM Noise". In: *IEEE Transactions on Power Electronics* 40.1 (2025), pp. 944–957. DOI: 10.1109/TPEL.2024.3463486.

Modelling of LLC Converters

[206] R. L. Steigerwald. "A comparison of half-bridge resonant converter topologies". In: *1987 2nd IEEE Applied Power Electronics Conference and Exposition*. 1987, pp. 135–144. DOI: 10.1109/APEC.1987.7067142.

[207] Xiang Fang, Haibing Hu, Z. John Shen, and Issa Batarseh. "Operation Mode Analysis and Peak Gain Approximation of the LLC Resonant Converter". In: *IEEE Transactions on Power Electronics* 27.4 (2012), pp. 1985–1995. DOI: 10.1109/TPEL.2011.2168545.

[209] R.L. Steigerwald, R.W. De Doncker, and H. Kheraluwala. "A comparison of high-power DC-DC soft-switched converter topologies". In: *IEEE Transactions on Industry Applications* 32.5 (1996), pp. 1139–1145. DOI: 10.1109/28.536876.

[210] Mladen Ivankovic. “Optimal LLC Converter Design: From First-Harmonic Approximation through Design-Oriented Analysis”. 2024.

PCB Layout

[89] Yuliang Cao, Minh Ngo, Ning Yan, Dong Dong, Rolando Burgos, and Agirman Ismail. “Design and Implementation of an 18-kW 500-kHz 98.8% Efficiency High-Density Battery Charger With Partial Power Processing”. In: *IEEE Journal of Emerging and Selected Topics in Power Electronics* 10.6 (2022), pp. 7963–7975. DOI: 10.1109/JESTPE.2021.3108717.

[240] Cletus A. Hoer and Carl H. Love. “Exact inductance equations for rectangular conductors with applications to more complicated geometries”. In: *Journal of Research of the National Bureau of Standards, Section C: Engineering and Instrumentation* (1965), p. 127. URL: https://api.semanticscholar.org/CorpusID:110002184.

[241] A. E. Ruehli. “Inductance Calculations in a Complex Integrated Circuit Environment”. In: *IBM Journal of Research and Development* 16.5 (1972), pp. 470–481. DOI: 10.1147/rd.165.0470.

[242] F.W. Grover. *Inductance Calculations*. Dover Books on Electrical Engineering. Dover Publications, 2013. ISBN: 9780486318356.

[243] Zheng Chen, Dushan Boroyevich, and Rolando Burgos. “Experimental parametric study of the parasitic inductance influence on MOSFET switching characteristics”. In: *The 2010 International Power Electronics Conference - ECCE ASIA -*. 2010, pp. 164–169. DOI: 10.1109/IPEC.2010.5543851.

[244] Kazuhiro Umetani, Ryunosuke Matsumoto, and Eiji Hiraki. “Prevention of Oscillatory False Triggering of GaN-FETs by Balancing Gate-Drain Capacitance and Common-Source Inductance”. In: *IEEE Transactions on Industry Applications* 55.1 (2019), pp. 610–619. DOI: 10.1109/TIA.2018.2868272.

Component Datasheets

[91] VICOR Corporation. *DC-DC Converter DCM4623TD2H31E0y7z - Datasheet*. Datasheet, accessed on 2025-07-26. 2020. URL: https://www.vicorpower.com/products/dcm/dcm4623td2h31e0y7z.

[211] Ltd. Proterial. *MnZn Soft Ferrite Cores for High Frequency Power Supplies*. Hitachi. Ferrite core materials datasheet series. Dec. 2022. URL: https://www.proterial.com.

[216] DMEGC Magnetics. *DMR51W Material Characteristics*. Rev. E. Material characteristic datasheet, ferrite magnetic cores. Dec. 2018. URL: https://www.chinadmegc.com.

[217] TDG Holding. *TP5H High-Frequency Power Material*. Ferrite material datasheet for high-frequency power applications. 2020. URL: https://www.tdgcore.com.

[220] *E4990A Impedance Analyzer: 20 Hz to 10/20/30/50/120 MHz*. 5991-3890EN. Datasheet. Keysight Technologies. URL: https://assets-us-01.kc-usercontent.com/ecb176a6-5a2e-0000-8943-84491e5fc8d1/cbf0020f-72d8-4c09-8357-b13c3abec010/5991-3890ENE4990A.pdf (visited on 08/16/2025).

[222] GaN Systems Inc. *GS66506T 650 V Enhancement-Mode GaN Transistor Datasheet*. Rev. Oct. 2015. Accessed: Aug. 21, 2025. GaN Systems Inc. 2015. URL: https://www.infineon.com/dgdl/Infineon-GS66506T-DataSheet-v01%5C_00-EN.pdf?fileId=8ac78c8c8d2fe47b018e5160f3b95235.

[223] GaN Systems Inc. *GS66508T 650 V Enhancement-Mode GaN Transistor Datasheet*. Rev. Jan. 2020. Accessed: Aug. 21, 2025. GaN Systems Inc. 2020. URL: https://www.infineon.com/dgdl/Infineon-GS66508T-DataSheet-v01%5C_00-EN.pdf?fileId=8ac78c8c8d2fe47b018e5161cc5853e2.

[224] Efficient Power Conversion Corporation. *EPC2308 200 V Enhancement-Mode eGaN FET Datasheet*. Rev. Jul. 2023. Accessed: Aug. 20, 2025. Efficient Power Conversion Corporation. 2025. URL: https://epc-co.com/epc/portals/0/epc/documents/datasheets/EPC2308_datasheet.pdf.

[225] Efficient Power Conversion Corporation. *EPC2307 150 V Enhancement-Mode eGaN FET Datasheet*. Rev. May. 2023. Accessed: Aug. 20, 2025. Efficient Power Conversion Corporation. 2025. URL: https://epc-co.com/epc/portals/0/epc/documents/datasheets/EPC2307_datasheet.pdf.

[229] Infineon Technologies AG. *BSZ018N04LS6 40 V N-Channel MOSFET Datasheet*. Rev. Dec. 2019. Accessed: Aug. 20, 2025. Infineon Technologies AG. 2019. URL: https://www.infineon.com/dgdl/Infineon-BSZ018N04LS6-DataSheet-v02%5C_01-EN.pdf.

[230] Infineon Technologies AG. *IQE013N04LM6CG OptiMOS 40 V Power MOSFET Datasheet*. Rev. Mar. 2020. Accessed: Aug. 20, 2025. Infineon Technologies AG. 2020. URL: https://www.infineon.com/dgdl/Infineon-IQE013N04LM6CG-DataSheet-v02%5C_00-EN.pdf.

[231] Toshiba Electronic Devices & Storage Corporation. *TPWR8004PL 40 V N-Channel MOSFET Datasheet*. Rev. Dec. 2023. Accessed: Aug. 20, 2025. Toshiba Electronic Devices & Storage Corporation. 2023. URL: https://toshiba.semicon-storage.com/info/TPWR8004PL_datasheet_en_20231218.pdf.

[232] ON Semiconductor. *NVMFS5C410N 40 V N-Channel MOSFET Datasheet*. Rev. Jun. 2023. Accessed: Aug. 20, 2025. ON Semiconductor. 2025. URL: https://www.onsemi.com/download/data-sheet/pdf/nvmfs5c410n-d.pdf.

[233] Efficient Power Conversion Corporation. *EPC2302 100 V Enhancement-Mode eGaN FET Datasheet*. Rev. 1.0, Apr. 2021. Accessed: Aug. 20, 2025. Efficient Power Conversion Corporation. 2025. URL: https://epc-co.com/epc/portals/0/epc/documents/datasheets/EPC2302_datasheet.pdf.

[234] Efficient Power Conversion Corporation. *EPC2361 100 V Enhancement-Mode eGaN FET Datasheet*. Rev. Aug. 2025. Accessed: Aug. 20, 2025. Efficient Power Conversion Corporation. 2025. URL: https://epc-co.com/epc/portals/0/epc/documents/datasheets/EPC2361_datasheet.pdf.

[235] Efficient Power Conversion Corporation. *EPC2366 40 V eGaN FET for High-Density Designs Datasheet*. Rev. Aug. 2025. Accessed: Aug. 21, 2025. Efficient Power Conversion Corporation. 2025. URL: https://epc-co.com/epc/Portals/0/epc/documents/datasheets/EPC2366_datasheet.pdf.

[236] Efficient Power Conversion Corporation. *EPC2367 100 V eGaN FET for High-Density Designs Datasheet*. Rev. Nov. 2022. Accessed: Aug. 20, 2025. Efficient Power Conversion Corporation. 2025. URL: https://epc-co.com/epc/portals/0/epc/documents/datasheets/EPC2367_datasheet.pdf.

[237] Skyworks Solutions Inc. *Si827x 4 Amp ISOdriver with High Transient (dV/dt) Immunity (Si8271)*. Rev. Jul. 2022. Accessed: Aug. 20, 2025. Skyworks Solutions Inc. 2025. URL: https://www.skyworksinc.com/-/media/Skyworks/SL/documents/public/data-sheets/Si827x.pdf.

[238] Texas Instruments. *LM5114 Single 7.6-A Peak Current Low-Side Gate Driver*. Rev. Nov. 2015. Accessed: Aug. 20, 2025. Texas Instruments. 2025. URL: https://www.ti.com/lit/ds/symlink/lm5114.pdf.

[239] Texas Instruments. *LMG1210 200-V, 1.5-A, 3-A Half-Bridge MOSFET and GaN FET Driver*. Rev. Feb. 2019. Accessed: Aug. 20, 2025. Texas Instruments. 2025. URL: https://www.ti.com/product/LMG1210.

[245] *ADuM6210/ADuM6211/ADuM6212: Dual-Channel Isolators with Integrated DC-to-DC Converters*. Data Sheet, Rev. F. Analog Devices, Inc. 2025. URL: https://www.analog.com/media/en/technical-documentation/data-sheets/adum6210_6211_6212.pdf (visited on 09/24/2025).

This Work

[65] **Daniel Ríos Linares** and Miroslav Vasić. "High Power Density Three-Phase LLC DC/DC Converter with Coupled Resonant Inductor and Wye-Delta Transformer for Aircraft Applications". In: *2023 IEEE Applied Power Electronics Conference and Exposition (APEC)*. 2023, pp. 1729–1736. DOI: 10.1109/APEC43580.2023.10131660.

[66] **Daniel Ríos Linares**, Miroslav Vasić, and Pedro Alou Cervera. "Three-Phase LLC DC/DC Converter in Stack Configuration: A Topology for High-Voltage Conversion Ratio Applications". In: *2023 IEEE Applied Power Electronics Conference and Exposition (APEC)*. 2023, pp. 1747–1752. DOI: 10.1109/APEC43580.2023.10131367.

[67] **Daniel Ríos Linares**, Alberto Delgado Exposito, and Miroslav Vasic. "Magnetic Optimization for Three-Phase LLC Converters". In: *PCIM Europe 2023; International Exhibition and Conference for Power Electronics, Intelligent Motion, Renewable Energy and Energy Management*. 2023, pp. 1–8. DOI: 10.30420/566091133.

[68] **Daniel Ríos Linares**, Miguel Astudillo Martínez, and Miroslav Vasić. "Optimal Driving Strategies for GaN HEMT: A Numerical Non-Linear Datasheet-Based Model". In: *2024 IEEE Applied Power Electronics Conference and Exposition (APEC)*. 2024, pp. 2629–2636. DOI: 10.1109/APEC48139.2024.10509318.

[69] Xianghao Mo, **Daniel Ríos Linares**, Regina Ramos, and Miroslav Vasić. "FPGA-based Hybrid Simulator for Real-Time 3-D Temperature Monitoring of Power Converters". In: *2025 IEEE Applied Power Electronics Conference and Exposition (APEC)*. 2025, pp. 1375–1382. DOI: 10.1109/APEC48143.2025.10977068.

[70] Xianghao Mo, **Daniel Ríos Linares**, Regina Ramos, and Miroslav Vasić. "Thermal Transient Digital Twin Modelling for Power Converters". In: *PCIM Europe 2024; International Exhibition and Conference for Power Electronics, Intelligent Motion, Renewable Energy and Energy Management*. 2024, pp. 2381–2388. DOI: 10.30420/566262335.

[71] Marta Espinosa del Pozo, Xianghao Mo, **Daniel Ríos Linares**, Regina Ramos, and Miroslav Vasić. "Cosimulación Electrotérmica en Tiempo Real con Hardware-in-the-Loop para la Creación de Gemelos Digitales en Convertidores de Potencia". In: *SAAEI'2025*. 2025.

[72] **Daniel Ríos Linares**, Xianghao Mo, Regina Ramos, and Miroslav Vasić. "Digital Twinning for Power Converter Temperature Monitoring". In: *Proc. IEEE International Conference on Electrical Engineering (EE)*. Novi Sad, Serbia, 2025, *Accepted (August 2025)*.

[73] Miroslav Vasić and **Daniel Ríos Linares**. "Mastering the Art of High-Frequency LLC Converters". PCIM Europe 2024; International Exhibition and Conference for Power Electronics. 2024.

[74] Miroslav Vasić and **Daniel Ríos Linares**. "Mastering the Art of High-Frequency Multi-phase LLC Converters". 2025 IEEE Applied Power Electronics Conference and Exposition (APEC). 2025.

[75] **Daniel Ríos Linares**, Alberto Delgado Expósito, and Miroslav Vasić. "High-Gain High-Frequency Three-Phase *LLC* Resonant Converter Design Based on the Wye–Delta Transformer for Aircraft Applications". In: *IEEE Transactions on Power Electronics* 39.4 (2024), pp. 4367–4383. DOI: 10.1109/TPEL.2023.3339973.

[76] Xianghao Mo, **Daniel Ríos Linares**, Regina Ramos, and Miroslav Vasić. "Toward Embeddable Digital Twins: A Voxel-Based Approach for Power Converter Temperature Monitoring". In: *IEEE Journal of Emerging and Selected Topics in Power Electronics* 13.3 (2025), pp. 2781–2798. DOI: 10.1109/JESTPE.2025.3541343.

[77] **Daniel Ríos Linares** and Miroslav Vasić. "Detailed Description of the Three-Phase LLC Converter in Stack Configuration: A Topology for High Power Density DC/DC Conversion". In: *IEEE Transactions on Power Electronics* (2026), *To be submitted*.

[78] **Daniel Ríos Linares** and Miroslav Vasić. "High Output Capacitance (HOC) Model for Reconfigurable LLC Converters Design". In: *IEEE Transactions on Circuits and Systems II* (2026), *Work in progress*.

[79] Gabriel Luis Maldonado Roldán, **Daniel Ríos Linares**, and Miroslav Vasić. "Novel Bidirectional Capacitively Isolated Resonant Switched Capacitor DCX Topology for Voltage Reduction". In: *IEEE Transactions on Power Electronics* (2025-2026), *Submitted for review (May 2025)*.

[80] Gabriel Luis Maldonado Roldán, Esteban Martínez Barroeta, **Daniel Ríos Linares**, and Miroslav Vasić. "Volume Comparison of Isolated DC-DC converters for maximum power density". In: *SAAEI'2025*. 2025.